



University
of Glasgow

Wilson, Alasdair David (2016) *Finite difference simulations of neutral gas-MHD interactions in partially ionized plasmas*. PhD thesis.

<http://theses.gla.ac.uk/7209/>

Copyright and moral rights for this thesis are retained by the author

A copy can be downloaded for personal non-commercial research or study

This thesis cannot be reproduced or quoted extensively from without first obtaining permission in writing from the Author

The content must not be changed in any way or sold commercially in any format or medium without the formal permission of the Author

When referring to this work, full bibliographic details including the author, title, awarding institution and date of the thesis must be given

Finite Difference Simulations of Neutral Gas-MHD Interactions in Partially Ionized Plasmas

Alasdair David Wilson, M.Sci.

Astronomy and Astrophysics Group
SUPA School of Physics and Astronomy
Kelvin Building
University of Glasgow
Glasgow, G12 8QQ
Scotland, U.K.



University
of Glasgow

Presented for the degree of
Doctor of Philosophy
The University of Glasgow
January 2016

Abstract

This thesis deals with the theoretical and numerical modelling of partially ionized plasmas. The study of partially ionized plasmas is important in both astrophysical and laboratory contexts and we present a novel finite difference approach to modelling a magnetohydrodynamic plasma and hydrodynamic gas as well as some interaction terms between them. In particular we model fluid limits of a collisional drag, momentum coupling term and a critical velocity (Alfvén) ionization term.

Chapter 1 reviews the necessary background material relevant to this thesis. We introduce relevant plasma parameters that are useful to help understand the regimes at which MHD operates and which are later used when placing criteria on the conditions required for, and the rate equations of, ionization. We introduce the fluid limit model of non-resistive plasmas (ideal MHD), as well as theoretical models for gas-plasma collisions and Alfvén ionization.

Chapter 2 lays out the model of a linear finite difference gas-MHD momentum coupling code (GMMC) that we modify by the addition of a fluid Alfvén ionization term. We explore the codes stability and fidelity and we explore Fresnel interference patterns as a test scenario.

Chapter 3 lays out the model equations and derivation of a non-linear finite difference gas-MHD interactions code (GMIC).

Chapter 4 uses the code GMIC to explore the momentum coupling between the gas and plasma fluids in a non-linear regime. We show that the presence of a frictional drag term effects both fluids in a variety of simulated scenarios. Propagation of waves and diffusion are effected significantly across a range of parameter space. We show the

formation of ‘plasmoids’ by interacting, momentum coupled waves. We see that the momentum coupling has a somewhat similar effect on plasmas as a resistive term does.

Chapter 5 uses both the linear and non-linear codes to simulate Alfvén ionization in a variety of scenarios. With both codes we see that waves and flows can be sources of ionization if the relative velocity between the two simulated fluids exceeds a pre-set threshold. This ionization effects the dynamics of the system significantly, firstly the extraction of kinetic energy in order to ionize introduces a directional and amplitude dependant damping of waves; secondly by providing a source of new plasma that the fluid is forced to react to. Also in this chapter we discuss how Alfvén ionization might play a role in astrophysical contexts, in particular, the solar photosphere and brown dwarf atmospheres.

Chapter 6 deviates from the previous work to explore the possibility that dielectrophoretic forces may be able to stratify the dynamic atmosphere of the Sun. We derive a simple expression for the DEP-force due to a neutral particle moving through a magnetic field and becoming polarized and we examine the displacement caused by this field and the ambipolar field. We also simulate the ability of a hypothetical DEP-force to separate elements based on their polarizability to mass ratio.

Chapter 7 summarises the conclusion of the previous chapters and includes a brief discussion about possible extensions to this work.

Contents

Preface	ii
List of Tables	viii
List of Figures	ix
Acknowledgements	xiii
1 Introduction	2
1.1 Characteristics of a Plasma	4
1.1.1 Debye length	4
1.1.2 Plasma Parameter	7
1.1.3 Plasma Frequency	8
1.1.4 Cyclotron frequency	10
1.2 Collisions in Plasmas	13
1.2.1 Charged-neutral collisions	13
1.2.2 Electron-ion interactions	15
1.2.3 Relaxation Time	17
1.3 Ionization Processes	18
1.3.1 Electron Impact Ionization	19
1.3.2 Electrical Breakdown	23
1.4 Bulk Plasma Descriptions	27
1.4.1 Kinetic Theory	27
1.4.2 Magnetohydrodynamics	30

1.5	Modifications to MHD for a Partially Ionized Plasma	36
1.5.1	Momentum Coupling	37
1.5.2	Critical Velocity/Alfvén Ionization	39
2	Linear Gas/MHD Interactions Code	49
2.1	Introduction	49
2.2	The Model Equations	50
2.2.1	Numerical Scheme	53
2.2.2	Normalization	53
2.3	Finite Difference	56
2.3.1	Lax-Wendroff Scheme	58
2.4	Stability Criteria	64
2.4.1	Stability Test	67
2.5	Deviations from MHD	71
2.5.1	Momentum Coupling	71
2.5.2	Alfvén Ionization	73
2.6	Example Result: Interference Fringes	76
2.6.1	Simulation Setup	77
2.6.2	Numerical Results	78
2.7	Limitations of GMMC	85
3	Non-Linear Gas/MHD Interactions Code	90
3.1	Model Equations	92
3.1.1	Conservative Form MHD	92
3.1.2	Normalization	96
3.1.3	Flux Functions	99
3.2	Numerical Scheme	103
3.2.1	Lax-Friedrichs	103
3.2.2	Richtmyer Two-Step	104
3.2.3	MacCormack	105

3.2.4	Stability	107
3.3	Boundary Conditions	108
3.4	The Code	110
3.4.1	Scalability	112
3.5	Gas Plasma Interactions	113
4	Momentum Coupling in a Partially Ionized Plasma	114
4.1	Cylindrical bombs	115
4.1.1	Positive Gaussian Cylindrical Bomb	115
4.1.2	Negative Gaussian Density Cylindrical Bomb	121
4.2	Coupled Waves	126
4.3	Conclusions	133
5	Ionization in a Gas-MHD Plasma	136
5.1	Critical Velocity Ionization in a Linear Regime	136
5.1.1	Bulk Flows	136
5.1.2	Plane Waves	138
5.1.3	Cylindrically Symmetric Waves	148
5.2	Critical Velocity Ionization in a Non-Linear Regime	154
5.2.1	Ionization from Gas Bomb	154
5.2.2	Ionization from Double Bombs	159
5.2.3	Interplay with Momentum Coupling	164
5.3	Astrophysical Contexts	167
5.3.1	Brown Dwarfs	168
5.3.2	Solar Atmosphere	170
5.3.3	Epoch of Recombination	174
5.4	Conclusions	174
6	Dielectrophoresis in Astrophysical Plasmas	178
6.1	DEP-FFF	179
6.2	Theory	181

6.2.1	p/m Ratio of Select Elements	183
6.2.2	Solar Lorentz Field	190
6.2.3	Ambi-polar Field	191
6.3	Simulations	192
6.4	Conclusions	198
7	Conclusions	199
7.1	Further Work	203
	Bibliography	205

List of Tables

6.1	Selected atomic characteristics	188
6.2	Selected molecular characteristics	189

List of Figures

1.1	The equilibrium ionization fraction of hydrogen	24
1.2	The Paschen curve for an arbitrary gas	26
1.3	Electrical schematic of a homopolar CIV device	41
1.4	Burning voltage against discharge current for a homopolar device	42
1.5	Schematic showing Alfvén ionization mechanism	43
2.1	Time evolution of the 1-dimensional wave equation solved using a FTCS scheme	68
2.2	Time evolution of the 1-dimensional wave equation solved with an LF scheme	70
2.3	The time evolution of the 1 dimensional wave equation solved with a LW scheme	71
2.4	Flowchart showing the process for incorporation of an Alfvén ionization subroutine into a finite difference code	77
2.5	The spatial envelope, A_m for a set of discrete wave sources that will form Fresnel interference fringes.	79
2.6	Plasma density map showing interference patterns in an uncoupled gas-plasma mixture	80
2.7	Vector diagram of the magnetic field in the uncoupled case	81
2.8	Plasma density map showing interference patterns in a coupled gas-plasma mixture	83
2.9	Vector diagram of the magnetic field in the coupled case	84

2.10	A y-directed cross section of density through the line of symmetry . . .	86
3.1	A schematic for the predictor and corrector steps of the second order two step Richtmyer finite difference scheme.	105
3.2	Damping of a wave entering the sacrificial region	110
3.3	Scalability of GMIC	113
4.1	Evolution of a Gaussian over-density in the gas	116
4.2	The directionality of cylindrical symmetric gas expansion	118
4.3	Time evolution of an x-directed slice of plasma density	119
4.4	Integrated gas density (total mass within domain) over time	120
4.5	Integrated gas density at late times	121
4.7	Time evolution of the plasma density along a slice through the centre in the x direction for the negative bomb. This evolution shows the propagation rate of the wave as well as the amplitude dropping over time	123
4.8	Total density summed between the positive and negative disturbances at $t = 200$	124
4.9	Comparison between x-directed slices of the positive and negative den- sity disturbances	125
4.10	Time evolution of the gas density of the centre point of the domain . .	126
4.11	Snapshots of gas density showing the downwards propagation of an acoustic wave in the gas with no coupling	128
4.12	Snapshots of plasma density showing the leftwards propagation of a magnetosonic wave in the plasma with no coupling	129
4.13	Total density (gas + plasma) of interacting waves with momentum cou- pling	130
4.14	Superposition of total density (gas + plasma) of non-interacting waves	131
4.15	Plasma density and magnetic field in the coupled case show the forma- tion of plasmoids	132
4.16	Plasma density and magnetic field shows no plasmoids in the absence of coupling	133

5.1	Perturbations in gas density caused by a plane acoustic wave driven at the top boundary	140
5.2	Perturbations in plasma density as a result of AI from the plane wave in the gas	141
5.3	Evolution of integrated densities in the plane wave case	142
5.4	Perturbations in gas density as a result of a driven plane wave with momentum coupling	144
5.5	Perturbations in plasma density caused by AI with momentum coupling enabled	145
5.6	Integrated plasma density for various choices of Γ	146
5.7	Maximum amplitude of sympathetic magneto-acoustic waves	147
5.8	The perturbations around the mean gas density showing an initially cylindrically symmetric acoustic wave in the gas as a source of relative velocity for AI with $\Gamma = 10^{-5}$, $f = 0.01$. The equilibrium magnetic field is in the horizontal direction, the portion of the wave that propagates across the field loses significant amplitude due to the influence of AI whereas the fraction of the wave in the parallel-to-field direction is relatively unimpeded.	149
5.9	Perturbations around the mean plasma density with $\Gamma = 10^{-5}$, $f = 0.01$. Red indicates the areas where the most plasma has been created. The equilibrium magnetic field is in the horizontal direction, plasma is created by wave motion in the perpendicular-to-field direction but due to the $\mathbf{v} \times \mathbf{B}$ force it diffuses along the field lines at approximately the sound speed.	150
5.10	Evolution of total plasma density as a result of AI and the cylindrical wave	152
5.11	Gas density from gas bomb, uncoupled	155
5.12	Plasma density due to a gas bomb in the uncoupled case	156
5.13	Map of the relative velocity perpendicular to the field as a result of the gas bomb	157

5.14	Net ionization from the gas bomb	158
5.15	Initial conditions for the double bomb	160
5.16	Net ionization from the double bomb	161
5.17	Total ionization from a double bomb with varying β	163
5.18	Total ionization from a double bomb with varying Γ	164
5.19	Map of plasma density created by a double bomb, uncoupled	165
5.20	Map of plasma density created by a double bomb, coupled	166
5.21	FIP bias for select elements as a function of ionization potential and critical velocity	171
5.22	Observed FIP in various solar locations	173
6.1	Polarizability against mass for selected elements	184
6.2	p/m ratio against mass for selected elements	186
6.3	Gaussian magnetic field, an approximation of the shape of the field that might be found in a MBP.	193
6.4	The trajectories of free particles of select atomic species experiencing a DEP force.	194
6.5	The trajectories of fluid elements for select atomic species under a DEP force	195
6.6	The evolving gas density of a flow consisting of a polarized particle moving through a magnetic feature.	197

Acknowledgements

Four-years sounds like a long time but it feels like only yesterday that I first started this project. I am greatly indebted to many people for making this time pass by as enjoyably (and I suppose as successfully) as it did.

The path to getting a PhD would not have been possible without the support (genetic, financial and social) of my parents, Colin and Eleanor. Especially to Eleanor who gave up a week of her retirement to check this thesis for spelling and grammar; at the very least giving me someone to help shoulder blame for all the missed typos.

The entire astronomy department deserves a mention, I don't think there is a single person that didn't help out in some way, either scientifically or just with their company, so thank you all. This goes doubly for the various inhabitants of 604 during my tenure who managed to put up with me (in some cases for years) so in no particular order thanks to: Fraser, Christina, Ewan, Gerrard, Dave, Heather, Graham, Duncan, Salma, Pete, Tony, Stephen and Ben.

In particular, a huge thanks to my supervisor, Declan, for his endless patience, support and his unrivalled ability to convince me into thinking I understood what I was doing. It is just a shame that this clarity would sometimes fade before I made it back to my desk. Likewise, thanks go out to my second supervisor, Lyndsay, who also helped me out along the way.

Finally, thanks are in order for Lindsey for managing to put up with me for the duration without a complaint.

This thesis is my own composition except where indicated in the text.
No part of this thesis has been submitted elsewhere for any other degree
or qualification.

Copyright © 2015 by Alasdair D. Wilson

28th September 2015

Chapter 1

Introduction

A plasma is traditionally referred to as the fourth state of matter. Just as heating up a liquid generally creates a gas, heating up a gas causes a further transition towards a new state of matter, leaving us with a natural progression from solid to liquid, to gas and then plasma. This gas-plasma transition occurs when individual atoms receive enough energy to liberate one or more of their outer electrons leaving a positively charged ion and negatively charged electron. This gas-like mixture of positive and negative charges is an example of a plasma. The key difference that separates the behaviour of these two states is that while the evolution of the gas is dominated by binary collisions, the charged particles in the plasma interact via long range electric and magnetic forces. These forces give rise to the collective behaviour which becomes the defining characteristic of a plasma.

The description of a gas becoming ionized and producing a plasma composed of positively charged, massive ions and negatively charged, light electrons is incomplete. Any overall electrically neutral collection of charged particles can exhibit plasma behaviour. In alternative circumstances negatively charged ions can also be produced by capturing free electrons and the plasma can be composed purely of ions, both negative and positive. In very high energy circumstances it is possible, by pair production, to produce electrons and positrons ([Ruffini et al. 2010](#)). A gas composed of electrons and positrons would exhibit a full range of plasma behaviour ([da Costa et al. 2001](#)). At

the much larger end of the size scale, dust particles that have become charged can take the place of one or both of the plasma species.

By simply defining a plasma as a system where the collective electromagnetic behaviour is important, we broaden our definition somewhat. A gas does not have to be fully ionized in order to take on those dynamics which are associated with plasmas. Several commonly studied plasmas are actually only weakly ionized yet still exhibit a full range of plasma behaviour; for example, the ionosphere has a peak ionization fraction of $\approx 2 \times 10^{-3}$ (Delobbeau 1971). The transition from a weakly ionized to fully ionized plasma can occur over a very narrow temperature range purely due to thermal ionization (Saha 1921). It is often this middle ground, at the transition between two states, which is most interesting in physics; a partially ionized gas contains the behaviour of a plasma but with additional effects from the neutral atoms. This requires the development of more complex models for the behaviour of such materials and it is the creation of such models that is explored in this thesis.

In this thesis we are not concerned with all plasmas. When we talk about a plasma we will generally only be referring to ion-electron plasmas; ion-electron plasmas are by far the most common and the large difference in mass between the two species allows access to important simplifications that are exploited in the models described. Although we will discuss a variety of plasma parameters we are generally only concerned with low temperature plasmas which we define as a plasma that is hot enough that there are enough charged particles present to drive plasma behaviour but cool enough that neutral atoms are not completely absent, they continue to play a roll on the dynamics of our plasma. We shall also be concerned with plasmas where there are high-energy fluid motions which we define as plasmas where the kinetic energies of non-random motion can exceed the ionization threshold energy. Examples of such a plasma could be astrophysical in nature such as in the photosphere of the Sun or the atmosphere of a brown dwarf as well as created in laboratory experiments such as homo-polar devices.

In this chapter we examine some of the characteristics and behaviours that plasmas exhibit as well as the foundations of plasma physics that will be used for the remainder of the thesis. In particular, we are interested in the various scales (time, distance and

frequency) that plasma behaviour manifests itself at as well as the ionization processes in a plasma. We also examine bulk descriptions of plasmas with reference to kinetic theory and magnetohydrodynamics (MHD). We combine the theory of MHD with some additional terms, designed to model these influences from neutral atoms on an MHD plasma in [2](#) and [3](#).

1.1 Characteristics of a Plasma

1.1.1 Debye length

One of the criteria for a collection of charged particles to be considered a plasma is that of a net zero charge density. That is to say that the charge density of the positively charged particles is cancelled out by that of the negatively charged particles. This condition must generally be satisfied on a global scale due to any ionization process preserving charge; for every negative charge created there is an equal amount of positive charge which results in a net zero change to the total charge density. It is however also obvious that random, Brownian motion of the particles involved will spontaneously create regions where neutrality cannot be maintained over sufficiently small scales.

If we were to consider Coulomb's law then it may seem that an electric field's influence is infinite in extent and so the introduction of any charge imbalance to any part of the plasma would affect every other charged particle in the plasma. Debye was the first to realise that the free charges in a plasma will work to shield the bulk of the plasma from any deviations from a net zero charge density ([Boyd & Sanderson 2003](#)). As soon as a region of unbalanced charge is introduced, the electric fields produced by that imbalance acts on surrounding charges in such a way as to cancel out said imbalance.

The scale at which thermal deviations from net neutrality are shielded from the rest of the plasma is dependent on both the temperature of the plasma and its number density, the characteristic distance at which this shielding occurs is known as the Debye length. In order to derive an expression for the Debye length we consider what happens

when a test charge, Q , is placed into a homogeneous plasma with an electron number density of n_e and an electron temperature of T_e . The positive charge density is fixed at n_i . The negative charge will exert a force on surrounding electrons, lowering the electron density in its vicinity until an equilibrium is established. In this case Poisson's equation is given by (Boyd & Sanderson 2003)

$$\nabla^2\phi = -\frac{\rho_q}{\epsilon_0} = -\frac{e}{\epsilon_0}(n_i - n_e) \quad (1.1)$$

where ρ_q is the charge density, e is the electron charge and ϵ_0 is the permittivity of free space. If we assume that at an infinite distance from our test charge the electron number density is equal to the ion number density ($n_e = n_i = n_0$) and that the electric field falls to 0 at infinity then, using kinetic theory, we can show that the velocity distribution of the electrons in our plasma is given by

$$f_e(v) = n_0 \left(\frac{m_e}{2\pi k_B T_e} \right)^{3/2} \exp \left[\frac{-(\frac{1}{2}m_e v^2 + q\phi)}{k_B T_e} \right] \quad (1.2)$$

where k_B is the Boltzmann constant. This equation is the same as that for a standard Maxwellian distribution but with an additional factor of $\exp(-q\phi/\kappa_B T_e)$. This is because, in statistical mechanics, the number of particles at a given velocity is proportional to $\exp[-E/k_B T_e]$ where E is the total energy. The addition of the electric field has added a potential energy term to the existing $1/2m_e v^2$ kinetic energy term in the expression for total energy. If this distribution is integrated over all velocities then we can recover the electron number density as being:

$$n_e = n_0 e^{\frac{-q\phi}{\kappa_b T_e}} \quad (1.3)$$

This expression is then substituted into equation 1.1 and we obtain the non-linear differential equation,

$$\nabla^2\phi = -\frac{n_0 e}{\epsilon_0} \left(1 - e^{\frac{e\phi}{\kappa_b T_e}} \right). \quad (1.4)$$

If we assume that $e\phi/\kappa_b T_e \ll 1$ then we can perform a Taylor expansion of the exponential term and discard high order terms in order to retrieve the linear differential

equation,

$$\nabla^2\phi = -\frac{n_0e^2}{\epsilon_0\kappa_bT_e}\phi. \quad (1.5)$$

If we assume that ϕ is spherically symmetric then only the radial component of the differential remains,

$$\frac{1}{r^2}\frac{\partial}{\partial r}\left[r^2\frac{\partial\phi}{\partial r}\right] = \frac{n_0e^2}{\epsilon_0\kappa_bT_e}\phi, \quad (1.6)$$

where r is the distance from the test charge. This has the solution,

$$\phi = \frac{a}{r}e^{-\frac{r}{\lambda_D}}, \quad (1.7)$$

where a is a constant. The exponential part of this solution contributes a decay term with a characteristic scale length λ_D where

$$\lambda_D = \sqrt{\frac{\epsilon_0\kappa_B T_e}{n_0e^2}}. \quad (1.8)$$

This scale length is the Debye length. The constant, a , is found by requiring that we retrieve Coulomb's law as $r \rightarrow 0$. This gives us

$$a = \frac{Q}{4\pi\epsilon_0} \quad (1.9)$$

The Debye length depends only on the electron temperature and the number density of the plasma. Since it is inversely proportional to number density, more dense plasmas have a smaller Debye length. This is as we would expect, as more dense plasmas have more electrons to participate in the shielding. Hotter plasmas, due to the increased thermal velocities and thus the increased range of the random motion of electrons, have larger Debye lengths.

The Debye length is useful for a number of reasons. It defines the scale length above which the plasma is electrically neutral, this distance scale is very important when we come to talk about magnetohydrodynamics in section 1.4.2. It also defines how large the sheath region around a charged surface can extend into the plasma before

the electric field can no longer influence the bulk of the plasma. In essence λ_D also defines a minimum size your system must be to exhibit plasma behaviour as a plasma that is below this size can no longer maintain the assumption of net neutrality. (Chen 1984)

1.1.2 Plasma Parameter

The argument for Debye shielding depends on there being enough electrons in a Debye sphere (a sphere with radius λ_D) in order to quickly and effectively shield momentary deviations from neutrality. This number is known as the plasma parameter, or the Debye number. The plasma parameter can be thought of as a measure of the quality of the plasma as it indicates how many charged particles are doing the Debye shielding, the more particles there are then the smaller the rearrangement of them has to be in order to shield charge and the more capable the plasma is at cancelling out electric fields.

To get the plasma parameter, N_D , we integrate the electron number density across a sphere of radius λ_D which, for a constant number density gives us

$$N_D = n_e \frac{4\pi}{3} \lambda_D^3. \quad (1.10)$$

If we substitute in our expression for λ_D from equation 1.8 then this becomes

$$N_D = \frac{4\pi}{3} \frac{(\epsilon_0 \kappa_b T_e)^{3/2}}{e^3 n_e^{1/2}}. \quad (1.11)$$

This parameter scales with temperature and inversely with electron density, where $N_d \gg 1$, the mean kinetic energy \gg the mean electrostatic potential energy. For order of magnitude estimates the $4\pi/3$ term is often dropped leaving $N_D = n_e \lambda_D^3$. This plasma parameter is key as it can be used to separate plasmas into two categories; hot and diffuse plasmas with high plasma parameters, and cold and dense plasmas where the plasma parameter is low and there are comparatively fewer particles in a Debye sphere. The plasma parameter gives us an indication of how important collisions are to the dynamics of the plasma. A plasma with a large plasma parameter will generally

have the collective, electromagnetic behaviour dominate over collisions while a low parameter plasma will have these collective effects drowned out by binary collisions. (Chen 1984)

Many astrophysical plasmas, such as the solar wind or intergalactic medium, fall into this low density and high temperature regime where the plasma parameter is high and the electromagnetic forces dominate. Laboratory plasmas, on the other hand, will often fall on the opposite side of the scale, their behaviour can be fundamentally different.

1.1.3 Plasma Frequency

One of the most fundamental behaviours of a plasma is that of plasma oscillations. We can investigate the tendency of plasmas to undergo oscillations in the following way. If you start with a homogeneous ion-electron plasma and displace the electrons from their equilibrium position then the resulting charge imbalance will produce an electric field which in turn exerts a restoring force that acts on the displaced electrons. Since the magnitude of this electric field is directly proportional to the magnitude of their displacement from the equilibrium position and since the force acts in the opposite direction to their displacement then the restoring force can be expressed in the form of Hooke's law:

$$F = -kx, \tag{1.12}$$

where x is the displacement and k is some unknown spring constant. Since the electrons have inertia then this restoring force will give rise to harmonic behaviour at some characteristic frequency. These oscillations are known as electron-plasma oscillations or Langmuir waves after one of the authors in the paper that first described them (Tonks & Langmuir 1929). We must first assume that, due to the large difference in mass and thus acceleration between electrons and ions, these electron oscillations occur fast enough that the ions are effectively stationary. In order to calculate the frequency at which these oscillations occur, we first calculate the electric field.

$$E = \frac{n_e e x}{\epsilon_0}. \quad (1.13)$$

In such a field the electrons have an equation of motion given by

$$m_e \frac{\partial^2 x}{\partial t^2} = -\frac{n_e e^2}{\epsilon_0} x. \quad (1.14)$$

This can be rewritten into the differential equation

$$\frac{\partial^2 x}{\partial t^2} + \left(\frac{n_e e^2}{\epsilon_0 m_e}\right) x = 0. \quad (1.15)$$

This equation takes the form of a simple harmonic oscillator with a frequency ω_{pe} given by

$$\omega_{pe}^2 = \frac{n_e e^2}{\epsilon_0 m_e}. \quad (1.16)$$

This frequency is the electron plasma frequency.

If we step back and relax our restriction on ion motion then it is clear that they must also oscillate under the same electric fields. Indeed, we can define a frequency for every charged species, s , in a plasma with the formula

$$\omega_{ps}^2 = \frac{n_s e_s^2}{\epsilon_0 m_s}, \quad (1.17)$$

where e_s , n_s and m_s are the charge, number density and mass of that species. For ions this is the ion-plasma frequency. However, it is not the case that each species oscillates independently from each other. Instead the whole plasma oscillates at a frequency that is a hybrid of the contributions from each individual species. In an ion-electron plasma this frequency is given by

$$\omega_p = \sqrt{\omega_{pe}^2 + \omega_{pi}^2}. \quad (1.18)$$

This is the plasma frequency and $\omega_p \approx \omega_{pe}$ since $\omega_{pe} \gg \omega_{pi}$ due to the large mass ratio.

These oscillations should occur over distances of the order of the Debye length. We can combine the expressions for plasma frequency and Debye length into an expression which has the dimensions of speed,

$$\begin{aligned}\omega_p \lambda_D &= \sqrt{\frac{n_e e^2}{\epsilon_0 m_e} \frac{\epsilon_0 \kappa_b T_e}{n_e e^2}} \\ &= \sqrt{\frac{\kappa_b T_e}{m_e}} \\ &= v_{th}.\end{aligned}\tag{1.19}$$

We recognise this as the electron thermal speed v_{th} , it differs by a scalar factor of m_i/m_e from the sound speed, C_s . We will revisit acoustic waves in section 1.4.2.

Since the period of a wave is simply $2\pi/\omega$ we can also write down an expression for the plasma period, τ_p ,

$$\tau_p = 2\pi \sqrt{\frac{\epsilon_0 m_e}{n_e e^2}}\tag{1.20}$$

These electron-plasma waves can only be observed if the observation time is longer than this period and external forces do not drive the plasma behaviour at rates faster than this time-scale. Like the Debye length the plasma period is a useful concept when it comes to defining our limits on the application of MHD in section 1.4.2.

1.1.4 Cyclotron frequency

When a magnetic field is introduced into a plasma then you increase the complexity of the dynamics considerably. Magnetic fields interact with charged particles via the $\mathbf{v} \times \mathbf{B}$ term in the Lorentz force,

$$\mathbf{F} = q(\mathbf{E} + \mathbf{v} \times \mathbf{B}).\tag{1.21}$$

Consider a particle with charge q and velocity \mathbf{v} with $\mathbf{E} = 0$ encountering a homogeneous magnetic field in the z-direction, \mathbf{B} , it will experience a force in the $\mathbf{v} \times \mathbf{B}$ direction. We can write down the equation of motion for such a particle as

$$\mathbf{F} = m \frac{d^2 \mathbf{s}}{dt^2} = q(\mathbf{v} \times \mathbf{B}). \quad (1.22)$$

There is no component of this force in the z -direction. Magnetic forces can not change the magnitude of the vector, \mathbf{v} , only its direction. Kinetic energy is conserved when magnetic fields act on charged particles since work is given as the dot product $W = \mathbf{F} \cdot \mathbf{v}$ and the dot product of perpendicular vectors is always 0. This is sometimes summarised as ‘magnetic forces do no work’ (Griffiths & College 1999). We can split equation 1.22 into the x and y components of motion:

$$\begin{aligned} \ddot{x} &= \frac{qB}{m} \dot{y}, \\ \ddot{y} &= -\frac{qB}{m} \dot{x}. \end{aligned} \quad (1.23)$$

We have now switched to Newton’s notation or the dot notation, \dot{x} is the first derivative of x wrt time, or the velocity in the x direction and \ddot{x} is the second derivative of x wrt time or the acceleration in x . This notation will be used occasionally in the remainder of this thesis.

These equations of motion are simple to solve by first defining $s = x + iy$ such that

$$\ddot{s} + i\Omega \dot{s} = 0, \quad (1.24)$$

with $\Omega = |q|B/m_e$. By taking an exponential form where $s(t) = \exp(a * t)$ we can solve this differential equation giving us

$$\dot{s} = \dot{s}(0)e^{-i\omega t}. \quad (1.25)$$

By defining $\dot{s}(0) = v_{\perp} \exp(-i\alpha)$ we can split this back up into components:

$$\begin{aligned} \dot{x} &= v_{\perp} \cos(\Omega t + \alpha) \\ \dot{y} &= -v_{\perp} \sin(\Omega t + \alpha). \end{aligned} \quad (1.26)$$

We can then integrate these to determine their orbits:

$$\begin{aligned}x &= \frac{v_{\perp}}{\Omega} \sin(\Omega t + \alpha) + x_0 \\y &= \frac{v_{\perp}}{\Omega} \sin(\Omega t + \alpha) + y_0.\end{aligned}\tag{1.27}$$

The z-component of the velocity, parallel to the magnetic field, remains constant therefore $z = v_{\parallel}t + z_0$.

These equations define a circular motion around the centre point (x_0, y_0) . The frequency of this gyration is called the cyclotron frequency of species s, ω_{cs} and is given by

$$\omega_{cs} = \Omega = \frac{|q_s|B}{m_s}.\tag{1.28}$$

We note that although the frequency is independent of the sign of the charge, the orbit is not. Opposite charged particles orbit in opposite directions.

We can also define a length, the Larmor radius or cyclotron radius, (r_l), as being the radius of a single gyro orbit of plasma species s:

$$r_{ls} = \frac{m_s v_{\perp}}{|q_s| m_s}.\tag{1.29}$$

Since both the cyclotron frequency and Larmor radius have a $1/m$ dependence then, in an ion-electron plasma, the electrons orbit much faster in much smaller orbits. We shall exploit this behaviour in section [1.5.2](#).

The fact that magnetic fields naturally give rise to this predictable gyro-motion is exploited in plasma physics using particle orbit theory. Alfvén was the first to point out that the motion of particles in such a field can be split into two components, the motion of the centre of the orbit (the guiding centre) and the gyromotion of the particle around the magnetic field line ([Alfvén 1950](#)).

The success of particle orbit theory in describing many aspects of plasmas can be attributed to the fact that, for many plasmas, the scale length of interest, L , follows $L \gg r_l$. This means that the equations of motion can be simplified easily to this gyration around a guiding centre approach, even when complicated additional force terms are present. ([Gurnett & Bhattacharjee 2005](#))

These characteristic length and time scales will, like the plasma frequency and Debye length, allow us to define a regime where the bulk, fluid descriptions of a plasma remain valid as well as to define the particular regimes that are of interest during momentum coupling and Alfvén ionization in later chapters.

1.2 Collisions in Plasmas

The majority of the work described in this thesis is centred on the interactions that occur between the different species of a gas-plasma mixture. In a partially ionized plasma there exists neutral gas, positively charged ions and negatively charged electrons. The interaction between all the three of these species produce dynamics that are not present when one or more of them are absent.

One of the key, unavoidable interactions is that from collisions. In section 1.1.2 we saw that in a well defined plasma there exist many particles in a Debye sphere meaning that any given particle is constantly interacting with a large number of others. This means that in a plasma collisions are many-body interactions and binary collisions are much less important than in a neutral gas.

1.2.1 Charged-neutral collisions

In a partially ionized plasma we can define the collision frequency, $\nu_{g,s}$, of a plasma species with a stationary background of neutral gas as

$$\nu_{g,s} = n_g v_{th} \sigma_n, \quad (1.30)$$

where v_{th} is the thermal speed, $v_{th} = \sqrt{k_B T_s / m_s}$, and σ_n is the cross section for collisions between the species and neutral atoms. In kinetic theory, this cross section is often taken as just being the cross-section for elastic scattering. We can also define the mean free path, l , as being

$$\begin{aligned}
 l &= \frac{v_{th}}{\nu_{g,s}} \\
 &= \frac{1}{\sigma_n n_g}.
 \end{aligned}
 \tag{1.31}$$

This is the average distance that a particle moves before interacting with a neutral.

The cross-section is only very weakly dependent on energy so can reasonably be assumed as a constant equal to the cross-sectional area of the interacting particle. This gives rise to simple ‘billiard ball’ style collisions where we can make a substitution for σ :

$$\sigma_{g,s} = \pi r^2, \tag{1.32}$$

where r is the atomic radius. In the case of the electron-neutral collisions there is an exception: a low-energy (approximately 1 eV) electron encounters a heavy noble gas atom then the cross-section is significantly reduced from a simple collisional ‘billiard’ model. This transparency of the heavier noble gasses to low energy electrons was first noted independently by Ramsauer and Townsend in the mid 19th century, leading to the name *the Ramsauer-Townsend* or simply *the Ramsauer effect*, but it took until the 20th century and quantum mechanics before the effect was explained. Essentially, the de Broglie wavelength of these electrons closely matches the size of the potential well of the atoms allowing the electrons to diffract around, instead of interacting with, the atoms. ([Golden & Bandel 1966](#))

The weak energy-dependence is also absent once the energy of the electrons becomes sufficient to elevate a bound electron to an excited state or even to ionize one. This leads to inelastic as opposed to elastic collisions and a much stronger energy dependence.

The strength of the effect that these interactions have on the plasma is dictated by the collision frequency and the time-scale of interest, t . If $\nu_{g,s}t \ll 1$ then we would expect that the effect of these collisions is small. This would occur when either the neutral gas density is small or when the temperature of the plasma is low. In this regime the presence of neutrals only weakly damps motion of the plasma ions, there is only a slow transfer of energy from the charged to neutral species and vice versa.

On the other end of the scale, if $\nu_{gs}t \gg 1$, then we are in a regime dominated by collisions. This would occur when the neutrals are dense, when the plasma is only weakly ionized or when the thermal speed is high. In this case the plasma is almost completely dominated by the motions of the neutral gas; plasma considerations are not as important.

Somewhere between those two extremes there must exist a regime where the motions of the plasma are noticeably effected by the presence of the neutrals but the collective behaviour of the plasma is not completely damped out. The investigation of this regime is one of the principal motivations for this work. We shall discuss a fluid description of these elastic collisions between the neutrals and ions in section 1.5.1.

Electron-neutral collisions (and neutral-neutral collisions) work in the same manner as ion-neutral collisions do. Electrons have a higher thermal speed so collide more frequently but their significantly lower momentum means they do not contribute much to a momentum exchange between the plasma (ions and electrons) and the gas (atoms).

1.2.2 Electron-ion interactions

The calculation of the cross-section of interaction between two charged particles is much more complicated. Unlike the ion-neutral or neutral-neutral interactions where these occasional strong collisions dominate, the motion of a charged particle in a plasma is dominated by many weak interactions. This means understanding the collective effect of these interactions requires integrating over all of these weak interactions.

This process is taken in part from [Gurnett & Bhattacharjee \(2005\)](#). We first define

$$\sigma_c(\chi)d\Omega = \frac{\text{number of particles scattered into solid angle } d\Omega}{\text{incident intensity}}. \quad (1.33)$$

where χ is the angle by which the particle is deflected. We use the Rutherford formula ([Rutherford 1911](#)) for the scattering cross-section between an electron of charge $-e$ and mass m_e encountering an ion of charge $+e$ and mass m_i where $m_i \gg m_e$. We have

$$\sigma_c(\chi) = \frac{1}{4} \left(\frac{e^2}{4\pi\epsilon_0 m_e v^2} \right)^2 \frac{1}{\sin^4(\chi/2)}. \quad (1.34)$$

This expression is highly anisotropic and, from the $1/\sin^4(\chi/2)$ dependence, strongly peaked at small angles. We can obtain a total cross-section σ_T by integrating over the total solid angle

$$\sigma_t = \int_0^\pi \sigma_c(\chi) 2\pi \sin\chi d\chi. \quad (1.35)$$

We then use equation 1.30 to obtain an electron-ion collision frequency, $\nu_{e,i}$, of

$$\nu_{e,i} = \frac{n_0 e^4}{32\pi^{1/2} \epsilon_0^2 m_e^{1/2} (2\kappa_b T_e)^{3/2}} \ln(12\pi N_D). \quad (1.36)$$

This result tells us two things: it has a weak dependence on N_D , the number of particles in a Debye sphere, and that it has a $1/T_e^{3/2}$ dependency. This is in stark contrast with the $\sqrt{T_e}$ dependence of the ion-neutral collision frequency. This means that instead of collisions becoming more common as the temperature rises they become less common. Unlike a neutral gas, it is possible to have a plasma hot and diffuse enough that collisions are practically non-existent.

To define the regime where this occurs we calculate a mean free path as in equation 1.31 and note that if the scale of the system, L , is comparable in magnitude to the mean free path l (i.e. $L \approx l$) then particles interact infrequently enough that we would expect the particle velocity distributions to evolve non-thermally and that our fluid approximations of such a plasma would fail. In other words, if we were to perturb a particle then it would not undergo sufficient interactions with other particles in order to communicate the disturbance to the rest of the plasma. This would prevent such a plasma from relaxing into a thermal equilibrium once perturbed.

The solar corona and solar wind exist in this regime and it is surprising how well fluid descriptions (which necessarily assume collisionality) of these plasmas succeed at capturing their dynamics (Marsch 1991).

1.2.3 Relaxation Time

Via the electron-ion, electron-electron and ion-ion collision frequencies it is possible to define *relaxation times* for both the electrons and the ions respectively: (Goedbloed & Poedts 2004)

$$\tau_e = 6\pi\sqrt{2\pi}\epsilon_0^2 \frac{m_e^{1/2}(kT_e)^{3/2}}{\ln LZ^2 e^4 n_i}, \quad (1.37)$$

$$\tau_i = \frac{m_i}{2m_e}\tau_e. \quad (1.38)$$

Here L is the size of the plasma and the rest of the symbols have their usual meanings.

The relaxation time immediately has use: If we have a plasma in thermal equilibrium and perturb it then the relaxation time is the typical time scale over which the electrons (or ions) relax back into a new thermal equilibrium. The ion relaxation is a factor of $m_i/(2m_e)$ slower than the electron relaxation meaning that ion relaxation is the slower process.

In the event that a perturbation from thermal equilibrium involves electrons that are of sufficient energy to undergo inelastic collisions with neutrals, either bound-free reactions (ionization) or bound-bound (atomic transitions), then the rate at which these electrons return to a more temperature appropriate energy is only increased due to the relatively large cross-section of these reactions and the substantial reduction in electron energy after one takes place.

The relaxation time for the neutrals is given by a similar expression:

$$\tau_n = \frac{1}{n\pi r^2} \frac{m_n}{6k_B T} \quad (1.39)$$

Therefore, if we inject a non-thermal population of electrons into a plasma (e.g. from an unbalanced charge pocket consistent with AI in section 1.5.2) then they will remain non-thermal for at most a time $\tau \approx \tau_e$. After this time has elapsed the plasma will relax into a new equilibrium.

1.3 Ionization Processes

The previous section was concerned with elastic collisions, collisions where energy is conserved. Collisions between particles in a plasma can also be inelastic. In the case of an inelastic collision, kinetic energy from the colliding particles can be used to excite one of the electrons bound inside a colliding atom, or partially ionized ion. This can only occur if the energy in the collision is high enough for the electron to reach an excited state. Once excited the electron is free to decay back to the ground state, or another lower energy state, emitting a photon as it does. (Carroll & Ostlie 2007)

This is a very useful process for astronomers. A huge amount of what we know about stars, galaxies, nebula, planets comes from looking at the spectra produced by these interactions. Atomic spectra are dependent on, and can therefore reveal, many physical properties of a distant object; the temperatures, radial velocity, elemental composition, energy distributions, and more can be determined from any object we can observe spectroscopically. (Pradhan & Nahar 2011)

If the energy in the collision is high enough, above the ionization energy, then it is possible for the collision to transfer enough energy from the colliding particles to the bound electron such that the bound electron breaks its bond with the atomic nucleus and the atom becomes ionized. This process produces a free electron and a positively charged ion and is obviously central to understanding the formation and equilibrium position of plasmas. It is this ionization by energetic electrons that is central to this work.

Not all collisions are created equal. The cross section for excitation for a collision between an ion and a neutral is many orders of magnitude below the corresponding cross-section between an electron and neutral at the same energy. This means that if the ions and electrons in a partially ionized plasma have similar energy distributions (temperatures) then most of the ionization and excitation is done by the free electrons. It is also possible to ionize atoms via collisions with photons of sufficient energy in a process called photo-ionization. While this mechanism is very important for many laboratory and astrophysical considerations it will not be discussed in any further

detail.

In general we can say that if we have electrons of sufficient energy then collisions between those electrons and neutrals will cause ionization. The source of the energetic electrons does not matter; they could be from a non-equilibrium electron beam accelerated by any number of astrophysical mechanism such as in a solar flare (Brown 1973); they could be from the tail end of the Maxwellian distribution in an appropriately hot plasma; they could originate from electrical discharges such as in lightning (Fridman et al. 2005) or grain discharge in a dusty plasma (Helling et al. 2011b); they could be produced by the self coulomb repulsion of unbalanced pockets of electrons produced by Alfvén ionization (Stark et al. 2013) and so on. This last example is of particular interest and is discussed in depth later.

In order to form a basis for understanding ionization and the consequences of Alfvén ionization we will briefly discuss ionization reactions and some of the traditional mechanisms by which these energetic electrons are produced and ionize.

1.3.1 Electron Impact Ionization

We have already seen that electron-neutral collisions are the most energetically favourable ionization mechanism in an ion-electron plasma with equal temperatures for both species. When an electron of sufficient energy interacts with a neutral atom (A) the following reaction can occur



producing a positive ion (A^+) and an additional free electron (e^-). The rate that this reaction proceeds at is dictated by the energy dependent cross section.

If we assume a stationary column of neutrals with density n_g and an incoming beam of electrons of density n_e and velocity v then

$$\dot{n}_i = vn_g n_e \sigma_{eg}(v), \quad (1.41)$$

where $\sigma_{eg}(v)$ is the cross section for ionization at velocity v for a collision between

an electron and neutral gas atom. This cross section is of great interest to a huge range of modelling communities; in the semiconductor manufacturing industry understanding ionization processes can play as important a role in controlling the etching, deposition and cleaning processes as understanding surface chemistry does. (Huo & Kim 1999)

Early attempts at producing a theory able to calculate this ionization cross section, such as the plane wave Born approximation (PWBA), originally described by Bethe (Bote & Salvat 2008), were mostly successful at providing agreement with experiments at high energies. However, when the reaction energy is close to the ionization threshold then these approximations fail (Guerra et al. 2012). This is particularly problematic for plasma physics as, if your plasma is thermally ionized (in Saha equilibrium), full ionization occurs at temperatures where the mean particle energy remains well below the ionization threshold. The majority of ionization is carried out by reactions at energies close to the ionization energy. This means that the low-energy interactions cannot be ignored.

Many examples of empirical relationships can be made to fit the experimental data of ionization rates (e.g. Lotz (1967)). These are not ideal as they have to be produced by considering each ion species one at a time, tuning free parameters individually, and disagreement with experiment is common. These have frequently been put to use in conjunction with semi-analytical models (Inokuti 1971). Kim & Rudd (1994) proposed a theoretical model known as the binary-encounter-Bethe model (BEB),

$$\sigma_{BEB} = \frac{S}{t + u + 1} \left[\frac{Q \ln(t)}{2} \left(1 - \frac{1}{t^2} \right) + (2 - Q) \left(1 - \frac{1}{t} - \frac{\ln(t)}{t + 1} \right) \right], \quad (1.42)$$

where t and u are the electron energy and the orbital kinetic energy normalised to the ionization energy (E/E_i and U/E_i respectively). $S = 4\pi a_0^2 N (R_H/E_i)^2$ with R_H being the Rydberg constant, the ionization energy of hydrogen (13.6057 eV) and Q is the dipole constant which can either be obtained from the continuum dipole oscillator function or assumed to be 1 when this is unknown. The BEB method for calculating cross-sections shows good agreement at both the high energy Bethe limit as well as at lower energies, comparable to the ionization energy.

With a known cross-section then equation 1.41 can be used to calculate an ionization rate that results from a beam of electrons at one energy (velocity).

For a distribution of electron velocities, v , equation 1.41 becomes an integral, and the rate of change of the number density of ions is given by

$$\dot{n}_{i,i} = \int v n_g n_e(v) \sigma_i(v) dv. \quad (1.43)$$

The reverse reaction to ionization, recombination, can be expressed in the same form,



and the rate of change of ions as a result of recombination is given by

$$\dot{n}_{i,r} = - \int v n_i n_e(v) \sigma_r(v) dv. \quad (1.45)$$

This cross section has a different energy dependence; the free electron needs to be sufficiently low energy to be captured by the ion and form an atom. The reaction rate still depends on the densities of the two reactants, electrons and ions in this case.

If the plasma is in ionization equilibrium, i.e. with an ionization fraction that is constant, then the rate of change of the ion density must be 0 such that

$$\dot{n}_{i,i} + \dot{n}_{i,r} = 0. \quad (1.46)$$

This remains true only when your plasma is contained. If particles are able to exit the region you are considering, such as by interacting with a wall or simply by flowing out a fluid cell, then this constraint will be violated and the ionization fraction may evolve.

For a singly ionized ion-electron plasma it is obvious that for each ion produced there is a neutral atom lost and that each neutral atom produced by recombination removes one ion such that

$$\dot{n}_{g,i/r} = -\dot{n}_{i,i/r}. \quad (1.47)$$

1.3.1.1 Thermal Equilibrium

For any plasma both of these reactions, ionization and recombination, are continually ongoing. However, if there is a sufficiently energetic electron population, either from a high temperature or otherwise, then the recombination reaction rate will be ≈ 0 due to so few electrons being in the energy range required to recombine. Likewise, a cool enough plasma with no non-thermal energetic electrons will have such a low ionization rate that its ionization fraction will remain ≈ 0 .

The Saha equation could be used to calculate the equilibrium ionization fraction of a plasma, however, this approach only remains valid for low T plasmas, where the ionization fraction is very small. Since a plasma in thermal equilibrium has a well defined distribution of electron energies it is entirely possible to obtain the Maxwell-Boltzmann distribution function and carry out the integral of the energy dependent cross-section multiplied by the electron distribution function in equations 1.41 and 1.45. This method would allow us to retrieve the ionization and recombination rates as well as the equilibrium ionization fraction from the number densities when the two rates are equal and opposite.

In fact, this approach continues to work for a non-thermal plasma, where the electron distribution function deviates from that of a Maxwellian, as long as we are able to define this energy distribution. However, for any plasma, this is not only a computationally intensive approach but is very complex, it requires the combination of all the cross-sections for ionization and recombination to and from each electron energy state. (Annaloro et al. 2012) This is a complex task for even the simplest atoms. (Drawin 1969)

The Arrhenius' equation (or modified Arrhenius' equation), which originated from Arrhenius in 1889, is a surprisingly simple yet highly effective way of approximating the rate of a chemical reaction, including ionization and recombination. The Modified Arrhenius' equation for an arbitrary reaction gives us a corresponding reaction rate coefficient, k , (Laidler 1977)

$$k = AT^a \exp \left[\frac{E_A}{k_b T} \right], \quad (1.48)$$

where A is a constant, a is a reaction dependent constant and E_a is the activation energy of the reaction.

In this way we can replace our cross sections with reaction rate coefficients for a plasma in thermal equilibrium. If this process is carried out for both the ionization and recombination cross-sections then equations 1.41 and 1.45 become,

$$\dot{n}_{i,i} = k_i(T)n_g n_e, \quad (1.49a)$$

$$\dot{n}_{i,r} = -k_r(T)n_i n_e. \quad (1.49b)$$

Knowing these temperature dependent reaction rates allows equilibrium ionization fraction to be calculated. If we assume a single species gas such that $n_i = n_e$ and that $n_i + n_g = \text{constant} = n_0$ then we can find the equilibrium ionization fraction (n_i/n_0), which occurs when $\dot{n}_{i,i} + \dot{n}_{i,r} = 0$ in figure 1.1.

Figure 1.1 is produced by calculating this equilibrium position using the ionization and recombination rate coefficients from the CHIANTI atomic database (Dere et al. (1997); Landi et al. (2012)). Note the narrow temperature range (10000 – 12000K) at which the gas goes from almost fully unionized to fully ionized. This is mostly due to the very large increase in the ionization rate coefficient at these temperatures as the number of electrons above the ionization energy increases dramatically.

It is not always possible to describe a plasma as being in a thermal equilibrium and even then not all ionization is the result of thermal electrons but this Arrhenius approach at least allows us to set a base ionization fraction from which deviations occur.

1.3.2 Electrical Breakdown

The electrical breakdown of a gas by the application of a high voltage is commonly used to create plasmas in a lab environment but is also relevant in nature (such is

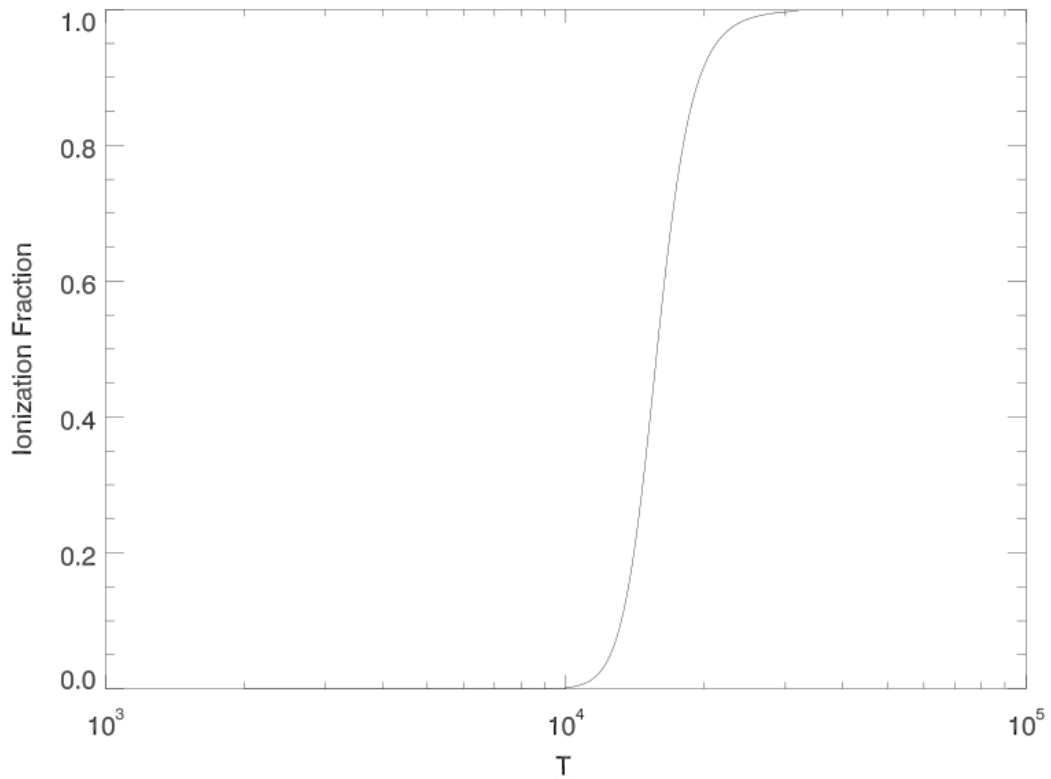


Figure 1.1: The equilibrium ionization fraction of hydrogen as a function of T in kelvin given obtained using ionization and recombination rate coefficients from the CHIANTI atomic database.

from lightning). Applying an external electric field, E , to a gas will result in any free electrons (or ions), which are present in some fraction in a gas of any temperature, being accelerated. If these free electrons are able to gain sufficient energy in between inelastic collisions that they can reach the ionization energy then, when they do collide with a neutral, they are able to deliver enough energy that the neutral can be ionized.

The acceleration of electrons by an electric field to energies that allow ionization to take place is a core concept in Alfvén ionization as charge imbalance pockets are analogous. An understanding of the electrical breakdown of a gas between two electrodes is useful since essentially the same core process will result in ionization in the case of AI (1.5.2).

We can estimate the electric field requirement using our expression for the mean free path of an electron travelling through the gas in equation 1.31. If the voltage across the mean free path is equal to or greater than the ionization energy, E_i , then the gas can be ionized,

$$\begin{aligned} El &\geq E_i, \\ E &\geq E_i \sigma_{gs} n_{gs}. \end{aligned} \tag{1.50}$$

In truth, this is not a strict relationship as the distance that a given electron travels is statistical in nature but it does suffice as a first order approximation for the minimum electric field necessary for ionization.

If an electron is successfully accelerated to the ionization energy and does indeed ionize then an additional free electron will be liberated from its parent atom. This now means there are 2 free electrons that will continue to accelerate under the electric field and there is the potential for these to undergo more ionizing reactions allowing the population of electrons to exponentially increase. This is known as the Townsend electron avalanche, after the first person to describe it, John Sealy Townsend. (Brown 1966) We can quantify this exponential increase in electron number,

$$n = n_o e^{\alpha x} \tag{1.51}$$

where α is the first Townsend Ionization Coefficient, simply the number of ionizing collisions in a unit length which is a function of the electric field, pressure and the properties of the gas in question.

The voltage at which a parallel plate capacitor is able to start an electrical arc between the plates is known as the breakdown voltage, V_B .

$$V_B = \frac{aPd}{\ln(Pd) + b}, \tag{1.52}$$

where P is the gas pressure, d is the plate separation distance and a, b are constants that depend on the gas composition. For a given gas, this breakdown voltage is entirely a function of the product of pressure and electrode separation, Pd and has a

minimum where the derivative of equation 1.52 is 0. The Paschen curve normalised to the minimum breakdown voltage is given in figure 1.2.

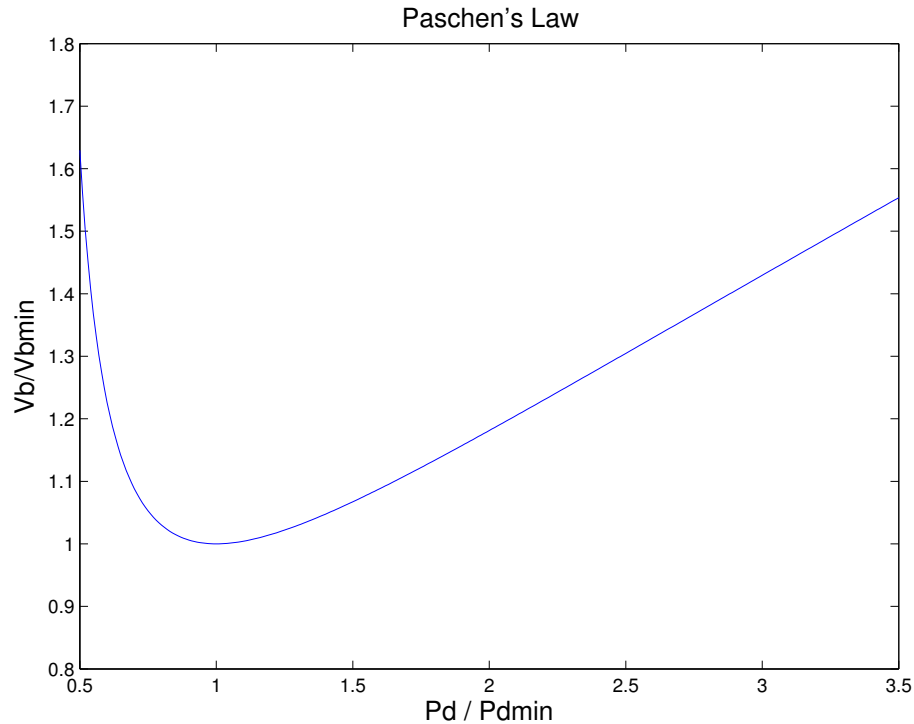


Figure 1.2: The Paschen curve for an arbitrary gas using normalized units for constants a and b . The y axis is the breakdown voltage normalised to the minimum breakdown voltage and the x-axis is in units of Pd normalised to the value of Pd that gives this minimum. The minimum indicates the value of Pd where the lowest voltage needs to be applied before electrical breakdown of the gas takes place.

The presence of an optimal value of Pd for which the required voltage is minimum allows us some insight into the mechanism. When this product is low, < 1 , then although the electrons gain sufficient energy for ionization, the mean free path is high compared to the electrode separation. This means few ionizing collisions occur and a higher voltage is necessary to ensure a reasonable fraction of the gas becomes ionized. To the right of the minimum, where $pd > 1$, electrons frequently lose energy due to

collisions with neutrals before they reach the ionization energy and as such the voltage required for breakdown is higher.

1.4 Bulk Plasma Descriptions

If we wished to describe the evolution of a plasma using the Lorentz force for every particle present then we face a serious challenge. The electric and magnetic fields are not simply prescribed but instead they are a result of the motion of those same charged particles. Since a typical plasma can contain 10^{20} particles per m^3 then it is neither possible nor desirable to model the motion of each one individually.

Instead, we are forced to think of the average motion of many particles.

1.4.1 Kinetic Theory

Kinetic theory averages out the microscopic motions of individual charged particles in a plasma to produce a statistical, kinetic description.

To specify the state of a particle in a plasma we must know its position and its velocity, we can combine this information into a coordinate in 6-D phase space. In this system a particle's phase space position is given by:

$$(\mathbf{x}, \mathbf{v}) = (x, y, z, v_x, v_y, v_z) \quad (1.53)$$

Since we wish to be dealing with a plasma of many particles then we define a distribution function $f(\mathbf{x}, \mathbf{v}, t)$ such that the number of particles in a given volume element of $d^3x d^3v$ is,

$$dN = f(\mathbf{x}, \mathbf{v}, t) d^3x d^3v, \quad (1.54)$$

and the total number of particles (N) in our plasma is,

$$N = \int dN = \int f(\mathbf{x}, \mathbf{v}, t) d^3x d^3v, \quad (1.55)$$

where we are integrating over all 6-dimensions of our phase-space.

From this description it is possible to derive the Boltzmann equation though such a derivation is not included here; (for example see [Gurnett & Bhattacharjee \(2005\)](#))

$$\frac{\partial f}{\partial t} + \mathbf{v} \cdot \frac{\partial f}{\partial \mathbf{x}} + \frac{\mathbf{F}}{m} \cdot \frac{\partial f}{\partial \mathbf{v}} = \left(\frac{\partial f}{\partial t} \right)_{\text{collisions}}, \quad (1.56)$$

where the RHS is an unspecified collisional operator. This partial differential equation describes how the distribution function evolves; it has no particular terms that associate it with a plasma, indeed it could be used to describe a gas. We replace the general force term, \mathbf{F} , with the Lorentz force and we remove the collisional term by assuming that the collective electromagnetic forces dominate over binary collisions to obtain the Vlasov equation;

$$\frac{\partial f}{\partial t} + \mathbf{v} \cdot \frac{\partial f}{\partial \mathbf{x}} + \frac{q}{m} (\mathbf{E} + \mathbf{v} \times \mathbf{B}) \cdot \frac{\partial f}{\partial \mathbf{v}} = 0 \quad (1.57)$$

This kinetic equation describes the evolution of the particle distribution function of a plasma.

Since the most important properties of a plasma are not usually the motion of individual particles but instead the changes in the mean motion of particles then the distribution function can be used to define those averages. For example the average velocity, \bar{v} , can be gotten by; ([Boyd & Sanderson 2003](#))

$$\bar{v} = \frac{1}{n} \int_V \mathbf{v} f(\mathbf{x}, \mathbf{v}, t) d^3v \quad (1.58)$$

This same process can be repeated for any bulk quantity that is desired such as density (ρ), kinetic energy (W) and the tensor pressure (\mathbf{P}).

A similar process can be undertaken to calculate the so-called *moment equations*. These are obtained by multiplying the Boltzmann equation (1.56) by increasing powers of v and integrating over velocity space. Each power of velocity produces a corresponding moment equation. We will not include all these derivations but below are the first 3 moment equations, the so-called zeroth, first and second moments: ([Gurnett & Bhattacharjee 2005](#))

$$\frac{\partial n_s}{\partial t} + \nabla \cdot (n_s \mathbf{v}_s) = 0, \quad (1.59)$$

$$m_s n_s \frac{\partial \mathbf{v}_s}{\partial t} = n_s q_s [\mathbf{E} + \mathbf{v}_s \times \mathbf{B}] - \nabla \cdot \mathbf{P}_s + \frac{\partial \mathbf{p}_s}{\partial t} \frac{1}{c}, \quad (1.60)$$

$$\frac{\partial W}{\partial t} + \nabla \cdot \mathbf{Q} = \mathbf{E} \cdot \mathbf{J}. \quad (1.61)$$

The zeroth is the continuity equation for species s . The first is the momentum equation, the left hand side of which is the change of momentum in a unit volume over time and the right hand side has the electromagnetic force per unit volume, the pressure gradient and the collisional drag force per unit volume ($\frac{\partial \mathbf{p}_s}{\partial t} \frac{1}{c}$). We make particular note of this collisional drag term as it is lost both in the change from the Boltzmann to the collisionless Vlasov equation and is lost in the development of the MHD equations. However, as we will see shortly, collisional drag is a central concept in much of the models developed in this thesis. Although it features in a different manner.

The second moment equation tells us that the time variation of the total kinetic energy in a unit volume plus the divergence of the kinetic energy flux of all species (\mathbf{Q}) is equal to the joule heating ($\mathbf{E} \cdot \mathbf{J}$). We note that this last equation is a single equation rather than one per species like the first 2. Collisions between different species only transfer energy from one species to another; collisions do not effect the total energy. Total energy is not conserved in this way if radiation is free to leave the volume. To deal with this a theoretical approach that involves radiative transfer is necessary.

Kinetic theory contains details of this distribution function, f , that can evolve on very fast time-scales and very short distances, comparable to the plasma frequency (ω_p) and Debye length (Λ_D). Even though kinetic theory allows large numbers of particles to be described without describing each individually it still remains difficult to implement to describe large plasmas.

We have already indicated that often average motion is much more important for large scale lengths where the time and distance scales that kinetic theory is able to capture are far smaller than the typical scale lengths of the system. As such a model that can capture the macroscopic instead of the microscopic physics of plasmas is

desirable, this is the regime of magnetohydrodynamics, the fluid description of plasmas.

1.4.2 Magnetohydrodynamics

Originally magnetohydrodynamics (MHD) was developed as an extension to fluid dynamics for use with a conducting fluid, like a plasma. The full set of equations were formed by taking the starting point of fluid dynamics and adding appropriate terms to account for electromagnetic forces (e.g. [Cowling \(1976\)](#)). It is however possible to obtain the governing equations from first principles. This process that will not be undertaken here. One can be found in [Goedbloed & Poedts \(2004\)](#), for example.

Instead, we shall focus on what the fluid limit means in terms of our already derived plasma characteristics and what assumptions and simplifications go into developing the equations of MHD with the aim of setting the stage for our the additional, non-MHD physics that we aim to add.

1.4.2.1 Motivation

A fluid model attempts to ignore the microscopic motion of the fluid's constituent particles and instead focuses on describing their motion in terms of macroscopic quantities, or fluid variables. These variables are continuous (though not necessarily continuously variable) across the entire fluid. This set of macroscopic fluid variables are a function of both position and time. The typical scale length of the smallest scale of these variations is the hydrodynamic scale, L_H , and it naturally leads us to describe a fluid element. A fluid element is a volume of our fluid that is small enough such that our macroscopic fluid parameters do not vary significantly throughout the volume yet large enough that it contains a sufficient number of particles to become insensitive to stochastic particle motions; that naturally leads us to a definition based on the Debye length and Larmor radius ([1.8 & 1.29](#)). ([Boyd & Sanderson 2003](#))

$$L_H \gg \lambda_D \tag{1.62}$$

$$\gg r_i. \tag{1.63}$$

Since a fluid element is much larger than λ_D then our plasma has zero net charge at this scale. To justify our concept of a fluid element then the electrons and ions must undergo frequent collisions (the assumption of frequent collisions by itself, in combination with kinetic theory, gives rise to two-fluid theory). This allows us to define a hydrodynamic time scale, τ_H , based on the relaxation times (1.37).

$$\tau_H \gg \tau_i \tag{1.64}$$

We use the ion relaxation time as the limit because it is naturally the longer time-scale.

If we are working at length scales larger than the microscopic motion of particles then we must also be working at time scales slower than these motions. We use the plasma frequency and cyclotron frequency here 1.18 & 1.28:

$$\tau_H \gg \Omega^{-1} \text{ and} \tag{1.65}$$

$$\tau_H \gg \omega_p^{-1} \tag{1.66}$$

This is enough for us to recover resistive MHD, if we wish to go one step further towards *ideal* MHD then we put the additional requirement that our time-scale must be faster than dissipative time-scale of the magnetic field, τ_r : [Goedbloed & Poedts \(2004\)](#)

$$\tau_H \ll \tau_r \approx L^2/\eta, \tag{1.67}$$

where η is the resistivity of the plasma. In practical cases plasmas are so conductive that η is small enough that this condition is often easily met. Ideal MHD is a theory that describes the macroscopic behaviour of such a perfectly conducting fluid.

The importance of these spatial and temporal limitations of MHD can be easy to forget. Since the MHD equations themselves do not explicitly contain these limitations it is instead necessary for the user to keep them in mind.

1.4.2.2 Governing Equations of Ideal MHD

Since ideal MHD is the set of governing equations that describe the motions of a perfectly conducting fluid interacting with a magnetic field, then we simply take Maxwell's equations of electromagnetics: (Griffiths & College 1999)

$$\nabla \times \mathbf{E} = -\frac{\partial \mathbf{B}}{\partial t}, \quad (1.68)$$

$$\nabla \times \mathbf{B} = \mu_0 \mathbf{J} + \frac{1}{c^2} \frac{\partial \mathbf{E}}{\partial t}, \quad (1.69)$$

$$\nabla \cdot \mathbf{E} = \frac{\rho_q}{\epsilon_0}, \quad (1.70)$$

$$\nabla \cdot \mathbf{B} = 0, \quad (1.71)$$

where \mathbf{E} and \mathbf{B} are the electric and magnetic field vectors, \mathbf{J} is the current density and ρ_q is the charge density. We combine these with Euler's equations of fluid dynamics:

$$\frac{D\rho}{Dt} + \rho \nabla \cdot \mathbf{v} = 0, \quad (1.72)$$

$$\frac{D\rho \mathbf{v}}{Dt} + \gamma p \nabla \cdot \mathbf{v} = 0, \quad (1.73)$$

$$\rho \frac{D\mathbf{v}}{Dt} = \mathbf{F} = -\nabla P + \mathbf{J} \times \mathbf{B} + \rho_q \mathbf{E} = 0. \quad (1.74)$$

Where ρ is the mass density, \mathbf{v} the fluid velocity, γ is the adiabatic constant and P the thermal pressure. We have introduced ($D/Dt = \frac{\partial}{\partial t} + \mathbf{v} \cdot \nabla$) as the convective derivative, the derivative taken while co-moving with the fluid. We require that in a frame of reference that is moving with a perfectly conducting fluid the electric field vanishes,

$$\mathbf{E}' = \mathbf{E} + \mathbf{v} \times \mathbf{B} = 0 \quad (1.75)$$

Equation 1.74 is where the two systems of equations are linked as the change in the momentum of a fluid element depends on the forces that act on that element, including the electromagnetic force. Here it is convenient to make another simplification that we are concerned with *non-relativistic velocities*, such that $v \ll c$.

In this case the displacement current term of 1.69 is assumed to be 0 since;

$$\frac{1}{c^2} \frac{d\mathbf{E}}{dt} \approx \frac{v^2}{c^2} \frac{\mathbf{B}}{t} \ll \nabla \times \mathbf{B} \approx \frac{\mathbf{B}}{L}. \quad (1.76)$$

This allows us to rewrite Ampère's law as $\mathbf{J} = 1/\mu_0 \nabla \times \mathbf{B}$. We are also able to simplify 1.74 significantly since by the same argument we can see that $\rho_q \mathbf{E} \ll \nabla \times \mathbf{B}$. This has the consequence of making the force from space charge separation irrelevant, as such we can state that $\rho_q = 0$ and Gauss' law (1.70) disappears.

Finally, purely in the interest of clarity we shall drop gravity from the force equation so that 1.74 becomes:

$$\rho \frac{D\mathbf{v}}{Dt} + \nabla P - \mathbf{J} \times \mathbf{B} = 0 \quad (1.77)$$

We have now reached the stage where we are ready to write down the system of equations for ideal MHD.

$$\frac{\partial \rho}{\partial t} + \nabla \cdot (\rho \mathbf{v}) = 0, \quad (1.78a)$$

$$\rho \left(\frac{\partial \mathbf{v}}{\partial t} + \mathbf{v} \cdot \nabla \mathbf{v} \right) + \nabla P - \frac{1}{\mu_0} (\nabla \times \mathbf{B}) \times \mathbf{B} = 0, \quad (1.78b)$$

$$\frac{\partial P}{\partial t} + \mathbf{v} \cdot \nabla P + \gamma P \nabla \cdot \mathbf{v} = 0, \quad (1.78c)$$

$$\frac{\partial \mathbf{B}}{\partial t} - \nabla \times (\mathbf{v} \times \mathbf{B}) = 0, \quad (1.78d)$$

$$\nabla \cdot \mathbf{B} = 0. \quad (1.78e)$$

In chapters 2 and 3 we use these equations, and the equivalent for a non-conducting fluid (a gas), as the basis for gas-MHD interaction codes. We shall express this same system of equations in different forms and using different variables which offer specific advantages for the purpose. Their general content remains the same.

1.4.2.3 Plasma Beta

This is a convenient time to define the plasma beta, β ,

$$\beta = \frac{P_{thermal}}{P_{magnetic}}, \quad (1.79)$$

$$= \frac{nk_B T}{B^2/2\mu_0} \quad (1.80)$$

The plasma beta is the ratio of thermal to magnetic pressure. It dictates which term in [1.78b](#) is more important, i.e. whether the gas pressure or the magnetic field plays a more significant role in the dynamical evolution of the system.

1.4.2.4 MHD Waves

Since wave motion is the focus of much of the modelling carried out in chapters [4](#) and [5](#) we shall briefly discuss one of the principle features of magnetohydrodynamics, the presence of MHD waves.

In the interest of brevity we shall not undertake the derivation of the dispersion relation for MHD waves here. The dispersion relation is given by, ([Boyd & Sanderson 2003](#))

$$(\omega^2 - k_{\parallel}^2 v_A^2) (\omega^4 - k^2 (c_s^2 + v_A^2) \omega^2 + k^2 k_{\parallel}^2 c_s^2 v_A^2) = 0 \quad (1.81)$$

where we have introduced 2 velocities,

$$c_s^2 = \frac{\gamma P}{\rho_0}, \quad (1.82)$$

$$v_A^2 = \frac{B^2}{\mu_0 \rho_0}. \quad (1.83)$$

The sound speed and Alfvén speed respectively. [1.81](#) has roots given by:

$$\omega^2 = k_{\parallel}^2 v_A^2, \quad (1.84)$$

$$\frac{\omega^2}{k^2} = \frac{1}{2} (c_s^2 + v_A^2) \pm \frac{1}{2} \left[(c_s^2 + v_A^2)^2 - 4c_s^2 + v_A^2 \frac{k_{\parallel}^2}{k^2} \right]^{1/2}. \quad (1.85)$$

These equations have solutions that are real and represent waves that neither dissipate or grow over time (instabilities).

The first equation, 1.84, represents the *shear Alfvén wave* or just the Alfvén wave. This propagates with \mathbf{k} parallel to \mathbf{B} . The perturbations in plasma velocity and magnetic field are perpendicular to both \mathbf{k} and \mathbf{B} meaning that the wave is completely transverse and induces no longitudinal motion. Further the wave produces no perturbations in either pressure or density meaning this wave is an incompressible mode. Its phase speed (ω/k) is the Alfvén speed. The energy of an Alfvén wave oscillates between plasma (ion) kinetic energy and magnetic energy.

The second equation represents the dispersion relation of compressional disturbances in an MHD plasma called magneto-acoustic or magneto-sonic waves or compressional Alfvén waves. This equation has two solutions from the two signs of the square root, the plus and minus solutions are sometimes referred to as the *fast* mode and *slow* mode respectively.

The second equation, 1.85, offers two solutions, the fast and slow modes corresponding to the plus and minus signs respectively they can best be thought of as the case where the gas pressure and magnetic pressure oscillate in phase and the case where they oscillate out of phase. These modes are coupled but we can look at special cases where k is either completely parallel or completely perpendicular to the field.

When the direction of propagation is perpendicular to the field then $k_{parallel} = 0$ and so the equation 1.85 simplifies to

$$\frac{\omega^2}{k^2} = (c_s^2 + v_A^2). \quad (1.86)$$

this is the fast mode and it has a phase velocity at the magneto-sonic velocity of $v_{ms} = \sqrt{c_s^2 + v_A^2}$. There is no slow mode when k is completely perpendicular.

For these compressional waves propagating in the parallel then $k_{\parallel} = k$ and so both roots remain,

$$\frac{\omega^2}{k^2} = [c_s^2 + v_A^2 \pm (c_s^2 - v_A^2)], \quad (1.87)$$

The two solutions have phase speeds of either c_s or v_A depending on the choice of sign. This corresponds to a Alfvén wave moving at the Alfvén speed or an ion acoustic wave moving at the sound speed.

For magneto-acoustic waves, perturbations in density and pressure are in the direction if k and the magnetic field perturbations are in the direction of B i.e. transverse. In the case of the fast mode the perturbations in pressure and magnetic pressure are in phase and they work together and in the case of the slow mode the magnetic pressure perturbation is out of phase with the pressure perturbation.

For arbitrary directions for propagation the shear Alfvén wave smoothly transitions into the fast mode and the fast and slow modes are coupled together. We shall refer to the compressional Alfvén wave and the acoustic mode of the plasma collectively as magneto-acoustic waves.

1.5 Modifications to MHD for a Partially Ionized Plasma

Part of the primary motivation of this thesis is to develop a beyond-MHD model; we wish to develop a fluid model for a partially ionized plasma; in particular, a partially ionized plasma where interactions between the gas and the plasma particles play a significant role in the dynamics. Since neutrals and ions behave differently, with only the latter feeling the magnetic Lorentz force and with their collisional operators being of different forms, a two fluid description of a partially ionized plasma is necessary.

Such a model should be applied when the difference between the behaviour of the neutrals and ions is sufficiently large.

Focus has been on the partially ionized nature of astrophysical plasmas with studies giving consideration to the role that the neutrals play in these plasmas. In solar physics much consideration has been made towards the damping of MHD waves in the solar chromosphere and corona (for example [Khodachenko et al. \(2004\)](#); [Pandey & Wardle \(2008\)](#); [Russell & Fletcher \(2013\)](#) and references therein), in the emergence of magnetic

flux (e.g. [Arber et al. \(2007\)](#)) or even in magnetic reconnection (e.g. [Zweibel et al. \(2011\)](#) & [Leake et al. \(2012\)](#))

It is clear that the neutrals do make a difference in the physics of partially ionized plasmas and their influence may be able to explain many unresolved astrophysical phenomena.

Most of the studies mentioned (and those not mentioned) are limited in some fashion, as most of theoretical physics is. Often they are analytical in nature, low-dimensional or make educated decisions on unimportant terms to be neglected. They are designed with specific scenarios rather than general usefulness in mind.

The goal of the work described in this thesis is therefore to design a numerical framework which incorporates the effects of neutrals with as little compromise as possible. We wish to describe both the plasma and gas as well as the interaction between them.

We shall focus on adding two pieces of physics to ideal MHD, both of which are a consequence of ion-neutral collisions where the ions (and electrons) collide with neutral atoms both elastically, transferring momentum, and inelastically, where they can excite and ionize the atoms. We shall focus on two modifications to MHD. The first is the addition of a frictional drag term, or momentum coupling term, and the second is the addition of a mechanism for ionization which depends on the relative velocity between the gas and plasma fluids called *critical velocity ionization*.

1.5.1 Momentum Coupling

Hopefully it is clear from our discussion on charged-neutral, electron-ion and kinetic theory that collisions can play an important role in plasma dynamics. Collisions have an energy dependence and whilst kinetic theory describes the energy distribution function, in MHD this detail is lost. In its place we wish to create fluid proxies for collisional effects.

Suppose the two fluids interact via collisions such that a net momentum is able to be transferred from one to the other. If we consider, in the fluid limit, a partially

ionized plasma where the gas is at rest with respect to the plasma. In the kinetic limit the distributions in velocity in this case are symmetrical about all axes. This leads to a collision with velocity v being equally as likely as $-v$. If we were to integrate over all collisions between the neutrals and the ions then we would find that all these random collisions will cancel out such that there is zero net momentum transfer.

Now consider the case where there is a background plasma at rest encountered by a gas moving with a fluid velocity of v . The kinetic distribution of the gas particles is skewed in the direction of v ; there are more gas particles with velocities in the positive v direction than in the $-v$ direction. In this case there will be more collisions between the neutrals and the ions that transfer momentum to the plasma in the $+v$ than transfer momentum in the $-v$ direction. The average (fluid) velocity of the plasma will thus increase and the average fluid velocity of the gas must decrease such that momentum is conserved.

If nothing else changes then this process will continue with the fluid velocities of the two species tending towards equality until there the relative velocity is reduced to zero. Once this has happened, we are back to the case of each fluid being at rest with respect to the other, the integral of the transfer of momentum from collisions being 0 and there being no net transfer from one fluid to the other.

The salient point here is that just because we are considering a macroscopic, fluid description of our gas and plasma does not mean that these microscopic collisions no longer occur. If we wish to model a partially ionized plasma with accuracy then we must allow there to be a transfer of momentum from one to the other of our separate species.

Since the collision operator for charged-neutral collisions is very simple (1.30) then we can take a fluid equivalent of it very easily.

The change in momentum in the plasma due to collisions with neutrals is given by,

$$\frac{\partial \rho_p v_p}{\partial t} = \Gamma \rho_g (v_g - v_p) \quad (1.88)$$

Where we have introduced Γ as a scalar between 0 and 0.5 which determines what

fraction of the gas momentum is transferred to the plasma in a unit time. In truth inside Γ is encoded the relative size difference between the fluid time-scale (the typical length/typical velocity) and the collisional frequency. If the collision frequency is high compared to the fluid time-scale then Γ will be high since more collisions will occur in a characteristic time allowing a larger fraction of momentum to be transferred. If Γ is 0 then we are saying that over the duration of the fluid time-scale collisions are so infrequent as to be negligible.

An interesting extension is the case where the relative velocity is so high that we are able to transfer large amounts of energy, comparable to the gas ionization energy from (non thermal) collisions between the species. This regime gives rise to an ionization mechanism known as Alfvén ionization or critical velocity ionization.

1.5.2 Critical Velocity/Alfvén Ionization

A logical progression of this momentum coupling is to extend it to incorporate ionization, allowing the collisions between a neutral gas and ionized plasma to create more plasma. In a 1942 paper Alfvén proposed an explanation for the differing compositions of planets to be a result of an as yet unrecognised mechanism for the ionization of a neutral gas flow that encounters a magnetized plasma (Alfvén 1942), this mechanism is now known as the Alfvén ionization or critical velocity ionization (CVI) effect. His idea was simply that as gas falls towards the Sun it gains energy, once this kinetic energy exceeds the ionization energy of the gas then there is the potential for ionization to occur. This argument is purely one based on energetics although proposed mechanisms now exist.

When Alfvén ionization (AI) does occur then it allows the normally fixed ionization fraction of neutral gas to ionized plasma to evolve in a non transient fashion (although the relative fraction of gas to plasma could always change dynamically as waves or flows propagate through the plasma). What is unique about the energetics of this process is that the energy used for ionization is contained in the kinetic energy of a bulk fluid motion; this is in contrast to the energy present in e.g. a thermal distribution.

The obvious consequence being that a plasma in motion has a different equilibrium ionization fraction than one at rest. A conclusion that is absent from standard MHD.

We shall use both *Alfvén ionization* (AI) and *critical velocity ionization* (CVI) to refer to this such mechanism.

We estimate, for a fluid composed of a single species, the velocity at which we would expect AI to take place using an argument based on the relevant energetics. This would be at or above the speed where the kinetic energy per gas molecule exceeds the ionization energy of that same gas. (Diver et al. 2005)

$$v_c = \sqrt{\frac{2E_i}{m_g}} \quad (1.89)$$

Experimental evidence for such a mechanism is abundant so we shall present a small sample. Fahleson (1961) used a 'Rotating plasma device', shown in figure 1.3, this device utilizes the $E \times B$ drift to drive the plasma through a neutral gas in the azimuthal direction. Their results, shown in figure 1.4, show a limit near the critical ionization velocity (CIV) that indicates that the plasma cannot be driven through the neutral gas at velocities greater than the CIV. This limit can only be exceeded once the plasma is almost entirely ionized. This total ionization is associated with a sharp rise in plasma velocity. This experiment verified the existence of AI for the first time. Many other similar laboratory experiments have subsequently verified these results in several different kinds of discharges (Angerth et al. (1962), Lehnert et al. (1966)); or reviews by Danielsson (1973) and Sherman (1973) for example) and also in industrial discharges, such as thin film deposition magnetron plasmas (Brenning & Lundin 2012).

There is also a slightly more limited number of results from astrophysical experiments and observations that show the existence of an critical velocity ionization process. The effect is thought to have been observed in cometary comae (Formisano et al. (1982); Haerendel (1986)), in the interaction between Venus and the solar wind (Wallis 1972) and in the magnetosphere of Jupiter's moon, Io, (Cloutier et al. 1978). It is also thought to be important to the solar wind itself, including its composition (Petelski et al. (1980); Geiss & Bochsler (1985)) as well as the atmospheres of stars, both in

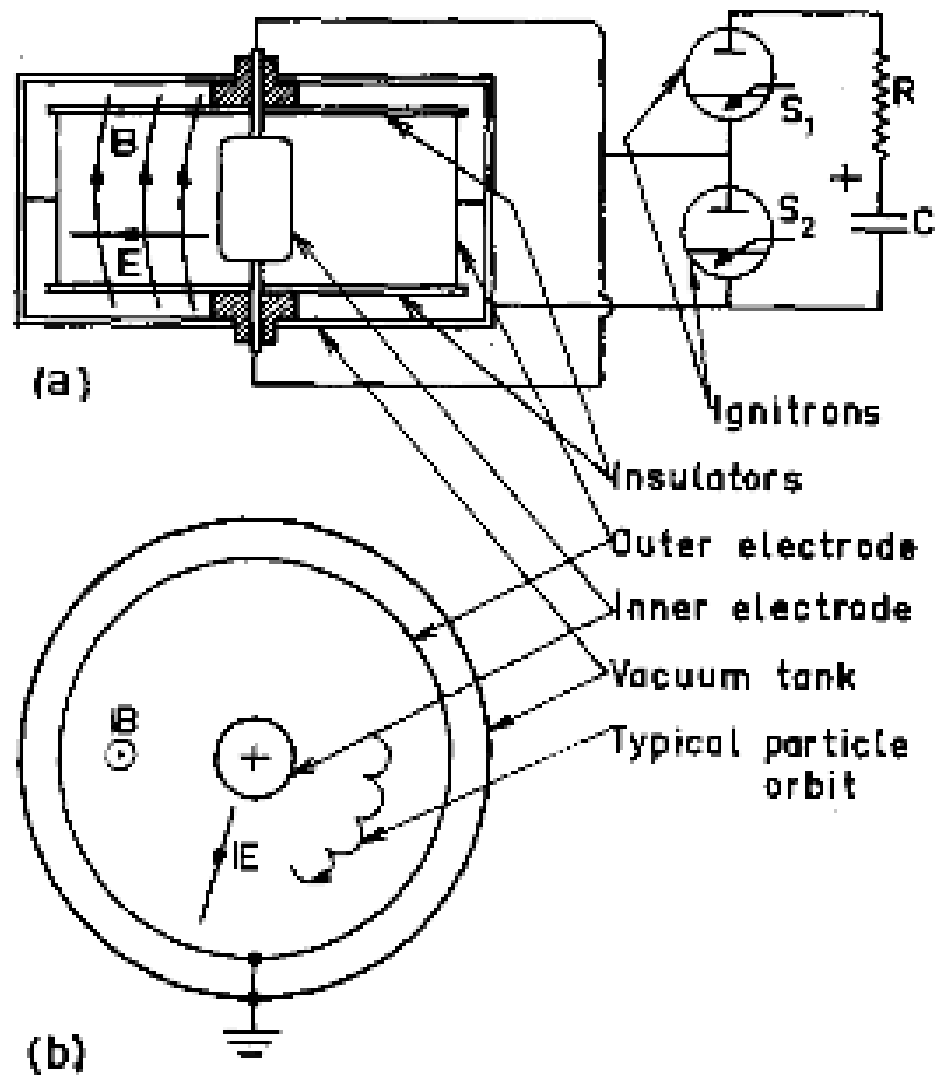


Figure 1.3: The rotating plasma device used by [Fahleson \(1961\)](#) to measure critical ionization velocities (a) front view with electrical connections (b) top down view. Figure taken from [Fahleson \(1961\)](#).

the Sun ([Diver et al. 2005](#)) and in the cooler atmosphere of brown dwarfs ([Stark et al. 2013](#)).

There have also been experiments conducted in the Earth's ionosphere by releasing gas either from sounding rockets or from satellites and other spacecraft. (e.g. reviews by [Newell \(1985\)](#) and [Torbert \(1990\)](#))

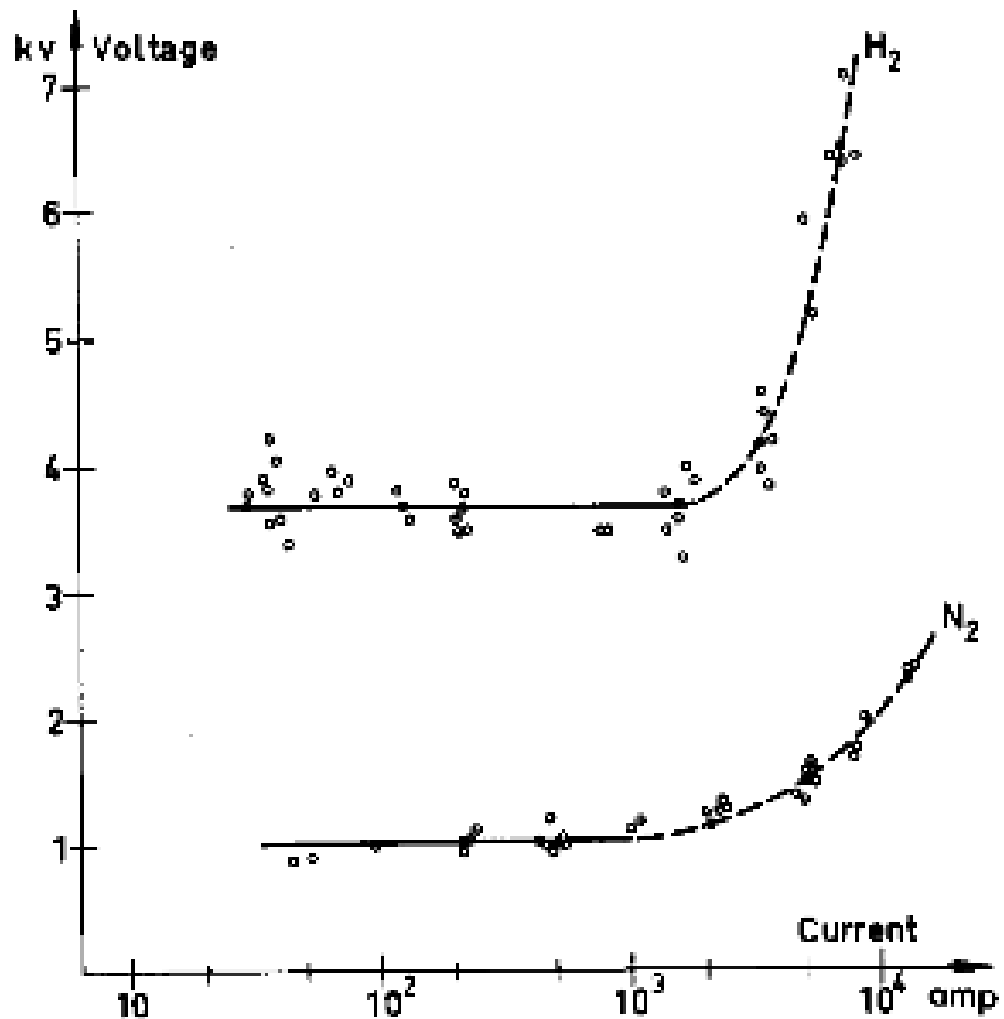


Figure 1.4: Burning voltage (which is proportional to plasma velocity) against discharge current for H₂ and N₂. Figure taken from [Fahleson \(1961\)](#). The plateau represents a plasma velocity, with respect to the neutral background, above which the plasma can not be driven faster even as the current is increased. The voltage of this plateau closely matches the theoretically predicted critical velocity.

1.5.2.1 CIV Mechanism

[Alfvén \(1960\)](#) attempted to explain the mechanism by suggesting that pockets of charge imbalance produced by stochastic collisions could result in accelerated electrons. The process he proposed was very simple: a gas flows, at speed v , and impedes upon a

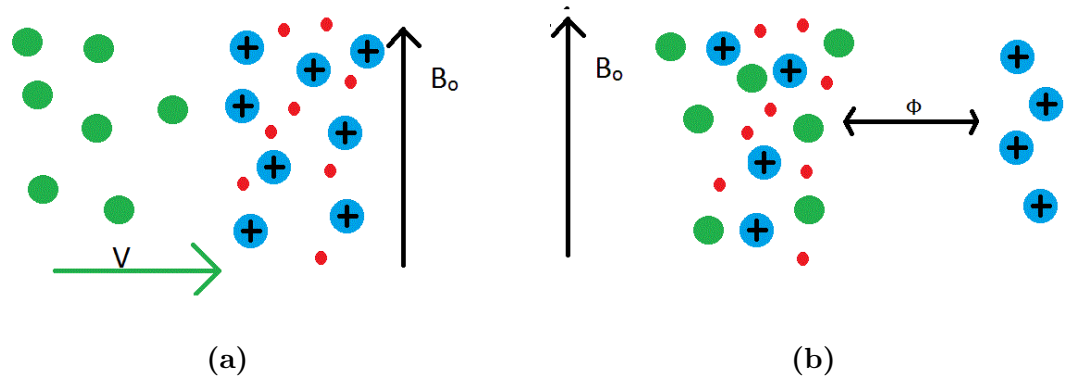


Figure 1.5: (a) A stream of neutrals with velocity, v , encounter a stationary plasma with magnetic field perpendicular to the flow (b) Ions are displaced via collisions with the neutrals, the electrons cannot follow and a resultant potential, ϕ , is created

stationary plasma with a perpendicular field of sufficient magnitude to magnetize the electrons. There will be collisions between the two species resulting in a net transfer of momentum, working to cancel out their relative motion. Collisions between the neutral atoms and the stationary plasma ions displace the ions from the surrounding electrons, creating a charge separation. If a magnetic field perpendicular to the flow direction is introduced then the electric field cannot be immediately rectified by electron transport as the electrons, due to their smaller Larmor radius, have their motion in the perpendicular direction impeded. This means the electric field can continue to increase as more ions are displaced until the potential is equal to the kinetic energy of the incoming gas. At that point collisions have insufficient energy to displace further ions against the temporary electric field. We are left with an electric potential that can be up to that of the incoming gas' kinetic energy, $E_{al} = \frac{1}{2}m_g v^2$. This electric field is able to accelerate local electrons to this energy, E_{al} . A cartoon of the formation of a charge imbalance by impinging neutrals is given in figure 1.5.

Once a charge imbalance is formed in this way then electrons can be accelerated. Particle-In-Cell (PIC) simulations (e.g. MacLachlan et al. (2009)) show that a charge imbalance with electric potential E_{al} is able to accelerate a fraction (10^{-3}) of the

electrons present to E_{al} and above. Consequently if the pocket of charge imbalance has a potential equal to the ionization energy then it is capable of producing electrons at or above the ionization energy. In fact, the presence of the magnetic field helps this acceleration process. By hindering the expansion of the electron cloud under their self field to be mostly one-dimensional (along the field) then the energy can be unevenly given to a small subset of the electrons, the ones which have a net force mostly in the parallel magnetic field direction. This results in even more electrons reaching the ionization energy when compared to a spherically symmetric expansion of the electron cloud.

Alternative processes have been proposed since, mostly depending on the formation of these regions of charge imbalance with variations in the electron acceleration mechanism. [Lehnert \(1967\)](#) showed that newly created ions formed in a magnetic field at rest relative to a background flow can create spatially varying potential structures with typical size of the order of the ion gyroradius. These potentials would be capable of accelerating electrons crossing the charge imbalance to energies comparable to the ion kinetic energy.

A modified two stream instability is popular for describing the electron heating ([McBride et al. 1972](#)).

In truth it is not definitively known how the energy is transferred from the neutral flow but as the mechanism is predictable in terms of the conditions required then we proceed as if our simple charge imbalance picture is correct and base our arguments for rates on the simple energetics argument made by Alfvén originally.

1.5.2.2 Criteria for CIV

All proposed electron heating mechanisms share a set of similar characteristics and these must remain important in deriving a fluid description of the process.

- The AI process has a minimum seed plasma number density before it proceeds. [Brenning \(1992\)](#)
- The process invokes a perpendicular magnetic field of sufficient strength. AI is

only observed when a component of the relative motion between the charged and neutral species is perpendicular to a magnetic field. Experiments have shown the field must be strong enough such that the electron gyro frequency is comparable to the plasma frequency. If the field either has no perpendicular component, wrt the flow direction, or is sufficiently weak then the AI mechanism is no longer observed. [Brenning \(1981\)](#); [Stark et al. \(2013\)](#)

- The plasma must have electron density large enough that the maximum electric potential (after all ions are removed from a Debye sphere) can accelerate electrons to the ionization energy of the neutral.
- The process must transfer energy from the flowing neutrals to the electrons, via the ions. At the flow energies for which AI is observed the cross sections for ionization by a neutral-neutral collision or ion-neutral collision are far too low ([Danielsson 1973](#)). The cross-section for ionization by an ion-neutral collision does not reach a value comparable to the electron-neutral collision until the velocity of the ion is comparable to that of the electron, this only occurs at energies several orders of magnitude above the ionization energy. [Kaganovich et al. \(2006\)](#); [Kieffer & Dunn \(1966\)](#)
- Ionization proceeds only when the relative velocity between the species exceeds the threshold, critical velocity.

Since the Debye length defines the scale below which charge neutrality can be violated then, if we require a localized pocket of charge imbalance to form, we require that the Debye length, λ_D , to be much smaller than the Larmor radius of the ions, r_{li} . [Stark et al. \(2013\)](#)

$$\lambda_D \ll r_{li}, \quad (1.90)$$

$$\left[\frac{\epsilon_0 k_B T_e}{n_e e^2} \right]^{1/2} \ll \frac{m_i v_\perp}{eB}, \quad (1.91)$$

$$n_e \gg \frac{\epsilon_0 k_b t_e B^2}{m_i^2 v_\perp^2}. \quad (1.92)$$

Here we have used our definition of Debye length (1.8), Larmor radius (1.29 and rearranged in terms of electron density.

The second thing we need is a perpendicular magnetic field of sufficient magnitude to magnetize the electrons. In more strict terms we require the electron cyclotron frequency to be greater than the electron-neutral collision frequency. If the collisional frequency is too high then electrons will not remain long enough in a region of charge imbalance before they do a random walk out of our charge pocket. In mathematical terms, the Larmor frequency from 1.28 must be larger than the collision frequency from 1.30 which involves the thermal speed $v_t h$.

$$\frac{qB}{m_e} \gg n_g \sigma_g v_t h, \quad (1.93)$$

$$B \gg \frac{m_e n_g \pi r^2}{e} \left[\frac{k_B T_e}{m_e} \right]^{1/2}. \quad (1.94)$$

Since we require that there is sufficient electron density such that the maximum potential of a charge pocket is greater than the ionization energy (ϕ_i) then if we assume our charge pocket has a radius equal to the ion Larmor radius then the solution to Poisson's equation becomes:

$$\phi = \frac{n_e e R_{li}^2}{4\pi\epsilon_0}. \quad (1.95)$$

This gives a threshold of electron number density, (Stark et al. 2013)

$$n_e \geq \frac{4\pi\epsilon_0 \phi_i e B^2}{m_i^2 v_\perp^2}. \quad (1.96)$$

At the critical velocity of $v_\perp = v_c = \sqrt{2e\Phi_i/m_h}$ this becomes:

$$n_e \geq \frac{2\pi\epsilon_0 B^2}{m_g} \quad (1.97)$$

giving the third prerequisite.

If we satisfy both of our minimum density constraints (1.97 & 1.92) and the magnetic field constraint (1.94) then there is the potential for CIV. If we then exceed the critical velocity threshold in the perpendicular to field direction then ionization will take place. This ionization is powered by a transfer of momentum from the neutrals to the electrons, perhaps via the ions. The acceleration of these electrons up to the kinetic energy of the incoming neutral flow results in a non-thermal electron distribution function. Collisions between the high energy tail of this distribution and neutral atoms results in the formation of ions, shifting the ionization fraction.

1.5.2.3 CIV in the fluid limit

We have discussed the various components of the CIV mechanism throughout chapter 1: we have talked about the Debye scale for charge imbalance; the Larmor radius for particle orbit sizes; the binary collision operator for ion-neutral displacement; the acceleration of electrons under electric fields; ionization reactions and rate coefficients from electron distribution functions. None of these processes are present formally in an MHD description of a plasma. CIV must take place at a small scale, not much larger than the ion gyroradius. It must take place quickly, sub-nanosecond time-scales are typical of both the acceleration of electrons into the non-thermal distribution but also typical of the electron-neutral collision rate. This makes the CIV mechanism a microscopic process.

However, our criteria that we lay out in section 1.5.2.2 above have not involved any of these processes. We have derived a magnetic field strength condition, placed a condition on the density and we require a prerequisite, sufficiently large relative velocity between a neutral gas and seed plasma. These are all macroscopic quantities. These are all quantities that are contained in a fluid description of the plasma, $B, \rho_p, \rho_g, v_p, v_g$ can be solved for with the equations of MHD.

An MHD model can tell us the magnetic field, plasma density and plasma velocity and a hydrodynamic model can tell us the gas density and velocity. A combined MHD-Hydrodynamic description allows the creation of a physically consistent model for CIV. A code which simultaneously simulates the evolution of a co-existing gas and MHD plasma as well as their collisional interactions can predict the presence and the magnitude of critical velocity ionization.

The following two chapters describe the development of two pieces of numerical code intended to do just that. The first, in chapter 2 is a linear finite difference MHD code which incorporates both momentum coupling and Alfvén ionization. The second code, in chapter 3, is a necessary move to a fully non-linear model of the same mechanisms. Momentum coupling and CIV results from these two codes are discussed in chapters 4 and 5 respectively.

The goal of the second code is to provide the starting point for a completely general purpose numerical model for a partially ionized plasma.

Chapter 2

Linear Gas/MHD Interactions Code

2.1 Introduction

As we have already seen, in a partially ionized plasma there exist neutral atoms as well as the charged species. These atoms interact with the plasma primarily through collisions which allows momentum to be exchanged between the charged and neutral species. The atoms and plasma also interact by ionization and recombination. Atoms can be ionized, producing a free electron and ion, if they undergo collisions of sufficient energy. Likewise, electrons and ions can recombine into neutral gas atoms if they undergo interactions of the right energy.

In order to understand the evolution and dynamics of such a partially ionized system then you must be able to describe these interactions and their knock on effects onto the plasma. This means understanding how the presence of a neutral gas influences the plasma. For plasmas in thermal equilibrium, there is a range of temperatures for which both these species exist in notable quantities; there is then also a range of temperatures for which these inter-species interactions are most relevant. Not all plasmas are in an ionization equilibrium, with a steady-state ionization fraction, progress in modelling partially ionized plasmas can lead to progress in modelling plasmas where the ionization

fraction is evolving.

As was discussed in section 1.4.2, fluid descriptions of both plasmas and gas have been successful in describing many plasmas throughout a large parameter space. The fluid description of a plasma, MHD, is also one of the simplest descriptions of plasma physics. This combination of simplicity and accuracy motivates us to model the interactions between the gas and plasma within the framework of MHD. Meshing large scale fluid dynamics with the particle-particle kinetics that dictates these binary interactions presents a unique challenge.

This chapter describes the process of creating a 2-dimensional linear fluid code that models both the gas and MHD plasma as well as interactions between them, namely momentum coupling and Alfvén ionization (although ionization in general is considered). A linear code is significantly simpler in both creation and operation so it makes a sensible starting point. Diver et al. (2006) created a simple linear momentum-coupling gas-plasma interactions code and so was used as a base for this work. The work that went into making a linear gas-MHD momentum coupling code (GMMC) is recreated here in more detail along with details of the addition of Alfvén ionization to existing functionality.

This complete set of model equations and the numerical routines were written in Fortran77 and compiled with the Absoft compiler.

2.2 The Model Equations

The plasma is modelled by the set of ideal MHD equations from section 1.4.2:

$$\dot{\rho} = -\nabla \cdot (\rho \mathbf{v}_p) \quad (2.1a)$$

$$\rho \dot{\mathbf{v}} = -\rho(\mathbf{v} \cdot \nabla)\mathbf{v} - \nabla P + \mathbf{J} \times \mathbf{B} \quad (2.1b)$$

$$P\rho^{-\gamma} = \text{constant} \quad (2.1c)$$

$$\dot{\mathbf{B}} = \nabla \times (\mathbf{v} \times \mathbf{B}), \quad (2.1d)$$

where ρ_p , \mathbf{v} , P , \mathbf{J} and \mathbf{B} are the plasma density, plasma velocity, pressure, current

density and magnetic field. For the gas the standard hydrodynamics equations are applied:

$$\dot{\hat{\rho}} = -\nabla \cdot (\hat{\rho}\hat{\mathbf{v}}_g) \quad (2.2a)$$

$$\hat{\rho}\dot{\hat{\mathbf{v}}} = -\hat{\rho}(\hat{\mathbf{v}} \cdot \nabla)\hat{\mathbf{v}} - \nabla\hat{P} \quad (2.2b)$$

with $\hat{\rho}$, $\hat{\mathbf{v}}$, and \hat{P} being the gas density, velocity and scalar pressure. The dot indicates the derivative wrt time, $\gamma = 5/3$ is the adiabatic constant. Reassuringly if we set $\mathbf{B} = 0$ in equations 2.1 we recover equations 2.2. Since in our derivation of MHD we eliminate the displacement current and charge separation then once the magnetic field is also eliminated, all of the contributions from Maxwell's equations to the plasma dynamics are gone and we are left with the equations for an unionized gas.

Next, the equations are linearised. The first step is to split the vector equations into components for each direction, in this case x and y . We also express each variable in the fluid equations as being the sum of a mean value and time dependent perturbations around that mean. The linear limit is when these perturbations are small in nature ($dU < U$). Any contributions to the model equations which consist of the product of two of these fluctuations are very small and as such can be ignored. Many terms can be ignored in this manner. This can be seen mathematically as:

$$A = A_0 + dA$$

$$B = B_0 + dB$$

$$AB = A_0B_0 + A_0dB + dAB_0 + dAdB$$

$$dAdB \approx 0$$

The equations can be further simplified by a sensible choice of initial conditions. We assume a homogeneous equilibrium density $\rho_{p,g} = \rho_{p,g0} + d\rho_{p,g}$ and homogeneous isotropic magnetic field aligned in the y direction $B_y = B_0 + dB_y$ and $B_x = 0 + dB_x$. For the velocity we take both the gas and plasma as being at rest at $t=0$ such that

$v_{x(g,p)} = 0 + dv_x(g,p)$ and $v_{y(g,p)} = 0 + dv_y(g,p)$. Consequently, any product of the mean of any component of either velocity or B_y with any other term will also be 0.

Putting all of this together we can obtain a set of 8 equations that govern both fluids behaviour. (Diver et al. 2006)

$$\dot{\hat{\rho}} = -\hat{\rho}_0 (\partial_x v_x + \partial_y v_y), \quad (2.3a)$$

$$\dot{\rho} = -\rho_0 (\partial_x \hat{v}_x + \partial_y \hat{v}_y), \quad (2.3b)$$

$$\hat{\rho}_0 \dot{\hat{v}}_x = -c^2 \partial_x \hat{\rho} - K_x, \quad (2.3c)$$

$$\hat{\rho}_0 \dot{\hat{v}}_y = -c^2 \partial_y \hat{\rho} - K_y, \quad (2.3d)$$

$$\dot{B}_x = B_0 \partial_y v_x, \quad (2.3e)$$

$$\dot{B}_y = -B_0 \partial_x v_x, \quad (2.3f)$$

$$\rho_0 \dot{v}_x = -\sigma^2 \partial_x \rho + \left(\frac{B_0}{\mu_0} \right) (\partial_y B_x - \partial_x B_y) + K_x, \quad (2.3g)$$

$$\rho_0 \dot{v}_y = -\sigma^2 \partial_y \rho + K_y, \quad (2.3h)$$

where we have introduced σ and c as the sound speed at equilibrium for the plasma and neutral gas respectively (1.19). We have also taken this opportunity to introduce the useful notation ∂_x and ∂_y to represent the partial derivatives ∂/∂_x and ∂/∂_y .

We have added an extra term to the momentum equations, K . This term represents the exchange of momentum between species (see equation 1.88 in 1.5.1). It is based on the Boltzmann collision operator (e.g. Jancel & Kahan (1966)) in that it is a linear coupling of the form,

$$\mathbf{K}_{x,y} = \pm \Gamma (v_{x,y} - \hat{v}_{x,y}) \quad (2.4)$$

where the term Γ is a constant. Equation 2.4 operates as a drag term which is non-zero when there is a relative velocity between the two fluids. Since it operates in the momentum conservation equations of the two fluids we call it the momentum coupling term.

The coupling constant Γ must have a value between 0 and 0.5. If the value is near 0.5 then the two fluids are locked together, one cannot move without the other

following. This would happen when collisions between the gas and the plasma particles happen frequently enough to transfer significant amounts of momentum within the time of a plasma period. On the other end of the scale, when $\Gamma \rightarrow 0$, the two fluids do not interact strongly, there exists the ability of the two fluids to slip past each other and large relative velocities can be sustained for longer. From the equation for mean free path (1.31) we can define this regime as being when the mean free path for ion-neutral collisions is larger than the hydrodynamic scale, $l_{mf} \gg l_H$.

These equations now have to be reformed in order for them to be solved numerically. They first need to be normalized and then a numerical scheme for solving partial differential equations can be applied.

2.2.1 Numerical Scheme

2.2.2 Normalization

If we were to take an example of some of the relevant plasma parameters from the upper portion of the ionosphere (in SI units), (Huba (2011); Froula et al. (2011))

$$\lambda_D = 2 \times 10^{-3} \text{m}, \quad (2.5)$$

$$n_e = 3 \times 10^{10} \text{m}^{-3}, \quad (2.6)$$

$$\omega_{ci} = 180 \text{s}^{-1}, \quad (2.7)$$

$$\omega_{pe} = 2.8 \times 10^6 \text{s}^{-1}, \quad (2.8)$$

$$\nu_{ni} = 2 \times 10^3 \text{s}^{-1}, \quad (2.9)$$

$$\nu_{ne} = 1.5 \times 10^4 \text{s}^{-1} \quad (2.10)$$

we can see large differences in the order of magnitudes of the numerical values of these parameters, the range of parameters will only get worse when you wish to apply your calculations to a variety of regimes. This presents a problem for a numerical simulation as a wide range of magnitudes can result in large numerical errors. For example, when a subtraction operation is carried out on two large numbers producing

a small difference the resultant error can be unacceptably large. It is therefore beneficial to normalize our equations such that the numbers that the computer works with are close to unity. This minimizes these numerical errors. (Overton 2001)

A sensible choice of typical values for the system need to be chosen. All simulation variables are then presented as a fraction of these typical values leaving you working with dimensionless numbers that are less prone to error. We produce a set of normalized parameters to replace our parameters in equations 2.3. These are:

$$\hat{\rho}' = \hat{\rho}/\hat{\rho}_0 \quad \text{normalized gas density} \quad (2.11a)$$

$$\rho' = \rho/\rho_0 \quad \text{normalized plasma density} \quad (2.11b)$$

$$v'_x = v_x/v_\alpha \quad \text{normalized gas velocity in } x \text{ - direction} \quad (2.11c)$$

$$v'_y = v_y/v_\alpha \quad \text{normalized gas velocity in } y \text{ - direction} \quad (2.11d)$$

$$b'_x = b_x/B_0 \quad \text{normalized magnetic field in } x \text{ - direction} \quad (2.11e)$$

$$b'_y = b_y/B_0 \quad \text{normalized magnetic field in } y \text{ - direction} \quad (2.11f)$$

$$w'_x = w_x/v_\alpha \quad \text{normalized plasma velocity in } x \text{ - direction} \quad (2.11g)$$

$$w'_y = w_y/v_\alpha \quad \text{normalized plasma velocity in } y \text{ - direction} \quad (2.11h)$$

The dash denotes normalized quantities. We have normalized the density and magnetic field strength to the equilibrium values and have used the Alfvén speed, $v_A = \sqrt{B_0^2/\mu_0\rho_0}$, to normalize all velocities. We must also normalize our coordinate system into dimensionless values:

$$t' = t/T \quad (2.12a)$$

$$x' = x/L \quad (2.12b)$$

$$y' = y/L \quad (2.12c)$$

$$L/T = v_a \quad (2.12d)$$

We use L and time, T , as our characteristic length and time scales of the simulation. These are related by the Alfvén speed, i.e. L is the distance something moving

with a velocity equal to the Alfvén speed moves in time T .

We can now combine all this numerical work to express our model equations in a linearised, normalized, component form:

$$\dot{\hat{\rho}}' = -\partial_{x'} v'_{x'} + \partial_{y'} v'_{y'}, \quad (2.13a)$$

$$\dot{\rho}' = -\partial_{x'} \hat{v}'_{x'} - \partial_{y'} \hat{v}'_{y'} \quad (2.13b)$$

$$v'_{x'} = -s^2 \partial_{x'} \hat{\rho}' - \Gamma (v'_{x'} - \hat{v}'_{x'}) / \kappa, \quad (2.13c)$$

$$v'_{y'} = -s^2 \partial_{y'} \hat{\rho}' - \Gamma (v'_{y'} - \hat{v}'_{y'}) / \kappa, \quad (2.13d)$$

$$\dot{B}'_{x'} = \partial_{y'} \hat{v}'_{x'}, \quad (2.13e)$$

$$\dot{B}'_{y'} = -\partial_{x'} \hat{v}'_{x'}, \quad (2.13f)$$

$$\hat{\dot{x}}' = -r^2 \partial_{x'} \rho' + \partial_{y'} B'_{x'} - \partial_{x'} B'_{y'} + \Gamma (v'_{x'} - \hat{v}'_{x'}) / \kappa, \quad (2.13g)$$

$$\hat{\dot{y}}' = -r^2 \partial_{y'} \rho' + \Gamma (v'_{y'} - \hat{v}'_{y'}) / \kappa, \quad (2.13h)$$

All of our parameters are now the normalized variables, marked with $'$. Our time derivatives continues to use the dot notation but now refers to $\partial/\partial t'$. $\partial_{x',y'}$ refers to the partial derivatives with respect to x', y' which are our normalized spatial coordinates. We will drop the prime notation from now on and just assume normalized quantities.

We have introduced 4 key parameters that, along with any initial conditions and driving terms, dictate the evolution of the equations. These are,

$$r = \sigma/v_A \quad (2.14a)$$

$$s = c/v_A \quad (2.14b)$$

$$\Gamma \quad (2.14c)$$

$$\kappa = \hat{\rho}_0/\rho_0 \quad (2.14d)$$

These are the normalized plasma and gas sound speeds, the normalized momentum coupling coefficient and the ratio of densities respectively. To go one step further we can eliminate κ as it is simply a function of the sound speeds.

$$r/s = c/\sigma \tag{2.15}$$

$$= \sqrt{\frac{\hat{P}/\hat{\rho}_0}{P/\rho_0}} \tag{2.16}$$

$$= \sqrt{\frac{\hat{\rho}_0^{5/3}/\hat{\rho}_0}{\rho_0^{5/3}/\rho_0}} \tag{2.17}$$

$$= \left(\frac{\rho_0}{\hat{\rho}_0}\right)^{1/3}, \tag{2.18}$$

where we have invoked the ideal gas law for pressure. Setting r,s and Γ is sufficient to define the plasma parameters that dictate the simulation.

A further benefit to normalizing the equations, beyond numerical considerations, is now apparent. Our simulation parameters r,s and Γ do not define a unique set of real plasma parameters, they only define their relative values. This means a single simulation run can be applied to an infinite combination of plasma parameters, depending on how you choose to work backwards from the normalized to real-valued variables. This demonstrates how two plasmas that initially seem so different behave identically when examined at the right scales.

Our model equations are in differential form, computers obviously cannot solve derivatives directly as they require the idea of infinitesimally small changes to variables. To solve equations 2.13 it is necessary to make an approximation for the derivatives and we can then change the calculation into one that computers *can* handle. The method of finite difference, which essentially changes infinitesimal differences into differences of a finite size, was chosen. The next section describes finite difference, the algorithm used and its implementation.

2.3 Finite Difference

A finite difference of a function, f , has the form $\Delta f = f(x+a) - f(x+b)$. By dividing this by $(a-b)$ we obtain a difference quotient. It is obvious that this difference quotient becomes the derivative of f (df/dx) when $(a-b) \rightarrow 0$. The first finite difference method

was published in Newton's *Principia Mathematica*. Newton's interpolation formula is a discrete form of the Taylor expansion of an arbitrary polynomial. By looking at the Taylor expansion around $f(x)$ for $a, b = \pm h$ we get, (Riley et al. 2006)(Boas 2006)

$$f(x \pm h) = f(x) \pm h \left(\frac{df}{dx} \right)_x + \frac{h^2}{2!} \left(\frac{d^2f}{dx^2} \right)_x \pm \frac{h^3}{3!} \left(\frac{d^3f}{dx^3} \right)_x + \dots \quad (2.19)$$

where we have used the subscript x to denote that the derivatives were evaluated at point x . From equation 2.19 it is obvious we can make some approximations for our derivative, $(df/dx)_x$. If we subtract $f(x)$ from our Taylor expansion of $f(x+h)$ we get,

$$\left(\frac{df}{dx} \right)_x = \frac{f(x+h) - f(x)}{h} - \frac{h}{2!} \left(\frac{d^2f}{dx^2} \right)_x + \dots \quad (2.20)$$

The first term in this equation, $(f(x+h) - f(x))/h$, is known as the forward difference approximation and if we were to use it to approximate our derivative then our error would come from the second term, $\frac{h}{2} \frac{d^2f}{dx^2} + O(h^2)$.

By instead subtracting the expansions for $f(x+h)$ and $f(x-h)$ from equation 2.19 we can obtain a better approximation for our derivative,

$$\left(\frac{df}{dx} \right)_x = \frac{f(x+h) - f(x-h)}{2h} - \frac{h^2}{2 \cdot 3!} \frac{d^3f}{dx^3} \quad (2.21)$$

This time, the first term is the central difference approximation, $(f(x+h) - f(x-h))/2h$. It is apparent that this approximation is more accurate as the residual is given by $\frac{h^2}{12} \frac{d^3f}{dx^3} + O(h^3)$. (Mitchell & Griffiths 1980)

The second order central difference approximation can be constructed by using the above central difference approximation for the gradient at two new points at $x+h/2$ and $x-h/2$ then applying a second central difference approximation to those new points in order to approximate the second derivative of f wrt x .

$$\frac{\partial^2 f}{\partial x^2} = \frac{f(x+h) - 2f(x) + f(x-h)}{h^2} \quad (2.22)$$

We can continue to construct higher order finite difference approximations for any derivatives by combining any number of difference approximation to reduce these residual errors further or improve stability. Both the scheme used here, for the linear code

GMMC, and both schemes used for the non-linear code GMMC (described in chapter 3) are second-order schemes. Any finite difference method works on the same principle of replacing these derivatives with a choice of finite difference approximations.

Finite difference methods are popular ways to solve partial differential equations (PDEs) and although the derivation and forms of finite difference methods varies they all are held together by the same idea. This idea is that by replacing the derivatives present in a PDE by finite differences approximations then they become solvable.

2.3.1 Lax-Wendroff Scheme

Our model equations have the form of a hyperbolic equation,

$$\frac{\partial u}{\partial t} + \alpha \frac{\partial u}{\partial x} = 0 \quad (\alpha > 0), \quad (2.23)$$

in 1 dimension for variable or system of variables, u . The numerical scheme chosen to solve these was the Lax-Wendroff formula from [Lax & Wendroff \(1960\)](#); it is probably the most well known and widely used formula used to solve first order hyperbolic equations. ([Mitchell & Griffiths 1980](#)) To numerically solve the equation we create a grid of equally spaced points both in x and t , spaced k and h apart as above. If we were to simply use a central difference operator we would encounter problems with stability. In particular such a scheme is affected by an instability called the mesh-drift instability which comes about as a result of odd and even-numbered points being decoupled from each other, only odd points are used to calculate the evolution of even points and vice versa. This results in short wavelength signal being amplified without bound. ([Press et al. 1994](#)) ([Reese, D. R. 2013](#))

In order to decrease the truncation error and eliminate mesh-drift the Lax-Wendroff method further introduces midpoints at $x + 1/2k$ and $t + 1/2h$ where values for u are calculated by a Lax scheme then central difference approximations of these half-grid points are used to calculate the point and x and $t + 1$. For brevity we introduce the central difference operator and second order central difference operator, δ_x and δ_x^2 , as being:

$$\delta_x u_m^n = u_{m+1/2}^n - u_{m-1/2}^n \quad \text{and} \quad (2.24)$$

$$\delta_x^2 u_m^n = u_{m+1}^n - 2u_m^n + u_{m-1}^n \quad (2.25)$$

With this notation, the Lax-Wendroff formula for equation 2.23 is,

$$U_m^{n+1} = (1 - p\alpha\delta_x + \frac{1}{2}p^2\alpha^2\delta_x^2)U_m^n \quad (2.26)$$

$$= U_m^n - \frac{1}{2}p\alpha(U_{m+1}^n - U_{m-1}^n) + \frac{1}{2}p^2\alpha^2(U_{m+1}^n - 2U_m^n + U_{m-1}^n) \quad (2.27)$$

$$= (1 - p^2\alpha^2)U_m^n - \frac{1}{2}p\alpha((1 - p\alpha)U_{m+1}^n - (1 + p\alpha)U_{m-1}^n) \quad (2.28)$$

where we have introduced some new notation. U means the numerical approximation of the variable u , the subscript donates the spatial coordinate, the superscript denotes the timestep with n being the current timestep and $n + 1$ the next timestep. p is our mesh ratio which is the ratio of the time step to the spatial step $p = k/h$. The Lax-Wendroff method is second order in both time and space (Mitchell & Griffiths 1980).

This equation allows us to express the numerical approximation for variable u at position m at the next time $t = t + h$ based on the previous value of u at position m and the current time $t = t$ plus the values of two adjacent points at $m - h$ and $m + h$.

We can easily extend this to 2-dimensions and to an array of unknowns \mathbf{u} of size n . Our system of equations in 2.13 can be expressed in vector form as,

$$\frac{\partial \mathbf{u}}{\partial t} + A \frac{\partial \mathbf{u}}{\partial x} + B \frac{\partial \mathbf{u}}{\partial y} = 0, \quad (2.29)$$

where A , B are $n \times n$ matrices of coefficients from equations 2.13 and \mathbf{u} is an n -component vector consisting of our set of n variables (plasma/gas density, velocity components and magnetic field components). The Lax-Wendroff method for systems of hyperbolic equations in two-dimensions is,

$$U_{l,m}^{n+1} = \left(I - \frac{1}{2}pAH_x - \frac{1}{2}pBH_y + \frac{1}{2}p^2A^2\delta_x^2 + \frac{1}{2}p^2B^2\delta_y^2 + \frac{1}{8}p^2(AB + BA)H_xH_y \right) U_{l,m}^n \quad (2.30)$$

We have kept the $\delta_{x,y}$ notation as being the central difference operator at half grid points and introduced $H_{x,y}$ as being the central difference at full grid points i.e.

$$H_x = U_{l+1,m}^n - U_{l-1,m}^n.$$

To simulate the evolution of \mathbf{u} we just need the matrices A and B which tell us how the variables in our system of equations depend on each other and then we can apply equation 2.30. These matrices are easily constructed; we enumerate each variable then each row, n , corresponds to one of our model equations and dictates the time evolution of variable n . Within that row each column, m , contains the coefficient of the derivative of the corresponding variable m . A contains the coefficients for the x-direction derivatives and B is for the y-direction derivatives' coefficients.

For example, for the gas density, equation '1', which corresponds to the first row of our matrices,

$$\dot{\rho} = -\partial_x v_x - \partial_y v_y,$$

has a coefficient of 1 (we switch signs to fit the form of equation 2.3.1 to that of 2.29) for the x-derivative of v_x , variable '3' and no other x-derivatives so the first row of A becomes:

$$[0 \ 0 \ 1 \ 0 \ 0 \ 0 \ 0 \ 0],$$

and it has a coefficient of 1 for the y-derivative of v_y , variable '4', so the first row of B becomes:

$$[0 \ 0 \ 0 \ 1 \ 0 \ 0 \ 0 \ 0],$$

By repeating this process for all the model equations we end up with,

$$A = \begin{bmatrix} 0 & 0 & 1 & 0 & 0 & 0 & 0 & 0 \\ 0 & 0 & 0 & 0 & 0 & 0 & 1 & 0 \\ s^2 & 0 & 0 & 0 & 0 & 0 & 0 & 0 \\ 0 & 0 & 0 & 0 & 0 & 0 & 0 & 0 \\ 0 & 0 & 0 & 0 & 0 & 0 & 0 & 0 \\ 0 & 0 & 0 & 0 & 0 & 0 & 1 & 0 \\ 0 & r^2 & 0 & 0 & 0 & 1 & 0 & 0 \\ 0 & 0 & 0 & 0 & 0 & 0 & 0 & 0 \end{bmatrix} \quad (2.31)$$

$$B = \begin{bmatrix} 0 & 0 & 0 & 1 & 0 & 0 & 0 & 0 \\ 0 & 0 & 0 & 0 & 0 & 0 & 0 & 1 \\ 0 & 0 & 0 & 0 & 0 & 0 & 0 & 0 \\ s^2 & 0 & 0 & 0 & 0 & 0 & 0 & 0 \\ 0 & 0 & 0 & 0 & 0 & 0 & 1 & 0 \\ 0 & 0 & 0 & 0 & 0 & 0 & 0 & 0 \\ 0 & 0 & 0 & 0 & 1 & 0 & 0 & 0 \\ 0 & r^2 & 0 & 0 & 0 & 0 & 0 & 0 \end{bmatrix} \quad (2.32)$$

From these two matrices we can calculate A^2 , B^2 , AB and BA and substitute these into equation 2.30. Now we end up with a system of 8 equations which show us what finite difference operators to use on what equations weighted by the correct coefficients. Sticking with our example of the gas density we end up with the finite difference equation,

$$\hat{\rho}^{n+1} = \hat{\rho}^n - \frac{1}{2}pH_x v_x^n - \frac{1}{2}pH_y v_y^n + \frac{1}{2}p^2 s^2 \delta_x^2 \hat{\rho}^n + \frac{1}{2}p^2 s^2 \delta_y^2 \hat{\rho}^n, \quad (2.33)$$

where we continue to use our shorthand for difference operators. This method is repeated for the other 7 variables to retrieve a set of equations that calculate what the value of each variable is at the next timestep given the values of these variables at the current time.

We can however immediately tell that even a simple differential equation ends up with many terms. This gets worse for the more complicated PDEs.

One thing to note about the Lax-Wendroff scheme is that the entire right hand side of the equation depends only on the value of each variable at the current timestep, this makes it an explicit finite difference scheme.

Contributions from the momentum coupling term, K , are not present in any of these finite difference equations. This is because K never appears as a gradient, the magnitude of the momentum coupling is only dependent on the absolute values of the gas and plasma velocities and not on their spatial variations. This means that the momentum coupling can be added trivially onto the numerical equations, just as they appear on the model equations, without any further thought.

2.3.1.1 Boundary Conditions

The Lax-Wendroff method relies entirely on central difference operators. This means that to calculate the evolution of point (l, m) we need to know \mathbf{u} at 4 different points $(l + 1, m)$, $(l - 1, m)$, $(l, m + 1)$ and $(l, m - 1)$ as these are the points that the central difference operators use when they act on point (l, m) .

Since a computational domain must have an edge this presents us with a problem. To calculate the evolution of the end points we require an additional point, one that is controlled by something other than the finite difference algorithm. This boundary point can then be used to calculate the final finite difference point. For example, if our computational domain extends from $x = 1, lt$ then we need boundary points at $x = 0$ and $x = lt + 1$.

It is often remarked, perhaps facetiously, that most of physics is dictated by an appropriate choice of boundary conditions. There is some truth to this; all else being equal the entire evolution of the same initial conditions in a computational domain are dictated by the boundaries.

Boundaries can be physically real and therefore easy to define, for example in thermodynamics you might impose a surface with a fixed temperature or in fluid dynamics

you might impose the no-slip condition, where the velocity of a fluid at a solid boundary is zero. However, if your simulation has no obvious edges that can be defined easily then there are other ways in which these ghost points could be defined. By continuing to set these points to a fixed value you create nodes in any wave solution but, like a solid boundary, this would cause reflections from your edge points. This type of approach is sometimes physically reasonable, for example, in an electrostatics simulation where the electric field sufficiently far away from test charges can be set equal to zero.

A transparent boundary or non-reflecting boundary condition (NRBC) is a boundary at which the intention is for any signal to pass through to the exterior of the simulated region without influencing the behaviour of the interior points.

When the governing equations are linear, concerned only with small amplitude fluctuations around a steady mean, then analytic solutions for the creation of a non-reflecting boundary condition (NRBC) are possible. Theoretical solutions for this have existed for many years ([Bayliss et al. \(1982\)](#); [Givoli \(1991\)](#); [Hagstrom \(1999\)](#)) but problems in implementation can still be present.

We implement a simple expression for the variables at the ghost points by fitting a parabola through the interior points that are adjacent to the edge. The equation of a parabola is given by

$$u(x) = ax^2 + bx + c, \tag{2.34}$$

which has 3 unknown coefficients (a , b and c). By constructing a set of 3 linear equations which correspond to the 3 interior points that are adjacent to the ghost points we can solve for these unknowns and thus calculate the value for u at our ghost point. For simplicity, we use a grid-size of 1 and make our ghost point occur at $x = -1$ and our 3 adjacent interior points are $x = 0, 1, 2$. $u(x)$ is the value of u position x . Our

system of equations becomes

$$u(0) = c, \tag{2.35a}$$

$$u(1) = a + b + c, \tag{2.35b}$$

$$u(2) = 4a + 2b + c. \tag{2.35c}$$

By rearranging, this gives us values for our coefficients of,

$$a = 1/2(u(2) - 2u(1) + u(0)), \tag{2.36a}$$

$$b = u(1) - u(0) - a, \tag{2.36b}$$

$$c = u(0). \tag{2.36c}$$

For $x = -1$ this gives us,

$$u(-1) = 3u(0) - 3u(1) + u(2) \tag{2.37}$$

These are our polynomial boundary conditions and are applied along all 4 edges of the 2-dimensional computational domain.

2.4 Stability Criteria

A necessary step in working with a numerical scheme is determining the extent of its stability. Stability is intrinsically linked with the error in the numerical solution. A numerical scheme is only stable if the error on one timestep does not cause an increase in the error on the next. By looking at how an error changes over time we can define 3 regimes: if the error remains constant then the scheme is said to be neutrally stable; if the errors decay over time then the scheme is said to be stable; if the error terms grow over time then the scheme is said to be unstable. Along those lines, we can use the Von Neumann stability analysis as a useful tool that can provide us the first step towards validating a finite difference scheme.

The Von Neumann stability analysis is local, it does not account for boundary conditions. We assume that the coefficients of the finite difference equations are only slowly changing, meaning they can be considered as roughly constant in both space and time. This is a reasonable assumption for the linear regime of GMMC. If u_l^n remains our system of variables at time $x = n$ and position $x = l$ and U_l^n the numerical approximation of those variables from finite difference then we can define our error term ϵ ,

$$\epsilon_l^n = U_l^n - u_l^n. \quad (2.38)$$

Under our assumptions we can rewrite this in terms of the sum of eigenmodes,

$$\epsilon(x) = \sum_j A_j e^{ifx_j}, \quad (2.39)$$

where f is some arbitrary frequency. We can consider the time evolution of a single one of these eigenmodes. Suppose we start at $t = 0$ then we would want to know how the initially small error propagates as t increases. If, we expect the solution to either exponentially grow or decay in time then we can write this solution at timestep n as: (Mitchell & Griffiths 1980)

$$u_j^n = \xi^n e^{ikx_j}. \quad (2.40)$$

It is clear that the evolution of this single eigenmode is dictated by integer powers of this complex number, ξ . This leads to it being called the *amplification factor*. We can easily see that this error does not grow in time only when the magnitude of the amplification factor is always less than 1. i.e. where

$$|\xi|^2 = \xi\xi^* \leq 1 \quad (2.41)$$

is satisfied.

To determine stability we must work out the amplification factor for the Lax-Wendroff scheme (in one dimension) we can simply substitute equation 2.40 into equation 2.26 to get.

$$\xi = 1 - i\alpha \sin(k\Delta x) - \alpha^2(1 - \cos(k\Delta x)) \quad (2.42)$$

where $\alpha = v\Delta t/\Delta x$. So,

$$|\xi|^2 = 1 - \alpha^2(1 - \alpha^2)(1 - \cos^2(k\Delta x)) \quad (2.43)$$

This means our stability condition is satisfied when $\alpha^2 \leq 1$, in order to keep our scheme stable we enforce

$$v\Delta t \leq \Delta x. \quad (2.44)$$

This is the famous Courant-Friedrichs-Lewy (CFL) condition. ([Press et al. 1994](#)) It can be simply understood as the following: the point u_j^{n+1} is computed from its neighbouring points, $u_{j\pm i}$. These 3 points ($u_{j-1,j,j+1}^n$) define a region where information is allowed to influence point u_j^{n+1} . Since a wave would propagate at v then, if we were to exceed the CFL condition, point u_j^{n+1} would require information from further away the finite difference supplies it and, lacking that necessary information, an instability arises. In practice this means lowering the ratio of the time to spatial step (the mesh-ratio) until this criteria is met.

What should be noted is that, if $\alpha < 1$ then there is some damping to be expected. However, we find that this effect is small for wavelengths which are large when compared to the grid resolution. If we expand [2.43](#) for small values of $k\Delta x$ then,

$$|\xi|^2 = 1 - \alpha^2(1 - \alpha^2)\left(\frac{(k\Delta x)^4}{4}\right) + \dots \quad (2.45)$$

The amplification factor only differs from unity with the fourth order in k . Since we are most concerned with accurately studying waves are those that cover several grid points (otherwise we would choose a finer grid) then $k\Delta_x \ll 1$ and our amplification factor is almost unity. This makes such a scheme very accurate for these modes with next to no dissipation. An added benefit is that short scales, with $k\Delta_x \sim 1$, have an amplification factor less than 1 and as such these unwanted modes decay over time, removing them from the simulation.

This approach can be extended for when u is a vector of variables instead of a scalar. In such a case equation 2.40 simply becomes a vector equation and the result is not significantly changed.

The CFL condition is not the only way to assess the stability of a numerical scheme, especially for non-linear schemes, though it is surprisingly effective given the simplicity of its derivation. (Press et al. 1994) We shall next set out to judge the stability and accuracy of the Lax-Wendroff two-step scheme with a simple test.

2.4.1 Stability Test

We base the success of our numerical scheme on the presence of numerical dissipation and the presence of spurious signal, or the fidelity and stability; we wish our code to both give the correct result and to do it without crashing. We examine the fidelity and stability of the Lax-Wendroff scheme in this section.

Also including the boundary conditions, given by equation 2.37, we can simultaneously judge the suitability of these boundary conditions. For comparison we introduce the forward-time centred-space (FTCS) scheme (a scheme suited for solving parabolic equations) and the Lax-Friedrichs scheme.

The FTCS scheme is a second-order centred in space scheme, like LW,

$$U_m^{n+1} = u_m^n + \alpha p(u_{m+1}^n - 2u_m^n + u_{m-1}^n). \quad (2.46)$$

The Lax-Friedrichs method can be understood as the FTCS method but with the introduction of an artificial viscosity term,

$$U_m^{n+1} = (u_{m+1}^n + u_{m-1}^n) + \alpha p(u_{m+1}^n - u_{m-1}^n). \quad (2.47)$$

For our test case we use the 1-dimensional wave equation,

$$\frac{\partial^2 u}{\partial t^2} = v^2 \frac{\partial^2 u}{\partial x^2}. \quad (2.48)$$

This second order differential equation is split into a set of first order differential equations which can be solved by our numerical schemes.

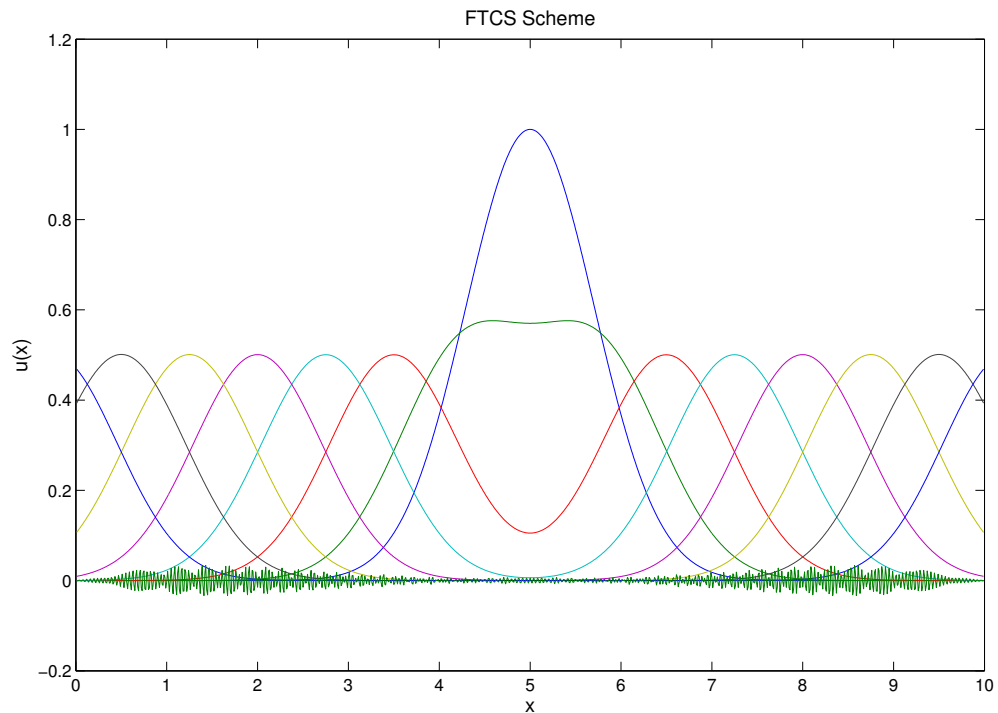


Figure 2.1: Time evolution of the 1-dimensional wave equation solved using a FTCS scheme, note the high frequency (compared to the initial wave) oscillations of the dark green line, after \sim one crossing time has elapsed. This indicates the presence of numerical noise and is not a genuine solution.

Figure 2.1 shows the FTCS method in use. The initial condition is a Gaussian at $x=5$ in u with a full-width half-maximum of 1 which causes 2 symmetric wave packets to form travelling in opposite directions towards the code boundaries. The values for u are plotted at a selection of timesteps. We can immediately see a problem at times later than 1 crossing time; numerical noise at scales comparable to the grid spacing begins to develop. This numerical noise, shown by the noisy green line, grows quickly and soon exceeds the value of the rest of the solution and crashes the simulation. The noise problem is worse than it appears as the mesh ratio must be lowered (to $p \ll 1$), far below what the other two schemes require, to obtain even a semblance of stability. At higher mesh ratios not only does the simulation go unstable much quicker, after just a few timesteps, but the wave solution advects, growing in amplitude over time.

It is also of note that the boundary conditions for this test case are not the simple polynomial equations. Those conditions caused dramatic instabilities as soon as any signal reached the boundaries. Instead the ghost points are determined by switching to the 1-dimensional advection equation at the edge of the computational domain. This has the effect of forcing all signal to move outward from the final grid point, preventing reflection.

This dramatic failure is not unexpected, the FTCS scheme is known to be only suitable for solving parabolic equations. If we carry out a Von-Neumann stability analysis for hyperbolic equations we find there to be no choice of mesh ratio that results in error terms being damped. This is known as being *unconditionally unstable* as there are no conditions in which the solution will remain stable.

Our second example scheme seems much more promising. The Lax-Friedrichs scheme demonstrated in figure 2.2 does not show the same numerical noise as the FTCS method. However, it is clear that the amplitude of the solution decays over time which is not in agreement with the model equation which, once the wave packets have formed, should result in constant amplitude. In physics simulations care must be taken to ensure the fidelity of solutions as well as their stability. An incorrect solution is just as undesirable as an unstable one.

Figure 2.3 shows the evolution of a wave simulated using a LW scheme. The initial condition is the same Gaussian in u that quickly evolves into two waves, propagating in opposite directions. This test case demonstrates several useful features of our chosen numerical scheme. We note the complete absence of numerical dissipation, the amplitude of the wave remains constant as it crosses the domain. We also note the lack of any reflection off or anomalous propagation as the wave reaches the boundaries of the finite difference regime. After many crossing periods have elapsed there is no error growth, this late time behaviour is plotted as the flat green line at $u = 0$.

This lack of dissipation and apparent stability makes the LW scheme suitable for our needs; Lax-Wendroff is certainly one of the most popular choices (Mitchell & Griffiths 1980). The unsuitability of either the LF or FTCS method is something that may be hard to predict by simply looking at their respective equations. Making the

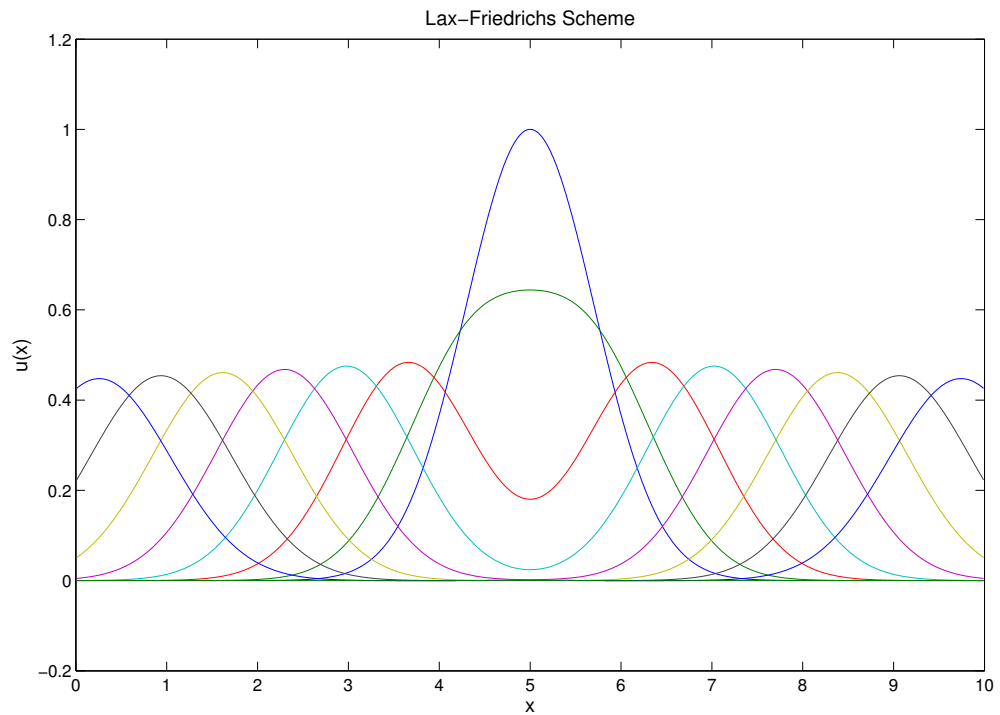


Figure 2.2: Time evolution of the 1-dimensional wave equation solved with an LF scheme, note the dissipation of the solution over time leading to this scheme's low fidelity. Unlike the FTCS solution, this has no numerical noise even after many crossing times have elapsed. We see this by the late time solution shown by the flat green line at $y = 0$.

correct choice of scheme when creating a numerical code (whether it is finite difference or some other group of numerical methods) for solving partial differential equations is tricky, often being more like an art than a strict science. The choice of numerical scheme is even trickier when it comes to non-linear equations as our simplified methods for calculating stability no longer provide reliable data as we shall discuss further in chapter 3.

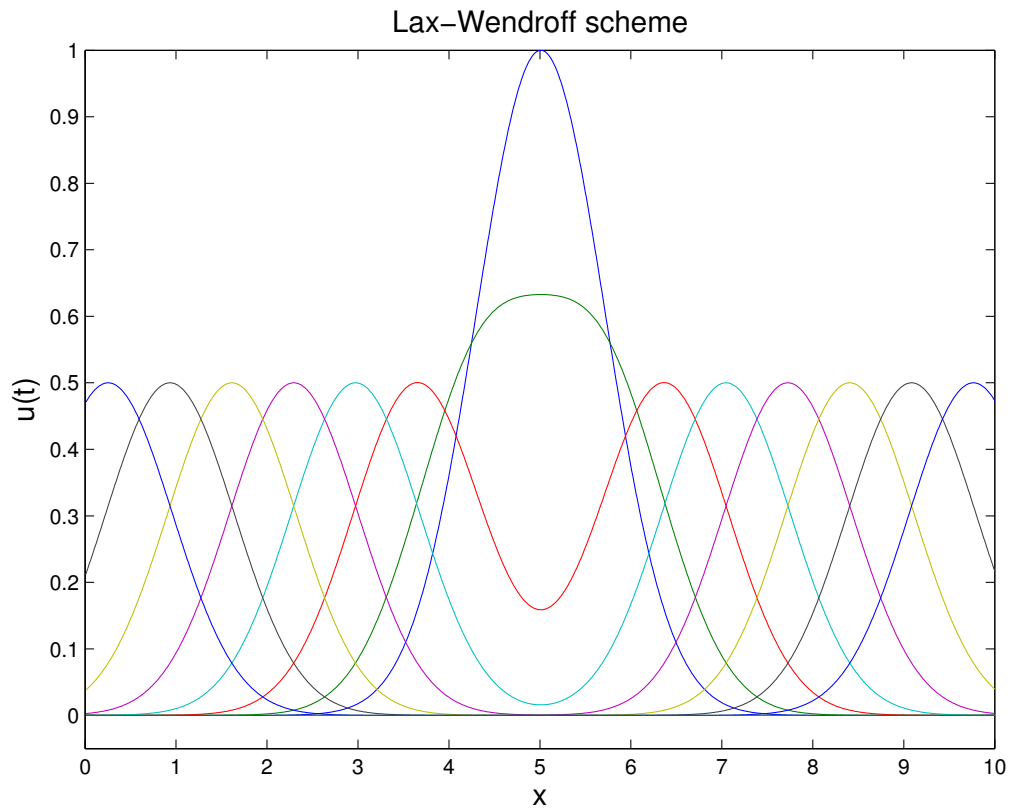


Figure 2.3: The time evolution of the 1 dimensional wave equation solved with a LW scheme, note both the lack of numerical dissipation and the late time stability.

2.5 Deviations from MHD

2.5.1 Momentum Coupling

We have already noted the additional term, K , in the model equations that differentiate the physics of this code from that of ideal MHD. This addition of momentum coupling by separately simulating a neutral gas fluid that is able to interact with the plasma is trivially included as adjustments to the momentum equations of both components of both fluids.

This must have the effect of adding some degree of magnetic diffusion as, although the MHD plasma is still frozen in flux with the magnetic field, the continuous transfer

of momentum from the plasma to the gas and back allows the magnetic field to slip through the fluids to some extent. This property is similar to the addition of resistivity in a non-ideal MHD model.

In terms of wave modes we can write down the dispersion relation of both the gas and plasma from our model equations (2.1) by carrying out a Fourier transform to examine the response of them to a wave of the form $\exp[i(\mathbf{k} \cdot \mathbf{r} - \omega t)]$.

$$\rho[\omega^4 - k^2(\alpha^2 + \sigma^2)\omega^2 + k_y^2 k^2 \alpha^2 \sigma^2] = i\omega^2[k_x K_x + \delta k_y K_y], \quad (2.49a)$$

$$\hat{\rho}(\omega^2 - k^2 c^2) = -i(k_x K_x + k_z K_z), \quad (2.49b)$$

where α and σ are the Alfvén speed and plasma sound speed and c is the gas sound speed. What we notice is that only in the absence of any momentum coupling ($K_x = K_y = 0$) can we recover any pure modes. This is due to the roots of these equations being complex. In the case of $K = 0$ we recover the familiar expressions for the fast and slow magneto-sonic modes and gas acoustic waves (for example [Goedbloed & Poedts \(2004\)](#)). The magneto-sonic modes become the transverse Alfvén mode when their direction of propagation is parallel to the magnetic field.

It is clear that the coupling terms will not be zero everywhere unless all waves in both fluids are perfectly in phase. This cannot simultaneously be true for all directions due to the anisotropy of the phase speeds of waves in the plasma and the isotropy of the phase speeds of acoustic waves in the gas. This means there are always directions in which the coupling is non-zero and as such, directions in which our system has a hybrid response which does not contain the modes of either individual species when treated separately.

This anisotropy is a key difference between dissipation from this momentum coupling term and a standard ohmic dissipation term. The presence of a momentum coupling term gives rise to damped waves.

2.5.2 Alfvén Ionization

Adding AI in the fluid limit presents a unique challenge. Although the fluid velocities in MHD are mean velocities that represent an underlying distribution we shall assume that all particles (plasma or neutrals) are moving at their respective fluid velocity. Since we are operating in a regime where velocities at or above the critical velocity are typical then this assumption will be valid as long as the thermal energy of the plasma is small compared to the ionization energy ($k_B T_e \ll E_i$). When in this regime the random thermal velocities of the gas molecules are small compared to the critical velocity for ionization. AI occurring at close to the theoretical critical velocity, from equation 1.89, should be expected for such plasmas but as the temperature increases then this simple expression may become inappropriate. Since plasmas with a temperature that is a significant fraction of the ionization energy are already fully ionized (e.g. from Saha (1920)) then AI will not be relevant for plasmas where this assumption ceases to be valid.

The inclusion of Alfvén ionization to an existing two-dimensional, two-fluid finite difference model proceeds as follows: At each timestep the fluid code advances giving updated velocity and density fields. These fluid parameters are used to calculate an ionization rate. First we calculate an AI energy reservoir, E_{ai} that comes from the difference in the kinetic energy of the gas, in the frame of reference of a stationary plasma, at the relative velocity and the kinetic energy at the critical velocity. The reason for this reservoir is that once the relative velocity drops to below the critical velocity then AI must cease as the two fluids are no longer capable of generating sufficiently high potential pockets of charge imbalance.

$$E_{ai} = \rho_g (v_{rel}^2 - v_c^2), \quad (2.50)$$

where ρ_g is the gas density and v_{rel} is the relative velocity in the perpendicular to the magnetic field (e.g. y) direction, given by $v_{rel} = |v_{p,y} - v_{g,y}|$. This energy reservoir represents the total amount of energy that could be utilised for AI, if the process was 100% efficient; ionization can only take place when $E_{ai} > 0$. The number of particles

that are ionized by this energy source per unit time is:

$$\dot{n}_{ai} = f \frac{E_{ai}}{E_i}, \quad (2.51)$$

where E_i is the ionization energy. We have introduced f as the *ionization efficiency factor* that represents the fraction of the maximum possible ionization that is performed in a given fluid timestep.

There are four major factors that contribute to the value of f :

1. The number of charge-imbalance pockets formed per unit fluid cell per unit time;
2. The number of electrons per pocket;
3. The fraction of electrons within a given pocket that are accelerated to energies exceeding the ionization threshold energy;
4. The probability that an ionization energy electron undergoes an ionization reaction in a fluid timestep.

The final term clearly has a value close to unity (the plasma is highly collisional) and so f is determined largely by the first three factors. [MacLachlan et al. \(2009\)](#) suggests the third factor is of the order of 10^{-3} . The second factor is well defined as the ambient plasma electron density multiplied by the volume of a pocket. The first factor can be greater than unity because the pocket lifetime is much smaller than the fluid timestep. Given that the fluid timestep is at least an order of magnitude greater than the cyclotron period it is not unreasonable to assume $f \approx 10^{-2}$.

If $f = 1$ then the entire energy reservoir would be exhausted in order to ionize an appropriate number of atoms and the relative velocity would be reduced to the critical velocity in a single fluid timestep, along with a significant perturbation to the plasma and neutral gas densities. As f approaches 1 then a higher time resolution may be required to capture the essential physics. In such cases the total volume of plasma that experiences a charge imbalance pocket approaches the volume of the fluid cell

itself. This is possible when the difference between the ion cyclotron period and the characteristic fluid time-scale is sufficiently large.

Equation 2.51 is then used to calculate a rate of change of density, $\dot{\rho}_{pai}$,

$$\dot{\rho}_{pai} = m_i f \frac{E_{ai}}{E_i}. \quad (2.52)$$

The ionization from AI introduces some deviation in the electron distribution function from thermal equilibrium that results in a momentary excess of electrons at energies that can undergo ionizing collisions with neutral atoms. The electron distribution function then relaxes back to a new equilibrium. The electron relaxation time is shorter than the fluid time-scale in an MHD framework allowing this to take place before the fluid can react. [Goedbloed & Poedts \(2004\)](#)

The relative sizes of the ionization efficiency factor, f , and Γ , the momentum coupling constant, tell us the relative portions of kinetic energy in the relative velocity that goes into AI versus into frictional drag. f/Γ essentially dictates how many atoms are ionized before relative motions are damped by ion-neutral collisions.

Since the experimental results of [Fahleson \(1961\)](#), [Danielsson & Brenning \(1975\)](#) and others show a limit, at the critical velocity v_c , where it is impossible to drive further relative velocity between the two fluids then their experiments were consistent with an f close to unity.

In section 5, to explore the principle; our choice of f is motivated purely by a desire to investigate the behaviour caused by AI. For a given set of plasma parameters (temperature, density, etc.) there is a choice of f that will allow the AI rate to be correctly calculated. It is not unreasonable to

Equation 2.52 allows the fluid densities to be updated; each increase in plasma density has a corresponding decrease in gas density such that total density is preserved,

$$\rho'_p = \rho_p + \dot{\rho}_{pai} dt \quad (2.53)$$

$$\rho'_g = \rho_g - \dot{\rho}_{pai} dt, \quad (2.54)$$

where the prime notation, $'$, denotes the new species density resulting from AI. In order to maintain energy conservation, the energy used for ionization is extracted from the velocity field of the gas. This can be pictured as being a result of the gas atoms that come to rest in figure 1.5 lowering the mean velocity of the gas fluid as the fluid transfers some of its kinetic energy to electrostatic potential.

$$dE = \dot{n}_{ai} dt E_i, \quad (2.55)$$

$$E'_g = E_g - dE, \quad (2.56)$$

$$v'_{g,y} = v_{g,y} \mp \sqrt{\frac{2dE}{\rho_g}}, \quad (2.57)$$

where dE is the energy required to ionize the quantity of gas dictated by equation 2.53. The \mp indicates that a negative velocity is increased and a positive velocity is decreased such that the absolute velocity always decreases. The ionization rate tends to 0 as the relative velocity tends to the critical velocity.

The plasma velocity must also be updated; since the freshly ionized plasma used to be gas then it is born with $v = 0$ in the rest frame of the gas. The mean plasma velocity is now a combination of the plasma velocity and the gas velocity, weighted by density:

$$v'_p = v_p + \frac{\rho_{pai}}{\rho_p} v_g, \quad (2.58)$$

The updated densities, energy density and velocities are the fed back into the fluid code which advances to the next timestep. From here the process repeats itself. Figure 2.4 is a flow chart showing the incorporation of the AI subroutine to the MHD-gas momentum coupling code.

2.6 Example Result: Interference Fringes

As a test case for GMMC in operation we present a simple scenario by examining the response of a frictionally coupled partially ionized plasma when a wave propagates

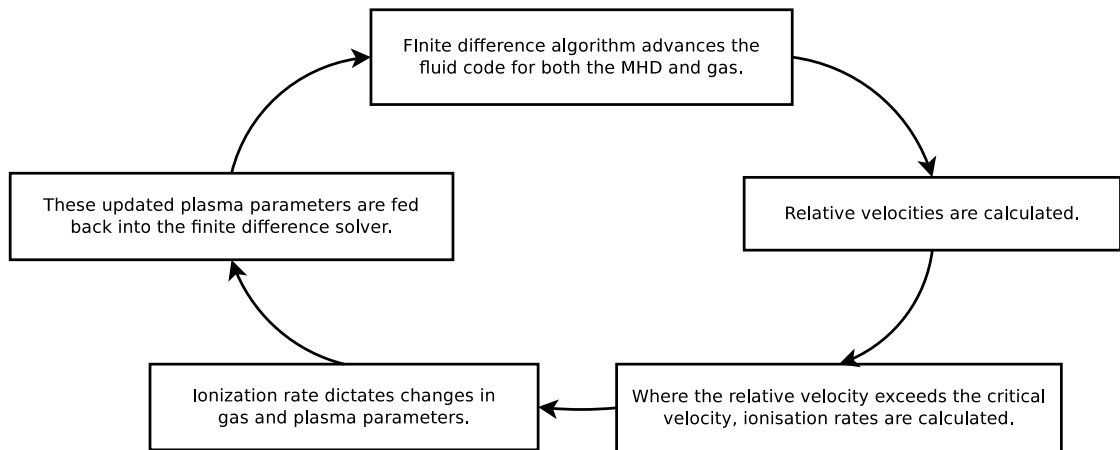


Figure 2.4: Flowchart showing the process for incorporation of an Alfvén ionization subroutine into a finite difference code.

through the domain. We do this by solving the system of equations given in 2.13. This example result does not contain Alfvén ionization, which we will see in chapter 5. The simulations for this example result were carried out on an Intel i7 desktop PC and an Intel Xeon E5 server.

2.6.1 Simulation Setup

Consider a partially ionized, magnetized gas-plasma mixture upon which periodic drivers operate at a boundary edge producing multiple sources for compressional waves in one of the species. These waves propagate throughout the computational domain driving and coupling with waves in the other, unstimulated species. The coherent sources result in interference patterns of alternating bright and dark zones corresponding to constructive and destructive interference.

The properties of the interference pattern produced depend on the driving term as well as the fluid parameters. Particularly we are interested in how the behaviour depends on the presence of the momentum coupling term and the magnitude of its effect.

The driving term operates on the velocity and consists of a static spatial envelope (A_m), which gives rise to the size and placement of the sources along the x-direction,

and a sinusoidally varying (in time) term, A_t . We define $m_{1,2}$ as the coordinates for the end points of our source and m_- as $(m_2 - m_1)$ the difference between the end points. The source is modelled by the following equations:

$$A_t = \cos [(n - 1)2\pi\omega], \quad (2.59)$$

$$A_m = \sin \left(\frac{mk_x 2\pi}{m_-} \right) \exp \left[-d_x \left(m - \frac{m_-}{2} \right)^2 \right], \quad (2.60)$$

$$A = A_0 A_t A_m, \quad (2.61)$$

ω is the frequency of the oscillations, k_x as the spatial wave number of the discrete sources and A_0 is an externally controlled amplitude where $0 < A_0 < 1.0$. d_x is an x-coordinate decay term and controls an additional exponential envelope on top of the discrete sources. This envelope ensures that the wave sources are stronger near the centre of the domain as opposed to the edges. Figure 2.5 shows an example of the spatial envelope amplitude, A_m , as a function of coordinate m . We can see the driving term is dominated by 2 sources at $m \approx 45$ and $m \approx 75$, symmetrical around the centre point ($m = 60$).

The driving term is added to the simulation by replacing the boundary conditions at one edge with values supplied by equation 2.59. For waves at the top boundary being driven perpendicular to the magnetic field we have:

$$v_{y,0,m} = A \quad (2.62)$$

2.6.2 Numerical Results

The above simulation is carried out on a 200x200 grid with a mesh ratio, p , of 0.25. The simulation consists of a fluid plasma and a gas fluid. If we take the mean density of the 2 fluids to be the same then $r = s = 1.0$, this corresponds to an ionization fraction of 0.5. The equilibrium position of both densities are considered to be homogeneous throughout the domain (equal to 1.0) and both fluids are considered to be initially

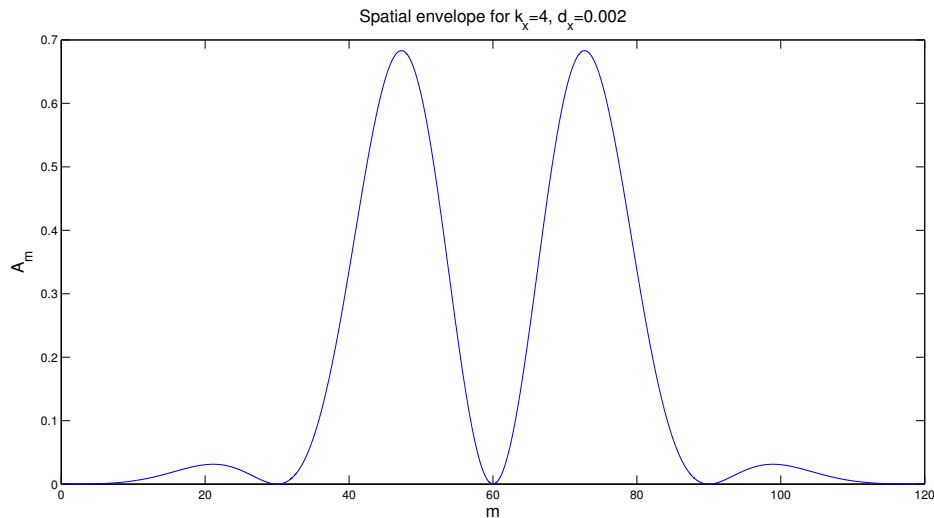


Figure 2.5: The spatial envelope, A_m for a set of discrete wave sources with $d_x = 0.002$, $k_x = 4.0$. The interference pattern from these sources will form interference fringes.

at rest, with both components of both velocities zero. The magnetic field has an x-component (horizontal) value of 1.0 and is zero in the y-direction (vertical).

Waves of the form described by equation 2.59 above are driven at the top boundary in the plasma by oscillating the plasma density and the vertical component of the velocity. These propagate through the domain in the perpendicular to magnetic field direction. The spatial envelope for these waves is defined as in figure 2.5 with $d_x = 0.002$ and $k_x = 4.0$. The time variation is controlled by $f = 12.6$.

We first look at the case of zero momentum coupling, $\Lambda = 0$. Figure 2.6 shows the evolution of the plasma with the absence of momentum coupling, that is $\Lambda = 0$. The presence of 2 discrete wave sources, clearly visible as roughly circular regions with large amplitude changes in density, causes the formation of interference patterns. Due to the symmetry around the simulation's centre point, at $m = 100$, we see constructive interference along this line.

We also note the lack of reflection from the boundaries, the results on stability and boundary conditions from 2.4 remain valid for 2-dimensions and for the equations of MHD/Hydrodynamics.

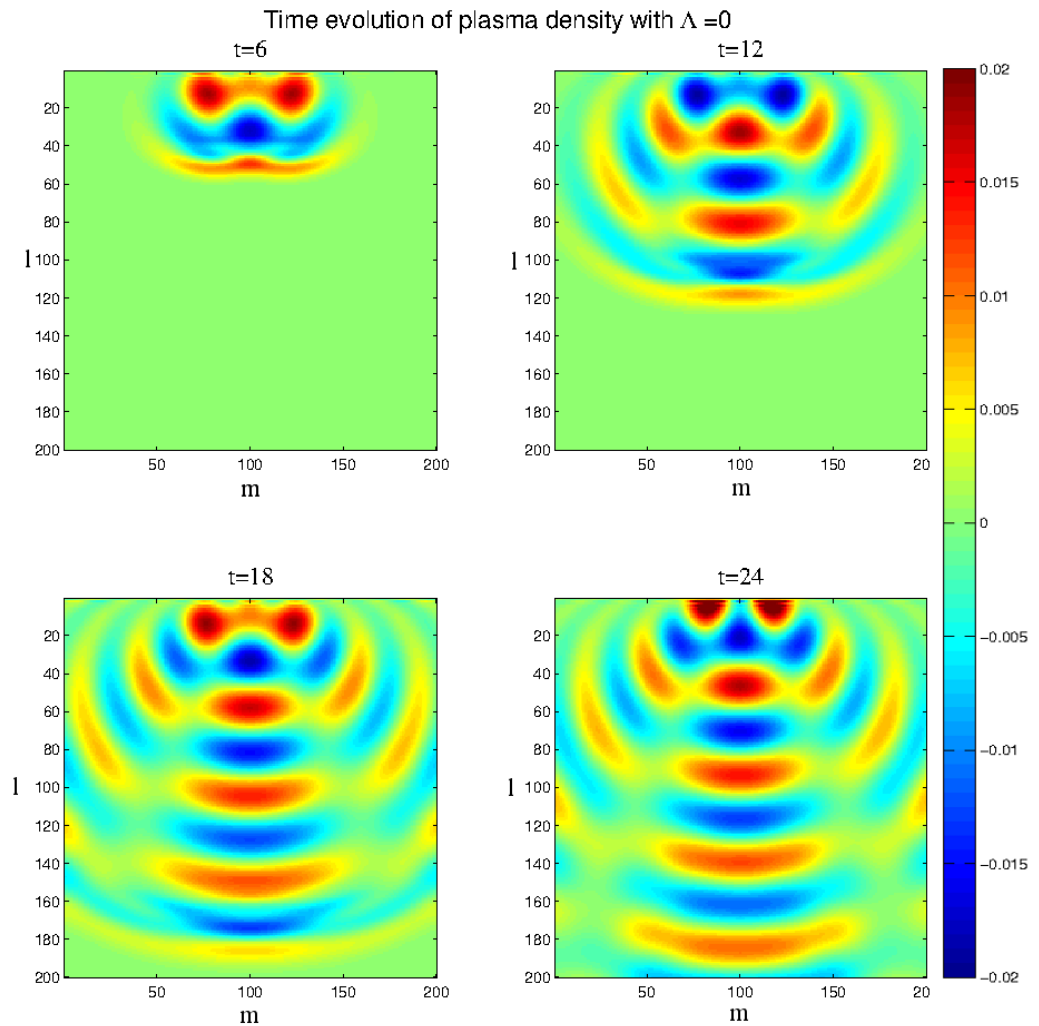


Figure 2.6: Colour maps of the plasma density at increasing times showing the time evolution in the absence of momentum coupling. We clearly see the interference fringes caused by constructive and destructive interference from the two wave sources. The equilibrium magnetic field is orientated horizontally.

Next we look at the magnetic field. Figure 2.7 shows the vector magnetic field perturbation (mean field subtracted) at a late time. The perturbation is obtained by subtracting the background magnetic field. This is necessary since the perturbations are small when compared to the mean, not exceeding more than a few %. The regions of maximum magnetic field perturbation coincide with the regions of maximum density

perturbation. This is predictable since a non-zero $\mathbf{v} \times \mathbf{B}$ produces a magnetic field change.

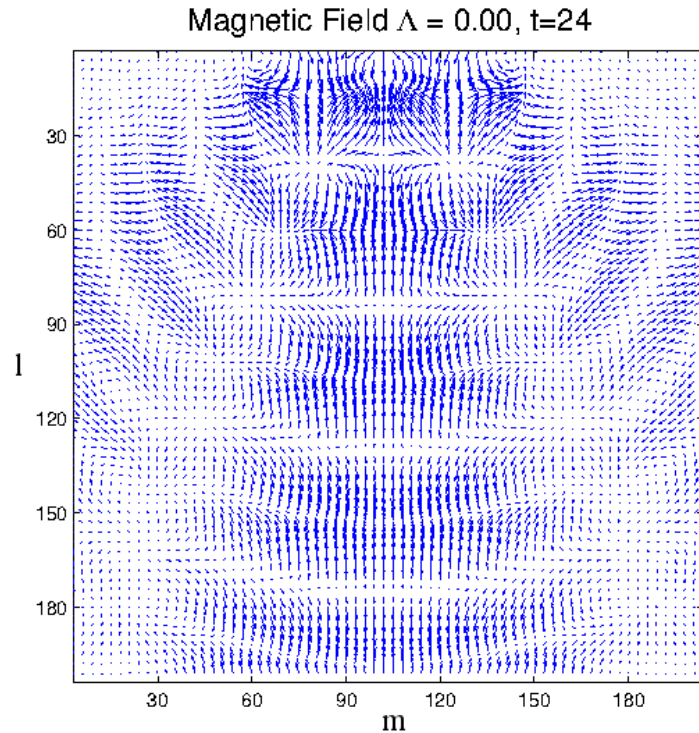


Figure 2.7: Vector diagram of the magnetic field (with background subtracted) at $t=24$ for the uncoupled case. Regions of high curl lie between the regions of largest density perturbation.

As the wave passes a fixed point this oscillating magnetic field is typical of a magneto-acoustic mode producing a magnetic field perturbation in the transverse direction. We can see this is most obviously as a left-right-left pattern of oscillation in figure 2.7 as you follow the path of a wave propagating in the downwards direction along the central line of symmetry.

Due to the background magnetic field, B_0 being orientated in the horizontal direction (and as the linearisation of $\mathbf{v} \times \mathbf{B}$ only includes the terms with B_0) then the angle with respect to the magnetic field that the waves make is a huge factor in terms of the strength of the perturbations created; waves propagating in the perpendicular

direction produce the largest magnetic perturbations.

$$\nabla \times \mathbf{B} = \mathbf{J}, \quad (2.63)$$

$$\frac{d\mathbf{B}}{dt} = \nabla \times (\mathbf{v} \times \mathbf{B}). \quad (2.64)$$

If we increase the momentum coupling term then the presence of the gas effects the propagation of the waves. Figure 2.8 is taken with the same setup and driving terms but with $\Lambda = 0.01$. This means that each timestep there is a transfer of 1% of the relative velocity between the two species. $\Lambda = 0.5$ would be a transfer of 50% of the relative velocity from one fluid to the other. In the case where the mean fluid densities are the same this means an equalisation of the two fluid velocities every timestep, this would result in no relative velocity ever persisting.

Figure 2.8 shows us the plasma density, as before, but in this case with the addition of a small frictional drag term. We take notice that the qualitative appearance of the pattern remains unchanged but there are dramatic differences in the quantitative appearance.

The magnetic field perturbations in the coupled case are seen in 2.9. The perturbations continue to align with the instances of maximum plasma velocity however, they are understandably damped by the presence of momentum coupling. As energy is transferred into motion of the neutral gas then the motion of the plasma is reduced and so the magnetic field perturbations are reduced in amplitude.

The presence of the neutral component allows some measure of slip between the magnetic field and the plasma. Since the two fluids are inherently linked momentum is transferred from the wave in the plasma to build the amplitude of a wave in the gas. The gas is free to move across the magnetic field but continues to collisionally exchange momentum with the MHD fluid. This allows the MHD to bypass the frozen-in-flux (Alfvén 1950) condition to a certain extent because the plasma becomes effectively resistive due to the interactions with the neutrals. In contrast to a resistive dissipation though the energy removed from the ion's velocity does not become thermal energy but instead is exchanged in to gas velocity and can, in return, be exchanged back. This

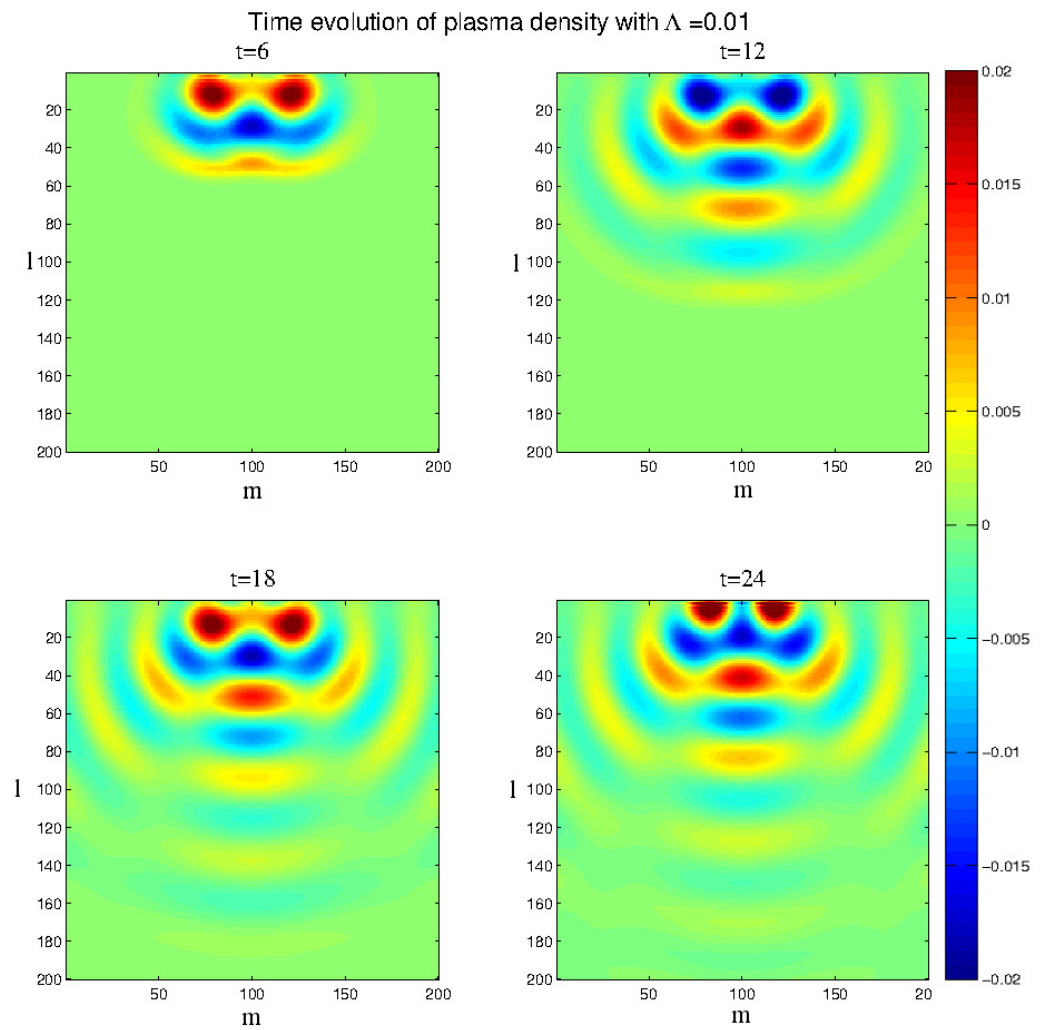


Figure 2.8: Plots of the plasma density at increasing times with momentum coupling enabled. The appearance of the fringes is qualitatively similar to the that the $\Lambda = 0$ case but with a reduced amplitude, phase lag and a change in the position of the maximum destructive interference.

not only modifies the propagation of waves but allows diffusion across the field to be enhanced.

The most obvious difference is that before the wave exits the bottom boundary it is significantly reduced in amplitude compared to the uncoupled case. The maximum amplitude of the final peak is reduced from 6% to 0.55% of the mean density. This

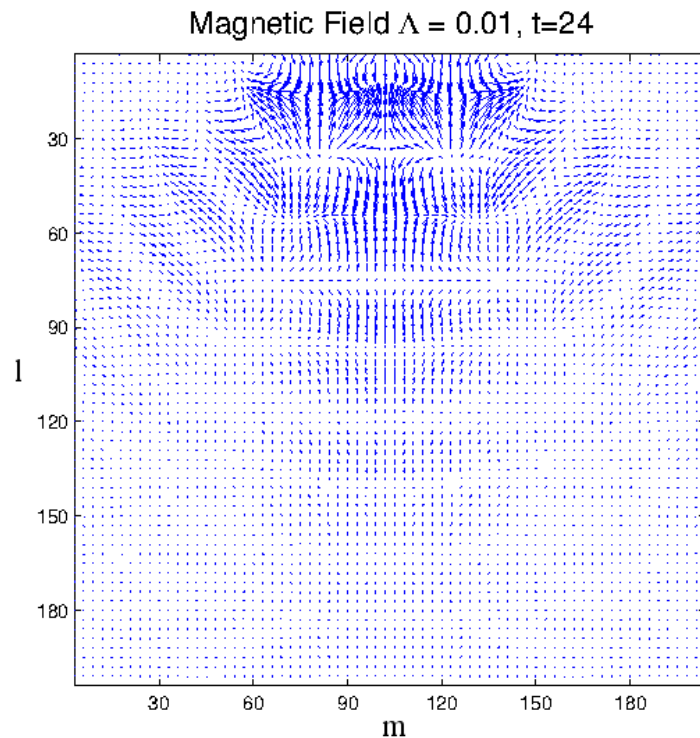


Figure 2.9: Vector diagram of the magnetic field (with background subtracted) at $t=24$ for the coupled case. Regions of high magnetic perturbation are associated with high plasma current. We can see a clear reduction in the strength of the magnetic perturbation that is a result of the damping of the magneto-acoustic wave and the build up of a sympathetic acoustic wave in the gas.

constitutes reduction, of roughly an order of magnitude, due to the energy injected into the domain being spread across more wave modes. The position of the interference pattern is also slightly modified, with the first destructively interfered fringe appearing at a shallower angle with respect to the source than before.

This is best understood as being a result of the change in the phase speed of waves moving in both the perpendicular and parallel to the field directions. Before we had a pure magneto-acoustic mode in the plasma and we now have a coupled magneto-acoustic-acoustic mode.

We also notice a phase difference as a result of the difference in phase speed between the purely magneto-acoustic waves in the uncoupled case and the coupled magneto-

acoustic-acoustic waves. This phase difference is highlighted in figure 2.10. Here we can clearly see both the reduction in the amplitude of the perturbations and a phase difference between the two cases which builds over time. By tracking the relative position of peaks and troughs in the two cases we can calculate the difference in phase speed between the magneto-acoustic mode in the uncoupled case to the hybrid mode in the coupled case to be 0.92.

From a simple test case we can see how the introduction of even a small amount of momentum coupling causes significant changes to the wave and flow dynamics of a gas-plasma mixture such as a partially ionized plasma.

2.7 Limitations of GMMC

During the discussion about the creation of this linear Alfvén ionizing, momentum coupling MHD-gas interactions code we have touched on some of the limitations that it presents us with. We will now discuss these limitations in detail as an argument towards developing a more sophisticated non-linear MHD-gas interactions code that has the same potential to investigate the effects of the presence of a neutral gas in a partially ionized plasma but without the drawbacks inherent to the more simple code.

Linear perturbation limit: One of the most obvious limitations is one inherent to all linear approaches in that the code output only remains physically correct if we remain limited to perturbations that are linear in nature. In practice, this means that perturbations cannot exceed 10% or so of the background; as the perturbation grows in amplitude eventually the non-linear terms become non-negligible. This obviously places a limit on the size of any perturbation of any of the fluid parameters (density, velocity, magnetic field); it also, less obviously, places a limit on the total amount of ionization that the code is capable of. If the ionization, either thermal, Alfvén or by any other mechanism, causes the ionization fraction (either locally or globally) to change by a significant amount then the assumptions that go into linearising the equations become invalid. Since the ionization fraction evolves continually as an integral of the

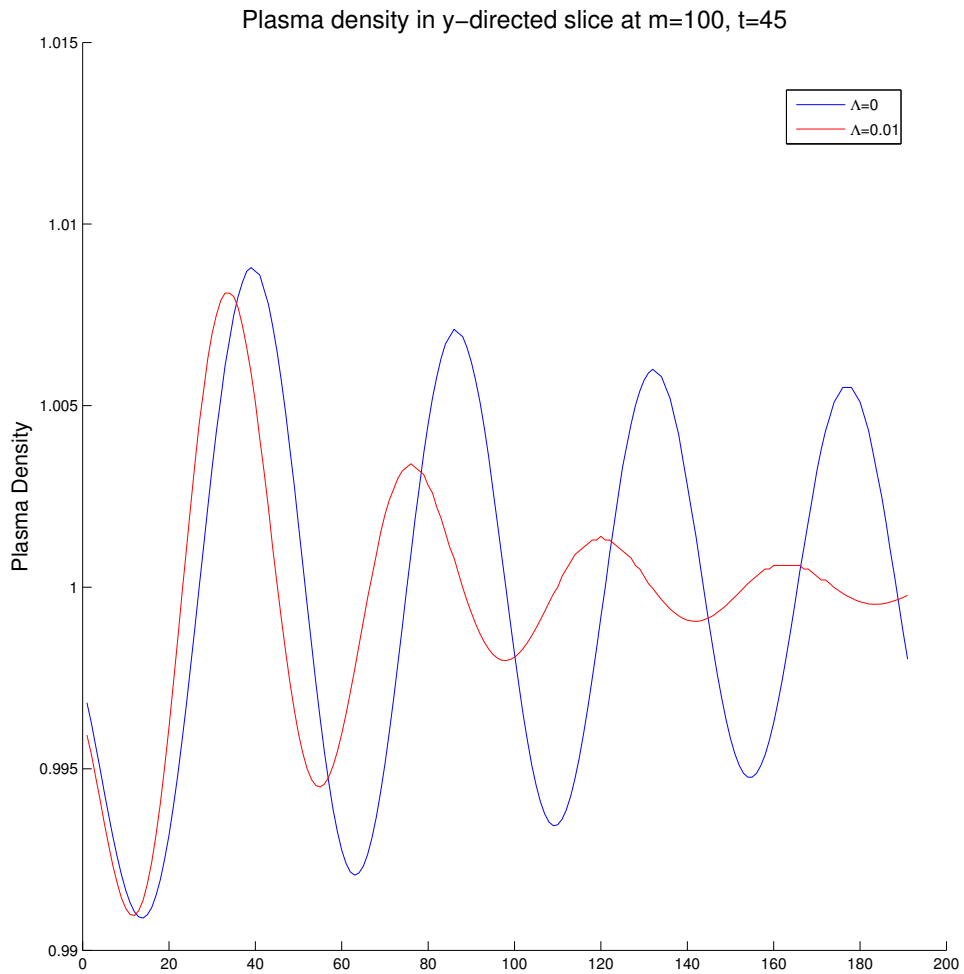


Figure 2.10: A y-directed slice through the line of symmetry at $m=100$ reveals the difference in phase speed caused by the introduction of a small amount of momentum coupling.

ionization rate then we become not just limited by the instantaneous amplitude of perturbations but the integrated ionization change caused by the perturbations.

Readability: If you take the ideal MHD equations in 2.1 which describe the physics intended to be simulated and compare them to the form of the finite difference equation for the evolution of gas density given in 2.33 then we can recognise a problem that is

present to some extent throughout numerical physics. The lines of code to calculate the time evolution of a finite difference scheme are necessarily different in appearance to the differential equations from which they are derived. Our example hides the problem somewhat as well; not only was the gas density equation used as an illustration because it is the most simple of the finite difference equations but we also used shorthand operators that simplify the expression greatly. When it comes to writing the equivalent line in Fortran then these are replaced by references to specific array locations and this simplification is lost. This makes even the most simple finite difference equations very lengthy and very different in appearance to the more familiar physical expressions. The difficulties caused by this are obvious; any small mistake in any one of what are very complicated expressions may be hard to spot but invalidate all calculations done by the numerical code. Even if no mistakes are made the expression in the source code is unrecognisable even to someone who is very familiar with MHD, or fluid dynamics. This makes modifying the physics challenging as one must be very careful not to make such mistakes.

Multi-step derivation process: A closely related problem is that of the lengthy and complicated process of converting the governing equations into the finite difference expressions, ready to be solved by a computer. The process of normalization, linearisation and then deriving the matrices of coefficients is acceptable if it is a one off but until you wish to change the governing equations. If you wished to change to resistive MHD or add a source term, like gravity, to the equations then this process would have to be repeated from scratch. Not only is this time consuming but it introduces further potential for mistakes. If changes could be made to one line of code, especially if such a line was recognisable as part of the governing equations, and the translation into a machine readable format was simple, then adjustments to the physics could be made at will.

Separated equations: Each plasma and gas variable has a unique equation that is a combination of all the variables that have non-zero matrix elements in the corre-

sponding rows of the matrices of coefficients. This poses a problem for parallelisation. Modern Fortran is capable of automatic parallelisation of any piece of array mathematics. By expressing each equation separately we can still use parallelisation within each equation but we cannot easily exploit parallelisation across equations; they must be tackled one at a time. Run time savings could be made by combining the numerical method into a single array operation. This is how the non-linear formulation proceeds.

Hard-coded equilibrium values: As seen in the linearisation of the model equations, all equilibrium values are hard coded into the finite difference expressions. This means that not only are equilibrium values (as opposed to current values) used for the linear calculations but initial conditions cannot be changed. The domain is always homogeneous in density, it always has an initial value 0 for both components of both fluid's velocity and it always has an initial magnetic field that is directed only in the x-direction. While dynamic motion of the fluids can cause perturbations around these means, there is no ability to study any other, more novel, set of initial conditions without creating a new set of governing equations with alternative initial conditions.

Ionization fraction: The ionization fraction can be determined by comparing the densities of the two fluids. Since the two fluid densities are independently normalized then, at first glance, it appears we have freedom to choose any ionization fraction we wish to study. However, we encounter problems due to the ratio of the densities determining the values of r and s , the sound speeds of the two fluids with respect to a fixed Alfvén speed. Since the two fluids are not independent, the dynamics of one effects the evolution of the other. Since they are both stepped in time together then the stability conditions must simultaneously satisfied for both fluids independently. In reality this either requires the sound speeds to be broadly similar or it places such strict requirements on the mesh ratio that the code becomes severely handicapped. Momentum coupling is important across a number of orders of magnitude in ionization fraction and Alfvén ionization is most interesting when changes to the ionization fraction are extreme. The linear code is ineffective in these conditions.

These numerous issues are either inherent to a linear approach or are a consequence of decisions made in the development of the code described in this chapter. In either case the creation of a new non-linear gas-plasma interactions code is capable of resolving them all.

For the most part this ends the usefulness of the linear code, GMMC. We shall revisit this code in chapter 5 to use it for the purposes of Alfvén ionization but the majority of remaining results are simulated using the more advanced, non-linear code GMIC. The following chapter describes the derivation and characteristics of this code.

Chapter 3

Non-Linear Gas/MHD Interactions Code

In this chapter we set out the model equations and numerical methods used in the creation of a non-linear gas/MHD interactions code (GMIC). The construction of the code differs in several ways which will be explored.

Alfvén ionization provides several good reasons to move to a non-linear fluid code, a simple argument is that there is clearly a kinetic energy dependence in AI and kinetic energy is a non-linear term. More practically, non-linearity is desirable because the most obvious applications are in low ionization fraction plasmas where AI can induce large, order-of-magnitude changes in plasma density which places them out of reach of linear considerations.

The creation of a non-linear version of the gas-plasma interactions code outlined in the previous section was undertaken. Using an existing MHD code such as BOUT++ ([Dudson et al. 2009](#)) or Lare3d ([Arber et al. 2001](#)) was considered. Using an existing code would seem to eliminate the large time investment in writing a physics code from scratch as well as bringing the advantage that these existing codes having already been tested against standard scenarios and generally have been well optimized for parallel computing.

For our purposes, the new code requires the interaction between the two separate

species of neutral atoms and ionized plasma ions to be simulated. This is often not the approach used when considering the influence of the neutrals that are present in a partially ionized plasma where additional terms are added to the model equations of the plasma rather than the complete simulation of an entirely separate fluid. Even more crucially, Alfvén ionization requires changes to the fundamental MHD equations to include ionization sources not present in a standard MHD model. This means that any existing code would need to be heavily modified to fit our needs wiping out much of, if not all of the time saved.

Any available MHD codes are also products of many years of development effort. This can lead to them evolving into highly complex pieces of science with many aspects of plasma behaviour included. While this allows a wide variety of studies to be conducted with the same code and increases the ability of such simulations to match the real world, complexity is not always a good thing. By using an advanced model your simulations are not only much more computationally intensive but, if you want to study a specific mechanism, such as we do with AI, all these layers of complexity, each influencing the plasma in their own way, can obfuscate the influence of your chosen mechanism. This makes it unclear what is caused by your mechanism of interest and what is caused by secondary effects. When you have a more basic code then the mechanism of interest and its effects can be isolated more readily.

Writing a new code from scratch allows it to be kept simple, allows both AI and momentum coupling to be incorporated from the start, and eliminates the reliance on external help in order to understand the operation of the code.

Lessons learned from GMMC can be put to use in the creation of a non-linear gas-magnetohydrodynamics interactions code (GMIC). In GMMC the physical equations are hard-coded into the numerical scheme; if a change in physics is required then the numerical scheme must be rewritten from scratch. This makes the addition of Alfvén ionization tricky and it has to be added as an external function. By making the numerical scheme and the physics completely separable, several advantages can be gained. Firstly it allows greater readability of the code meaning bugs and errors are far easier to spot and resolve. Modifying the code for a variety of purposes is also

easier via changes to the physics. The modular nature also means that the entire finite difference scheme can be swapped for an alternative.

Instead of separate arrays for each variable we make the various parameters just an additional dimension in a multi-dimensional array. This allows the numerical scheme to be a single array operation, making it far easier to parallelise. A non linear code has inherently significantly slower runtime due to additional terms in equations and with most robust schemes being multi-step and thus slower. This is compounded by the necessary addition of an absorbing boundary layer, described in section 3.3, which is very computationally costly. Any increase in parallel performance becomes important towards keeping runtime reasonable.

A secondary benefit of switching to a single array for all parameters is that switching between 1, 2, or 3 dimensional simulations becomes trivial. Though this functionality is not exploited much as this thesis deals only with 2-dimensional simulations.

In this chapter we describe the model equations for non-linear MHD in conservative form, including the necessary normalization and derivation of flux functions. We describe the numerical schemes and boundary conditions used to solve those model equations in GMIC and we explore some of the differences between GMIC and the linear gas-MHD momentum coupling code GMMC.

3.1 Model Equations

3.1.1 Conservative Form MHD

The first deviation from the linear computational scheme is in the equations of MHD themselves. Whereas before the model equations were expressed in primitive form we shall switch to the conservative form. [Hou & LeFloch \(1994\)](#) show how any non-conservative scheme used to solve scalar conservation laws - like MHD - will result in unacceptable errors that grow over time. For an example see [Falle \(2002\)](#) which demonstrates significant errors in the MHD code ZEUS compared to an upwind conservative scheme.

The conservation form looks like:

$$\frac{du}{dt} + \nabla \cdot f(u) = 0 \quad (3.1)$$

for a conserved quantity u and a suitable choice of *flux function* f . What the conservative form does is show explicitly that the change of a conserved quantity within a volume can only come as a result of the amount of this quantity that flows into or out of the volume. For example, the mass conservation equation tells us that the only way for the mass inside a volume to increase is if more mass flows into the volume than out, a negative divergence. (Mitchell & Griffiths 1980)

The use of such a form for our equations is not readily apparent but they allow both local and global conservation laws to be established as well as provide jump conditions for shocks. Further, many quality numerical schemes exist that can solve any conservative form partial differential equation.

The equations of MHD are such a system of conservation laws. We start with the non-linear equations of MHD: (Goedbloed & Poedts 2004)

$$\frac{\partial \rho}{\partial t} + \nabla \cdot (\rho \mathbf{v}) = S_1, \quad (3.2a)$$

$$\rho \frac{\partial \mathbf{v}}{\partial t} + \nabla P + \rho \mathbf{v} \cdot \nabla \mathbf{v} - \mathbf{J} \times \mathbf{B} = S_2, \quad (3.2b)$$

$$\frac{\partial e}{\partial t} + \mathbf{v} \cdot \nabla e + (\gamma - 1)e \nabla \cdot \mathbf{v} = S_3, \quad (3.2c)$$

$$\frac{\partial \mathbf{B}}{\partial t} + \nabla \times \mathbf{E} = 0, \quad (3.2d)$$

they are conservation equations for mass, momentum, energy and magnetic flux. Φ is a source term (e.g. from ionization), e is the internal energy and the rest of the symbols have their usual meanings. We continue to work in units of $\mu_0 = 1$. To the right hand side of these equations we have added some sources (S_{1-3}) these represent the contributions from various physical processes beyond the most basic formulation of MHD. For example, any ionization process, such as AI, will change the value of S_1 from 0 since ionization results in changes in density. S_2 would include the gravitational term, $-\rho \nabla \Phi$, and so on.

We note that these equations are not all in the form of 3.1 so we first make the substitutions for our electric field, \mathbf{E} , our current density, \mathbf{J} , based on the assumptions inherent in formulating MHD from section 1.4.2. To close this system of equations we assume the plasma is an adiabatic gas with an adiabatic index γ and can relate the thermal pressure, P , to the internal energy e . This pressure term is known as a scalar-pressure term as it has no directional dependence; this assumes that the plasma temperature is the same in the parallel and perpendicular to the magnetic field directions.

$$\mathbf{E} = -\mathbf{v}\mathbf{B}, \quad (3.3a)$$

$$\mathbf{J} = \nabla \times \mathbf{B}, \quad (3.3b)$$

$$\nabla \cdot \mathbf{B} = 0, \quad (3.3c)$$

$$P = (\gamma - 1)\rho e \quad (3.3d)$$

This allows us to write our MHD equations in conservation form. (Goedbloed & Poedts 2004)

$$\frac{\partial \rho}{\partial t} + \nabla \cdot (\rho \mathbf{v}) = S_1, \quad (3.4a)$$

$$\frac{\partial}{\partial t}(\rho \mathbf{v}) + \nabla \cdot [\rho \mathbf{v} \mathbf{v} + (P_t)\mathbf{I} - \mathbf{B}\mathbf{B}] = S_2, \quad (3.4b)$$

$$\frac{\partial E}{\partial t} + \nabla \cdot [(E + P_t)\mathbf{v} - \mathbf{v} \cdot \mathbf{B}\mathbf{B}] = S_3, \quad (3.4c)$$

$$\frac{\partial \mathbf{B}}{\partial t} + \nabla \cdot (\mathbf{v}\mathbf{B} - \mathbf{B}\mathbf{v}) = 0. \quad (3.4d)$$

The biggest change comes in 3.4c where we have switched from an expression in terms of internal energy to an expression in terms of total energy density which we have defined as

$$E = E_{kinetic} + E_{internal} + E_{magnetic}, \quad (3.5)$$

$$E = \left(\frac{1}{2}\rho v^2 + \rho e + \frac{1}{2}B^2 \right). \quad (3.6)$$

We have defined the total pressure as $P_t = (\gamma - 1)\rho e + \frac{1}{2}B^2$, the sum of the magnetic and thermal pressure.

We have introduced some tensor notation; I is the identity matrix and \mathbf{ab} is the dyad of vectors \mathbf{a} and \mathbf{b} formed by multiplying the column vector \mathbf{a} with the row vector \mathbf{b} such that $ab_{ij} = a_i b_j$.

We have kept the same source terms on the right hand side of our equations, these source terms differ from the rest of the equation because their values are not necessarily dictated by the divergence of a scalar/vector field (or combination of fields) and as such, whenever they are involved, are not solved by the main finite difference algorithm.

For a closer understanding of pressure in an MHD plasma we split the pressure term in 3.4b into parts, the *Reynolds stress tensor* $\rho\mathbf{v}\mathbf{v}$, the *isotropic thermal pressure* $P\mathbf{I}$, and the magnetic part of the *Maxwell stress tensor*, $\frac{1}{2}B^2\mathbf{I} - \mathbf{B}\mathbf{B}$. We can see that the Reynolds stress tensor is a positive pressure ρv^2 directed along \mathbf{v} , equivalent to the *ram pressure*. The other part $p + \frac{1}{2}B^2\mathbf{I} - \mathbf{B}\mathbf{B}$ is expressed in matrix form, taken in a coordinate system where B is directed along the z-axis.

$$\begin{bmatrix} p + \frac{1}{2}B^2 & 0 & 0 \\ 0 & p + \frac{1}{2}B^2 & 0 \\ 0 & 0 & p - \frac{1}{2}B^2 \end{bmatrix} \quad (3.7)$$

This is a combination of the thermal pressure which acts in all directions and the magnetic pressure which is applying a positive pressure in the perpendicular direction and a negative pressure along the field. (Goedbloed & Poedts 2004) A very low beta plasma has $p \ll \frac{1}{2}B^2$ which means that the pressure is mostly provided by a magnetic field and as such is, by nature, very anisotropic. In contrast, in a high beta plasma $p \pm \frac{1}{2}B^2 \approx 0$ and so the pressure, mostly provided by the thermal pressure, is isotropic.

We can similarly express Euler's equations for a gas in conservation form as:

$$\frac{\partial \hat{\rho}}{\partial t} + \nabla \cdot (\hat{\rho} \hat{\mathbf{v}}) = \hat{S}_1, \quad (3.8a)$$

$$\frac{\partial}{\partial t} (\hat{\rho} \hat{\mathbf{v}}) + \nabla \cdot (\hat{\rho} \hat{\mathbf{v}} \hat{\mathbf{v}} - \hat{p} \mathbf{I}) = \hat{S}_2, \quad (3.8b)$$

$$\frac{\partial E}{\partial t} + \nabla \cdot (\hat{E} \hat{\mathbf{v}}) = 0, \quad (3.8c)$$

where we have used $\hat{\cdot}$ to indicate the equivalent gas variables. Reassuringly, Euler's equations can once again be recovered by setting $B = 0$ in our MHD equations.

The sets of differential equations in 3.4 and 3.8 are those solved by GMIC.

3.1.2 Normalization

As in section 2.2.2 we first normalize the MHD equations in 3.4 so they can be appropriately stored in computer memory. We once again replace all our 'real' variables with 'normalized' variables as shown in 2.11. We can make any choice for which variable we wish to normalize; we shall use the magnetic field in order to exploit the definitions of plasma beta and Alfvén speed.

The mass conservation equation given in 3.4a is rewritten in normalized variables as

$$\frac{\partial \rho}{\partial t} = -\nabla \cdot (\rho \mathbf{v}), \quad (3.9)$$

$$\frac{\partial \rho_0 \rho'}{\partial t_0 t'} = -\frac{1}{l_0} \nabla' \cdot (\rho_0 \rho' v_0 \mathbf{v}'), \quad (3.10)$$

$$\frac{\partial \rho'}{\partial t'} = -\frac{\rho_0 t_0 v_0}{\rho_0 l_0} \nabla' \cdot (\rho' \mathbf{v}'), \quad (3.11)$$

$$\frac{\partial \rho'}{\partial t'} = -\nabla' \cdot (\rho' \mathbf{v}') \quad (3.12)$$

where by choosing an appropriate velocity $v_0 = l_0/t_0$ all leading terms have cancelled. Next is the momentum conservation equation

$$\frac{\partial}{\partial t}(\rho \mathbf{v}) = -\nabla \cdot \left[\rho \mathbf{v} \mathbf{v} + \left(p + \frac{1}{2} \mathbf{B}^2 \right) \mathbf{I} - \mathbf{B} \mathbf{B} \right], \quad (3.13)$$

$$\frac{\partial \rho_0 \rho' v_0 \mathbf{v}'}{\partial t_0 t'} = -\frac{1}{l_0} \nabla \cdot \left[\rho_0 v_0^2 \rho \mathbf{v}' \mathbf{v}' + \left(p_0 p' + \frac{B_0^2}{2} \mathbf{B}'^2 \right) \mathbf{I} - B_0^2 \mathbf{B}' \mathbf{B}' \right], \quad (3.14)$$

$$\frac{\partial \rho' \mathbf{v}'}{\partial t'} = -\frac{t_0 \rho_0}{\rho_0 l_0 v_0} \nabla \cdot \left[v_0^2 \rho \mathbf{v}' \mathbf{v}' + \frac{B_0^2}{2 \rho_0} \left(\frac{2 p_0}{B_0^2} p' + \mathbf{B}'^2 \right) \mathbf{I} - \frac{B_0^2}{\rho_0} \mathbf{B}' \mathbf{B}' \right], \quad (3.15)$$

$$\frac{\partial \rho' \mathbf{v}'}{\partial t'} = -\frac{1}{v_0^2} \nabla \cdot \left[v_0^2 \rho \mathbf{v}' \mathbf{v}' + \frac{v_A^2}{2} \left(\frac{2 p_0}{B_0^2} p' + \mathbf{B}'^2 \right) \mathbf{I} - v_A^2 \mathbf{B}' \mathbf{B}' \right], \quad (3.16)$$

$$\frac{\partial \rho' \mathbf{v}'}{\partial t'} = -\frac{v_A^2}{v_0^2} \nabla \cdot \left[\frac{v_0^2}{v_A^2} \rho \mathbf{v}' \mathbf{v}' + \frac{1}{2} (\beta p' + \mathbf{B}'^2) \mathbf{I} - \mathbf{B}' \mathbf{B}' \right], \quad (3.17)$$

$$\frac{\partial \rho' \mathbf{v}'}{\partial t'} = -\nabla \cdot \left[\rho \mathbf{v}' \mathbf{v}' + \frac{1}{2} (\beta p' + \mathbf{B}'^2) \mathbf{I} - \mathbf{B}' \mathbf{B}' \right]. \quad (3.18)$$

Here we have substituted the Alfvén speed from 1.83 in place of $\frac{B_0^2}{\rho_0}$ and the plasma beta, β , from equation 1.79 replaces $\frac{2p_0}{B_0^2}$ since p_0 is the thermal pressure and $B_0^2/2$ is the magnetic. Finally we are free to make the further choice that $v_0 = v_A$.

We take the same approach for the energy conservation equation, 3.4c,

$$\frac{\partial E}{\partial t} = -\nabla \cdot [(E + P_t) \mathbf{v} - \mathbf{v} \cdot \mathbf{B} \mathbf{B}], \quad (3.19)$$

$$\frac{\partial E_0 E'}{\partial t_0 t'} = -\frac{1}{l_0} \nabla' \cdot \left[v_0 \left(\frac{\rho_0 v_0^2}{2} \rho' v'^2 + \rho_0 e_0 \rho' e' + \rho_0 e_0 (\gamma - 1) \rho' e' + B_0^2 B'^2 \right) \mathbf{v}' - v_0 B_0^2 \mathbf{v}' \cdot \mathbf{B} \mathbf{B} \right], \quad (3.20)$$

$$\frac{\partial E'}{\partial t'} = -\frac{t_0 v_0 B_0^2}{l_0 E_0} \nabla' \cdot \left[\left(\frac{\rho_0 v_0^2}{2 B_0^2} \rho' v'^2 + \frac{\gamma \rho_0 e_0}{B_0^2} \rho' e' + B'^2 \right) \mathbf{v}' - \mathbf{v}' \cdot \mathbf{B} \mathbf{B} \right], \quad (3.21)$$

$$\frac{\partial E'}{\partial t'} = -\frac{B_0^2}{E_0} \nabla' \cdot \left[\left(\frac{v_0^2}{2 v_A^2} \rho' v'^2 + \frac{\gamma \rho_0 e_0}{B_0^2} \rho' e' + B'^2 \right) \mathbf{v}' - \mathbf{v}' \cdot \mathbf{B} \mathbf{B} \right], \quad (3.22)$$

Here, we have a leading term of B_0^2/E_0 which we recognize as being the ratio of magnetic energy to our normalization energy. We make the sensible choice that E_0 will be the total energy of a unit of plasma at rest such that

$$E_0 = \rho_0 e_0 + \frac{B_0^2}{2}, \quad (3.23)$$

$$\frac{E_0}{B_0^2} = \frac{\rho_0 e_0}{B_0^2} + \frac{1}{2}, \quad (3.24)$$

$$\frac{E_0}{B_0^2} = \frac{\beta}{2(\gamma-1)} + \frac{1}{2}, \quad (3.25)$$

$$\frac{B_0^2}{E_0} = \frac{2}{\left(\frac{\beta}{\gamma-1} + 1\right)}, \quad (3.26)$$

where we have once again exploited the definition of plasma beta and the adiabatic relationship between pressure and internal energy. In the process of doing this we have also done the work to remove the final term from the energy equation, the $\frac{\rho_0 e_0}{B_0^2}$, and can write the final normalized energy equation:

$$\frac{\partial E'}{\partial t'} = -\frac{2}{\left(\frac{\beta}{\gamma-1} + 1\right)} \nabla' \cdot \left[(\rho' v'^2 + \frac{\gamma\beta}{2(\gamma-1)} \rho' e' + B'^2) \mathbf{v}' - \mathbf{v}' \cdot \mathbf{B}\mathbf{B} \right] \quad (3.27)$$

Lastly, we do the same to the magnetic flux equation

$$\frac{\partial \mathbf{B}}{\partial t} = -\nabla \cdot (\mathbf{v}\mathbf{B} - \mathbf{B}\mathbf{v}), \quad (3.28)$$

$$\frac{\partial B_0 \mathbf{B}'}{\partial t_0 t'} = -\frac{v_0 B_0}{l_0} \nabla \cdot (\mathbf{v}' \mathbf{B}' - \mathbf{B}' \mathbf{v}'), \quad (3.29)$$

$$\frac{\partial \mathbf{B}'}{\partial t'} = -\nabla \cdot (\mathbf{v}' \mathbf{B}' - \mathbf{B}' \mathbf{v}'). \quad (3.30)$$

We shall also simplify these expressions with appropriate definitions of the code units for energy and total pressure such that,

$$E' + P'_t = (\rho' v'^2 + \frac{\gamma\beta}{2(\gamma-1)} \rho' e' + B'^2) \quad (3.31)$$

We also use the same process to normalize the equations of the gas.

$$\frac{\partial \hat{E}'}{\partial t'} = -\frac{v_0}{v_A} \nabla \cdot [(\hat{E}' + \hat{P}'_t) \hat{v}'], \quad (3.32)$$

$$\frac{\partial \hat{\rho}'}{\partial t'} = -\frac{v_0}{v_A} \nabla \cdot (\hat{\rho}' \hat{v}'), \quad (3.33)$$

$$\frac{\partial \hat{\rho}' \mathbf{v}'}{\partial t'} = -\frac{v_0}{v_A} \nabla \cdot \left[\hat{\rho}' \hat{v}' \hat{v}' + \frac{1}{\gamma} P' \mathbf{I} \right]. \quad (3.34)$$

We have introduced another free parameter v_0/v_A this is the ratio of the *gas* sound speed to the Alfvén speed. Since inherent information on the plasma temperature is contained in the plasma beta and if we assume that the gas and plasma temperatures are equivalent then all we need is the ratio of gas to plasma density $\hat{\rho}_0/\rho_0$, which itself is just the inverse of the ionization fraction, to complete the set of tunable parameters. This ratio is 0 for a fully ionized plasma (which naturally sets all the gas equations to 0) and infinite for a completely neutral gas. This gives us a set of 3 parameters that together define a physical regime for our gas-plasma simulations.

$$\beta, \quad (3.35)$$

$$v_A = v_0 = l_0/t_0, \quad (3.36)$$

$$\frac{\hat{\rho}_0}{\rho_0}. \quad (3.37)$$

From here we shall continue to work in our new, normalized units but drop the prime notation. We are equipped with a full set of normalized non-linear MHD equations in conservation form. A PDE in conservative form contains an appropriate function f ; we now recover these flux functions from our normalized MHD equations.

3.1.3 Flux Functions

From our conservation form equations we can write down a set of 3 *flux functions* that will control the time evolution of our conserved variables \mathbf{u} . We first split the vector equations for momentum and magnetic field into 3, single direction, equations. These, along with the mass and energy equations give us a set of 8 scalar conservation laws.

The flux functions do not include the source terms that contribute to the right hand side of our model equations. These source terms differ from the rest of the equation because their values are not necessarily dictated by the divergence of a scalar/vector field (or combination of fields) and as such, whenever they are involved, they are not solved by the main finite difference algorithm.

When we defined the general form that a conservation law, in 3.1, we mentioned an appropriate function f . We want this function to be our *flux function*. By looking at one of our conservation laws and the general form side by side it is clear that we intend f to be the part of the law inside the divergence. So for the mass conservation equation we therefore define the flux function as:

$$f_1 = \rho \mathbf{v}. \quad (3.38)$$

Since v is a vector with 3 components for 3-dimensional space we can explicitly split it into these components,

$$\mathbf{v} = v_x \hat{x} + v_y \hat{y} + v_z \hat{z}, \quad (3.39)$$

$$f_1 = \rho v_x \hat{x} + \rho v_y \hat{y} + \rho v_z \hat{z}, \quad (3.40)$$

where \hat{x} is the unit vector in the x-direction. We shall next make a quality of life decision that we shall separate out each of these 3 components into their own flux function that we shall call F_x , F_y and F_z . The reason that this choice is sensible is because we are always taking the divergence of f and when calculating the divergence we take only the derivative of each component in the direction in which that component works. i.e. we take the x-derivative of the x-component, y-derivative of of the y-component and z-derivative of the z-component. This means we always take the x-derivative of F_x , y of F_y and z of F_z .

By splitting the flux function this way we can swap the divergence for a set of 3 derivatives, one of each flux function, with the divergence being the sum of those derivatives. The goal of this is to exploit finite difference methods which replace deriva-

tives not divergences. This will become clearer in the following section when we apply finite difference schemes onto our flux functions.

In this new format our mass conservation equations become:

$$F_{x,1} = \rho v_x, \quad F_{y,1} = \rho v_y, \quad F_{z,1} = \rho v_z. \quad (3.41)$$

we repeat the process of splitting by component for our complete set of 8 MHD equations. This gives us the following flux functions:

$$F_x = \begin{bmatrix} \rho v_x \\ \rho v_x^2 + P_t - B_x^2 \\ \rho v_x v_y - B_x B_y \\ \rho v_x v_z - B_x B_z \\ \frac{B_0^2}{E_0} [(E + P_t)v_x - B_x(\mathbf{B} \cdot \mathbf{v})] \\ 0 \\ v_x B_y - v_y B_x \\ v_x B_z - v_z B_x \end{bmatrix} \quad (3.42)$$

$$F_y = \begin{bmatrix} \rho v_y \\ \rho v_x v_y - B_x B_y \\ \rho v_y^2 + P_t - B_y^2 \\ \rho v_y v_z - B_y B_z \\ \frac{B_0^2}{E_0} [(E + P_t)v_y - B_y(\mathbf{B} \cdot \mathbf{v})] \\ v_y B_x - v_x B_y \\ 0 \\ v_y B_z - v_z B_y \end{bmatrix} \quad (3.43)$$

$$F_z = \begin{bmatrix} \rho v_z \\ \rho v_x v_z - B_x B_z \\ \rho v_y v_z - B_y B_z \\ \rho v_z^2 + P_t - B_z^2 \\ \frac{B_0^2}{E_0} [(E + P_t)v_z - B_z(\mathbf{B} \cdot \mathbf{v})] \\ v_z B_x - v_x B_z \\ v_z B_y - v_y B_z \\ 0 \end{bmatrix} \quad (3.44)$$

We recover the flux functions for the gas in an equivalent manner.

$$G_x = \begin{bmatrix} \hat{\rho} \hat{v}_x \\ \hat{\rho} \hat{v}_x^2 + \hat{P}_t \\ \hat{\rho} \hat{v}_x \hat{v}_y \\ \hat{\rho} \hat{v}_x \hat{v}_z \\ (E + P_t) \hat{v}_x \end{bmatrix} \quad (3.45)$$

$$G_y = \begin{bmatrix} \hat{\rho} \hat{v}_y \\ \hat{\rho} \hat{v}_x \hat{v}_y \\ \hat{\rho} \hat{v}_y^2 + \hat{P}_t \\ \hat{\rho} \hat{v}_y \hat{v}_z \\ (\hat{E} + \hat{P}_t) \hat{v}_y \end{bmatrix} \quad (3.46)$$

$$G_z = \begin{bmatrix} \rho \hat{v}_z \\ \rho \hat{v}_x \hat{v}_z \\ \rho \hat{v}_y \hat{v}_z \\ \rho \hat{v}_z^2 + \hat{P}_t \\ (\hat{E} + \hat{P}_t) \hat{v}_z \end{bmatrix} \quad (3.47)$$

These flux functions shall allow us to calculate the time evolution of our 8 MHD and 5 gas variables.

3.2 Numerical Scheme

A numerical scheme that can correctly model a non-linear system of equations requires more careful consideration than the linear case. A proper discretisation will allow proper treatment of discontinuous as well as smooth solutions to the differential equations. Continuing to use the notation from chapter 2 where U_i^{n+1} is the numerical estimation of a system of (conserved this time) variables u at timestep $n + 1$ then a general conservative scheme for our system is in the form

$$U_i^{n+1} = U_i^n - p [F_{i+1/2} - F_{i-1/2}]. \quad (3.48)$$

In which $p = k/h = \frac{\delta t}{\delta x}$, is the mesh ratio. Here we have also replaced our continuously varying flux function f with it's numerical approximation F . Since our fluid cells are centred on integer values of i the $F_{(i\pm 1/2)}$ are interpreted as the time average fluxes that cross the cell boundaries to the right and from the left respectively. We can clearly see that the difference between these two fluxes is mathematically equivalent to the numerical approximation of the divergence of f in equation 3.1. The terms on the right hand side of this expression can be replaced with any approximation based on a finite difference operator and doing so creates finite difference schemes.

3.2.1 Lax-Friedrichs

The first conservative numerical scheme we consider is the first order Lax-Friedrichs (in 1D) scheme written as (Goedbloed et al. 2010)

$$U_i^{n+1} = \frac{1}{2}(U_{i-1}^n + U_{i+1}^n) - \frac{p}{2}(F_{i+1}^n - F_{i-1}^n) \quad (3.49)$$

which is first-order in both time and space and is stable as long as the CFL condition

$$|pf'(u)| \leq 1, \quad (3.50)$$

is satisfied for all grid points $i = 1, n$.

The Lax-Friedrichs scheme is the most basic of the class that consists of all central difference schemes and is first-order accurate. We shall look at two more schemes that are second order accurate. They are both equivalent to the Lax-Wendroff scheme used in chapter 2 to a linear approximation.

3.2.2 Richtmyer Two-Step

In his review paper, Richtmyer (1963) proposed a two step algorithm equivalent to the Lax-Wendroff scheme for linear problems. Such a scheme involves first a *predictor* and then a *corrector* step.

$$\text{predictor : } U_i^{n+\frac{1}{2}} = \frac{1}{2}(U_{i-1}^n + U_{i+1}^n) - \frac{p}{2}(F_{i+1}^n - F_i^n), \quad (3.51)$$

$$\text{corrector : } U_i^{n+1} = U_i^n - p(F_{i+1}^{n+\frac{1}{2}} - F_{i-1}^{n+\frac{1}{2}}), \quad (3.52)$$

The predictor step uses the Lax-Friedrichs scheme to calculate values at grid points at half spatial mesh and half time step. The new values of our array of unknowns, U , at these intermediate values can be then used to calculate corresponding intermediate values for the flux function, F . The corrector step uses these new flux functions to update U at the full timestep by a leapfrog scheme. This is shown schematically in figure 3.1.

The Richtmyer two-step scheme is a popular formulation for tackling non-linear fluid dynamics problems. Ofman & Davila (1995) use it for resistive-MHD simulation of Alfvén waves in coronal loops while Costall et al. (2011) use it to model the performance of a turbocharger for a combustion engine.

The Richtmyer scheme in 3.51 is extended to 3-dimensions trivially. We shall reintroduce the finite difference operators that we originally used in chapter 2 (Mitchell & Griffiths 1980)

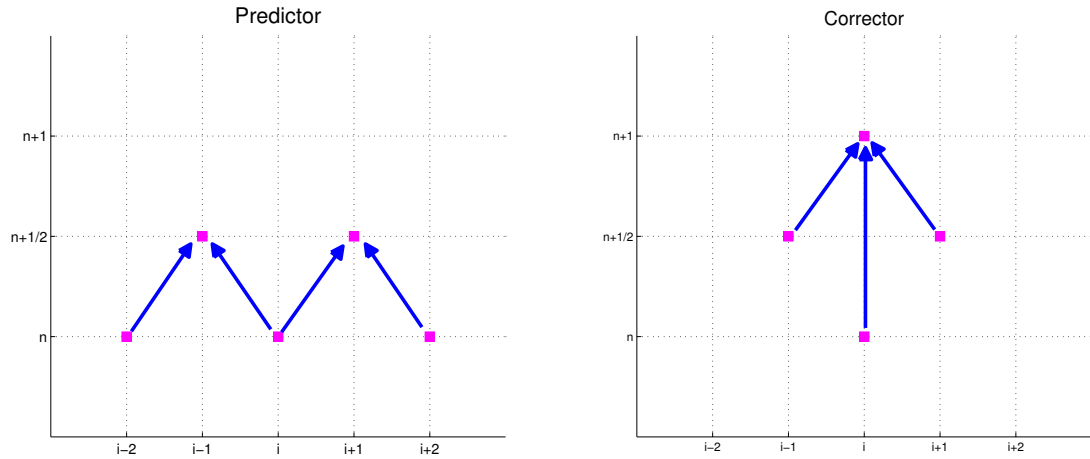


Figure 3.1: A schematic for the predictor and corrector steps of the second order two step Richtmyer finite difference scheme.

$$\text{predictor : } U_{i,j,k}^{n+\frac{1}{2}} = \frac{1}{2}(\mu_x + \mu_y + \mu_z)U_{i,j,k}^n - \frac{p}{2}(\delta_x F x_{i,j,k}^n + \delta_y F y_{i,j,k}^n + \delta_z F z_{i,j,k}^n), \quad (3.53)$$

$$\text{corrector : } U_{i,j,k}^{n+1} = U_i^n - p(\delta_x F x_{i,j,k}^{n+\frac{1}{2}} + \delta_y F y_{i,j,k}^{n+\frac{1}{2}} + \delta_z F z_{i,j,k}^{n+\frac{1}{2}}), \quad (3.54)$$

This scheme is one of the two finite difference schemes currently used by GMIC, the other being the MacCormack scheme.

3.2.3 MacCormack

The MacCormack scheme in 3 dimensions is: (MacCormack 2003)

$$\text{predictor : } U_{i,j,k}^{n+\frac{1}{2}} = U_{i,j,k}^n - \frac{p}{2} [\Delta_x F x_{i,j,k}^n + \Delta_y F y_{i,j,k}^n + \Delta_z F z_{i,j,k}^n], \quad (3.55)$$

$$\text{corrector : } U_{i,j,k}^{n+1} = \frac{1}{2}(U_{i,j,k}^n + U_{i,j,k}^{n+\frac{1}{2}}) - \frac{p}{2} [\nabla_x F x_{i,j,k}^{n+\frac{1}{2}} + \nabla_y F y_{i,j,k}^{n+\frac{1}{2}} + \nabla_z F z_{i,j,k}^{n+\frac{1}{2}}]. \quad (3.56)$$

where we are using $\Delta_{x,y,z}$ and $\nabla_{x,y,z}$ as the forward and backwards difference operators in x,y,z respectively i.e.:

$$\Delta_x U_i = U_{i+1} - U_i, \quad (3.57)$$

$$\nabla_x U_i = U_i - U_{i-1}. \quad (3.58)$$

The MacCormack scheme has (n^2) variants in n -dimensions so in 3-d there are 8 other variants. Equation 3.55 goes forwards in all 3 dimensions and then backwards in all 3 dimensions; a variant is obtained by changing the order of the forward and backward operator, for example you could reverse the order and go backwards then forwards in all directions or backwards in y and z first but forwards in x then reversing. It is useful to alternate the order that these operations are carried out to guarantee symmetry. (Mitchell & Griffiths 1980)

In operation the MacCormack scheme is identical to the Richtmyer for linear problems, with both of them reducing to the Lax-Wendroff formula. In non-linear problems the MacCormack scheme is superior. (Mitchell & Griffiths (1980) & Goedbloed et al. (2010))

Both the Richtmyer and MacCormack schemes are second order accurate in both space and time producing truncation errors $\mathcal{O}(C^3)$ where C is the Courant number $C = f'(u)p$. This means the scheme is able to give reasonable accuracy results for smoothly varying flux functions. However, in regions of shocks and steep gradients or where $f'(u)$ is large, the truncation error can become as large as the solution meaning our numerical result becomes tainted by short-wavelength oscillations.

This behaviour is a consequence of this scheme being *non-monotonicity preserving*. This limitation can be circumvented by the use of a *flux corrected transport* (FCT) scheme which adds artificial diffusion in the predictor step and removes the excessive dissipation with an anti-diffusion term in the corrector step. This has the net result of there being a small amount of artificial diffusion remaining which helps prevent high frequency noise from building up at the edges of shocks. The total amount of remaining diffusivity is an important choice for the accuracy of such schemes. Examples of FCT schemes can be found in e.g. DeVore (1991) or Steiner et al. (1994).

An alternative, more modern approach is that of a *total variance diminishing* (TVD)

scheme. In basic terms a TVD scheme has the property that the total variance (defined as the integral of the absolute value of the spatial gradients in u over the whole domain) does not increase between timesteps. This does not allow spurious oscillations to appear as they would always increase the total variance. In practical terms this is more difficult in implementation than the FCT method for first-order schemes and Godunov's theorem limits any linear monotonicity preserving scheme to first order. More advanced methods are necessary to gain second-order accuracy by using "hybrid" schemes that can circumvent this limit to only drop to first order accuracy in the vicinity of shocks e.g. by working in combination with finite volume methods.(Goedbloed et al. 2010)

For the purposes of modelling non-linear momentum coupling and critical velocity ionization we are mostly concerned with qualitative results so we shall make no attempt to remove this limitation and instead be careful to keep our simulations limited to those cases where the method remains accurate. That is, we avoid letting the Courant number approach unity by only considering regimes containing smoothly varying solutions.

3.2.4 Stability

It is not possible to properly assess the numerical stability of non-linear Lax-Wendroff type schemes. MacCormack (2003) showed that for our type of schemes then we are more restricted than the CFL condition, that we used in chapter 2. However, for the MacCormack scheme benefits can be gained by rotating the order in which the forward and backwards difference operators operate as this yields lower amplification factors for spurious signal. In the 2-d case we obtain this behaviour by alternating between two cases: forward-x backwards-y in the first step followed by backwards-x forwards-y in the second and then backwards-x forward-y followed by forward-x backwards-y. This makes MacCormack the preferred scheme for our simulations.

We satisfy the CFL condition for our fastest velocities (the fast magneto-acoustic mode, see 1.4.2). For a low beta plasma this is similar to the Alfvén speed which has been normalized to $v_A = 1$.

3.3 Boundary Conditions

Numerical simulations often require that computational boundaries are constructed between a region of interest and other regions one hopes to neglect. Artificial boundaries, especially those drawn through non-uniform flows, that do not affect the region of interest (and preserve the same order of accuracy as the solver of the governing equations) can be tricky to create. It is also always preferable to minimize the computational requirements of the boundary by keeping them as straightforward as possible and fitting them close to the region of interest.

When the governing equations are linear, concerned only with small amplitude fluctuations around a steady mean, then analytic solutions for the creation of a non-reflecting boundary condition (NRBC) are possible. Theoretical solutions for this have existed for many years ([Givoli \(1991\)](#); [Tsynkov \(1999\)](#) and [Hagstrom \(1999\)](#)) but problems in implementation can still be present. We exploit this for GMMC in section [2.3.1.1](#) with a polynomial NRBC.

In contrast, when the fluid can not be represented as linear perturbations around a static mean, there is very little chance to develop an NRBC. It is possible to proceed with the techniques developed for the linear fluid but this presents problems, the accuracy of the results will be diminished and the complexity of implementing these boundary conditions may not justify their use. Further, the discretisation of the equations for computation will result in instabilities in the non-linear case that can hinder efforts. ([Colonius 2004](#))

It is thus often preferable to use more simplistic, ad hoc methods. Sacrificial regions (SR) - regions surrounding the region of interest (ROI) that are governed by modified versions of the physical equations - can be created in order to minimise the effect of the boundaries on the interior at the cost of ‘wasted’ computational time. The equations in the absorbing layer are written as

$$U - \nabla \cdot f = -\sigma(x, y, z)(U - U_o) \quad (3.59)$$

Sigma is ramped up from 0 in the region of interest to a positive value in the

sacrificial region. Any disturbance that reaches the sacrificial region will be exponentially damped and, if signal reaches the computational boundary, any reflections will be similarly damped on their return to the ROI. Since the boundary between $\sigma = 0$ and $\sigma > 0$ is itself reflecting then we must be careful that sigma is increased slowly, over a reasonable distance, to minimize reflections. This results in a computationally inefficient solution. (Israeli & Orszag 1981)

After repeated problems encountered in developing a more elegant, analytic NRBC, the use of a sacrificial region was necessary for the non linear version of the MHD/gas-coupling and Alfvén ionization code GMIC.

We choose an exponentially increasing form for sigma. If we take x_a and x_b as the lower and upper limits on the ROI such that the SR runs on cells with $x < x_a$ and $x > x_b$ then

$$\sigma(x) = \begin{cases} \text{ROI}, & \text{if } x_a < x < x_b \quad \sigma = 0 \\ \text{SR}, & \text{if } x \leq x_a \quad \sigma = Ae^{B(x-x_a)} \\ & \text{if } x \geq x_b \quad \sigma = Ae^{-B(x-x_b)} \end{cases}$$

Where A and B are constants.

Figure 3.2 shows the absorbing layer in action with an acoustic wave in the gas from one of the simulations from chapter 4. The sacrificial region is between $x = 0, 200$. The wave enters the sacrificial region at $x = 200$ and begins to become damped. The damping increases in intensity as sigma increases the closer the wave gets to $x = 0$. The time slices show that by later times the wave has propagated deep into the sacrificial layer and has steadily lost amplitude. A completely negligible amount of signal reaches $x = 0$ which is where the real code boundary is.

We observe no reflection from the sacrificial region or from the real boundary.

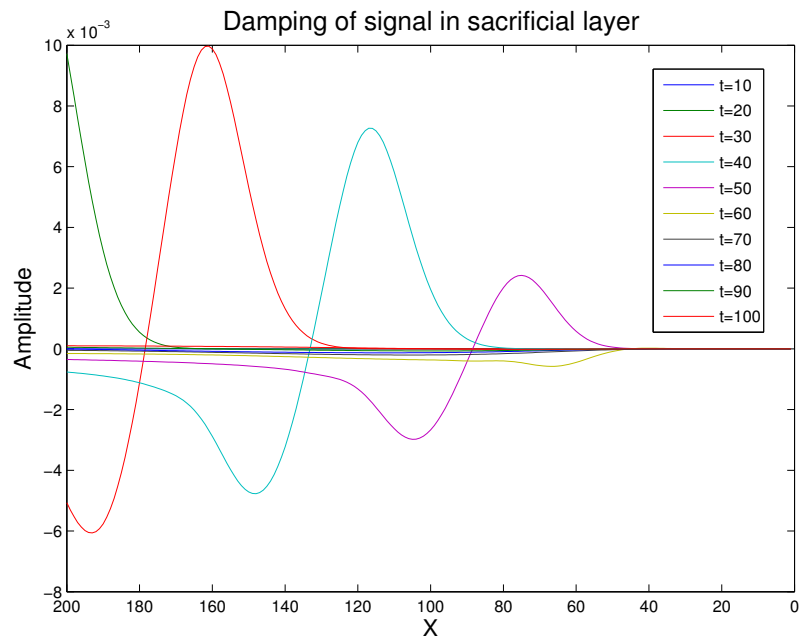


Figure 3.2: Slices across the sacrificial region for an acoustic wave entering the damping layer described above. Each line is a snapshot of the wavefront at a series of times. The start of the damping layer is at $x=200$ and the actual code boundary is at $x=0$ with σ increasing exponentially as x approaches 0. The values for the constants that define sigma are $A = 0.6$ and $B = 0.01$.

3.4 The Code

GMIC is written in Fortran90. Both the Richtmyer and MacCormack schemes from section 3.2 are included in a vectorised form to allow easy parallelisation. This also allows each of the two-steps in these algorithms to be written in a single line of code. Any other conservative finite difference scheme can be used in place of our schemes, allowing a great range of flexibility in the code.

The flux functions are expressed line by line for each variable and for each dimension meaning a total of 24 (8x3) lines for MHD and 15 (5x3) lines of code for the gas. This brevity provides a strong advantage. Not only is the physics extremely human readable by being very recognisable as the physical equations but they are also easily modifiable. For example, to add a buoyancy term or resistivity requires only a handful of obvious

changes to a small number of lines.

One of the benefits that GMIC has over GMMC is that it was designed with 3-dimensional operation in mind. The code is able to do 3-dimensional simulations with ease but this option is not exploited for any of the simulation runs in this thesis. Since a $200 \times 200 \times 200$ 3-dimensional grid is 200 times more expensive to compute than a 200×200 (typical example size) grid then computation times can rapidly grow. By sticking with 2-dimensional simulations we can still capture both the parallel and perpendicular to the field dynamics while keeping the code iterative. On a 16 core Intel Xeon, a run can be set up, simulated and analysed in 30 minutes without the several hour/day wait time for a 3-dimensional equivalent on the same machine.

The code's speed is significantly slower than GMMC. The numerical schemes used are two-step which immediately means a factor of 2 increase in runtime for an equivalent simulation. The non-linear model equations obviously require significantly more calculations. Terms which are 0 in a linear approximation become non-zero and must be calculated. The equilibrium condition is not as useful for removing terms since significant deviations from equilibrium must be expected, this alone increases run time for an equivalent simulation by a factor of 2-4.

The biggest hit to performance is the use of a sacrificial boundary. While GMIC is able to get away with an elegant, computationally efficient transparent boundary this is not possible in the non-linear regime. For a 200×200 region of interest we also include a 200 width damping layer on both sides bringing the total area to a 600×600 grid. This means only $1/9$ of the area is useful information, increasing run time by a factor of 9.

This all put together means that GMIC takes approximately 20 minutes for the simulation of a 200×200 box of plasma for 4 Alfvén crossing times (the box dimensions/Alfvén speed) on a 16 core Intel Xeon e5 (2.9 GHz). For the same scenario GMMC would only have a runtime of 1 minute on an 8-core Intel i7 (3.4 GHz) desktop. We do note that, despite the performance loss of GMIC compared to its predecessor, this is still extremely fast.

3.4.1 Scalability

To briefly ascertain how GMIC scales with number of CPU cores a quick test was carried out. The same simulation was carried out and the time to completion was measured for various numbers of CPU cores. The test was a short, 100 timestep, evolution of a 800x800 grid on one of the scenarios found in chapter 5. This is repeated for 3 scenarios that vary in compiler settings and the layout of the CPU cores used: Scenario 1, in blue, is labelled O5 consecutive, this is using the -O5 compiler flag, this flag handles various details of the parallelisation and vectorisation) and uses consecutively numbered CPUs (i.e. CPU numbers 0,1,2,3 for the 4 core test). Scenario 2 also uses the -O5 flag but uses split numbered CPUs (i.e. CPU numbers 0,2,4,6 for the 4 core test). Scenario 3 is labelled O3 consecutive, this is identical in setup to scenario 1 but uses the slightly less sophisticated optimizations from the -O3 flag in Absoft.

The results from these tests are shown in figure 3.3. The compiler flags makes a small difference to the run time with O5 slightly outperforming O3 as does the change from consecutive to split CPU allocation with the split CPU allocation with a slight performance edge as expected.

The code scales very well up until around 8 cores and fairly well up to 16. Beyond 16 the code scales very poorly with only a 10% reduction in runtime from doubling the number of cores. There are many technical reasons why the code does not scale well beyond that. More and more of the run time becomes dedicated to data input/output which is completely serial, the jump beyond 16 cores also coincides with the jump to using cores on multiple CPU chips since the physical layout is 2x8 core chips. This means that beyond 16 cores (the first 8 multi-threaded to 16) then data must be passed from chip to chip instead of residing in shared cache on the same chip.

Since most of the gain comes from the first 16 cores this was generally the number used for each run of GMIC. A more technical MPI setup would be necessary of additional performance was required by a specific application.

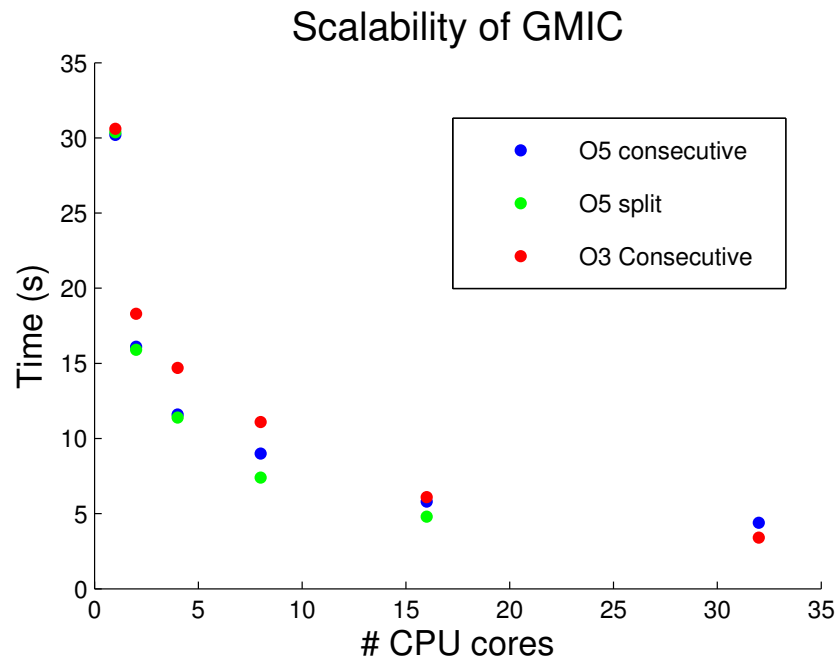


Figure 3.3: The run time (in seconds) for GMIC as the number of CPU cores is increased. The various scenarios do not show much difference in run time and the code scales well to 16 cores beyond which there is not significant performance gain

3.5 Gas Plasma Interactions

The code has two unique features. Firstly it is able to effectively model the impact of frictional drag from coupling in the momentum equations of the ionised and non-ionised species of a partially ionised plasma; unlike GMMC it can model this into non-linear regimes. The second is to simulate Alfvén ionization.

The same techniques to incorporate momentum coupling and Alfvén ionization described in chapters 1 and 2 are used in GMIC as they were in GMMC. Since the non-linear code GMMC was designed with the addition of interaction terms in mind there are significant logistical improvements compared to the linear code, GMIC.

The next chapter, chapter 4, deals with momentum coupling using GMIC. We explore how a partially ionized plasma behaves compared to a fully ionized one.

Chapter 4

Momentum Coupling in a Partially Ionized Plasma

Using the non-linear, 2-dimensional, finite difference code described in chapter 3 we examine the effects of a frictional drag term on a partially ionized plasma. We have a choice of two scenarios: either by using a non-equilibrium initial condition or a time dependant driving term (or a combination of the two).

In the case of an initial condition experiment then a set of non-equilibrium initial conditions are set at the start of the simulation and left to evolve. This evolution would either continue until the simulation reaches a new equilibrium or, if the conditions give rise to an instability, we may expect perturbations to grow over time until the simulation is ended or the criteria for stability are exceeded and the simulation would crash. We shall look at a set of non-equilibrium initial conditions in 4.1.

In the case of a driving term, you start with an equilibrium and you perturb it by providing an external source term, a driver. This source term can be of any nature, act on any of the fluid variables and can be at any part of the domain. By externally driving one or more of the fluid variables you can force the fluid to react. Such a driving term can drive for the duration or be switched off allowing the fluids to continue to evolve in its absence. We look at simulations involving driving terms in 4.2.

However the deviations from an equilibrium are made, the behaviours of the par-

tially ionized plasma are dictated entirely by the externally applied driving terms, the boundary conditions and the governing equations.

4.1 Cylindrical bombs

4.1.1 Positive Gaussian Cylindrical Bomb

A simple scenario that provides much insight into the gas-plasma system is obtained by taking an otherwise homogeneous gas (or plasma) and placing an over-density in the centre. If the temperature is kept constant across the domain then this results in a pressure gradient across the region, which drives a motion in the gas. If the initial density perturbation is cylindrically symmetrical then these motions will produce cylindrically symmetric acoustic waves.

This is the gas equivalent to throwing a pebble into a pond. The pebble disturbs the surface of the water at a central location and this disturbance generates a symmetrical wave. The difference is that, in the water, the waves generated are gravity waves on the water's surface instead of acoustic, compressional waves in the gas.

The initial conditions are shown in figure 4.1. This figure shows the gas density relative to the equilibrium density. The anomalous density is a symmetric Gaussian increase in density with a maximum amplitude of 0.1 (corresponding to a 10% increase in gas density) with an extent roughly a quarter of the size of the computational domain.

The distance from the centre of the Gaussian to the edge of the physical domain is 100 units meaning, with a mesh ratio of 0.2, the transit time for a sound wave to propagate from an edge to centre and back is 1000 timesteps. A total run time of 1000 timesteps was chosen in order to capture this characteristic time. All simulation parameters (density, energy density, velocity in both x and y directions) were output in normalised code units every 10th timestep for high cadence data.

Figure 4.1 shows us the wavefront created as over-density in the centre forces gas outwards producing a front of above the background density gas followed by a rarefac-

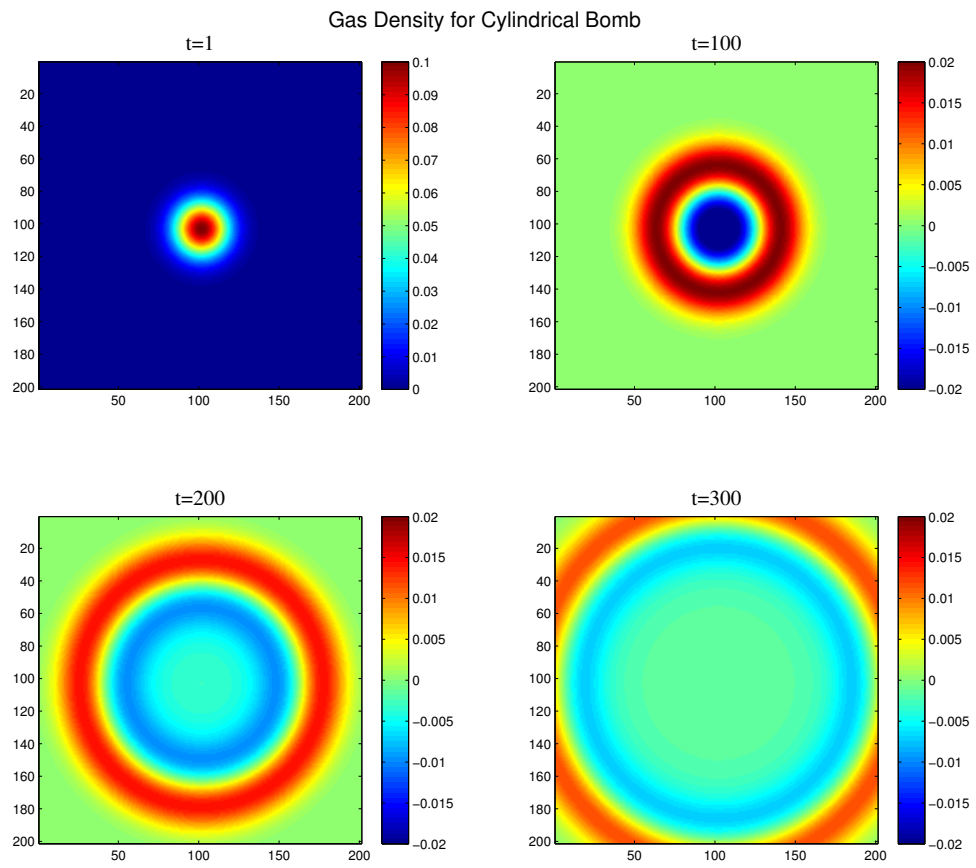


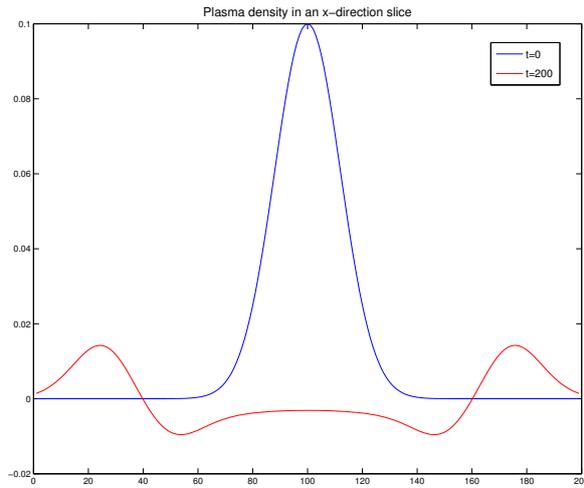
Figure 4.1: Gas density map showing the initial condition and time evolution of a Gaussian shaped over-density placed in the centre of the gas with a peak perturbation of 0.1. After 200 timesteps the wavefront is close to the boundary. The cylindrically symmetric form shows the isotropy of the gas sound speed. Note the change in colour bar between the first and the rest of the panels. The magnetic field is orientated horizontally.

tion as gas is evacuated from the central region. What is particularly interesting is that by the time shown in this figure there remains a 'hole' in density in the central area which due to the low gradients does not drive additional motion. This density rarefaction forms into an almost flat plateau that persists for much longer than expected as it is shielded from seeing the higher density outer region by the wave propagating outwards. This plateau is seen even more clearly in figure 4.3.

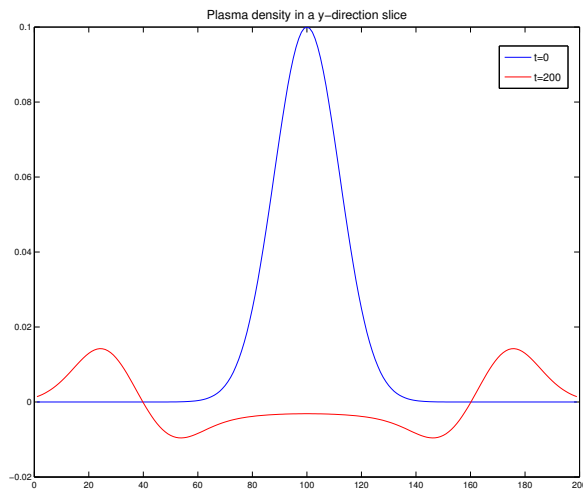
While figure 4.1 gives a good visual of the shape of the wavefront, it can be more beneficial to look at 1 dimension to see how the amplitude and velocity of the disturbance evolves as the wave propagates. Figure 4.2 shows two slices through the computational domain, one in the x-direction, figure 4.2a, and the other in the y-direction, figure 4.2b, both passing through the centre point. These show plasma density at $t=0$ and $t=200$ for each slice. This verifies what we can visually see in the density map; the disturbance is perfectly symmetrical in the two directions.

Next we take the same slice technique to examine the time evolution of our wave, this time just using our x-direction slice. We over-plot every 50th timestep in figure 4.3. This figure clearly shows the outwards motion of the cylindrical wave along with the formation of a low density plateau in the interior region enclosed by the wave. A visually interesting thing about this figure is the fall off in amplitude of the wave as it propagates outwards. Once the wave has been given enough time to establish itself from the initial conditions then this amplitude falloff has an approximate $1/r$ dependence. This is because the area of the wave is proportional to πr so, when the wave moves further from the origin, the amplitude must fall as the gas spreads out over the larger area. After a short time (~ 80 timesteps) during which the initial Gaussian density generates the cylindrical wave we can see the amplitude's $1/r$ dependence and the wavefront propagating at the sound speed.

Another interesting diagnostic is that of the total gas density. To study this a fresh simulation is run with a duration of 5000 timesteps in order to capture the later density evolution, once the wavefront has left the computational domain. The program parameters and initial conditions are kept the same but data is only output every 50 timesteps. The gas density is summed over the physical domain, not including the boundary layer and this total is plotted in figure 4.4. What we see here is an initially high density, due to the total density contained in the initial Gaussian, which persists for 250 timesteps until the disturbance reaches the edge of the domain. When the wave crosses this boundary the total density rapidly drops then rises again as the peak and trough respectively cross the boundary. After the wave has left the domain the density perturbation is close to 0.



(a) Plasma density along an x-directed slice, through the centre of the domain, at both $t=0$ and $t=200$



(b) Plasma density along a y-directed slice, through the centre of the domain, at both $t=0$ and $t=200$

Figure 4.2: Plasma density across the computational domain for slices in both the x and y directions. The magnetic field is orientated in the y-direction.

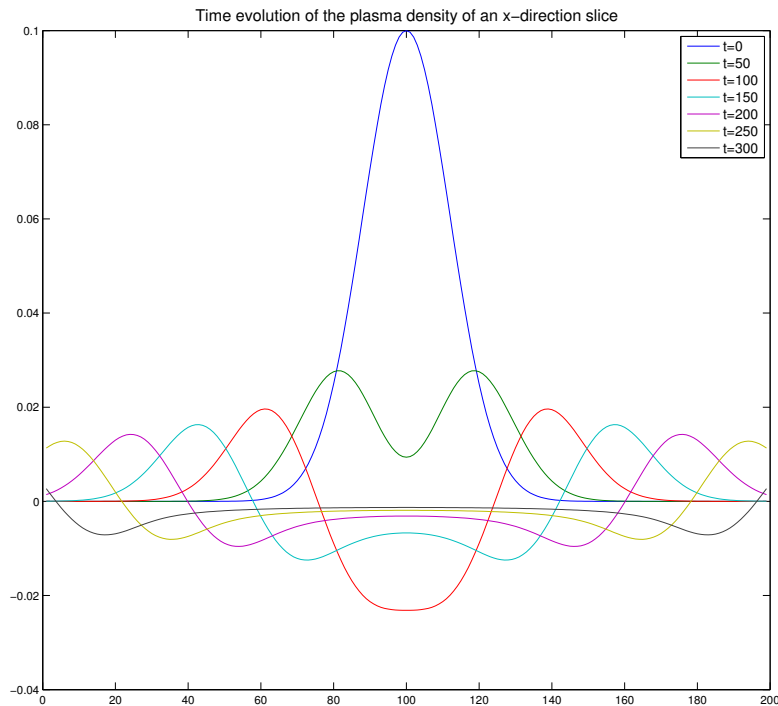


Figure 4.3: Time evolution of the plasma density along a slice, through the centre, in the x direction. This evolution shows the propagation rate of the wave as well as the decay in amplitude over time

The density seems to recover to the background density by 2000 timesteps but by re-plotting this time on a new x -axis (in figure 4.5) we reveal some further interesting behaviour. By looking at the total density at later times we can see that it continues to oscillate, tending towards 0, for the entire duration of the simulation, the amplitude constantly damping. This behaviour corresponds to a 2-dimensional standing wave with mode numbers 1,1. This single central antinode continues to oscillate up and down long after the initial disturbance has left the computational domain, analogous to a trampoline continuing to exhibit the same behaviour after the jumper gets off. This *trampolining* behaviour is expected from the implementation used for the boundary layer which naturally results in slow forcing of the global density towards the equilibrium density, resulting in these large scale oscillations. The sacrificial re-

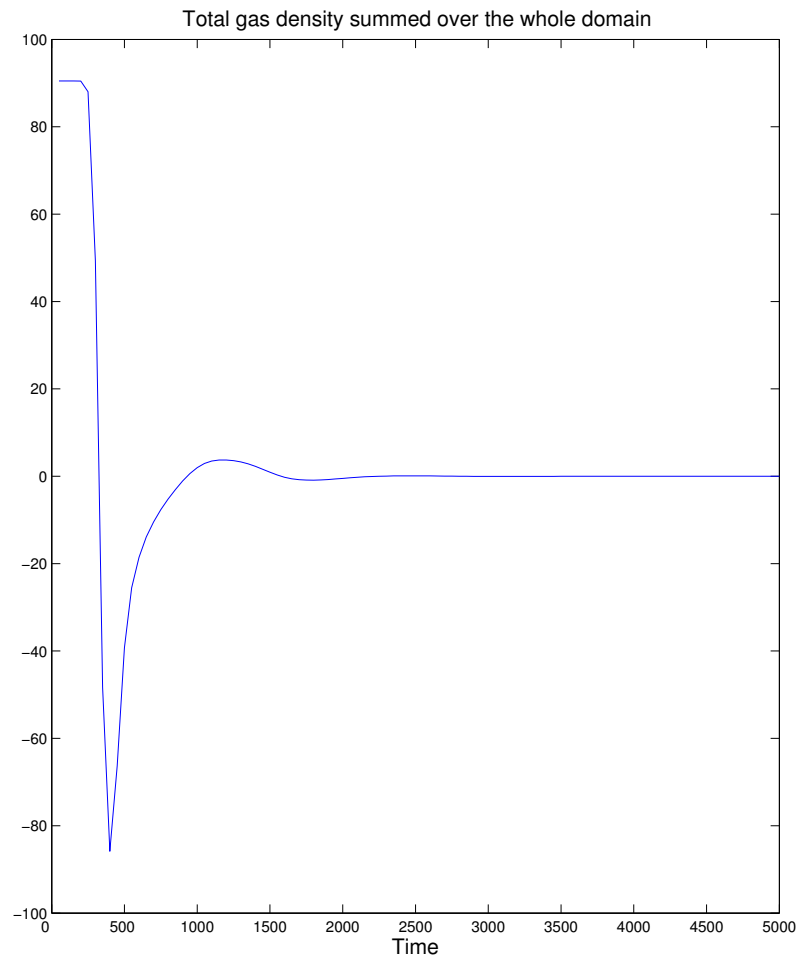


Figure 4.4: Total gas density integrated over the entire physical domain, a density of 0 on the x-axis corresponds to the average density being equal to the equilibrium density. The density changes as gas is transferred through the transparent computational boundaries.

gion continually extracts energy from these oscillations which causes a damping of the trampolining.

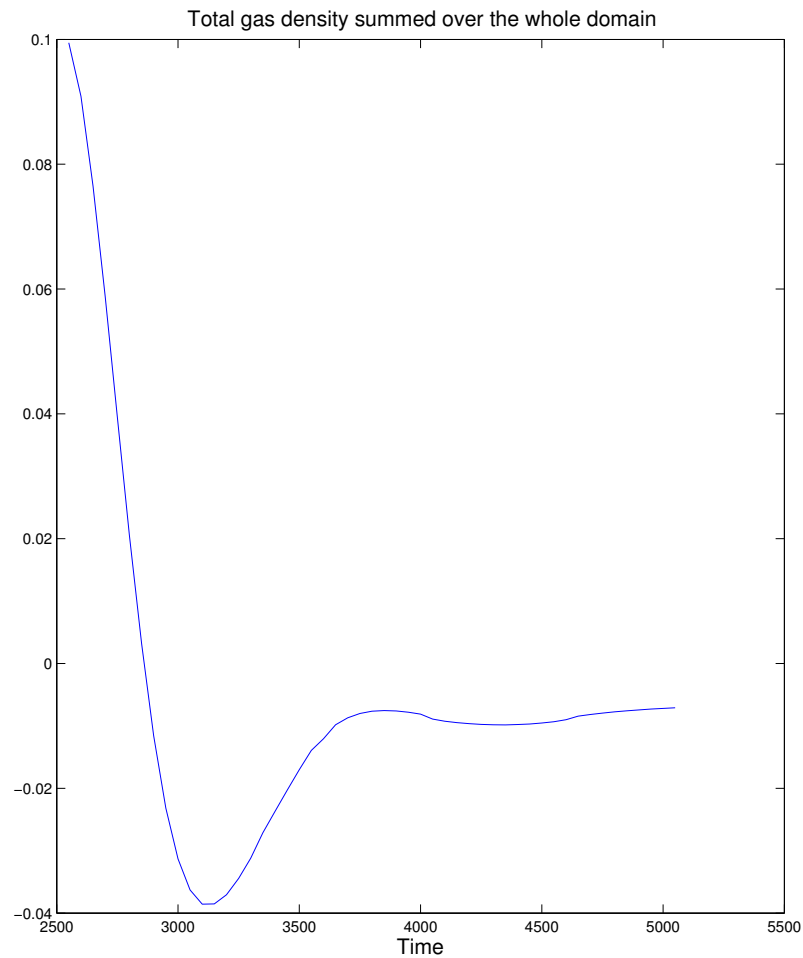
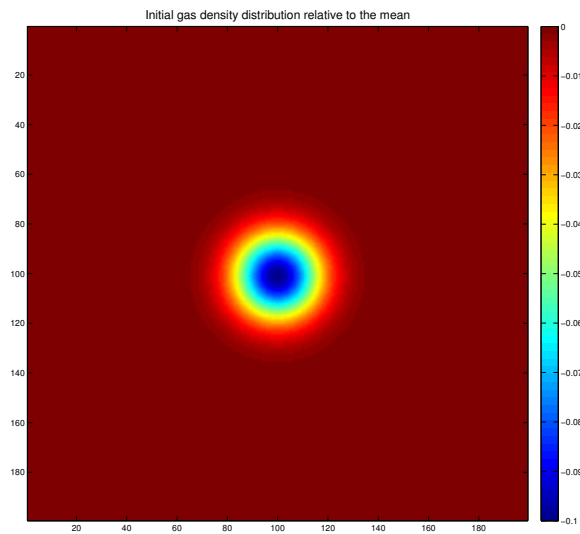


Figure 4.5: The total gas density over time, same as in 4.4 but with early times removed to more clearly show the trampolining behaviour of the gas at late times

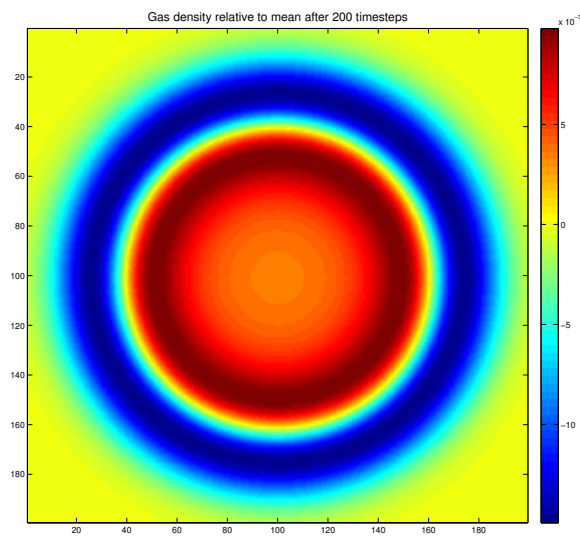
4.1.2 Negative Gaussian Density Cylindrical Bomb

More relevant to Alfvén ionization is the case of a low density region that is then filled by inflowing gas. In contrast to the positive density disturbance propagating outwards, we would expect a low density region to be filled quickly by inflowing gas that becomes focused on a small, central region. This could presumably result in much higher velocities and energy densities than the previous case.

The simulation is repeated with the same parameters to allow easy comparison.



(a) The initial conditions of a negative Gaussian reduction in density placed in the centre of the gas.



(b) After 200 timesteps the wavefront is about to enter the absorbing boundary layer.

The initial conditions are shown in figure 4.6a and consists of the reverse of a Gaussian shaped reduction in density with a maximum amplitude of 0.1. We can see this evolves

in an almost mirrored manner, with the gas density after 200 timesteps shown again in figure 4.6b.

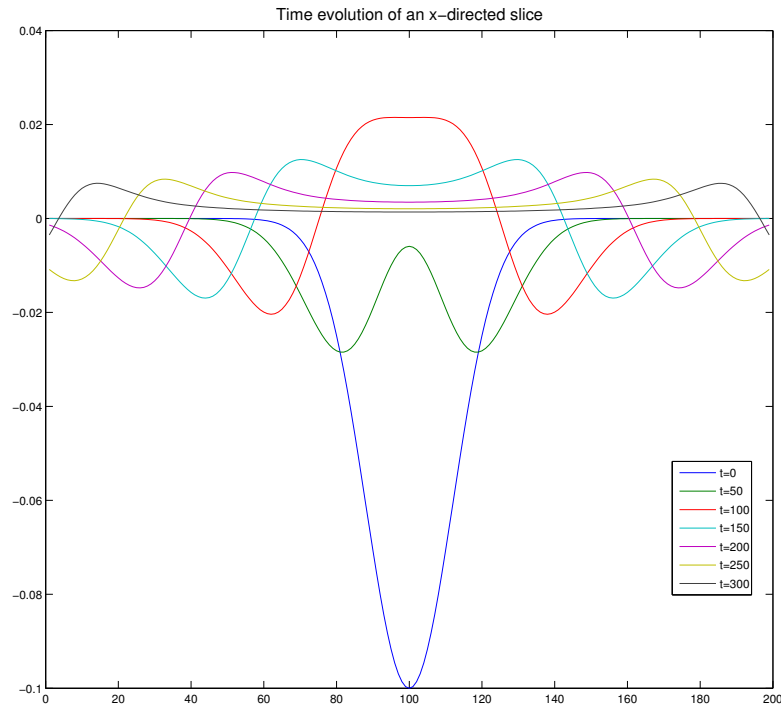


Figure 4.7: Time evolution of the plasma density along a slice through the centre in the x direction for the negative bomb. This evolution shows the propagation rate of the wave as well as the amplitude dropping over time

We repeat the same treatment as before and examine the time evolution of an x-directed slice through the domain. Figure 4.7 is similar to what was previously seen in the positive case: the same symmetry in all directions, the same $1/r$ dependence of amplitude, and the same propagation of the wavefront at the sound speed. If the simulations were extended to three dimensions then this amplitude decay would become $1/r^2$.

It may naively be expected that the two scenarios would be exact opposites; this would indeed be the case in a purely linear treatment. The non-linear terms in the

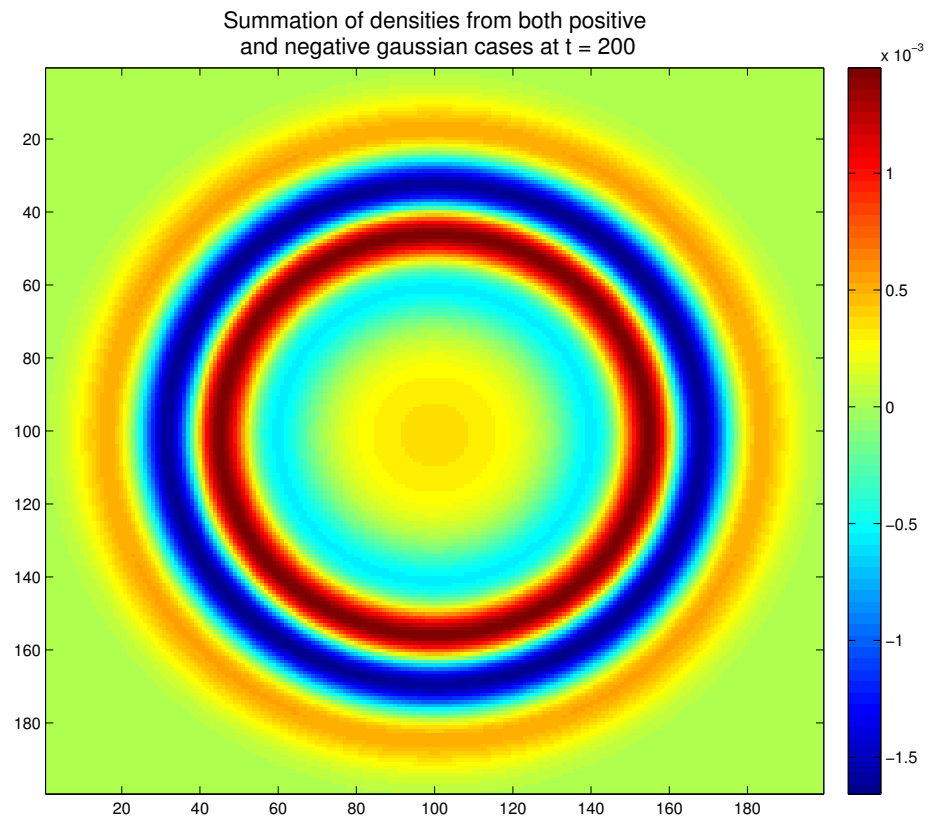


Figure 4.8: By summing the positive and negative density bomb densities at the same timestep we can see that the two cases are not identical and that there are differences between the two scenarios other than the sign of the disturbance

hydrodynamics cause a difference between the two cases. We can see the deviations of this new simulation from being an exact mirror of the positive cylindrical bomb case by summing the densities of the two runs. If they were opposite but identical we would expect this summation to be equal to zero for all cells at all times. A snapshot of this summed density, for $t = 200$, in figure 4.8 shows that there is a small but deviation from zero. A more informative examination of the differences can be seen in figure 4.9. This figure shows us gas density in both runs through a x-direction slice through the centre of the computational domain. The density of the negative scenario is inverted to make the differences clearer.

Figure 4.9 shows that the wave in the negative case, in red, is higher amplitude

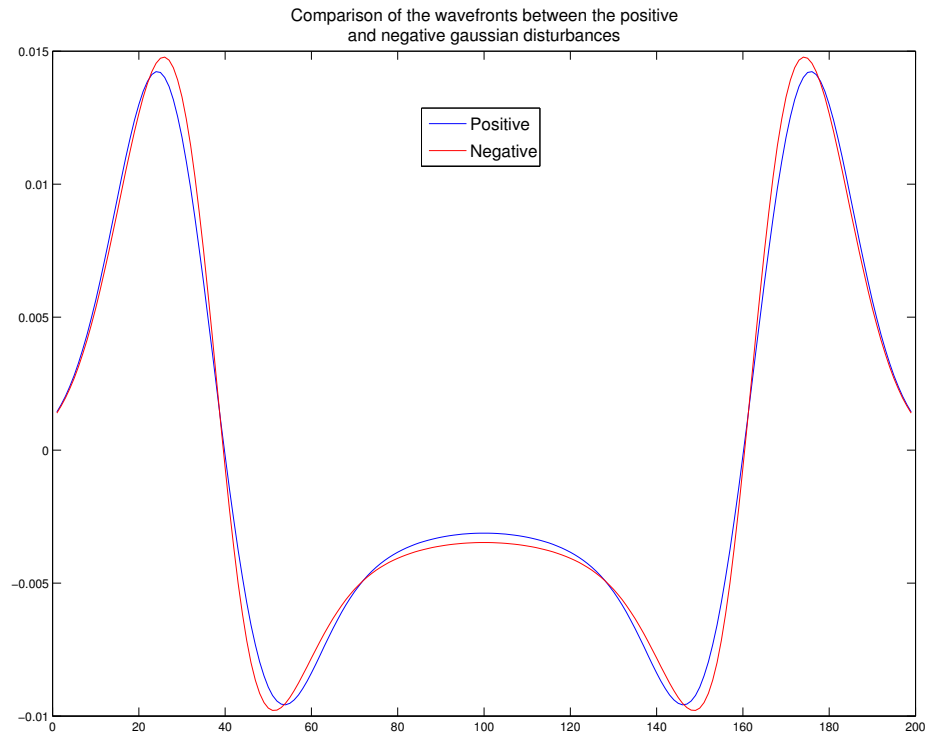


Figure 4.9: A single row of data at $t = 200$ shows the difference between the waveforms generated by the positive (in blue) and negative (in red) cylindrical bombs. The negative case has its axis inverted to allow clearer comparison

($\sim 5\%$) this is the same both in the primary wavefront, both peak and trough, as well as for the residual plateau. The wavelength is also different; both waves are centred on the exact same computational cell and move at the same speed but the positive case, in blue, has a longer wavelength. This results in the peak amplitude of the wavefront for the negative case being slightly retarded and its trough is slightly advanced. We can see the origin of this difference by looking at the beginning of the disturbance. We first plot density disturbance of just the very centre point for the positive case and the inverse of the density disturbance for the negative case of the bomb in figure 4.10. Although the evolution of the densities follow roughly the same shape; the difference between the two is noticeable from the start with the negative scenario immediately establishing a phase lead.

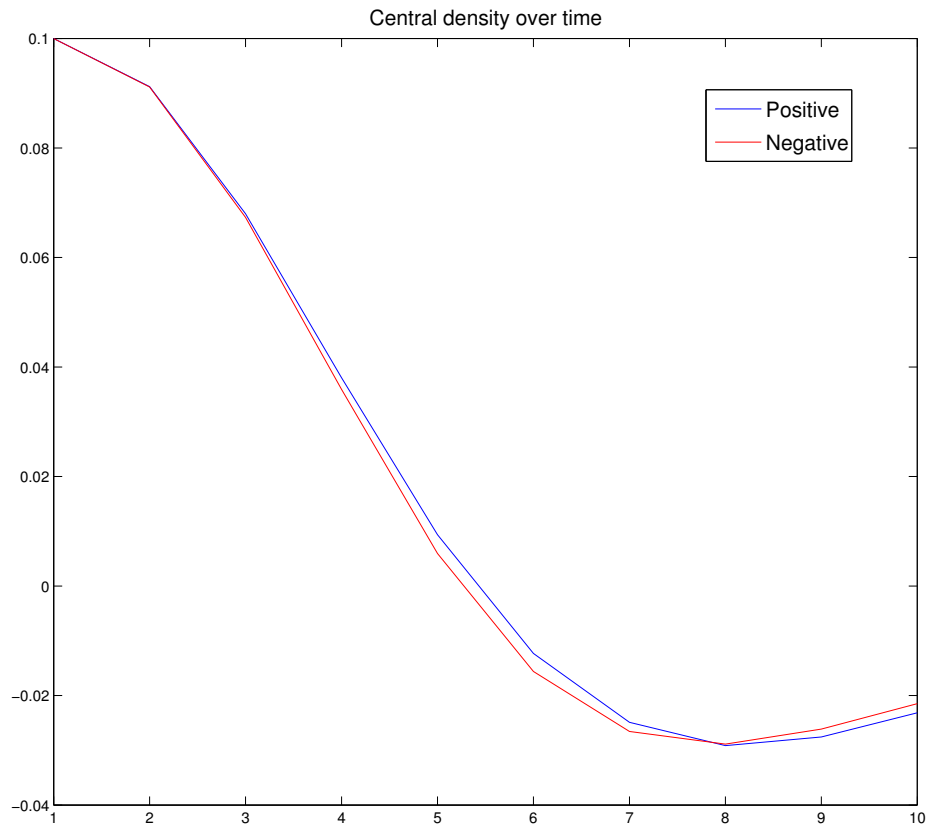


Figure 4.10: The gas density of the central point (100,100) of the domain to compare the behaviour of the positive and negative density setups. the simulation shows the density as it drops from an initial maximum to a minimum that is below the equilibrium density of 0 before then rebounding back to a positive density.

4.2 Coupled Waves

For another example of the unique dynamics that are available to a frictionally coupled partially ionized plasma we next take a look at the interaction that occurs between waves. This is very similar to the scenario in 2.6 except with two perpendicular wave sources.

For this set of simulations the non-linear code GMIC, described in chapter 3 was used. The initial conditions are on a 200x198 region of interest consisting of a homoge-

neous background partially ionised plasma with an ionization fraction of 0.33 meaning the gas density is 2 times higher than that of the plasma. The plasma beta is 1.0 and the magnetic field is 1.0, orientated in the x-direction.

The simulation is driven by two separate mechanisms. The first is a compressional, acoustic wave created at the top boundary by perturbing the gas density and velocity. This wave propagates downwards (in the negative y-direction). The second is a magneto-acoustic disturbance driven in the plasma density and velocity on the right hand side boundary. This generates a wave propagating in the negative x-direction in the plasma.

Both driving terms are Gaussian in shape with a FWHM of 10 code units and a maximum amplitude of 0.2 of the mean. Note that the mean in the gas is higher than in the plasma so, in real terms, the acoustic wave is higher amplitude. The driver operates until $t = 20$ which is 2.5 wave periods.

First we briefly look at the two driving terms individually. Figure 4.11 shows the acoustic wave created by the first driver acting alone and figure 4.12 the magneto-acoustic driver on its own. In both these cases the momentum coupling term, Γ , is 0.

Next we examine what happens when the two driving terms are simultaneously executed and momentum coupling is enabled with $\Gamma = 0.05$. We plot the total density in figure 4.13.

In order to isolate the effects of momentum coupling we run a control simulation. This is done by operating the two drivers simultaneously but keep $\Gamma = 0$, i.e keep no momentum coupling. Figure 4.14 shows this case. This control distinguishes between what is simply a transient superposition of the uncoupled waves and genuine dynamics as a result of the gas-plasma coupling.

By comparing the $\Gamma = 0$ and $\Gamma = 0.05$ cases we can see several differences. Firstly, in the coupled case some of the higher frequency signal is less well defined leaving behind less sharp peaks and troughs in the wave. This can be clearly seen by looking at the control case in 4.14 and identifying the high frequency oscillations that lag behind the main wave front, this is not nearly as clear in the coupled case.

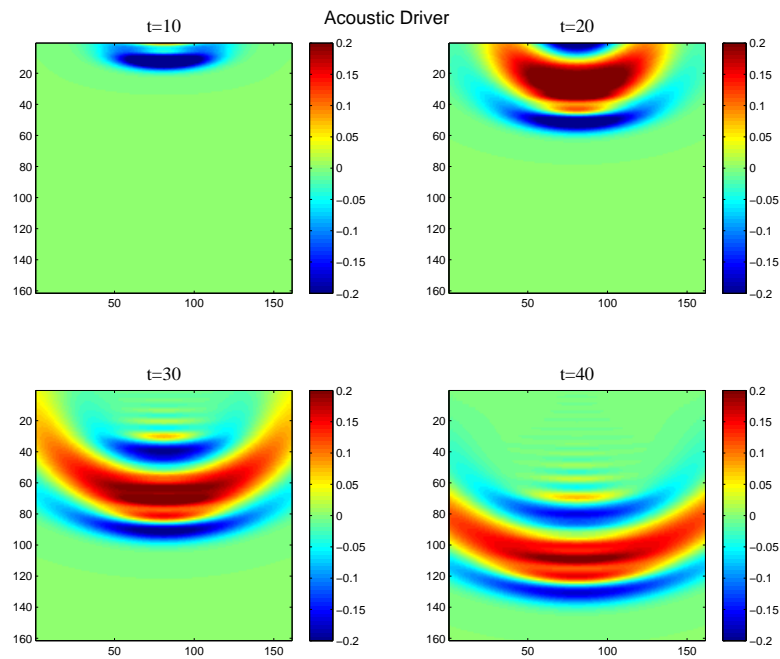


Figure 4.11: Perturbations in gas density from the equilibrium caused by an acoustic, initially Gaussian wave with $\Gamma = 0$. The wave is driven at the top boundary and crosses the domain at the sound speed. The magnetic field is orientated horizontally

This is mainly due to the fact that both waves are longitudinal modes propagating at right angles to each other. Naturally they have relative velocity at right angles to their wave vector which results in a non-zero coupling term. This has the effect of smearing out the peaks in space.

We also note that the clear dispersion as a result varying phase speeds in the plasma is almost not noticeable by late times. In 4.14 and 4.12, it is clear that waves travelling at a slight angle to the magnetic field arrive at the left hand boundary sooner (due to the presence of the fast mode in these directions). This is not the case when the gas-plasma is coupled, as in 4.13.

We would still see this lack of directional dependent phase velocity if the plasma driver was alone in a coupled fluid. This is because the plasma interacting with the

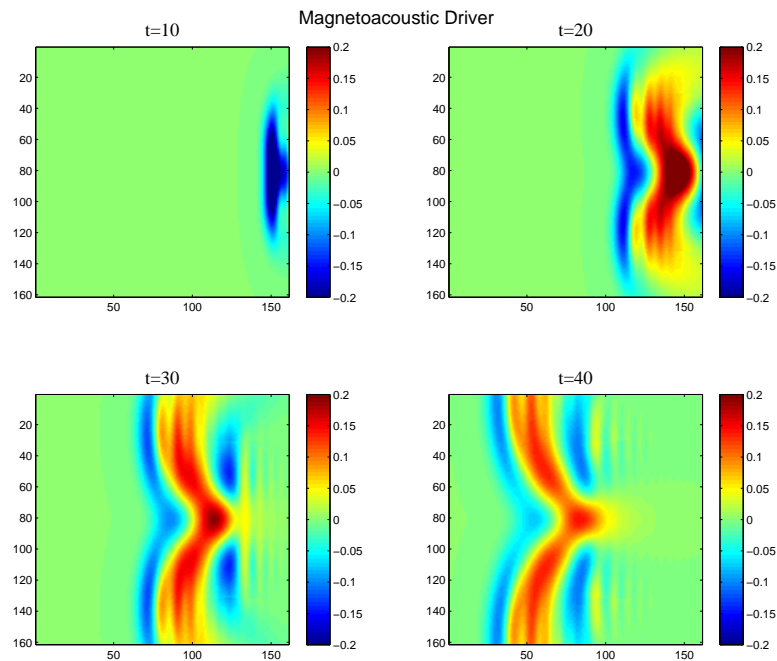


Figure 4.12: Plasma Density for a compressional plasma Gaussian wave with $\Gamma = 0$. The wave is a hybrid of the various compressional MHD modes. It propagates across the domain from the right hand boundary. Note the angular dispersion due to the changing phase speed when the angle of propagation with respect to the magnetic field changes. Waves with k completely parallel to the field (acoustic modes) have a lower phase speed than the magneto-acoustic modes propagating with some k -component across the field. Magnetic field is in the horizontal direction.

stationary background gas will destroy any pure modes, we saw this from the dispersion relations in chapter 2. Any wave trying to propagate through a partially ionized plasma creates a hybrid coupled-wave that contains a mixture of all possible compressional modes and the previously distinct phase velocities become blurred. The addition of the interaction with another wave compounds this by disrupting the smooth propagation of the plasma wave. This can be thought of as an orderly line of people trying to move through a crowd that continually jostles them. By the time the line has reached the other side of the room their orderly nature is gone.

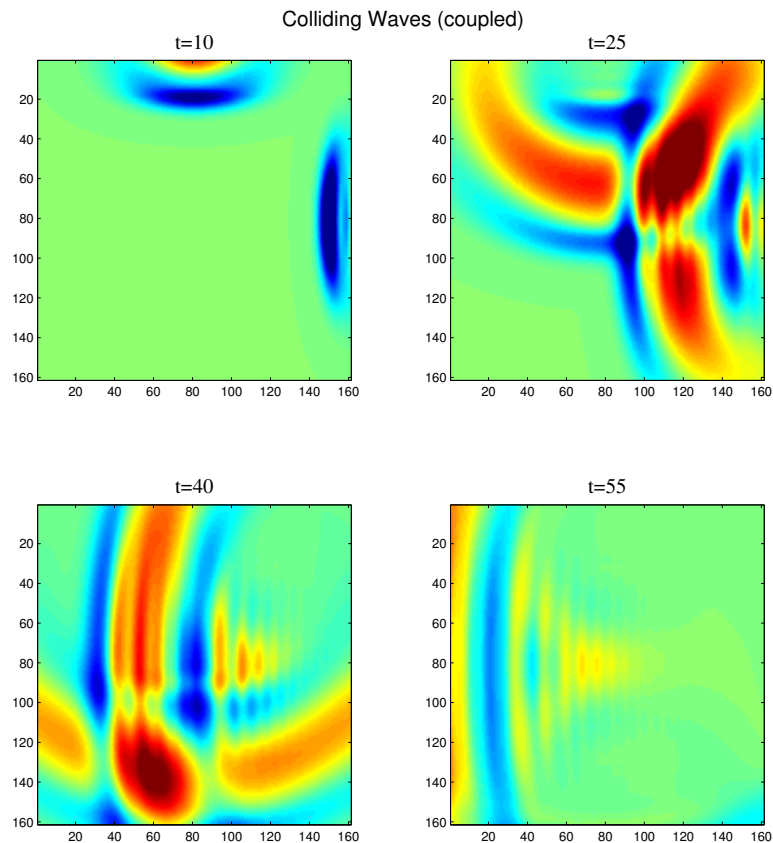


Figure 4.13: Total density (gas+plasma) perturbation showing the interaction between an acoustic wave in the gas and a compressional plasma wave with $\Gamma = 0.05$. The magnetic field is orientated horizontally

What we are most interested in are several features that we shall refer to as ‘plasmoids’. These plasmoids are blobs of hot plasma and magnetic field that are formed by the interaction between the two waves. The simulation parameters including the driving terms were chosen in order to get a good example of a plasmoid. Although we can see several that appear during the course of the simulation we are most concerned with the large one that can be seen forming at $t = 25$ in figure 4.13 at approximately (120,60) and is still there at (60,140) at $t=40$.

We can see that although it roughly coincides with the density maxima in the super-positioned case in 4.14 it differs in several details. It has a much larger volume,

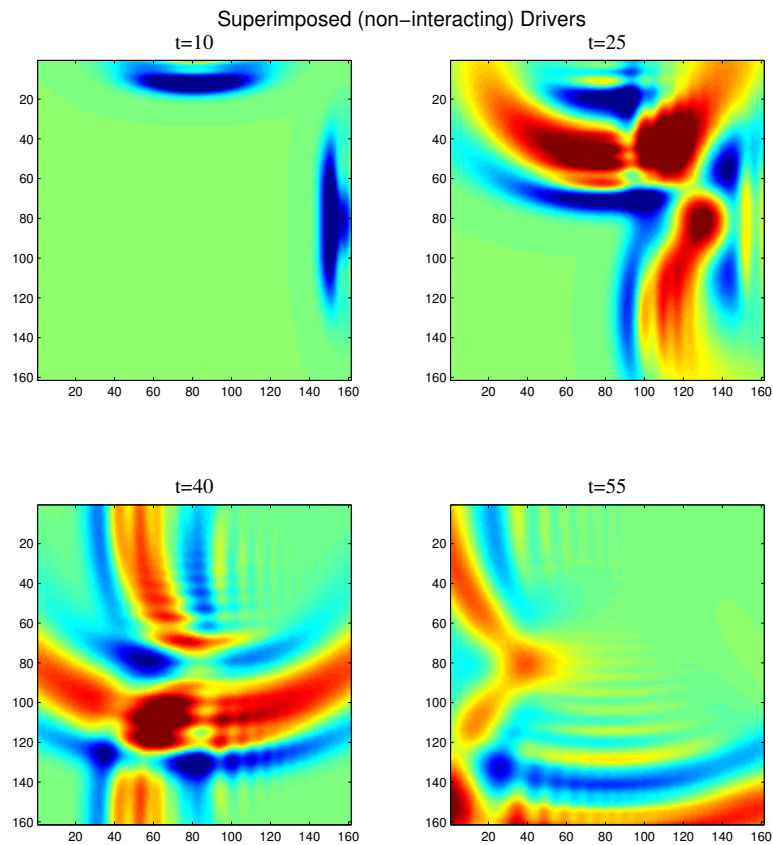


Figure 4.14: Total density (gas+plasma) perturbation at increasing times showing the two waves superimposed on each other with no cross interaction between them, i.e. $\Gamma = 0$. The addition of coupling significantly changes the dynamics. The magnetic field is orientated horizontally.

and it has a velocity independent to that of the wave that created it. It also have a lifespan longer than the maxima in the superimposed case, which obviously only lasts for as long as the two waves occupy the same position. As the driven waves disperse their amplitude drops at a much greater rate compared to the plasmoid. The plasmoid also carries out bulk transfer of fluid rather than just the sloshing back and forth of a wave. The plasmoid enters the sacrificial region where it dissipates.

We take a closer look at the magnetic field at $t = 40$ in figure 4.15. We can see the presence of several ‘loops’ of magnetic field. These are locations where the magnetic

field perturbation has 0 magnitude in the centre and $\nabla \times B$ (and therefore current density) is high. There are no such loops formed from simply the magneto-acoustic wave in the uncoupled case in figure 4.16. Magnetic field plotted over the density map in both figures are the perturbations only, i.e. with the mean magnetic field subtracted.

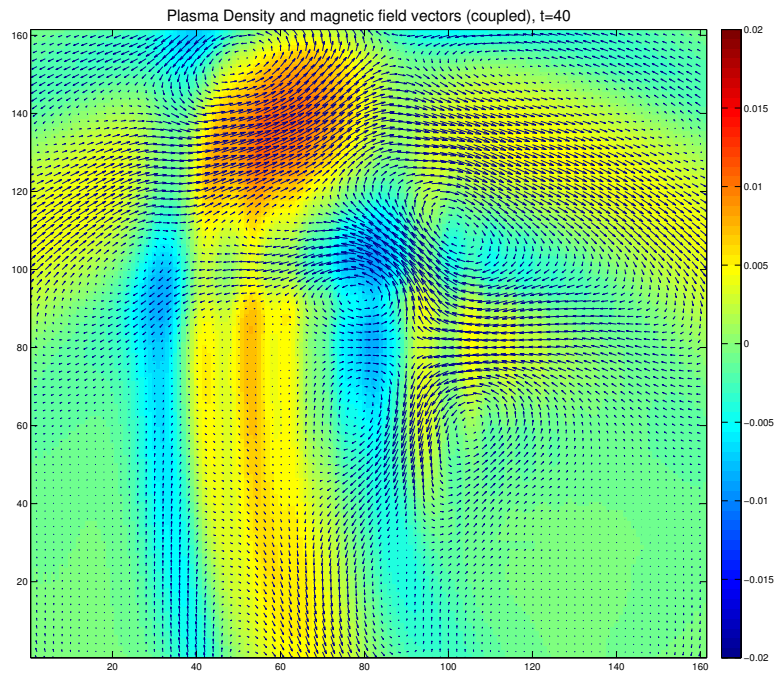


Figure 4.15: Plasma density perturbations and magnetic field perturbation vectors at $t=40$ for the coupled case ($\Gamma = 0.05$), showing the formation of loops of magnetic field in areas around where the two waves interacted. The equilibrium magnetic field is orientated horizontally but the mean is subtracted to highlight small perturbations around this position.

These loops move along with the compressional waves and while they do not coincide directly with the plasmoids they are generally adjacent and likely contribute to the persistence of those structures.

We do note that the idea of being able to drive a wave in each fluid separately as being perhaps experimentally unreasonable but after a reasonable number of timesteps

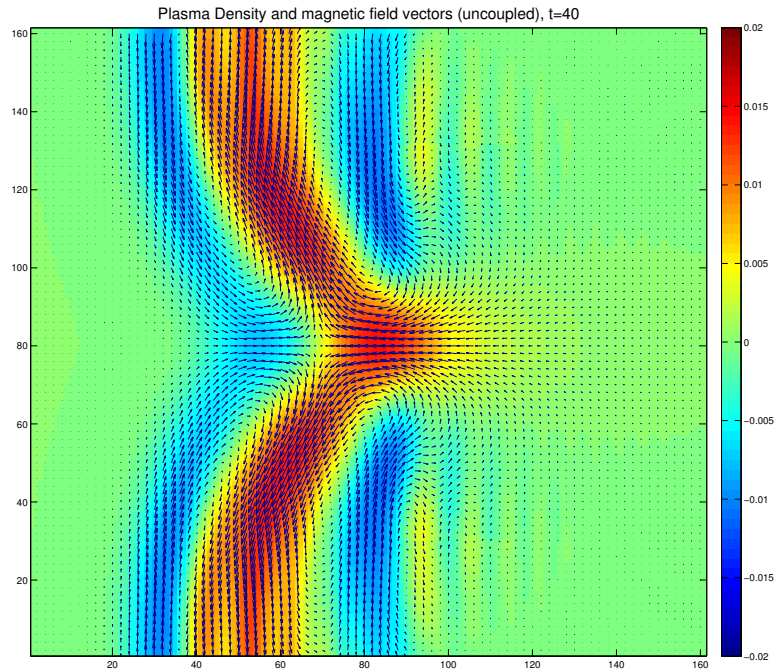


Figure 4.16: Plasma density and magnetic field vectors at $t=40$ for the uncoupled case ($\Gamma = 0.00$), no loops of magnetic field are formed. This shows that the loops of magnetic field are a consequence of the interactions between the neutrals and plasma.

(~ 20 for $1/\Gamma$ which corresponds to $t = 0.5$) the two fluids are heavily coupled with energy spread out between compressional motion in the gas, compressional motion in the plasma and magnetic perturbations. This means that, when the two fluids meet, it is a set of 2 coupled waves which are interacting, rather than a magneto-acoustic wave and a gas wave.

4.3 Conclusions

A plasma and a gas do not behave the same as a plasma and gas mixture. A partially ionized plasma has unique dynamics that can not be seen when considering either fluid individually. A non-linear finite difference MHD and gas interactions code (GMIC) can

simulate the effect that the presence of neutrals has on the behaviour of a plasma.

The plasma and neutrals interact via collisions and these collisions transfer momentum from one species onto the other. As a result, if the two fluids do not have equal velocities there is a net exchange of momentum. This net exchange of momentum prohibits one fluid from moving without disturbing the other. In GMIC this behaviour is modelled by the addition of a coupling term in the momentum conservation equation.

There must always be some resultant relative velocity when either or both of the fluids are perturbed. This is due to the directional dependence of the phase speed on the plasma that is absent in the gas. The only way to eliminate relative velocity is by very strong coupling. This limit is reached when the ion-neutral collisional mean free path is much smaller than the fluid scale length.

We have used GMIC to model a handful of scenarios where the plasma and gas fluids are forced to interact. This demonstrates the ability of a multi-dimensional fluid description to model what is a kinetic behaviour: ion-neutral collisions. Since a large amount of plasma modelling is done in the fluid limit and is concerned with partially ionized plasmas, this is potentially useful.

In section 4.1 either a Gaussian shaped density (and energy) excess or deficit (what we call cylindrical bombs) is set up in the centre of one of the fluids. Naturally the surrounding fluid will react at the sound speed either by flowing inwards or outwards to balance the initial perturbation. This reaction is modified by the presence of the second fluid. We also saw that the negative bomb case is not the inverse of the positive case, it produces larger disturbances both in terms of central amplitude and the amplitude of the outward moving disturbance.

We shall revisit these Gaussian bombs as a source for Alfvén ionization in the next chapter (5).

In chapter 2, we theoretically saw how the presence of the second fluid changes the dispersion relation to remove all pure modes. We also examined this behaviour by looking at the interference fringes in section 2.6. We have looked at waves again in section 4.2 and have seen the same behaviour. That is a modified phase speed and a blurring of the lines between modes when the coupling is enabled.

We also observe the formation of *plasmoids* and loops of magnetic field which form when waves in both fluids interact. These structures are not seen when there is only a single wave or when the fluids are uncoupled. They can be long lasting and have a velocity independent of the waves that created them.

The fact that loops of magnetic field are formed only in the coupled case is interesting. We hypothesise that this behaviour is allowed because of the way magneto-acoustic waves behave. Normally when magneto-acoustic waves perturb the ion velocity this in turn perturbs the magnetic field; in the coupled case energy is taken from the ion velocity into the gas velocity which does not perturb the magnetic field. In this sense the delicate exchange of energy from the internal energy and magnetic perturbations into ion velocity is disrupted. This small change to the waves behaviour allows this unique feature.

In section 1.5.2 we described an obvious extension to momentum coupling; what happens when momentum coupling occurs at extreme velocities? By extreme velocities we mean when the kinetic energy of the relative velocity between the gas and plasma is greater than or equal to the energy for ionization. In this case it is possible for these collisions to result in ionization, although it must occur via an intermediate process that can transfer the energy to the electrons.

In the next chapter we examine the modelling of this behaviour, known as Alfvén or critical velocity ionization, in both the linear limit with GMMC and the non-linear case with GMIC.

Chapter 5

Ionization in a Gas-MHD Plasma

In this chapter we examine results from simulations of gas-MHD interactions which include ionization in the form of Alfvén ionization. In particular the influence of the Alfvén ionization mechanism on the dynamics of a partially ionized plasma. Simulations are carried out with both the linear code GMMC and the non-linear code GMIC.

5.1 Critical Velocity Ionization in a Linear Regime

Firstly we will look at simulations made using the linear code GMMC described in chapter 2, these simulations are presented in [Wilson & Diver \(2013\)](#). We will look at the critical ionization velocity effect in a small number of scenarios. We follow this up with an investigation of the same AI effect in the non-linear code GMMC in section 5.2.

5.1.1 Bulk Flows

An obvious source of relative velocity for AI is that of a homogeneous flow of neutral gas impinging upon a stationary, magnetized seed plasma. This is an incredibly simple example.

Now critical velocities are very large, of the order of several km s^{-1} , but these are velocities frequently reached in laboratory experiments, theoretically expected in

Brown dwarf atmospheres (e.g. [Stark et al. \(2013\)](#)) or observationally detected in the Solar atmosphere. [Rubio \(2009\)](#), [Vitas et al. \(2011\)](#) and others, show supersonic flows in the solar photosphere, easily into the range of velocities necessary for critical velocity ionization, with flows of 20km s^{-1} being observed; such supersonic flows make up a not insignificant fraction of the solar surface. As telescopes improve both in terms of angular resolution and cadence then we continually see an increase in the maximum observed velocity; small features tend to evolve faster. The next generation of solar telescopes (e.g. DKIST) should be expected to observe higher velocities still. ([Elmore et al. 2014](#)) We discuss some of the astrophysical contexts where the conditions for AI are met and the resultant ionization might be important at the end of this chapter (5.3).

Any regime where flows of the order of the CIV in a magnetised plasma are typical we might also expect AI to be typical.

These examples all deal with bulk material transfer but a bulk flow is not the only possible source for relative velocity; any relative velocity between the ionized and neutral species can be exploited as a source of CIV. Any acoustic wave naturally comes with ion or gas motion in the longitudinal direction and an Alfvén wave comes with ion motion in the transverse direction, also perpendicular to the field. As we saw in 2.5.1 waves that are simultaneously propagating in the gas and plasma have different phase speeds and, due to the anisotropic speed of magneto-acoustic waves in the plasma, there can only be one direction where the relative motion between the waves in both species is completely damped (assuming scalar gas pressure). We also note that due to the presence of a momentum coupling term a wave that is driven in either species will result in complimentary wave motion in the other species. We know then that a wave driven in either the gas or the plasma will result in relative motion between the two which, if the perpendicular velocity is great enough, will result in the creation of new plasma via the CIV effect. Therefore, waves of sufficient amplitude can be exploited as sources of new plasma.

5.1.2 Plane Waves

To investigate the CIV effect in waves, we first test a plane wave that propagates through the gas-plasma mixture. Since motion in an acoustic wave is confined to the direction of propagation and only relative velocity in the perpendicular to the magnetic field direction can result in Alfvén ionization then only waves which have a component of the wave vector in the perpendicular direction are of interest.

Due to the linear nature of GMMC we are limited to small amplitude waves, those not exceeding 10% of the background density, or gas velocities of up to 10% of either the sound or Alfvén velocity. This also limits the maximum fluid velocity (produced by the compressional wave) to a few % of both the Alfvén speed and the sound speed.

We first look at an infinitely plane wave that is launched in the perpendicular direction. A driving term is applied to the top boundary of the computational domain. This driving term is sinusoidal in nature and acts on the y-direction gas velocity and the gas density in order to produce an acoustic wave in the gas. The frequency of the wave is set such that 2 complete cycles (4π) completes before the driver switches off.

The background is a partially ionized plasma with an ionization fraction of 0.5 meaning the same equilibrium densities in the plasma and neutral fluids. These densities are set to 1.0 each. The magnetic field is of strength 1 purely in the horizontal, x direction. The driver is a plane parallel wave generated at the top of the domain, this driver has a maximum initial amplitude of 0.1 in units normalized to the sound speed, $r = s = 1.0$ typical of an ionization fraction of 0.5 in a fluid where the sound and Alfvén speeds are the same.

The threshold for CIV is set at 0.01 in normalized energy units. This threshold is fairly arbitrary as no particular element is in mind for a corresponding critical velocity. The limitations of the linear nature of the code means that we wish to avoid large fractional changes in density. As such, this threshold is close to the kinetic energy of the maximum velocity of the driver ($0.01 \approx \gamma 0.1^2$).

The factor f is set to 0.01, meaning that 1% of the maximal CIV occurs on each fluid time-scale. The factor is more important than might be first thought; this factor

constrains the relative time-scales at work, on one hand the fluid time-scale (the sound speed multiplied by the mesh ratio) with the CIV time-scale - that is the characteristic time-scale for a constant flow, at v_c , to fully ionize our plasma.

Since our fluid parameters are all normalised to the sound (and Alfvén speed) then the choice of this time-scale will define the rest of the code units.

Our choice of the value of f is motivated purely by a desire for both the fluid dynamics and the AI mechanism to play a role in the evolution of our systems. We shall discuss f further in 5.4.

The driver runs for 200 timesteps (up to $t=5$) and the subroutine that controls the AI is enabled after 300 timesteps have elapsed ($t=6.5$). This delay is to ensure that the AI source wave has travelled some way into the domain before any ionization takes place, allowing AI to be more clearly observed.

Our simple energetics argument from chapter 1 tells us that (again for an ionization fraction of 0.5) if the kinetic energy of the relative velocity exceeds twice the energy at v_c then that fluid cell contains a high enough energy density that it could just reach an ionization fraction of 1.0 before the relative velocity drops below the threshold and ionization ceases. This leaves a window of between $v_c < v_{\perp} < 2v_c$ where the maximal possible ionization varies linearly between $0 < \dot{\rho}_p dt < \rho_{p,0}$. Obviously, in the presence of frictional drag then relative velocity is reduced without enhancing the ionization fraction and this maximum is not reached.

Although there is no reason to expect density changes to be small our fluid approximation for AI does not pose a problem for a linear approach for a few simple reasons. The wave is constantly moving meaning that the region of maximum relative velocity is always on the move. At one point a small amount of ionization takes place, the wave moves on and the amplitude of the wave decreases due to the redistribution of kinetic energy into internal energy. After a few timesteps, if the critical velocity threshold continues to be exceeded by the wave then this will cause more ionization but in a different fluid element. It is also obvious that for all but an extremely large amplitude wave then the velocity will only exceed v_c across a fraction of its wavelength. This taken together means that even large amplitude waves cannot fully ionize a plasma

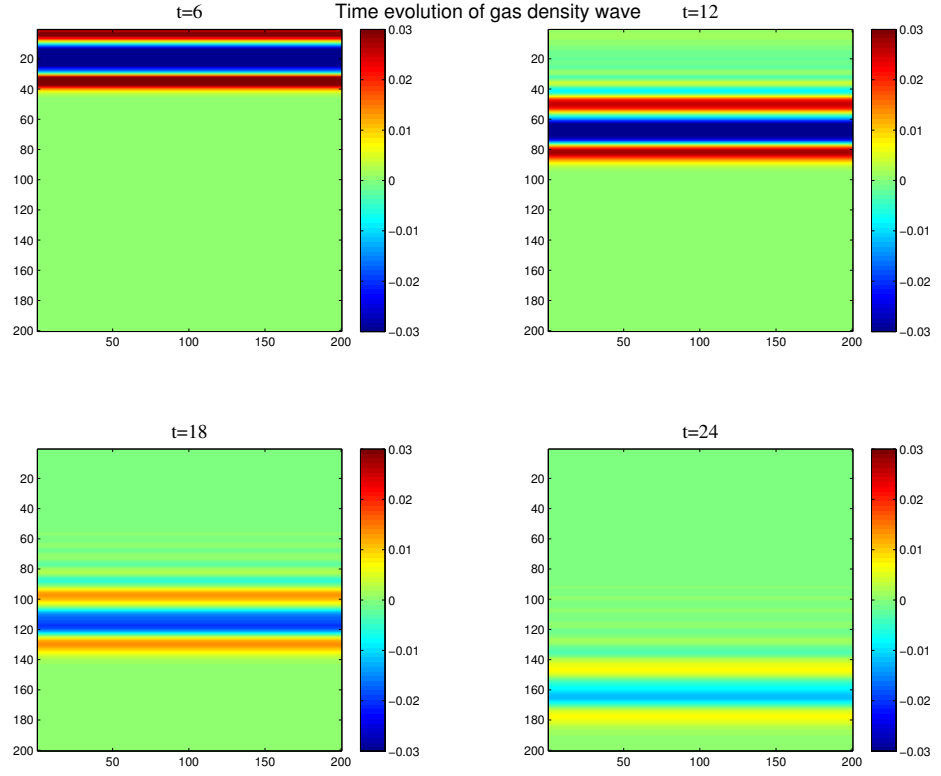


Figure 5.1: The perturbations around the mean gas density showing an acoustic wave in the gas as a source of relative velocity for AI with $\Gamma = 0$ and $f = 0.01$. The maximum and minimum perturbations are ± 0.05 . The magnetic field is orientated horizontally and, due to the plane nature of this wave, all fluid motion is in the perpendicular direction.

unless they persist for several periods.

In order to maximize the contrast between new plasma that is created by AI and plasma which is just perturbed due to collisions (momentum coupling) from the motion of the gas then the coupling factor is set to 0, $\Gamma = 0$.

Figure 5.1 shows time evolution of the wave in the gas. It starts at the top boundary and travels through the domain at the sound speed. $t=6$ corresponds to just before the AI subroutine is switched on. The wavefront remains perfectly flat throughout and the wave drops in amplitude as its energy is extracted for AI.

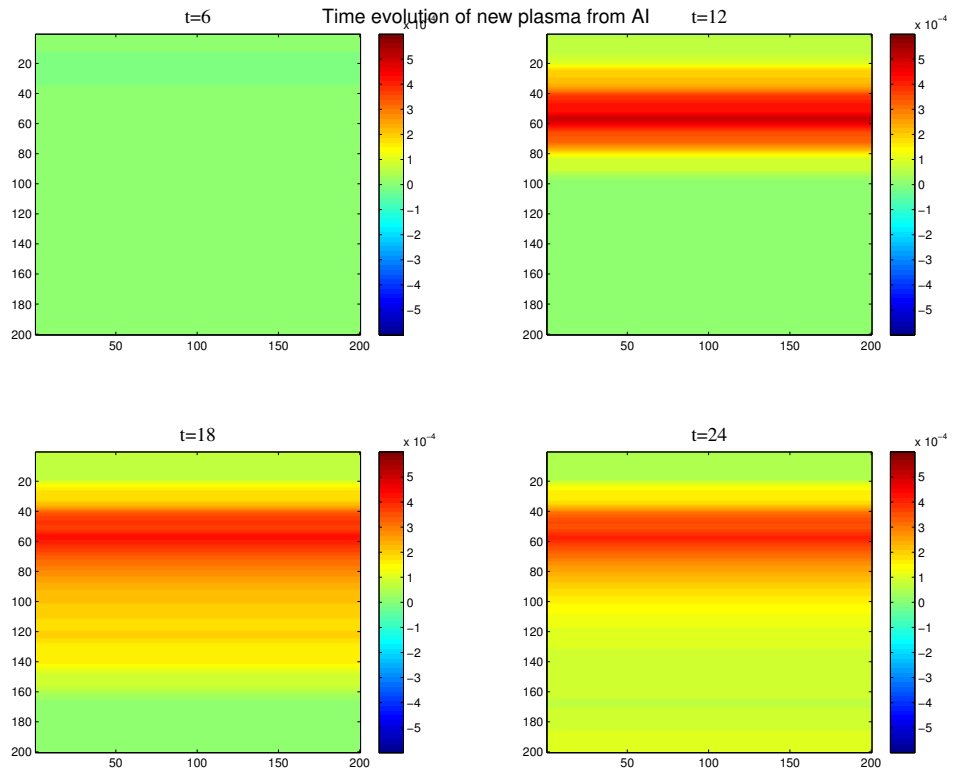


Figure 5.2: Perturbations around the mean plasma density with $\Gamma = 0$, $f = 0.01$. Red indicates the areas where the most plasma has been created. The maximum deviation from the mean is 0.001.

Figure 5.2 shows temporally matched snapshots (to 5.1) of the plasma density. This maps out the location of new plasma that has been created by Alfvén ionization. We can see, at $t = 12$, the first snapshot after AI starts, that there is a large burst of ionization across the full length of the wave packet. The intensity of the ionization drops off until the wave leaves the domain by which point it is much reduced in amplitude.

The formation of this new plasma causes divergences in the plasma partial pressure. This drives fluid motion of the plasma which is seen as the spreading out of the overdensity through the domain. The plane parallel nature on the wave means that any gradient is in the y (or cross field) direction which means that the magnetic field limits this plasma motion.

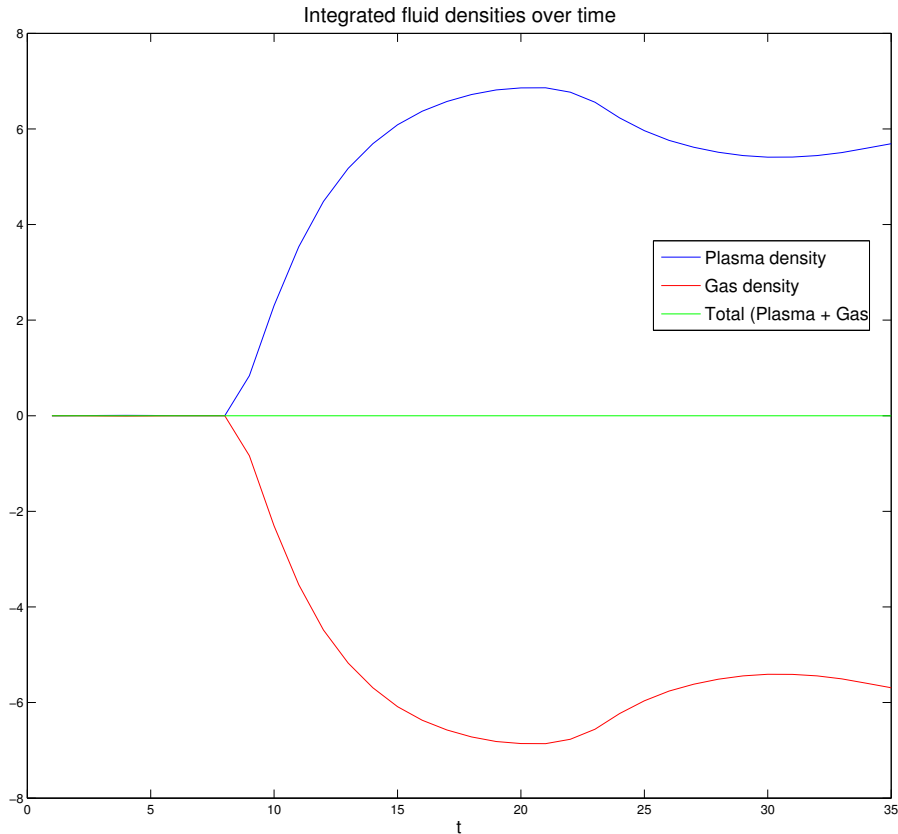


Figure 5.3: The evolution of the various densities in the computational domain, obtained by integration. Steeper gradients in the plasma density (blue) indicate more AI is taking place at that particular moment. The y-axis is in normalized (to the summed density) units while the x-axis is in code units of time.

We can look at the ionization over time in 5.3. There is a large amount of plasma created at $t = 7$, which is when the AI subroutine is enabled. The reaction rate then drops over time as both the energy available above the threshold and the number of fluid cells where the ionization threshold is exceeded shrinks over time. The drop in density resulting in a local minimum at $t = 30$ is due to a peak in density from a fast-mode wave (visible as a low amplitude wave in 5.2) leaving the domain and not due to any recombination. Time resolution of these data is limited by full data output (to reduce space and runtime) being restricted to every 40 timesteps. The gas and

plasma mirror each other with the total (in green) remaining constant, because each unit of plasma created comes from the removal of a corresponding unit of gas.

What we notice in particular is that the locations where Alfvén ionized plasma is created remain visible, even once the relative velocity has dropped below the critical threshold everywhere. There is a local change in ionization fraction not purely a global one. This has the interesting consequence that the ionization fraction of a given fluid cell depends on the history of that cell not simply its current conditions as would be expected for a plasma with thermal ionization as its only ionization mechanism.

Once AI has ceased then, over time, recombination and diffusion will smooth out these locally over-dense regions but for a while this history will persist. The plasma has a limited memory of the fluid velocities that have passed through it.

In general the rate of ionization follows an approximately exponential decay before the ionization fraction stabilises. This stabilisation occurs when there is no longer any part of the wavefront where relative velocity exceeds the CIV threshold.

5.1.2.1 Interplay with Momentum Coupling

The previous simulation was conducted with the momentum coupling factor Γ set to 0. To see how the introduction of a non-zero amount of momentum coupling effects the amount of Alfvén ionization that takes place; we repeat the same simulation with the only difference being the degree of momentum coupling.

First we look at the same output for a run that includes momentum coupling to get a qualitative understanding of how momentum coupling interacts with Alfvén ionization. We expect to see that momentum coupling negatively interferes with AI with high degrees of coupling, meaning the two fluids are closely tied together due to collisions between them, will result in low degrees of AI. This is exactly what we do see with an increase in Γ resulting in less new plasma being created by AI.

Figure 5.4 shows the gas density with the same colour scale as before. The wave starts out with the same amplitude - as momentum coupling takes time to affect a large change in the gas velocity - but over time it is more severely damped than the

uncoupled case. This is exactly as predicted; in the uncoupled case the only way to extract wave energy is by the creation of new plasma but now, with coupling included, the gas wave can be damped both by AI but also by the frictional momentum coupling term.

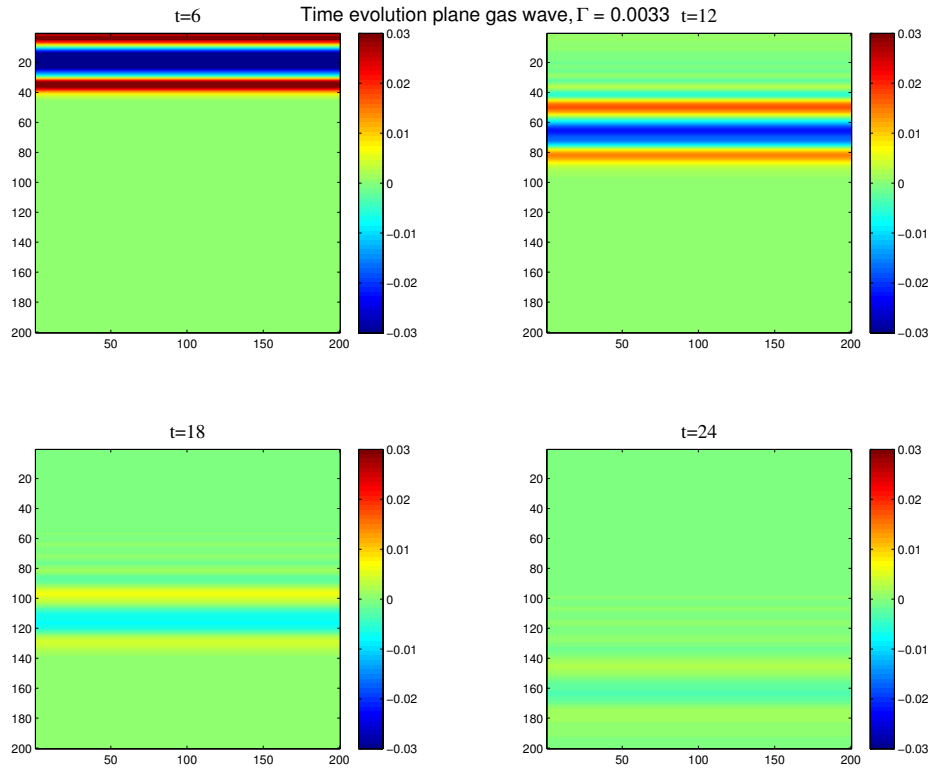


Figure 5.4: The perturbations around the mean gas density showing an acoustic wave in the gas as a source of relative velocity for AI with $\Gamma = 0.0033$, $f = 0.01$. The damping is significantly stronger with the inclusion of momentum coupling. Magnetic field is in the horizontal direction, perpendicular to the wave.

We next look at the behaviour of the plasma with $\Gamma = 0.0033$ in 5.5. The amount of plasma produced is lower in this case; by introducing momentum coupling the neutral and plasma fluids move more closely in phase. This lowers the relative velocity between the two species which not only reduces the energy reservoir that is available for AI but

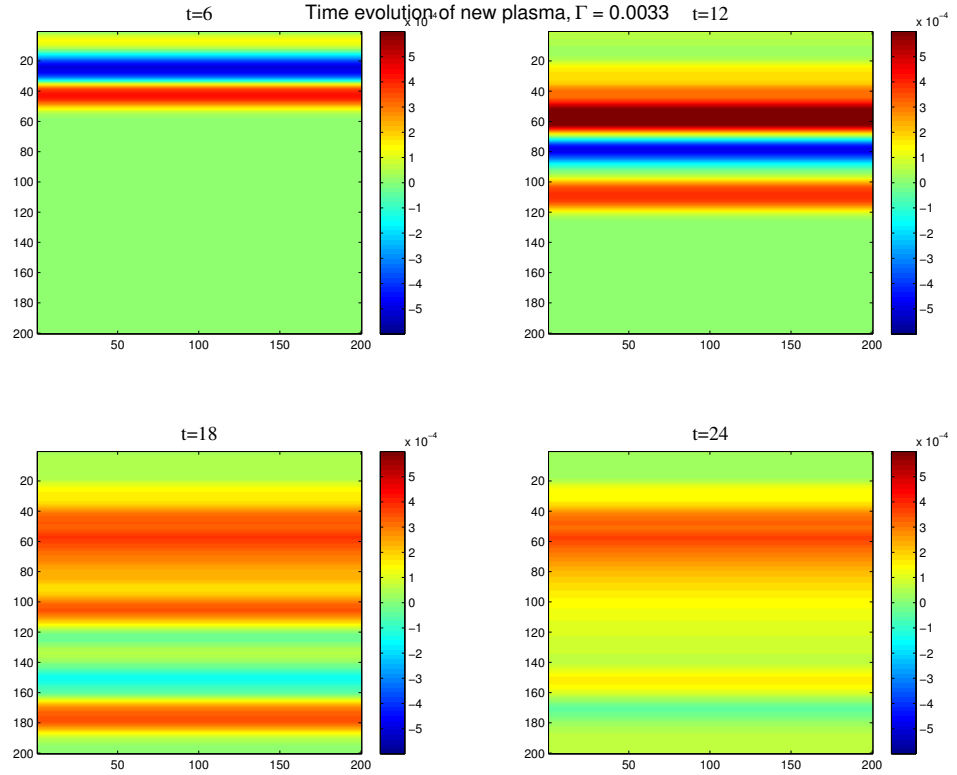


Figure 5.5: Perturbations around the mean plasma density with $\Gamma = 0.0033$, $f = 0.01$. Red indicates the areas where the most plasma has been created. Less plasma is produced for higher Γ . Magnetic field is in the horizontal direction.

also reduces the number of fluid cells where the relative velocity exceeds the CIV threshold.

Also visible is a fast magneto-acoustic wave that propagates ahead of the acoustic wave in the gas. It can be seen most clearly at $t = 18$ at $y \approx 180$ in figure 5.5. This wave propagates faster than gas sound speed so exits the domain first. It serves to show that, due to the different phase speeds, even coupled fluids do not move in sync.

To see exactly how much the momentum coupling changes the total plasma produced we look at figure 5.6 which shows the integrated plasma density over time for a varying degree of momentum coupling. There are a few specific features to point out, the first is the spike in plasma density between $t = 1 - 5$. This spike is merely an

artifact of the driver; the gas wave exchanges momentum with the initially stationary plasma which starts a flow. This flow drags in new plasma from outside the boundary until the first π of the wave-cycle completes and the direction of the flow reverses. The total amount of plasma that enters through the boundary is small (we can see that the total plasma density has approximately returned to 0 before the burst of ionization starts) compared to the total amount of Alfvén ionization that takes place in every case.

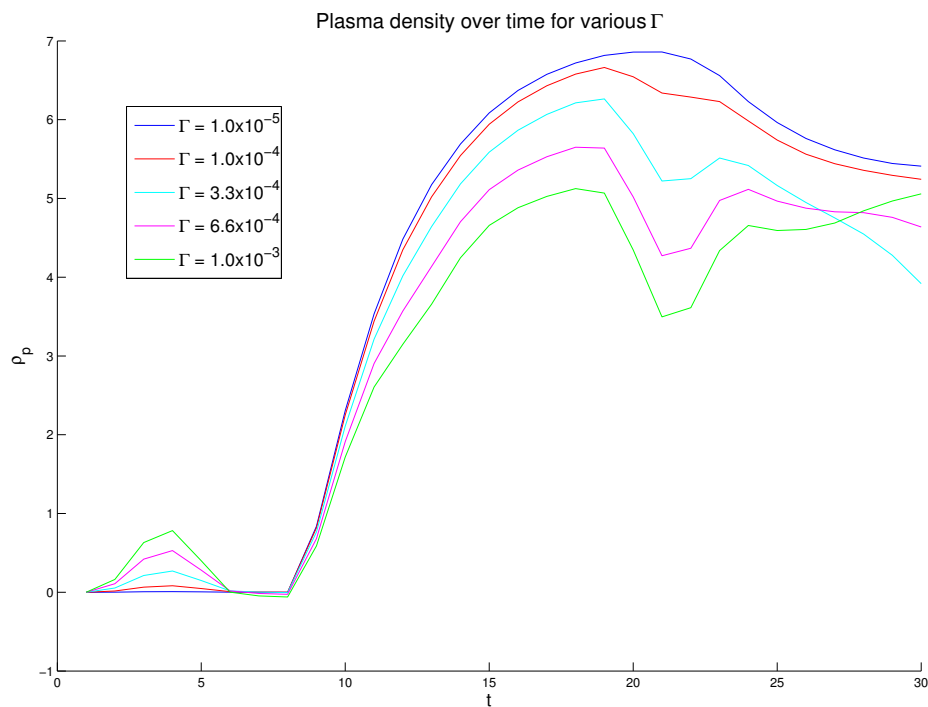


Figure 5.6: Integrated plasma density over time for varying Γ . As the coupling increases the total amount of plasma produced decreases. The y-axis is in normalized density units.

The next feature is when the sympathetic magneto-acoustic wave in the plasma exits the bottom boundary of the simulation ($t = 22$) and is not from an actual loss of plasma, this is the same wave visible during later times in 5.5. The amplitude of both these features scales linearly with Γ . This can be seen in 5.7 which compares

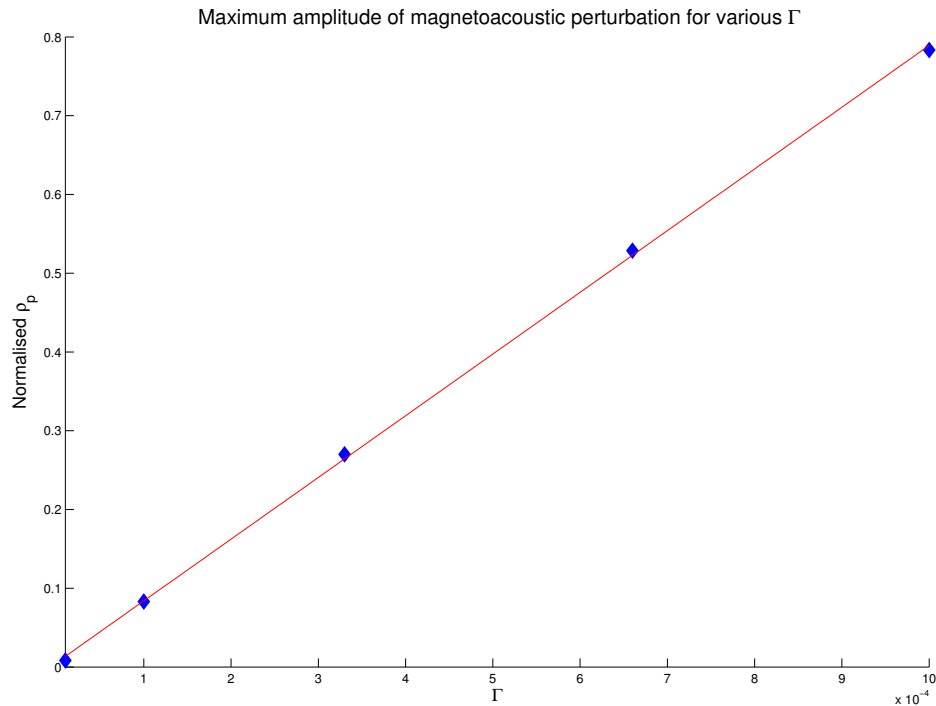


Figure 5.7: Plasma density corresponding to the maximum amplitude of the sympathetic magneto-acoustic wave for varying Γ . As the coupling increases the amplitude of the perturbation in plasma density increases. Y-axis is in normalized density units.

the amplitude of the magneto-acoustic coupled wave for various degrees of momentum coupling. This is exactly as expected. Since the degree of momentum coupling is low enough that only a small fraction of the gas velocity is reduced by drag each timestep then the maximal plasma velocity can be approximated as:

$$v_p \approx \Gamma v_g dt. \quad (5.1)$$

It is also clear from observing the evolution of the plasma density that the presence of coupling reduces the sum total of ionization that occurs. This is something that could be qualitatively seen from 5.5. Although it is clear that even coupled fluids will have relative motion that can be exploited to produce new plasma; an inescapable rule for AI is that a partially ionized plasma where the gas and plasma are closely coupled will

always have less opportunity for ionization than one where more independent motion between the two fluids is possible.

Since we require the ions and neutrals to interact via collisions in order for AI to take place then we require the two fluids to be collisionally coupled. AI will always be hindered somewhat by the frictional drag between fluids.

5.1.3 Cylindrically Symmetric Waves

Due to the anisotropic nature of Alfvén ionization we wish to examine the directional dependence of the ionization.

To do so we simulate a different scenario, that of a cylindrically symmetric wave driven in the centre of the computational domain. This acoustic wave is driven entirely by the gas velocity field.

The form of the driver is a 2-dimensional Gaussian in the centre of a 200×200 computational domain where amplitude falls off as distance from the centre increases. Initially, the driver pushes all gas velocity radially outwards and then radially inwards with a maximum amplitude of 0.1 corresponding to 10% of the sound speed. This repeats for several wave cycles before switching off. The result of this driver is a cylindrically symmetric acoustic wave moving outwards from the centre of the domain. The amplitude of the driving term decreases for each consecutive cycle. The total size of the region where the driver operates is 10% of the width of the computational area.

This driver is the MHD equivalent of throwing a pebble into a pond. The ripples from this pebble travel outwards in all directions towards the boundaries.

As before, both fluids have equivalent equilibrium densities, the magnetic field is orientated in the horizontal direction and $r = s = 1.0$. The ionization is treated the same, disabled until $t = 8.0$ and then with a threshold set at 0.01 of the total background energy density in perpendicular-to-field direction, this threshold allows the chosen driver to produce some ionization without altering the plasma density beyond the linear limit. The momentum coupling constant Γ is set to 10^{-5} , low but not completely disabled. This leaves us with the majority of the plasma motion being

from AI rather than the momentum coupling term. As before $t=1$ corresponds to 40 timesteps, this is approximately the duration for a wave to cross 10 units of length.

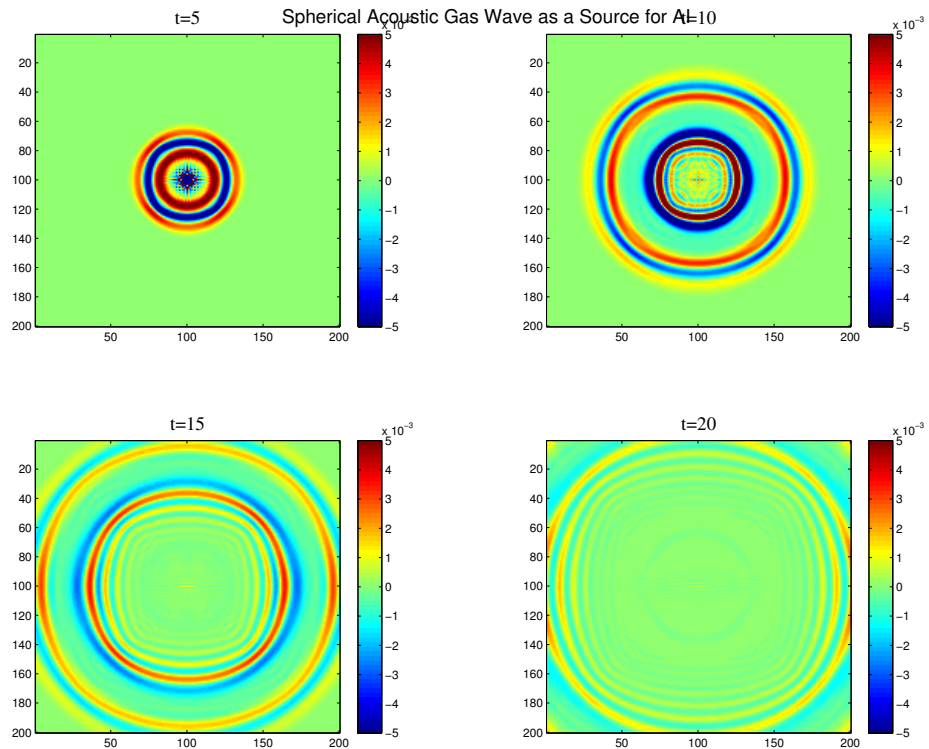


Figure 5.8: The perturbations around the mean gas density showing an initially cylindrically symmetric acoustic wave in the gas as a source of relative velocity for AI with $\Gamma = 10^{-5}$, $f = 0.01$. The equilibrium magnetic field is in the horizontal direction, the portion of the wave that propagates across the field loses significant amplitude due to the influence of AI whereas the fraction of the wave in the parallel-to-field direction is relatively unimpeded.

We first look at the driver in the gas in figure 5.8 and the excess plasma created by ionization in 5.9. At $t = 5$ we see only a small signal in the plasma which is purely motion induced by coupling not by ionization. When the ionization is enabled there is a sudden flash of new plasma created. This new plasma fairly readily spreads out in

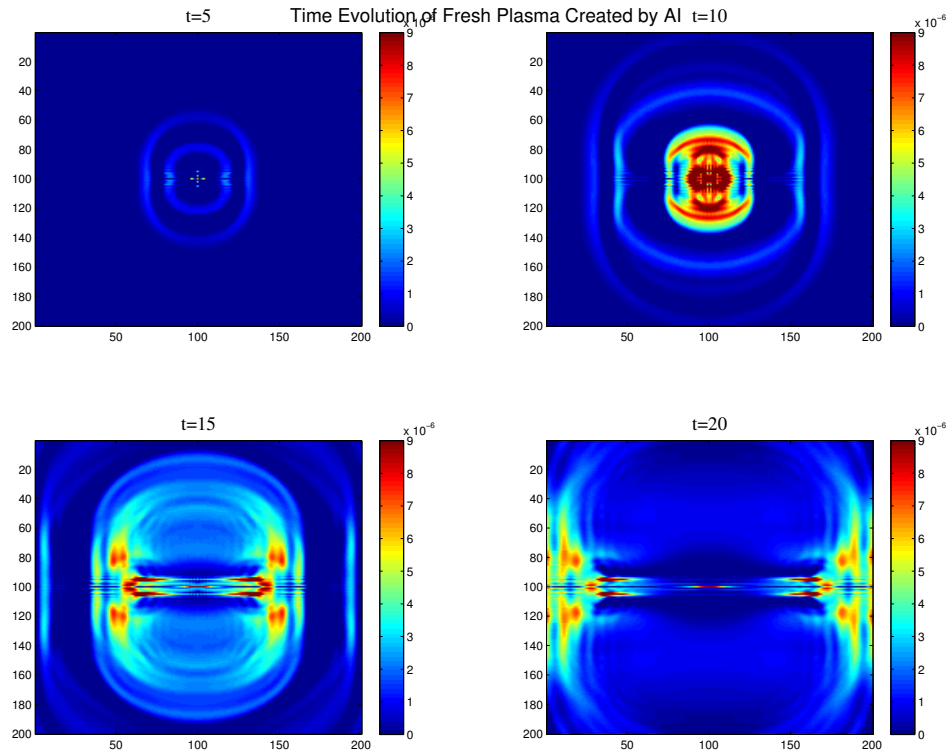


Figure 5.9: Perturbations around the mean plasma density with $\Gamma = 10^{-5}$, $f = 0.01$. Red indicates the areas where the most plasma has been created. The equilibrium magnetic field is in the horizontal direction, plasma is created by wave motion in the perpendicular-to-field direction but due to the $\mathbf{v} \times \mathbf{B}$ force it diffuses along the field lines at approximately the sound speed.

the parallel direction, along the field, as this is the direction where the plasma motion is not inhibited by a $\mathbf{v} \times \mathbf{B}$ force. We can visually see that new plasma continues to be created as time goes on as well as the "hotspots" where a large concentration of ionization took place have their density diffuse over time.

The acoustic wave in the gas starts out cylindrically symmetric but we can see that over time an asymmetry develops. The amplitude of the wave in all directions falls both from dispersion as the surface area of the wavefront increases as well as the momentum coupling providing a slow but steady transfer of energy from the moving

gas into the initially stationary plasma. Most of the asymmetry comes from AI only working with relative velocity orientated perpendicular to the field. This means that even if the wave has the same amplitude in all directions only in directions where v_{\perp} is large is the kinetic energy in the wave liberated and converted to internal energy.

Faintly in 5.9 we can see the formation of various MHD waves. This is due to two effects. The motion of the gas produces sympathetic motion of the plasma and as such there is mode conversion from acoustic modes to magneto-acoustic modes. The new plasma created by AI constitutes an increase in plasma density and pressure that the divergences of which drive new waves in the plasma. These waves do not have a corresponding wave in the gas but they will, again due to the coupling of the two fluid's momenta, induce motion in the gas over time. This produces quite a complex pattern that can be seen at later times.

It may be expected that the central region, where most of the initial ionization takes place would be where the plasma density would remain the highest; similar to the plane wave where most of the plasma remained in roughly the region it was created. However, at late times a cold region (dark blue) is seen towards the centre of the domain. This is where the plasma density is lower than the initial condition. This means the non-zero divergence caused by the increase in plasma density set up a net outward flow in the plasma that results in the centre actually ending up at lower plasma densities than it started with. This is behaviour completely contrasting with the plane perpendicular wave case.

If the simulation is left to run until late times then some plasma would diffuse back into this region until equilibrium is restored.

This same effect is not seen in the gas where the gas motion is purely one induced by waves. The density may rise and fall dynamically as the driving wave passes by but the fluid parameters of the gas return to the equilibrium fairly rapidly; there is no net transport of neutral material. This tells us that the driving is not the cause of the net plasma flow.

In figure 5.10 we look at the total amount of plasma created by Alfvén ionization. Approximately the same pattern is repeated here as in the perpendicular plane wave

with ionization being rapid at first and falling off as the amplitude of the wave drops off.

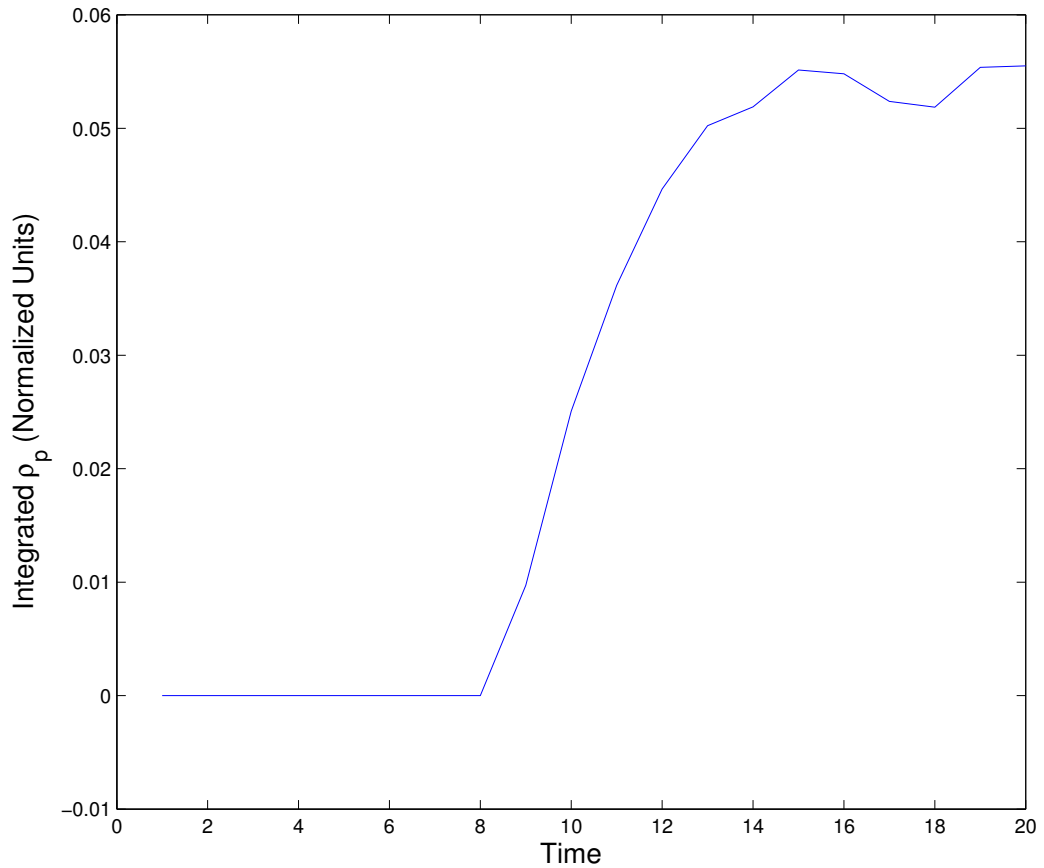


Figure 5.10: The evolution of the plasma density for the cylindrical wave case. The ionization follows a similar pattern, rapid at first then quickly falling away. Note the lower total degree of ionization due to the more rapid decrease in wave amplitude due to radial dispersion.

The y scale is the same as for the plane wave so we see roughly two orders of magnitude lower amount of plasma produced when the two are compared directly. Although the amplitude of the waves are the same in both the plane and cylindrical cases; in the cylindrical case the wavefront is approximately 30 units of length versus

the 200 units in the plane case. This means the total energy pumped in by the driving term is significantly lower. In addition, in the plane case the amplitude of the wave fell off gradually as a consequence of both momentum transfer and AI, in the cylindrical case not only are both of those effects present but the amplitude also falls off as $1/r$ due to the wave naturally spreading out in space. This contributes to the lower degree of ionization attained with a maximum amplitude being just 10^{-5} of the background.

Because the ionization rate in a given fluid cell depends on the excess velocity available above a threshold then we expect even a small difference in amplitude to be capable of large changes in ionization rate. Consider the following cases:

$$\begin{aligned} v_{rel} &= 1.01v_c, \\ E_k &= \rho_g v_{rel}^2, \\ E_{ai} &= E_{k,vrel} - E_{k,vc}, \\ &= (1.0201 - 1.00)(\rho_g v_c^2), \\ &\approx 0.02(\rho_g v_c^2). \end{aligned}$$

$$v_{rel} = 1.1v_c, \tag{5.2}$$

$$E_{ai} = E_{k,vrel} - E_{k,vc}, \tag{5.3}$$

$$= (1.21 - 1.00)(\rho_g v_c^2), \tag{5.4}$$

$$\approx 0.2(\rho_g v_c^2). \tag{5.5}$$

In these cases we have seen an increase of just 10% in relative velocity and 20% in kinetic energy density but have seen an increase of 1000% in the energy reservoir available for ionization. If the two cases ionize with the same efficiency (same f) then we will see the same increase of a factor of 10 in terms of plasma produced.

This means that, when you are close to the critical velocity, AI is very sensitive to changes in velocity. A small increase in wave amplitude might move you from a regime where there is no ionization to one where AI is complete. This behaviour is not unique to this numerical fluid approach but is also seen in experiment ([Fahleson 1961](#)).

5.2 Critical Velocity Ionization in a Non-Linear Regime

The implementation of critical velocity ionization is the same for the GMIC as the linear GMMC. At each timestep relative velocities between the ionized and neutral components of our partially ionized plasma are calculated. Any fluid cell that has relative velocity that exceeds the threshold has an ionization rate calculated by our AI proxy (equation 2.53).

We present the results from a set of two simulations which are extensions of the cylindrical bombs seen in section 4.1 to include an Alfvén ionization term. Two simulations are presented that show the influence of AI on the plasma dynamics as well as the ability of these over and under-density regions in causing AI.

The simulation parameters are: A background density in both the plasma and the gas of 1.0. A homogeneous magnetic field orientated in the y (vertical) direction of 1.0. The plasma beta is 1.0. The momentum coupling constant, Γ is 0.0. The ratio of plasma to gas density is 1.0. The Alfvén ionization factor f is 0.04. The threshold for ionization, v_c , is taken as 3% of the Alfvén speed (0.03).

The computational domain is 200x200 region of interest with a sacrificial damping region of width 200. All plasma and gas variables in the region of interest are output every 10 numerical timesteps. The ionization is disabled for the first 20 timesteps of the simulation (until $t=2$).

5.2.1 Ionization from Gas Bomb

In the first scenario we, as in 4.1, place a localized Gaussian shaped density in the centre of the ROI with a maximum amplitude of 0.4 in the gas. This density overabundance causes a cylindrically symmetric wave to expand outwards at the sound speed. The plasma is initially stationary, meaning a relative velocity exists between our two fluids. Where this relative velocity exceeds the critical velocity ionization takes place. The amount of ionization is proportional to both f and $v_{rel} - v_c$.

The evolution of the total density is show in figure 5.11. Since a significant amount of our time dependent gas density will become plasma, total density is a better visual-

isation of the disturbance. The acoustic motion generated by the Gaussian density is no different than in the momentum coupling. In the absence of momentum coupling, all damping is a result of AI.

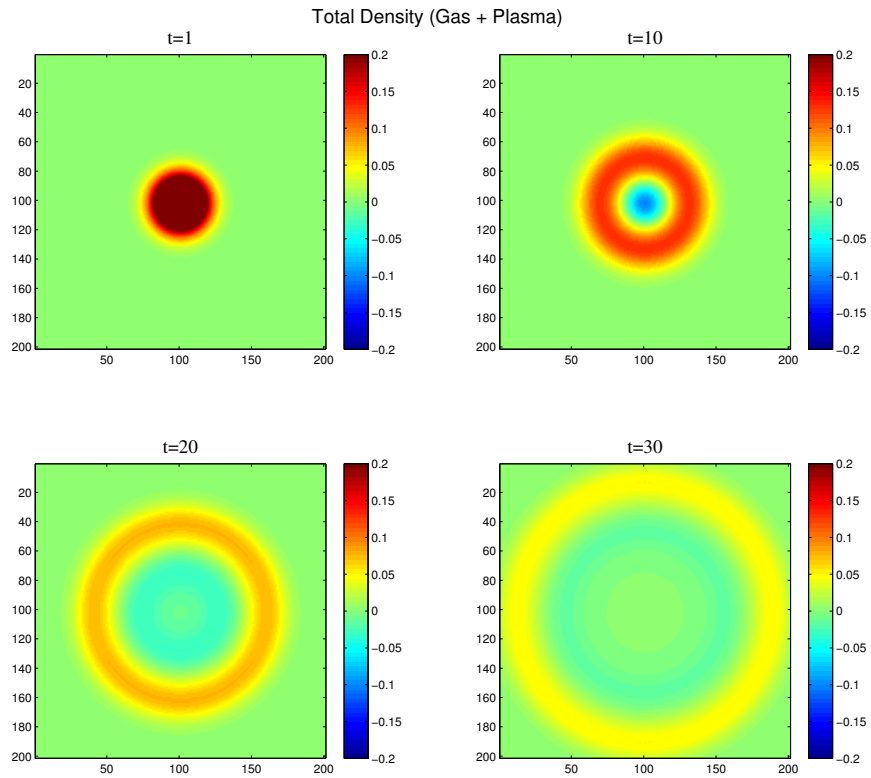


Figure 5.11: Gas density at select times with $\Gamma = 0$, $f = 0.04$, the magnetic field is orientated vertically. The initial disturbance has a central amplitude of 1.4 compared to the mean density of 1.0 and is shaped as a Gaussian. The resultant wave loses amplitude due to dispersion and Alfvén ionization. The magnetic field

Figure 5.12 shows newly created plasma from AI. The higher the plasma density the more ionization has taken place. As before, this is not ionization rate but rather total integrated ionization as new plasma does not recombine. This means that contained is both the AI as well as the standard MHD motion.

The location of maximum ionization is no surprise. The nearer the disturbance the

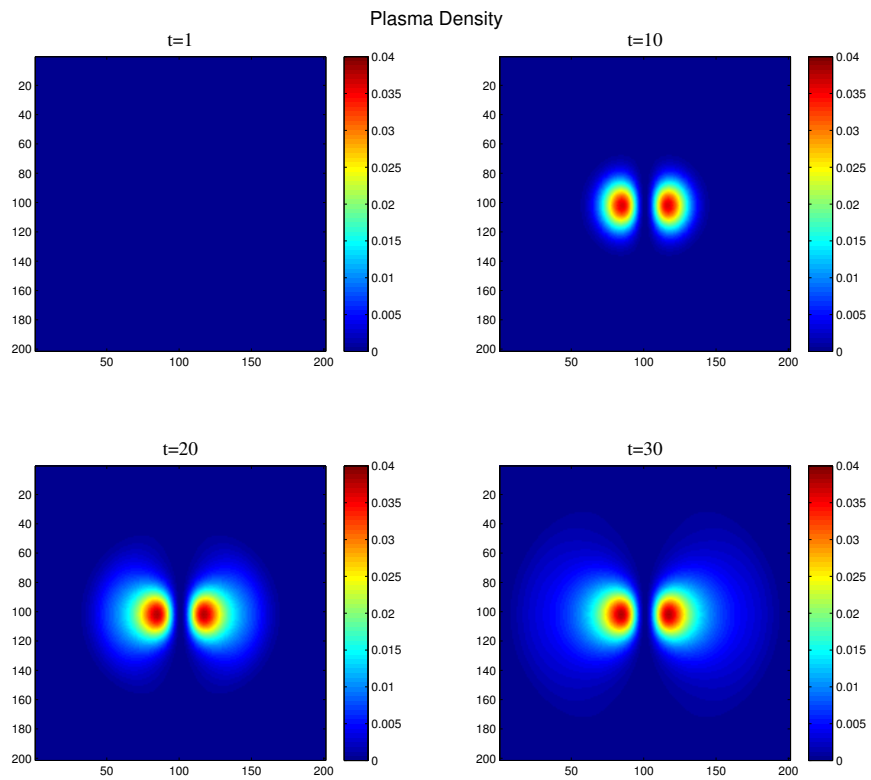


Figure 5.12: Plasma density due to AI with $\Gamma = 0$, $f = 0.04$, the magnetic field is orientated vertically. The most ionization occurs near the central perturbation at early times but continues until the perturbation exits the domain.

higher the wave amplitude and thus the higher the relative velocity and the higher the magnitude of the ionization. Since the magnetic field is vertical there is a symmetry around this axis. Ionization only occurs due to relative velocity in the perpendicular direction, therefore where the gas motion is mostly in the x-direction there is a higher rate of ionization.

We can see this clearly in figure 5.13 by looking at a plot of relative velocity in the x (cross-field) direction. This is obtained by subtracting the two fluid velocities although in practice the relative velocity is almost equal to the gas velocity for much of the simulation run since the plasma takes a while to react due to the lack of coupling.

We can see that, by $t = 30$ although the relative velocity is significantly lower than

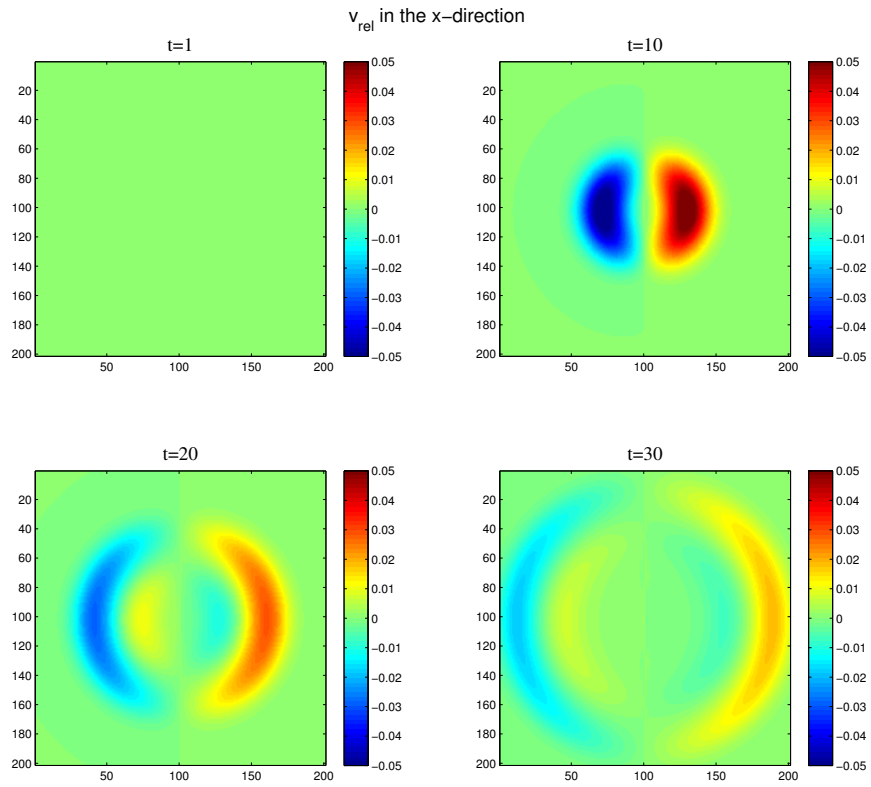


Figure 5.13: Relative velocity in the x-direction. The colour bar is in units of v_A . Then total amount of ionization in a given fluid cell is dependent only on the value of v_{rel} .

$t = 10$, it is still fairly large compared to the Alfvén speed. In fact it remains, for at least some of its span, higher than the critical velocity of 0.03. As such we should expect ionization to still be occurring at this time. In figure 5.14 that is indeed what we observe. Ionization rate is most significant at early times but continues up until the perturbation leaves the domain. The lack of momentum coupling allows the relative velocity to stay above the critical threshold for longer. The more persistent ionization means that new plasma is spread across a broader area but still peaks strongly near the disturbance.

The amount of ionization that takes place is much larger than in the linear case. In some places the ionization fraction is changed by $> 5\%$. This is a very significant

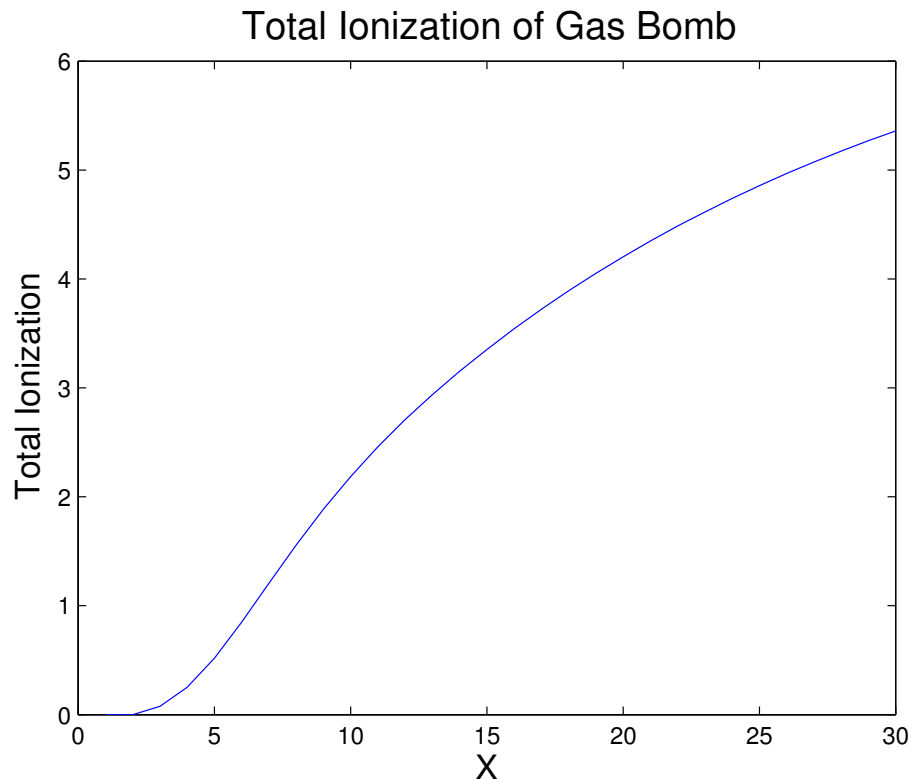


Figure 5.14: Total ionization from gas bomb. Ionization routine is disabled until $t = 2$ at which point the ionization rate is high. At late times ionization is still taking place but the rate has significantly slowed.

change to the ionization fraction, it is easy to imagine a situation where a region of plasma is repeatedly hit by waves which ionize a little at a time and, due to the different time-scales of recombination and ionization, the freshly ionized plasma is able to persist. In such a scenario we expect major departure from a thermal ionization equilibrium.

Just as the linear case the newly created plasma density causes fluid motion. We can see the new plasma is a source of fast and slow magneto-acoustic modes. Unlike the linear case we have disabled momentum coupling so we do actually see the presence of MHD modes rather than MHD-acoustic coupled waves.

Interestingly, the inhibited motion of the plasma across the field means that a large density gradient persists for some time. The simulation was ran up to $t=200$, or 2000

finite difference timesteps. This corresponds to 5 Alfvén crossing times. Even at this late time the plasma has not dispersed significantly and what limited dispersal there is mostly occurs in the parallel to field direction.

5.2.2 Ionization from Double Bombs

We next look at a more sophisticated simulation; all simulation parameters are the same except for the initial conditions. Instead of just an over-abundance in the gas we also include a plasma rarefaction. The rarefaction of the plasma is equal and opposite to the increase in gas density such that, at $t=0$, the total density is 1.0 across the entire domain. This is a combination of both the positive and negative cylindrical bombs from section 4.1 except with momentum coupling disabled and AI enabled.

Since the fluid equations depend on the partial pressure and not the total pressure then these initial conditions still drive fluid motion. The gas once again explodes outwards and the plasma implodes inwards. The idea behind a total density perturbation of 0 is to represent a region where plasma has spontaneously recombined. The idea being that if somehow a plasma were to locally recombine this would simultaneously cause pressure gradients in both the gas and the plasma. If this is an energetically dramatic event then the induced flows could result in AI which can re-ionize some fraction of the gas again.

In a sense this may offer plasmas in a particular regime some form of protection from rapid recombination. When a region of plasma recombines into gas then the changes to the partial pressures of both fluids will naturally lead to relative velocities and thus ionization. If this ionization is significant when compared to the original recombination then we could describe such a plasma as resilient against recombination.

We see the initial conditions of the plasma, gas and total in figure 5.15.

A colour-map of the plasma density is not as informative in terms of examining the AI mechanism as in the gas bomb case; the perturbation of the plasma drowns out the ionization signal. Instead we simply look at the total amount of ionization done over time. Figure 5.16 shows the comparison of the total ionization done between the

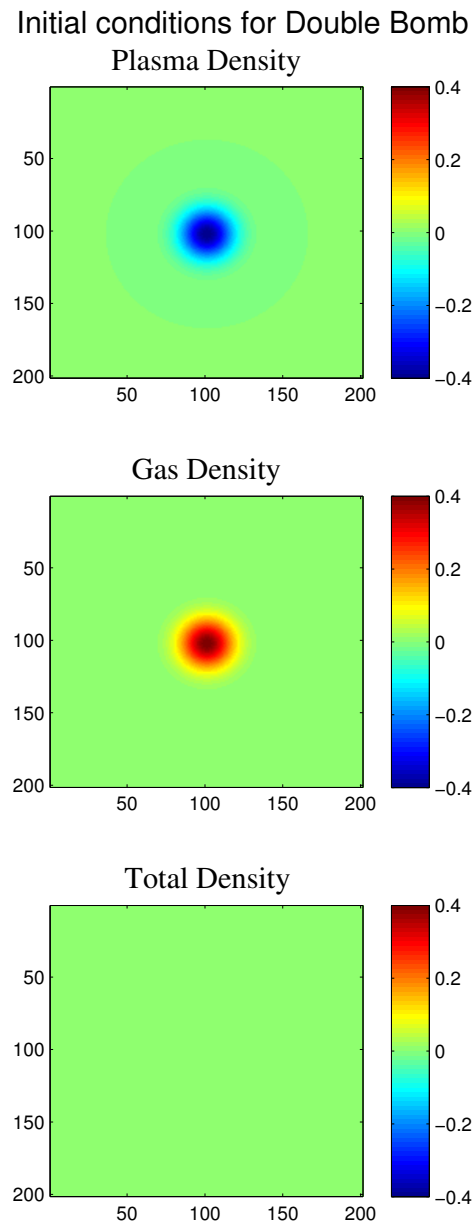


Figure 5.15: Initial conditions for the Double Bomb setup. Note that the plasma and gas initial perturbations are equal and opposite. The total perturbation is 0, the magnetic field is orientated vertically.

double bomb and the gas bomb simulation.

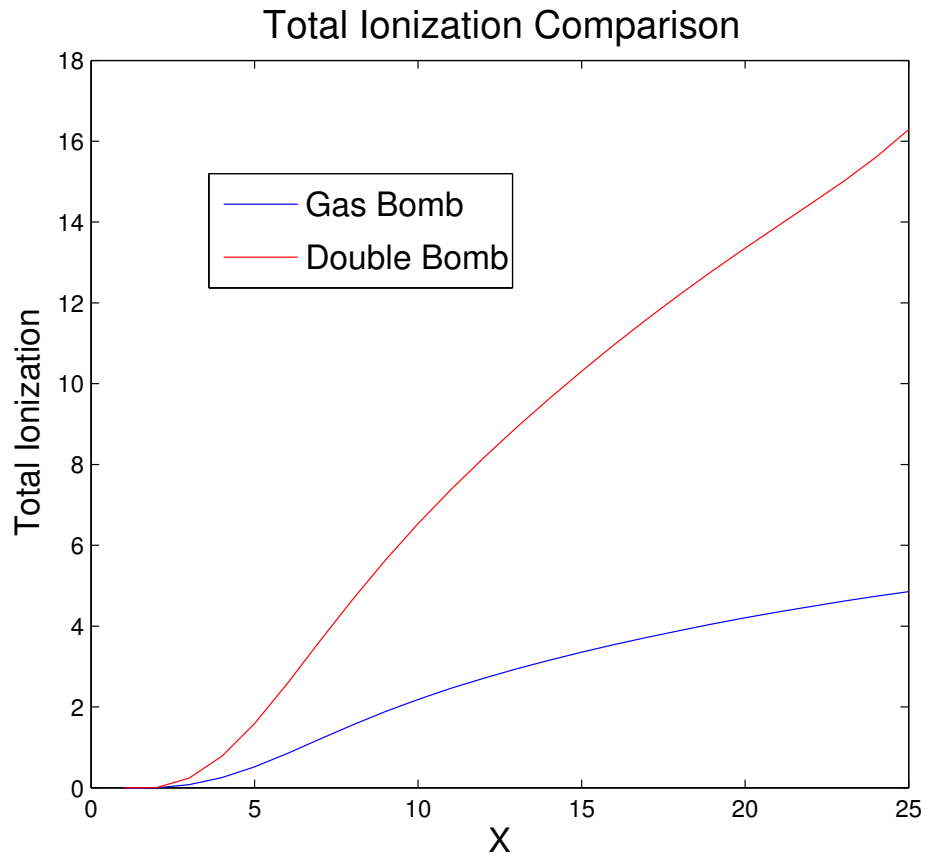


Figure 5.16: Total ionization from the double bomb. Ionization routine is disabled until $t = 2$ at which point the ionization rate is high. The double bomb significantly outperforms the gas bomb resulting in a factor ~ 3 more ionization at all times.

The total ionization is significantly higher in the double bomb case. The double bomb causes approximately 3 times more ionization than the gas bomb does. This is because the plasma is trying to move one way and the gas the other resulting in significantly higher relative velocities.

It is perhaps not as extreme as expected. The plasma is inhibited from moving in the x-direction due to the force exerted on it by the magnetic field. Alfvén ionization can only occur due to relative velocity in the perpendicular to field direction so the

plasma is unable to contribute as much to the relative velocity in the x-direction as the gas.

We choose a system of units where a completely unperturbed plasma has a total density of 0. On this scale, the integral of the initial conditions of the plasma density is -361.91 (negative because some of the plasma has recombined). We compare this to the final perturbation of -337.70, the plasma density has increased by 24 over the whole domain. This means AI was able to undo $\sim 7\%$ of the initial perturbation (the perturbation being totally undone would increase the plasma density to 0). The amount of AI able to occur can be increased by decreasing the critical velocity or by increasing f (as a higher f means more of the total wave energy is extracted before the wave naturally disperses).

This is a reasonable fraction of the initial perturbation but AI was not close to being able to re-ionize all of the initial recombination. Suggesting that if rapid recombination occurs high amplitude compressional waves may cause AI which would act to slow the recombination but would not be able to reverse it completely.

If the plasma beta is increased then the magnetic field is reduced and will do a worse job at preventing cross-field diffusion, this increases the ionization rate. This behaviour is shown in figure 5.17. We can clearly see that at low beta very little ionization takes place and this increases with increasing beta. There appears to be diminishing returns when increasing beta beyond 1.0. We attribute this to a plasma being, at most, as good as a gas at moving across the magnetic field (i.e. totally unimpeded). If β is sufficiently high then the relative velocity will not be increased by increasing β .

For a beta of 2 the total ionization done is 10% of the initial perturbation. So AI even in a reasonably high beta plasma does not manage to offset the initial recombination.

To see why, suppose that the plasma beta is infinite, the critical velocity was 0 and $f = 1$ then all energy in the perpendicular direction would be claimed for ionization. Since due to the problem symmetry 1/2 of the kinetic energy (in 2-dimensions) is in the perpendicular direction then, in such a scenario, 1/2 of the total perturbation energy would be converted to plasma internal energy. In 3-dimensions this problem

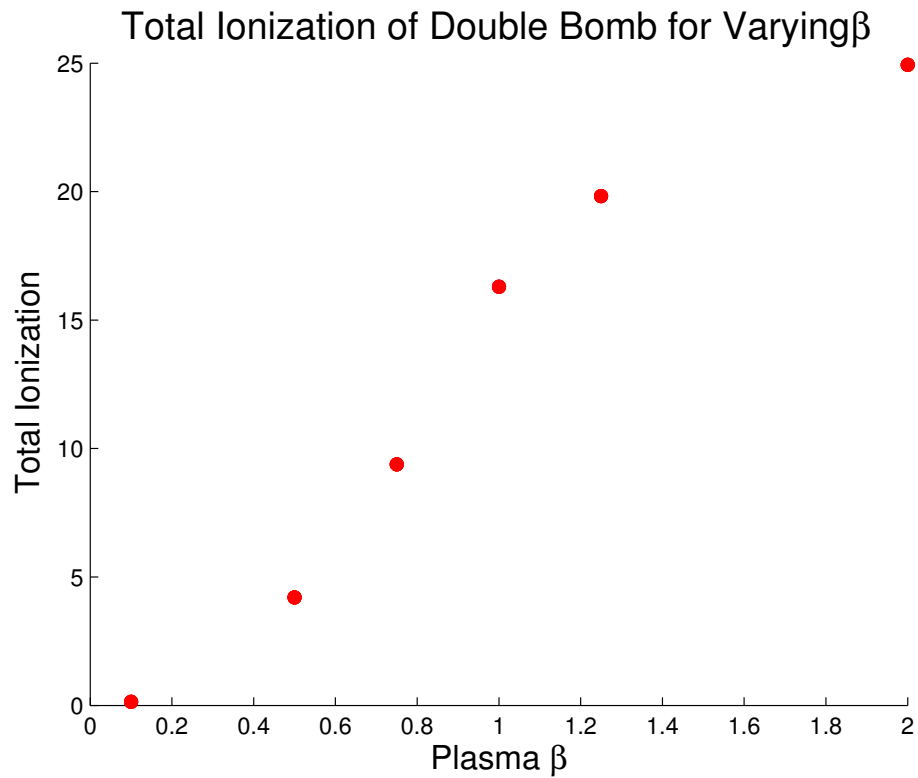


Figure 5.17: Total ionization from the double bomb changes as the plasma beta is varied. Higher beta corresponds to higher total ionization. The total ionization is taken at $t=25$.

is slightly better, assuming the same symmetrical disturbance in 3-d only 1/3 of the total perturbation is in the parallel to field direction with 2/3 of it in the perpendicular directions.

If we assume that the recombination, that triggered our double bomb scenario, resulted in radiation that escaped the system then it is not possible that the total perturbation energy is greater than the internal energy deficit that was caused by the initial recombination. It is therefore impossible for the AI to completely undo the initial recombination.

As beta increases then the kinetic energy of the plasma becomes more and more biased to the parallel to field direction and the total ionization possible decreases. If Γ , the momentum coupling coefficient, is non-zero then relative velocity is reduced

without ionizing (and if $f < 1$) then the wave will damp and disperse without complete extraction of the kinetic energy for the purpose of AI. We examine this next.

5.2.3 Interplay with Momentum Coupling

As in the linear code we repeat the double bomb scenario with the exact same conditions as before, with $\beta = 1$ and this time we vary Γ from 0.001 to 0.05. We expect that the presence of momentum coupling reduces the total Alfvén ionization by reducing the relative velocity between species and this is indeed what we find.

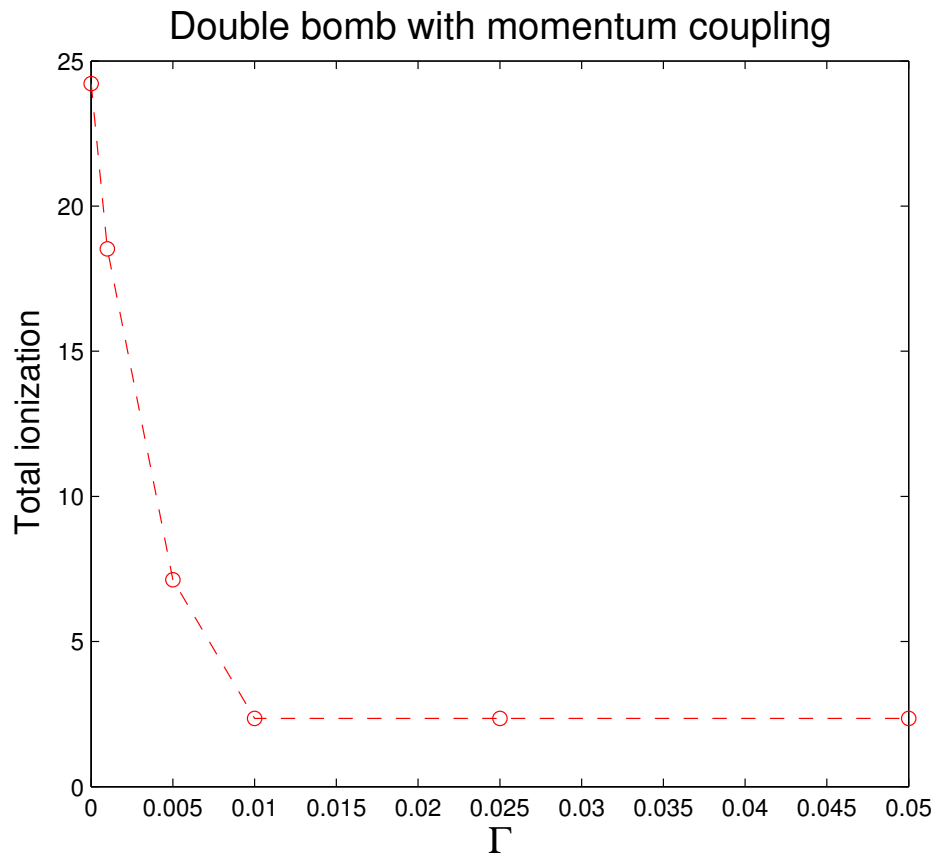


Figure 5.18: Total ionization from the double bomb for changing Γ . Higher momentum coupling corresponds to lower total ionization. The total ionization is taken at $t=30$.

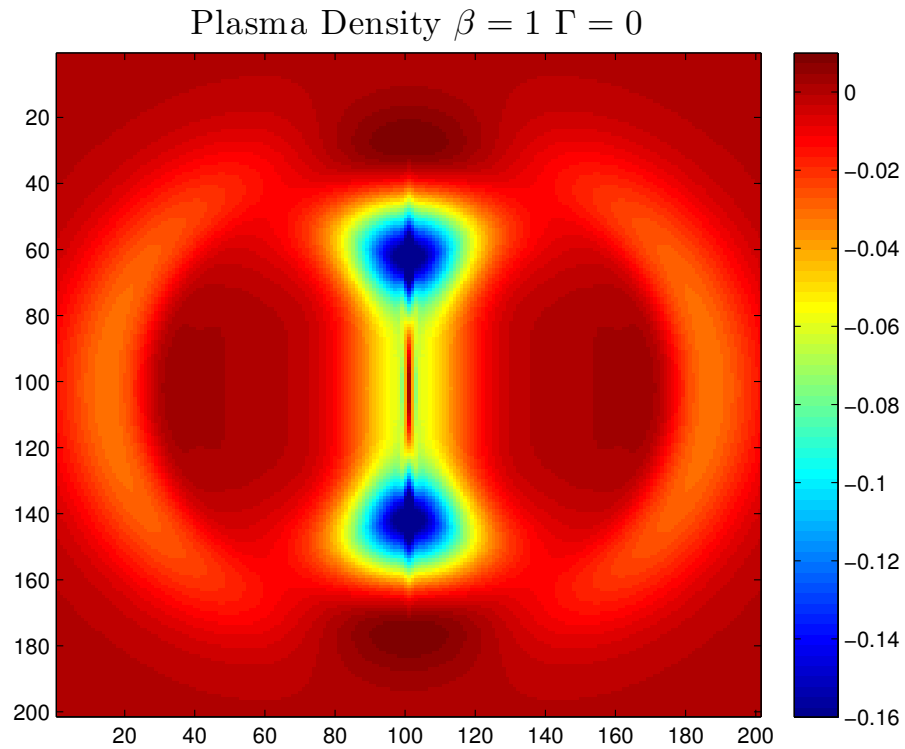


Figure 5.19: Plasma density for the double bomb with $\beta = 1$ and $\Gamma = 0$. Note that the centre region has been filled in significantly more than the coupled case by freshly ionized plasma. the magnetic field is orientated vertically.

Figure 5.18 shows the total ionization done in the double bomb case for varying Γ (the momentum coupling coefficient). We can see that an increase in momentum coupling has a corresponding decrease in total ionization. This trend continues until the ionization reaches a floor at $\Gamma = 0.01$ and the total ionization done of $\tilde{2}$. The total ionization done never reduces to 0, perhaps surprisingly. This limit is due to the numerical solution having a finite sized mesh ratio, if the mesh ratio was made arbitrarily small then the total ionization would continue to be reduced as Γ was increased tending to 0 at $\Gamma = 0.5$.

This behaviour is simply due to our finite time resolution meaning that we only equilibrate the two species velocity fields every timestep (or half timestep to be precise) this means that between timesteps there is a chance for more relative velocity to build

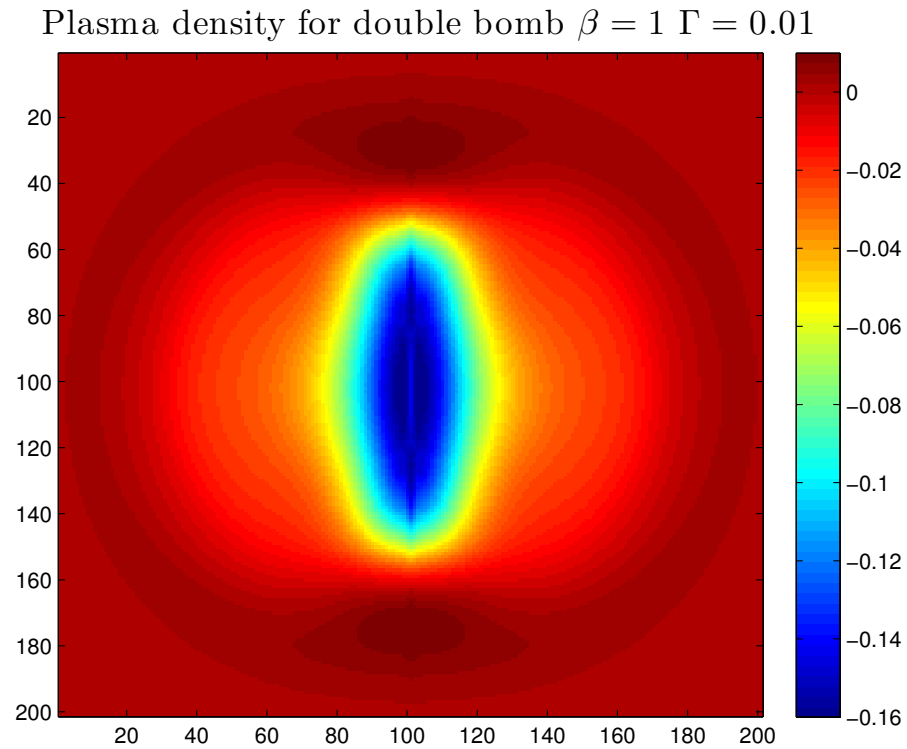


Figure 5.20: Plasma density at $t=30$ with $\Gamma = 0.01$. Momentum coupling has reduced the ability for the plasma to be re-ionized by Alfvén ionization which means a lower minimum in the centre of the domain. the magnetic field is once again orientated vertically.

up, due to the governing equations for the two species being different, before either species can communicate to the other that they are moving.

What is noticeable is that the falloff in ionization caused by the momentum coupling increases rapidly as we increase Γ . We actually attribute this to the low value of f (being 0.01). Since each turn both f and Γ reduce the velocity by an amount proportional to their values then the ratio of Γ to f effectively tells us what fraction of relative velocity is ‘wasted’ and doesn’t effect ionization rates. The exact fraction of velocity that is used to ionize is not as simple as the ratio of these two numbers because ionization only increases for relative velocities about the critical velocity whereas the momentum coupling increases no matter as long as the relative velocity is 0. That

means that the ratio of relative velocity used for AI and relative velocity used for momentum coupling is always at most the ratio of f/Γ but is most likely significantly lower. This maximum AI limit is reached when the relative velocity is very large compared to the critical velocity; when dealing with velocities only slightly above the critical velocity then the vast majority of relative velocity is used for AI.

By the time Γ is 5 times higher than f then the majority of relative velocity is wasted in adjusting the fluid velocities and not for ionizing the gas.

We next look at two colour-maps of plasma density, one for $\Gamma = 0$ (fig. 5.20) and one for $\Gamma = 0.01$ (fig. 5.19). Both of these snapshots show $t=30$ in their respective simulations. There are some similarities between these figures in that the perturbation on the plasma density remains large for some portion of the plasma. It is hard for the plasma to diffuse into the hole created by the recombination quickly, especially since cross field motion is inhibited. This is partly compounded by the slightly slower (20%) speed of sound in the low density regions.

These figures also show distinct differences in the two cases. In figure 5.20 we see that the AI mechanism has partly filled in the centre of the domain. There is a much higher density in this area than in the coupled case. This is the region where the majority of ionization takes place, with coupling on and ionization drastically reduced then the ability of AI to fill in the hole in the plasma is also reduced.

We can see clearly in figure 5.19 that the regions that have remained at low plasma density are *above* or *below* the original disturbance. This is because the fluids in this region have mostly moved parallel to the field (vertically) meaning relative velocity must also be mostly parallel. The ability for the AI mechanism to ionize in this direction is low.

5.3 Astrophysical Contexts

Critical velocity ionization (or Alfvén ionization) has been mostly discussed without context. Although we can place real numbers on the critical velocity as well as on the criteria that we determined in section 1.5.2.2 (on number density and magnetic field

strength) our simulation results have been dimensionless.

We shall now explore two astrophysical contexts where our criteria are met and we may expect that AI plays a role in both changing the local and global ionization fraction.

5.3.1 Brown Dwarfs

Brown dwarfs are sub-stellar objects that are not massive enough to attain high enough core pressure and temperature for hydrogen fusion. They are the natural midpoint between gas giants and stars although the exact cut off between high mass gas giants and low mass brown dwarfs is not clear. Brown dwarfs have very low surface temperatures $\approx < 2500\text{K}$ and as a result only glow dimly in the visible spectra though they can still remain luminous in infra-red. ([Carroll & Ostlie 2007](#))

In the case of brown dwarfs not only is the atmosphere only partially ionized but the low temperature and pressure gives access to complex chemistry including the condensation of molecules into dust particles (e.g. [Allard et al. \(2001\)](#) & [Stephens et al. \(2009\)](#)).

As a motivation for an Alfvén ionizing description of plasma we examine a problem that exists in the literature for brown dwarfs. This problem is described well and attempts are made to explain this problem in a series of papers by Helling and colleagues ([Helling et al. \(2011a\)](#); [Helling et al. \(2011b\)](#); [Helling et al. \(2013\)](#); [Rimmer & Helling \(2013\)](#) & [Stark et al. \(2013\)](#)). We shall provide a very brief overview of some of the most relevant ideas as motivation for our interactions codes.

There exist observations of emission from brown dwarfs at energies that cannot be explained. Brown dwarfs of a large variety of spectral types (down to about M7 ([Berger et al. 2010](#))) have been observed emitting X-ray and radio waves as a low-level background. On top of that, sporadic, high-intensity X-ray emissions are seen even for very cool dwarfs.

Spontaneous X-ray emission from our Sun and other stars is usually explained by the emergence of magnetic flux from the interior that becomes tangled, thus storing

magnetic potential energy. This field reconnects, releasing this stored energy in the form of a solar flare. (Heyvaerts et al. (1977) & Aschwanden (2002)) This process creates a non-thermal electron distribution that then generates high energy photons.

The key feature of the Sun's atmosphere is that the magnetic field and the convective atmosphere are sufficiently coupled that the magnetic field is advected along with the partially ionized plasma flows. This allows the convective motion of the gas in the star to be able to tangle and twist the magnetic fields in such a way that they can store this energy.

The ratio of magnetic advection to diffusion in MHD is known as the magnetic Reynolds number and is given by

$$R_m = \frac{vL}{\eta} = \frac{vLn_e e^2}{m_e \nu_c}. \quad (5.6)$$

v is the typical flow velocity, L the typical feature size, (η) is the resistivity and ν_c is the collision frequency, all the other symbols have their usual meanings.

If the Reynolds number is $\ll 1$ then diffusion dominates, we can clearly see from equation 5.6 that this happens when the feature sizes are small or the electron density is low. (Helling et al. 2011a) uses atmospheric modelling codes to show that the Reynolds number for a typical Brown dwarf is too low for the magnetic field to be advected. As such there can be no tangling of magnetic field lines, no stellar flares and no X-ray emission. In fact the magnetic Reynolds number is more than 15 orders of magnitude too low in some cases.

The observations tell us there must be a mistake in this calculation of the Reynolds number. The most obvious variable that could be wrong is the electron number density. If we have grossly underestimated the electron number density by neglecting an ionization mechanism that causes a deviation from thermal equilibrium (see section 1.3) then we need to increase our theoretical plasma density and the magnetic advection improves.

Essentially there must exist a source of non-thermal energetic electrons, or perhaps photons, that contribute to the ionization balance in the atmosphere of these cool stars.

The series of papers by Helling and colleagues go into some potential mechanisms e.g. due to dust, cosmic rays, lightning, and Alfvén ionization.

In the case of Alfvén ionization in, [Stark et al. \(2013\)](#) they conclude that not only do the atmospheres of the brown dwarfs meet the prerequisites for AI (see [1.5.2.2](#)) but that the potential for AI to modify the electron density is huge. However, there does remain some uncertainty in the exact translation from plasma conditions to electron energy distributions to ionization rates (see some discussion in [1.5.2](#) and [7](#)).

This presents an opportunity for a fluid AI model to simulate the conditions of brown dwarf atmospheres.

5.3.2 Solar Atmosphere

One of the major motivations for the development of our fluid Alfvén ionization model is a problem known as the first ionization potential (FIP) effect/bias in the upper solar atmosphere. The effect is characterized as an anomalously high proportion of certain elements in the solar wind, corona and chromosphere with respect to the abundances of the same elements in the photosphere. This has been a puzzle for many years as the plasma that makes up these upper solar atmospheric layers must originate from the photosphere. There must exist a process that is preferentially selecting certain elements in the photosphere for transfer upwards. There have been many recent efforts to study observationally this FIP effect as well as theoretical work attempting to explain its origin but it remains clear that there is still at least one part, perhaps a large part, of the puzzle missing. ([Laming 2012](#)), ([Feldman & Widing 2007](#)), ([Feldman & Laming 2000](#)) and ([Schmelz et al. 2012](#)).

A numerical value can be placed on the degree of FIP bias of any given element is given by the ratio of the observed abundance in any of the upper parts of the solar atmosphere to the model values of the relative abundances in the photosphere. This value can vary depending on the particular location studied as well as evolve over time.

FIP bias gets its name from the fact that, in general, the elements with the highest disparity in abundances are those with a low first ionization potential while elements

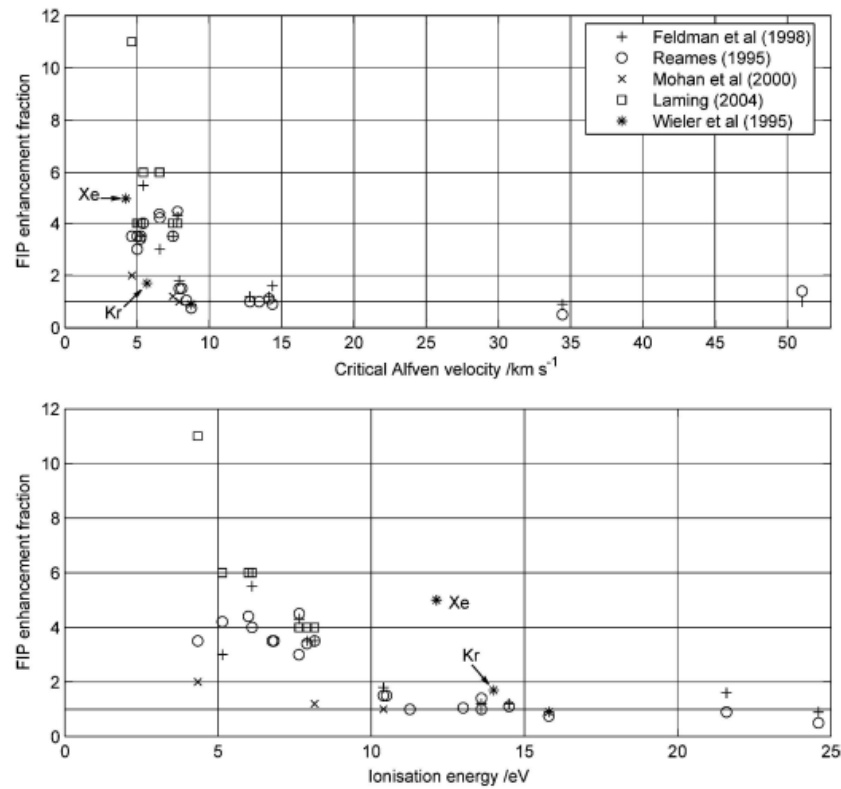


Figure 5.21: FIP bias, defined as the ratio of observed elemental abundance to the photospheric abundance, of select elements in the corona relative to their abundance in the photosphere from [Diver et al. \(2006\)](#). Reordering the elements with respect to the CIV instead of their FIP removes some of the anomalous abundances, e.g. Xenon and Krypton.

with high ionization potentials remain close to their photospheric abundances. There are however some outlying data where elements with a high first ionization potential are also enhanced in the corona. Figure 5.21, taken from [Diver et al. \(2005\)](#), shows the FIP bias of selected elements against first their ionization energy and then their critical ionization velocity, which was calculated using equation 1.89. The systematic trend in terms of critical velocity motivation to investigate the possible role of Alfvén ionization in adjusting the elemental abundance of the upper solar atmospheres.

For AI to be involved in the ionization of these elements, we require neutral flows of velocities greater than the CIV of these elements; for mixed species flows the picture is

more complex but the single species critical velocity from equation 1.89 is the simplest model. This means, to see enhancement of those elements given in figure 5.21 flows at speeds of 5kms^{-1} perhaps even reaching speeds of up to 15kms^{-1} , which is far above the photospheric sound speed of 7kms^{-1} , are required for some elements with high CIV. Flows of this magnitude are indeed present in the solar photosphere both in simulation such as Stein & Nordlund (1998), showing highly supersonic flows in granular simulations, and in observation with Utz et al. (2010) showing ubiquitous flows in the 5kms^{-1} range and Bellot Rubio (2009) showing supersonic flows. As higher resolution data become more and more readily available then we can only expect these speeds to become higher and more common.

The other thing Alfvén ionization requires is perpendicular magnetic fields - which for horizontal surface flows would include both vertical and in the plane of the surface fields. Vertical fields are everywhere on the sun with large portions of the surface being covered by sunspots, magnetic bright points and other, small scale vertical magnetic structures. Based on our criteria for AI in section 1.5.2.2 the magnetic field in the Sun is easily sufficient. Indeed, FIP bias is seen more clearly at regions of high magnetic field. Figure 5.22 from Feldman & Widing (2002) shows that the average FIP bias is larger in regions surrounding magnetic structure. Perhaps even more interesting is the observation of FIP bias increasing over time after the emergence of a sunspot given in 5.22b from the same paper. This points to some ongoing process at magnetic structures that enhances low FIP (or low CIV) elements over time.

More observation of this type of time series, where the FIP effect is seen to develop in real time, could shed important insight onto the involved mechanisms.

We have really two separate aspects of the same problem. First, what is ionizing these elements? Second, why are some elements preferentially selected? It is unlikely that the AI is implicated in the second question. Electrons generated by the AI mechanism (see 1.5.2) have no bias. A charge pocket can be created with a maximum potential up to the kinetic energy of the most massive gas particle in a flow and it can accelerate electrons to that energy. Once electrons have reached that energy, their ability to ionize any species which they collide with is purely predicated on the

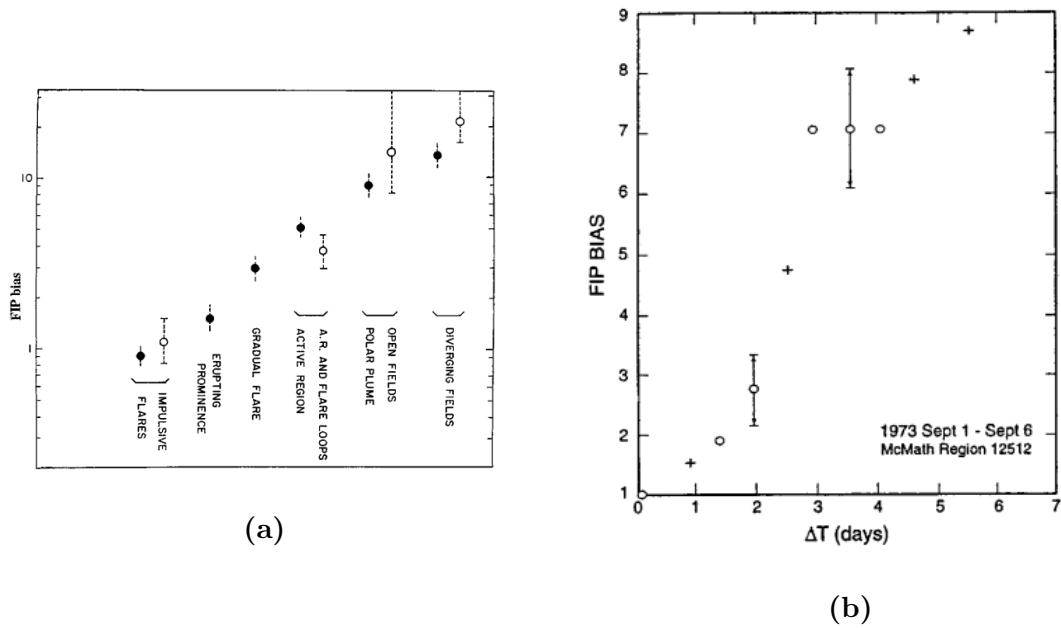


Figure 5.22: (a) The average observed FIP bias of various locations on the solar surface; regions with magnetic structures are seen to be more FIP enhanced than those without (b) The observed FIP bias of a single sunspot after emerging shows an increase in FIP bias over a number of days. Figures are from [Feldman & Widing \(2002\)](#).

cross-section for ionization of that species and not the value of that species CIV.

We therefore position AI as a contender for the first question. Given the distribution of flows across the photosphere and the presence of the necessary prerequisite fields then it is entirely possible that AI is providing a significant deviation from a thermal electron distribution function at the ionization energy of difficult to ionize species. This would result in anomalous ionization fractions of certain elements, selected by their FIP.

In order to examine the possible role of AI in the observations previously mentioned, a stronger understanding of how flows and magnetic fields interact, how AI would work given the parameters of the solar surface and how the flows of mixed species affects AI, is needed. The gas-magnetohydrodynamics interactions code (GMIC) is a step towards a more complete understanding of partially ionized plasmas such as those in

both brown dwarfs and the Sun.

5.3.3 Epoch of Recombination

In section 5.2.2 we explore the scenario where a partially ionized plasma has locally undergone recombination. We show the flows in such a scenario can induce significant Alfvén ionization.

This has the possible application to any cooling, perhaps by radiating, partially ionized plasma such that it is on the brink of recombining. We are in particular interested in the epoch of recombination, the time when the CMBR was emitted. We theorise that AI will give any such a plasma a resistance to recombination. However, we note by simulation and by thought experiment that AI will be unable to completely prevent recombination, even if it can reverse it somewhat.

5.4 Conclusions

In this chapter we have presented simulation results showing the effect that adding an Alfvén ionizing mechanism to a MHD-gas interactions code can have on both the local and global ionization fraction and the plasma dynamics.

The addition of this term allows the kinetic energy of the fluid motion to be extracted in order to ionize some gas, turning it into plasma. The magnitude of this effect is dependent on reaching a critical ionization velocity (1.89) in the direction perpendicular to the background magnetic field. The amount of excess energy above this threshold dictates the rate of ionization. We can think of the AI mechanism as an extension of the momentum coupling term taken to an extreme level.

Simulations were first carried out in a linear limit with GMMC (described in chapter 2) which has an AI term bolted on to a code designed for momentum coupling. In these linear cases we are limited to only small amplitude waves which restricted to small amplitude changes to a plasma with an ionization fraction of 0.5.

GMIC is the non-linear gas-magnetohydrodynamic interactions code, designed with

the interactions between the gas and plasma fluids in mind from the start. It allows large amplitude waves and large changes in ionization fraction which the motivating astrophysics, from e.g. brown dwarf atmospheric models, necessitates.

Both GMMC and GMIC agree on the qualitative effects of Alfvén ionization. By removing the kinetic energy from the flow we influence the plasma dynamics. The AI term is an amplitude, direction and frequency dependent damping term for wave motion as well as an additional drag term that works, along with standard momentum coupling, although drag from AI is only present when the velocity exceeds the CIV and only ever present in the perpendicular to magnetic field direction.

Further, the creation of plasma is shown to cause new gradients in partial pressure that drive flows and waves in one or both of the species. In an ideal experiment we recognize the diagnostic potential here; the creation of this new wave motion from freshly ionized plasma and the damping of existent wave motion as a result of Alfvén ionization means that there is potential for working backwards to detect ionization.

To determine the amount of ionization that is caused by a given set of plasma parameters we use the scalar factor f . A discussion of the meaning of f is enlightening. Just like Γ in momentum coupling it hides within it some details on the physics, details which are not necessarily explicit. A choice of f dictates much of the physics, within it is encoded information on the nature of the relative time-scales. While the collisional time-scale is always much shorter than that of the fluids; a high f means that the time taken to establish charge pockets from ion-neutral collisions, accelerate electrons and have ionizing electron-neutral collisions is very small compared to the fluid timestep. Essentially, much ionization takes place before the fluid can react. Conversely, a low f means that the ionization happens more gradually with time for the fluid to react quickly. The only step for this process that is adequately resolved is the acceleration of electrons in charge pockets in a magnetized plasma (MacLachlan et al. 2009).

In the experimental results of Fahleson (1961) we can presume f is very high, almost unity. This is because their experiment is physically unable to drive velocities more than a few percent above v_c . This must mean that any kinetic energy from the velocity above v_c is quickly changed into internal energy of the plasma via ionization. In fact,

it may very well be the case that the measured v_c of this sort of experiment being slightly higher than the theoretical v_c could be a manifestation of the deviation of f from unity.

This is a necessary weakness in our fluid approximation of AI.

Presumably, there is a choice of f that can correctly act as a proxy for these processes, even if that f is no longer scalar. It does not take a large leap of imagination to picture f as a function of many variables such as v_{rel} , T_e , $\rho_{p,g}$. Essentially all the variables that should effect the microscopic physics of AI may also effect our macroscopic proxy for AI.

To put this another way, if $f = a$ then it will take $O(1/a)$ fluid timesteps to extract all the excess relative velocity from a flow, in this time material moving at the sound speed will have crossed $(1/a)p$ fluid lengths, where p is the mesh ratio. Since, as we saw in chapter 1 that the AI mechanism is inherently related to the sizes of several plasma parameters (the collisional mean free path, ion Larmor radius and Debye length) then the value of f dictates the plasma regime that we are operating in.

As discussed in chapter 2, the ionization efficiency factor is dictated by the product of several terms. Namely: the number of charge imbalance events per unit fluid time (which, due to the time-scales involved is $\gg 1$), the number of electrons in a typical AI charge imbalance pocket ($\ll n_e$), the fraction of these electrons that can reach the potential of the pocket (based on PIC code such as [MacLachlan et al. \(2009\)](#) to be $\sim 10^{-3}$) and the fraction of those electrons that eventually undergo ionizing collisions (~ 1).

Our choice of f is motivated in two ways, first the first order guesses of those 4 separate terms gives a value of f that will approximately be equal to the 3rd term, the fraction of electrons that reach ionization energies (10^{-3}). In addition, our choice of f is also motivated by a desire to gain insight into the effect of AI on a partially ionized plasma's dynamics. In that sense we have generally chosen f to have a *middling* value of $10^{-2} < f < 10^{-3}$. This means we can simultaneously see the effect of the fluid dynamics on the Alfvén ionization rate and the Alfvén ionization's effects on the fluid dynamics. An extreme (either low or high) choice for f disguises either one or other of

these influences.

In both codes we show the ability for momentum coupling to reduce the effectiveness of the AI term. In particular we discuss that the relative magnitudes of f and Γ dictates how much AI is inhibited by the coupling of the fluids. Since AI and momentum coupling are both driven by the collision rate between neutrals and ions then they may be expected to be similar in value. However, AI also depends on several other physical mechanisms that are much more tricky to put rates on. It may be reasonable to expect that f will always be lower than Γ .

A brief discussion on some astrophysical contexts shows the possible application of a code that can simulate AI in a fluid limit. In particular we emphasise the validity and extensive use of fluid codes already in these partially ionized contexts.

We also note that the framework exists for further mechanisms that are unique to partially ionized plasmas to be incorporated. Photoionization from prescribed radiation fields and evolving thermal equilibrium based on fluid parameters would be natural additions.

The question of the FIP effect and its cause leads us to consider an alternate mechanism that can differentiate different atomic species without invoking ionization. That is the polarization of such atoms in the presence of an electric field gradient giving a stratifying effect; this force is known as the dielectrophoretic force. The following chapter discusses such a force, its magnitude in the the magnetic dynamic photosphere as well as some study into the possible consequences of the presence such a force in a magnetised atmosphere-in-motion.

While this next chapter does deviate a little from the finite difference simulation of MHD-gas interactions, which the previous 5 chapters have dealt with, we shall tie it together by the fact that it is an effect on a plasma due to the presence of neutrals, a unique dynamic that is only relevant for gas particles but, through the coupling of the mixed fluids, we may expect to see manifested in a partially ionized plasma.

Chapter 6

Dielectrophoresis in Astrophysical Plasmas

The unresolved issue of FIP bias in the upper solar atmosphere poses an interesting physics question. It is easy to look at the correlation between first ionization potential and observed abundances and see a causal link, even if an explanation for such a link does not exist. The bias originates low down in the solar atmosphere, with observed anomalous abundances in the low chromosphere, and extends all the way out to the highest extent of the atmosphere, in the solar wind. What is clear is that there is a mechanism that preferentially selects certain species over others in order to populate upper atmospheres. The easiest solution to this is a selective mechanism based on ionization; the FIP enhanced elements are those that are ionized and the non-FIP elements are those that are not. The evaporation of these elements into the upper atmosphere is then just selecting for charge, operating only on positive ions and not on neutral atoms.

The question can then be about the ionization mechanism. As discussed in chapter 5, the perpendicular magnetic field and horizontal flows present in the Sun, both in magnetic bright points (e.g [Golub et al. \(1977\)](#); [Keys et al. \(2011\)](#) & [Chitta et al. \(2012\)](#)) and sunspots (e.g [Lites & Skumanich \(1990\)](#) & [Beckers \(1968\)](#)), mean this could be critical velocity ionization but it does not have to be.

As an alternative proposal we remember that the photosphere is a partially ionized plasma and in fact, despite exhibiting a full range of plasma behaviour, is cool enough to remain mostly neutral. The idea that a mechanism that can differentiate between various neutral species could lead to the atmosphere becoming stratified and causing the observed FIP bias is the motivation for this chapter.

6.1 DEP-FFF

Dielectrophoresis is a phenomenon where a polarizable particle experiences a force when a non-uniform electric field is applied. The strength of the field depends on the electrical properties of the particle as well as on the properties of the applied electric field. (Pethig 2010) This force is the electric analogue of magnetophoresis, the force that results in iron filings collecting at magnetic poles. (Gascoyne & Vykoukal 2002) It is also comparable to electrophoresis except that electrophoresis requires the presence of surface charge whereas dielectrophoresis can act on purely neutral particles. (Revercomb & Mason 1975)

Dielectrophoretic field flow fractionation (DEP-FFF) is a technique used to separate different particles (cells) in biology contexts as well as manipulating nano-particles and micro-particles such as carbon nano-tubes (e.g. Wang et al. (2000); Wang et al. (1998) & Peng et al. (2006)). In these experiments the dependence on the polarization of the particles allows specific species to be selected.

To understand how it works we present the following scenario: A atom or molecule encounters an electric field and becomes polarized. This polarized particle aligns itself with the electric field. In a uniform electric field then there is no net force as the forces on each pole of the particle cancel out. However, in a non-uniform field, the force on the pole that is orientated towards the stronger side of the field is greater than the force that acts upon the pole orientated towards the weak field side. The result is a net force acting on the particle that induces a motion. The polarizability of the particle dictates the strength of the force.

Now, as we discussed in chapter 1, plasmas do not maintain electric fields along

distances larger than the Debye length. Indeed one of the defining characteristics of a plasma is its ability to shield out charge imbalance such that electric fields are transient and small scale. As such we would not expect electric fields that are necessary for DEP to exist inside a plasma and therefore, they should not play a role in the solar atmospheres which at all heights remains a plasma.

If there is an electric field though then the DEP force can preferentially act on some species over others. We consider two sources of electric field that are present in even a plasma with a high plasma number. The first is a Lorentz E field; if magnetic fields are abundant in the plasma then a frame of reference that is in motion to these magnetic fields will experience an electric field. This manifests itself in the Lorentz force as the $v \times B$ term.

Theoretically then we know that a particle that is moving through a magnetized plasma can become polarized and that this polarization will result in a DEP force. If the DEP force varies significantly between the species present in our plasma then we might imagine the mechanism has some ability to separate the various species. If the DEP force is large enough this effect may have a significant influence on the bulk plasma, causing it to become stratified. We would expect that, in a turbulent, convective, hot atmosphere with constant mixing, such as in the Sun, that the DEP force would not be significant enough to effect the composition.

The second source of E-field comes as a result of the difference in mass between electrons and ions which results in the ambi-polar diffusion of an electron-ion plasma.

In the remainder of this chapter we will satisfy this curiosity: first we examine what the exact force applied by DEP is; examine the variation of this force across select atomic species paying close attention to those that have significant solar abundance; carry out some simple calculations for the magnitude of this force due to the Lorentz electric field and the ambi-polar electric field of a typical solar magnetic feature; and examine some simple $0d$ and $1d$ models of DEP in the solar atmosphere. While we expect the DEP force to be small, we do not wish to underestimate the ability of a persistent force at affecting change over long time periods.

6.2 Theory

We shall consider the displacement that is caused by a dielectrophoretic force acting on a polar particle, i.e. atom or molecule and not ion. If this displacement is significant compared to the typical scale lengths of the system then the DEP force is capable of separating polar particles from each other based on the degree of their polarization. We consider a polarized (or polarizable) particle passing through a magnetic field gradient at speed v , which in it's frame of reference causes an electric field gradient. The field varies smoothly over a length scale, L .

The force exerted on a dipole by an electric field gradient is given by the scalar product between the polarization and the field gradient. (Griffiths & College 1999)

$$F_{DEP} = (\mathbf{p} \cdot \nabla) \mathbf{E}. \quad (6.1)$$

The polarization can consist of a permanent dipole moment, an induced dipole moment or a combination of the two.

$$\mathbf{p} = \mathbf{p}_{permanent} + \mathbf{p}_{induced}. \quad (6.2)$$

The permanent dipole moment is a constant that depends on the particle being considered. The induced polarization is the product of the polarizability, α , and the electric field.

$$\mathbf{p}_{induced} = \alpha \mathbf{E} \quad (6.3)$$

An approximation to the gradient is found by considering that the field varies from 0 to its maximum value, E , over the length of the feature, L . The force acting on a dipole is given by,

$$\mathbf{F}_{DEP} = \mathbf{p} \frac{E}{L} \quad (6.4)$$

This results in an acceleration of,

$$\mathbf{a}_{DEP} = \frac{\mathbf{p} E}{m L}, \quad (6.5)$$

where m is the mass of the particle. The total displacement of a particle that experiences this force compared to a particle that experience no forces is given by the classical kinematic expression:

$$\delta = \frac{1}{2} a_{DEP} t^2 \quad (6.6)$$

$$\delta = \frac{1}{2} a_{DEP} \frac{L^2}{v^2}. \quad (6.7)$$

Given that in the fluid limit of a plasma there is no electric field. This means that the only source of electric field is from the Lorentz transform of the magnetic field such that $|E| = |\mathbf{v} \times \mathbf{B}|$. Assuming that v is entirely in the perpendicular to field direction.

$$\delta = \frac{1}{2} \frac{p}{m} \frac{v B L^2}{v^2}. \quad (6.8)$$

$$\delta = \frac{1}{2} \left[\frac{\mathbf{p}}{m} \right] \left[\frac{BL}{v} \right]. \quad (6.9)$$

This displacement is in the $\mathbf{v} \times \mathbf{B}$ direction. We have deliberately split the expression into two parts. The first is the polarization to mass ratio. This term is dependent on the properties of the particle. The second term depends on the situation the particle finds itself in, it is the same for all particles but will change depending on the circumstances; for example, a higher magnetic field will increase this term.

This expression is mostly intuitive perhaps with the exception of the $1/v$ dependence. This is due to the total displacement having a square dependence on t , the time that the particle experiences the magnetic feature, but the electric field only has a linear relationship with v .

If we are to consider a particle that only has an induced contribution to its dipole moment then we can make a further substitution from equation 6.3.

$$\delta = \frac{1}{2} \frac{\alpha v B}{m} \frac{v B L^2}{L v^2}. \quad (6.10)$$

$$\delta = \left[\frac{1}{2} \frac{\alpha}{m} \right] [B^2 L] \quad (6.11)$$

In this case we have replaced the p/m with a α/m ratio and recovered the stronger B^2 dependence on magnetic field. The displacement also no longer depends on the velocity of the particles, instead it only depends on the size of the magnetic feature. In both the induced and permanent dipole cases it is obvious that higher field values and larger magnetic features produce a bigger displacement and thus will be more able to stratify the various species in the flow.

6.2.1 p/m Ratio of Select Elements

The first term in equation 6.8 is the polarization to mass ratio or p/m ratio. This term is species dependent so the range of values this term can have also tells us by how much the DEP force can vary between species.

In the case of a hot atmosphere, like a star, molecules are generally not a significant fraction of the total abundances, atoms make up the majority of the species present. In this case induced dipole moments are more important than permanent dipoles as atoms do not (usually) have permanent dipole moments (Sandars 1965). Since we are only interested in this induced dipole moment we shall talk about the p/m ratio as being the ratio of induced dipole moment to mass.

Larger atoms and molecules naturally have larger polarizability as the electrons can be rearranged across a bigger distance. However, larger atoms are also heavier so both p and m generally increase as we increase the atomic number.

Figure 6.1 shows the polarizability varying with mass for selected elements. The y-axis of polarizability is given in the units of Debyes per unit electric field ($\text{D} (\text{Vm}^{-1})^{-1}$) where a Debye is the cgs unit for dipole moment.

This figure shows an interesting pattern with large spikes - at $m = 7, 23$ and 39 - in polarizability followed by a gradual decrease before the next spike. These spikes

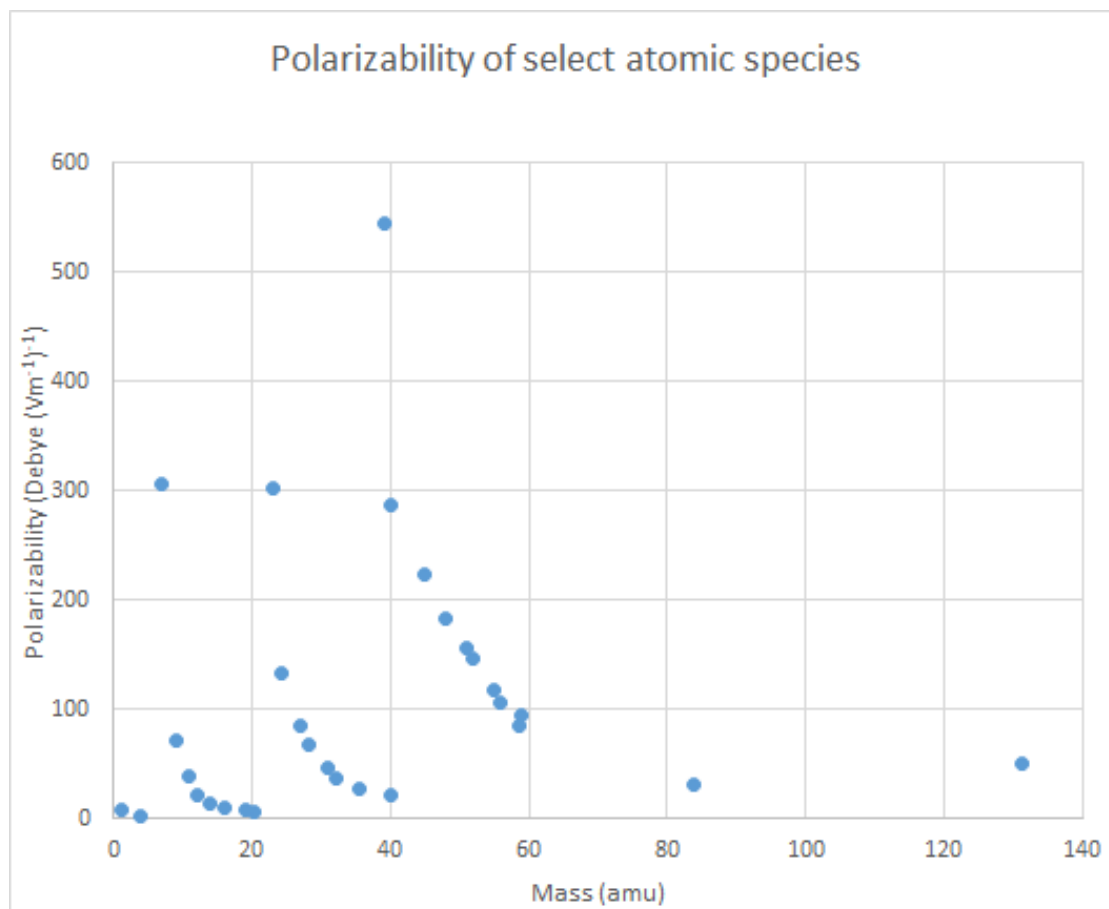


Figure 6.1: Polarizability against mass for our selected elements. The general trend shows an increase in polarizability as you increase in atomic mass. However this trend is dominated by a periodic cycle.

correspond to elements in the first column of the periodic table (the alkali metals), lithium, sodium and potassium respectively. This is due to them having a single electron in a fresh electron shell. The new electron shell has a larger radius than the row above and as such the electron in it can be moved by larger distances more easily than the previous shells and therefore achieve larger polarizations.

The general trend of lower polarizability as you move across the periodic table after these spikes is due to the increased charge of the nucleus meaning that the outer shell electrons need a greater field applied to get the same motion. The lowest polarizability of the row occurs with the noble gasses and their full electron shells.

Underlying this repeating pattern is a general trend upwards with the more massive atoms having higher polarizability.

This pattern of polarizability is the same as that for atomic radius. Atomic radius spikes in the first column of the periodic table and falls off as you move towards the noble gasses as well as having the increasing trend as you move down a periodic group.

Atoms with a high value of polarizability will have a larger DEP force, however we are concerned with the effect of the force so we instead look at the p/m ratio which will give the acceleration instead of the force. This is shown in figure 6.2.

The same cyclic pattern where p/m ratio changes dramatically across the periodic table but we can clearly see that there is only a small trend down a column of the periodic table i.e. elements in the same periodic group have approximately the same p/m ratio.

What is clear from these data is that by far the biggest influence on the p/m ratio and thus on the magnitude of the acceleration caused by the DEP force is the atoms periodic group. The difference between a group 1 element and a group 8 element, like lithium and helium, is always far far more significant than between a light group 8 element and a heavy group 8 element, like helium and xenon.

These data are obtained from the *CRC Handbook of Chemistry and Physics* (Lide 2008) and are presented in table 6.1. Also included are the first ionization potential, Φ_I . It is notable that the general trend is that low p/m elements have high FIP and high p/m elements have low FIP. This is unsurprising since the same qualities that make an electron easy to move around (polarize) with an electric field also make that electron easy to completely remove from the atom.

The chosen elements are those which have a significant solar abundance especially those for which FIP bias data is available. (Diver et al. (2005) & Asplund et al. (2005))

Table 6.2 shows the same data for some example simple molecules. These molecules are ones which exist in the solar photosphere and have easily obtainable polarizability data. (Asplund et al. (2009) & Pande et al. (1969)) These data are once again taken from Lide (2008).

In the case of the molecules we have sometimes calculated two ratios. One is the

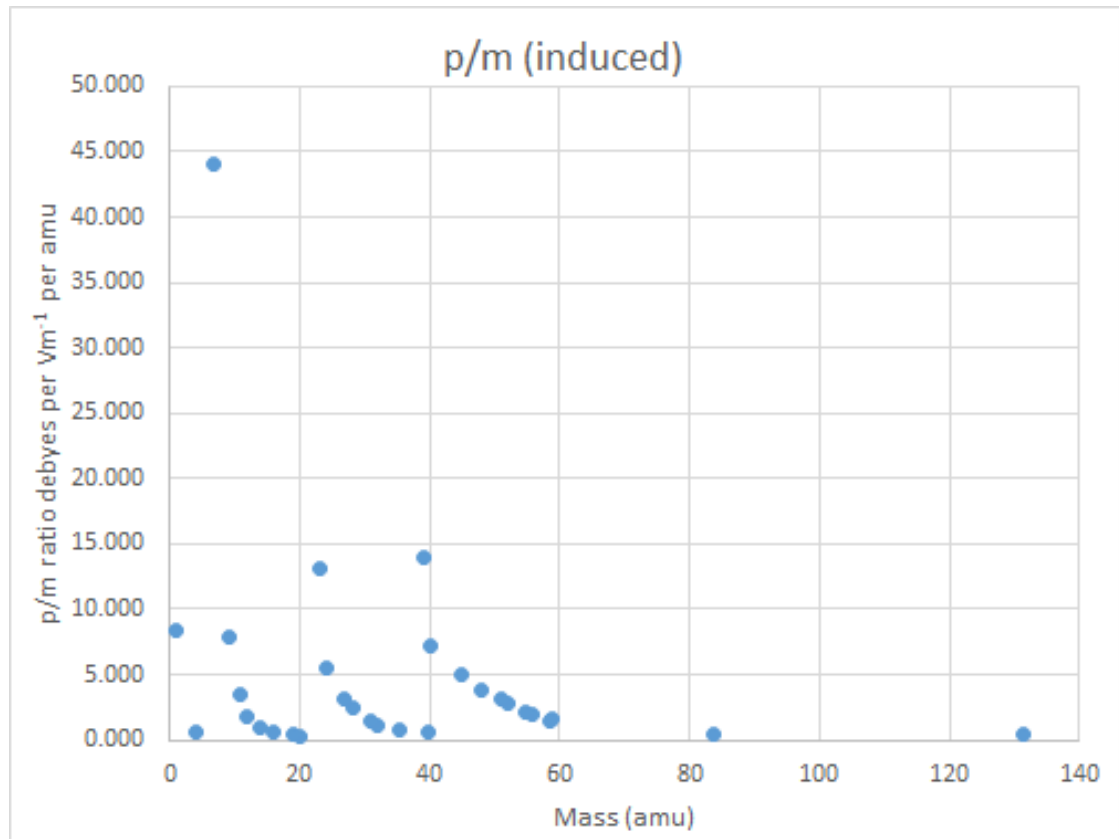


Figure 6.2: Re-plotting polarizability as p/m ratio against mass shows a similar cyclic trend. Elements to the left of the periodic table have consistently higher p/m ratios and there is a small increase in p/m ratio as we increase in mass for the same periodic group.

α/m (induced) ratio which is the same as the atomic case in the same Debyes per unit electric field divided by the mass in amu. The other ratio is the permanent p/m ratio obtained by the dipole moment in Debyes divided by the mass in amu. This is because molecules, unlike most atoms, can have permanent polarization due to the differences in electronegativity between the constituent atoms. This means that they will experience a DEP force even without an electric field to induce a dipole moment. Of course, the DEP force itself still depends on an electric field *gradient*.

We can see from the comparison of the induced p/m and the permanent p/m ratios that an electric field, of around 0.1 Vm^{-1} will result in the induced dipole being of comparable or stronger strength than the permanent dipole. We also notice by

comparing the molecular and atomic data that the induced dipole moments for atoms will be comparable to molecules which are exposed to the same strength electric field and thus similar DEP forces. The p/m ratios are of the same order of magnitude.

Table 6.1: Selected atomic characteristics

Element	α (polarizability) in D per (Vm^{-1})	m (amu)	α/m ratio	Φ_I (eV)
Ne	4.97	20.18	0.25	21.60
F	7.00	19.00	0.37	17.40
Kr	31.23	83.80	0.37	14.00
Xe	50.83	131.30	0.39	12.13
Ar	20.63	39.95	0.52	15.80
O	10.08	16.00	0.63	13.60
He	2.58	4.00	0.64	24.60
Cl	27.40	35.45	0.77	13.00
N	13.83	14.01	0.99	14.50
S	36.45	32.07	1.14	10.40
Ni	85.48	58.69	1.46	7.64
P	45.63	30.97	1.47	10.50
Co	94.28	58.93	1.60	7.88
C	22.12	12.01	1.84	11.26
Fe	105.59	55.85	1.89	7.90
Mn	118.16	54.94	2.15	7.43
Si	67.63	28.09	2.41	8.15
Cr	145.81	52.00	2.80	6.77
V	155.87	50.94	3.06	6.75
Al	85.48	26.98	3.17	5.99
B	38.09	10.81	3.52	8.30
Ti	183.52	47.88	3.83	6.83
Sc	223.75	44.96	4.98	6.56
Mg	133.24	24.30	5.48	7.65
Ca	286.60	40.08	7.15	6.11
Be	70.39	9.01	7.81	9.32
H	8.38	1.01	8.32	13.60
Na	303.06	22.99	13.18	5.14
K	545.54	39.10	13.95	4.34
Li	305.45	6.94	44.01	5.39

Table 6.2: Selected molecular characteristics

Molecule	m (amu)	α/m (induced) D per Vm^{-1} per amu	p/m (permanent) D amu $^{-1}$
H2	2.02	5.00	0.00
AlF	45.98		0.03
BF	29.81		0.02
CO	28.01	0.88	0.00
HBr	80.91	0.56	0.01
HCl	36.46	0.91	0.03
HF	20.01	0.50	0.10
HI	127.91	0.53	0.00
H2O	18.02		0.10
LiH	7.95	6.07	
LiO	22.94		0.28
MgO	40.30		0.15
N2	28.02	0.78	
NaCl	58.44		0.15
NO	30.01		0.01
NS	46.08		0.04
O2	32.00	0.62	

6.2.2 Solar Lorentz Field

Our second term in our simple DEP force calculation depends on the external parameters and is the same for all species. We can carry out a quick, back of the envelope calculation of the value of this term in the case of a magnetic bright point. The aim here is that, along with the above p/m ratio calculations, we can estimate the size of this effect for a flow of plasma that passes through the magnetic field of these features.

Small scale magnetic elements are constantly formed in the photosphere, they can be detected either by high resolution magnetograph (such as HMI on board SDO (Scherrer et al. 2012)) or they can manifest themselves as bright points in G-band images (such as those taken from SOT on board Hinode). (Steiner et al. 2001) These magnetic bright points (MBP) tend to be born inside granules and then move, along with the convective flows, into intergranular lane boundaries. An ever improving range of ground based telescope means an improved maximum resolution, the calculated magnetic fields of these spots gets higher and an improved cadence means faster moving spots can be tracked. These have been the subject of much study recently, for example see Utz et al. (2010); Moestl et al. (2006) & Crockett et al. (2010).

We take a typical MBP field of 1800 Gauss or $B = 0.18\text{T}$ (from Kneer et al. (2006)) and a flow velocity of $v = 1\text{km s}^{-1}$, which we have already discussed as a reasonable solar flow velocity. Utz et al. (2010) found, using the SOT instrument on board Hinode, that the mean diameter of these bright points was 200km although they expect that the actual diameter is lower and that these objects continue to be unresolved for now. Either way we take $L = 200\text{ km}$ as a typical MBP diameter.

We also examine the displacement of the same flow if it were to move through a sunspot with a magnetic field maxima $B = 0.5\text{T}$ and size $L = 10^8\text{m}$.

The electric field gradient from a Lorentz transform for these parameters is

$$\nabla E_{mbp} = 9 \times 10^{-4} \text{V m}^{-2}$$

$$\nabla E_{spot} = 5 \times 10^{-6} \text{V m}^{-2}$$

For the p/m ratio we take two examples of the induced dipole moments from table

6.1. We use equation 6.10 to calculate theoretical displacements caused by the DEP-force. To use our p/m values we use the conversion to SI units of polarization ($\alpha(SI) = 1.1165 \times 10^{-16} \cdot 10^{-24} \alpha cgs$) and mass ($1kg = 1.66 \times 10^{-27} amu$).

Kr

$$\delta_{mbp} = 1.29 \times 10^{-11} \text{m}$$

$$\delta_{spot} = 1.64 \times 10^{-4} \text{m}$$

Na

$$\delta_{mbp} = 4.55 \times 10^{-10} \text{m}$$

$$\delta_{spot} = 5.69 \times 10^{-3} \text{m}$$

These are small displacements, many orders of magnitude below the typical scale lengths of the features of this plasma. The magnitude of this displacement is lower than what we expected. Astrophysical plasmas may contain large absolute values for electric fields which may be expected to result in correspondingly large DEP forces. However, the field gradient not the magnitude of the field is what is important and the scales over which the magnetic field varies are equivalently large. This reduces the DEP force from Lorentz E-fields to an irrelevant strength.

We would require a value of δ of the order of km, i.e. around 10^6 times stronger, to expect the effect to be observable.

6.2.3 Ambi-polar Field

In an electron-ion plasma the electrons have significantly higher thermal velocities due to their lower mass, resulting in them having significantly higher diffusion rates. If the electrons diffuse out of a region of high density quicker than the ions then an electric field will build up between the diffused electrons and the ions they left behind. This electric field will grow until it is strong enough to accelerate the ions and slow down

the escaping electrons enough such that a balance is reached; the number of electrons leaving per unit time is equal to the number of ions leaving.

The maximum electric field produced in this manner depends on the diffusion rates of our two charged species ($D_{i,e}$). (Gurnett & Bhattacharjee 2005)

$$\mathbf{E} = \frac{(D_i - D_e) \nabla n}{\mu_i - \mu_e} \approx -\frac{k_B T \nabla n}{e n} \quad (6.12)$$

If we assume our plasma is at $T = 6000\text{K}$ (typical photospheric temperature) and the ratio of density gradient over density is 10% then this gives a maximum E-field of,

$$\mathbf{E} = 0.05\text{V m}^{-1}.$$

Since the electric field must not span more than a few Debye length the electric field gradient can be approximated as

$$\nabla \mathbf{E} = \frac{\mathbf{E}}{\lambda_D} \quad (6.13)$$

$$= 10^5\text{V m}^{-2}, \quad (6.14)$$

by taking the Debye length of the solar photosphere as $5 \mu\text{m}$. This is a factor of 10^{10} higher than the electric field that is a consequence of the Lorentz field in a MBP. This would mean an equivalent increase of 10^{10} in DEP-force. The scale length of this field is much smaller, spanning no more than a few Debye lengths. This means, despite the factor of 10^{10} improvement in electric field gradient this is more than counteracted by a factor $\sim 10^{-15}$ in the length over which there is a field. Overall, this means a reduction in the displacement when compared to the Lorentz field case.

6.3 Simulations

Despite the low DEP-displacements expected in the Sun from the Lorentz electric field we shall still examine the ability of a strong DEP force to successfully stratify an atmosphere by developing some simple models. Our first model is a simple 0-dimensional

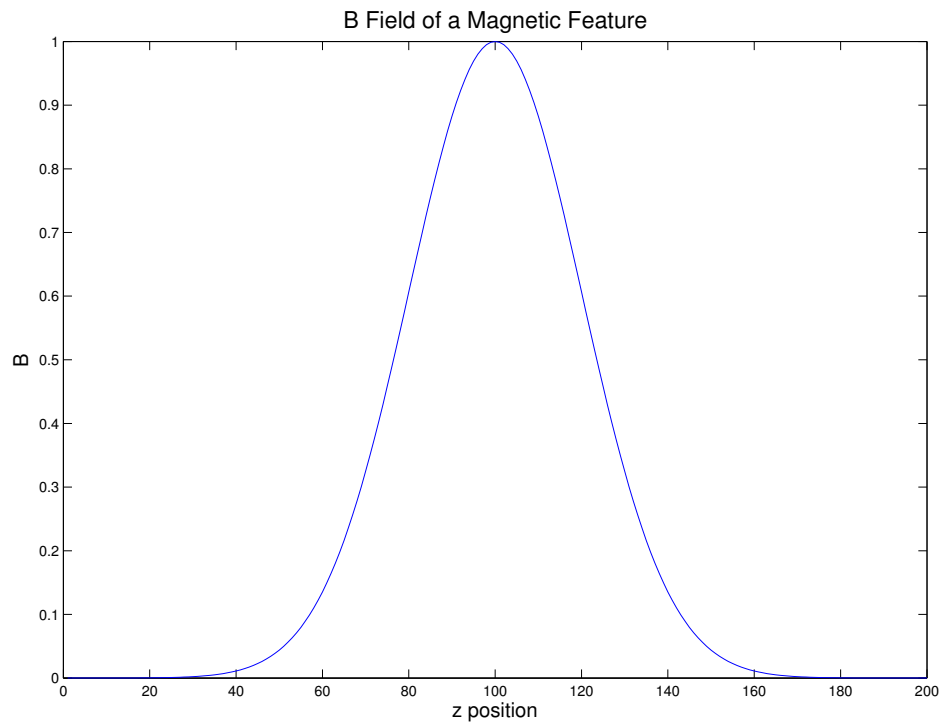


Figure 6.3: Gaussian magnetic field, an approximation of the shape of the field that might be found in a MBP.

model in which we apply a force to a single particle of a few select test species which have the p/m ratio corresponding to some common elements. The magnetic field is expressed as a Gaussian in time representing a Gaussian in the space that a particle is passing through in the frame of reference of the moving particle. The magnetic field is shown in figure 6.3.

We investigate two cases. The first case has the assumption that the particles are in free space and as such are under a continuous acceleration from the DEP force the entire time that they encounter the magnetic feature. This is shown in figure 6.4. We can see that the displacement grows over time and that the separation between the high α/m particles, such as Li, and those of low α/m , such as Ne, also grows over time. This difference in displacement is able to grow without limit.

The second case is more realistic for a fluid, in this case we operate under the

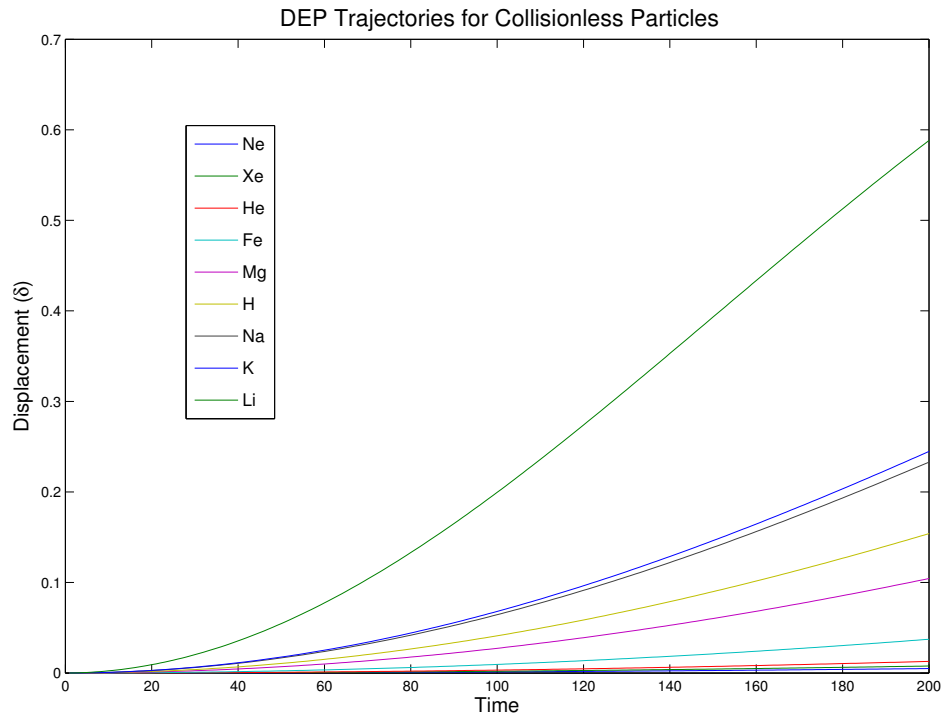


Figure 6.4: The trajectories of free particles of select atomic species experiencing a DEP force. The magnitude of the force and thus the particle's displacement depends on the polarizability to mass ratio of each species.

assumption that our particles are embedded in a fluid flow. This means they are not able to accelerate along free trajectories as the mean free path is sufficiently small that the particles undergo frequent collisions. In this case the DEP particles move with drift velocities that are a balance between the DEP force driving them and a drag term due to collisions preventing the DEP motion. This case is plotted in figure 6.5. We can see that the displacements still grow over time but at a linear rather than exponential rate. We also preserve the y-axis between cases and we can clearly see that the magnitude of this effect is significantly reduced in the fluid case. In this fluid limit we would need not just a DEP force but a divergence in DEP forces to enact a change to the fluid density of our gas.

Unlike before, this case is not able to grow without limit as the partial pressure will eventually cause the now stratified fluid to reach an equilibrium.

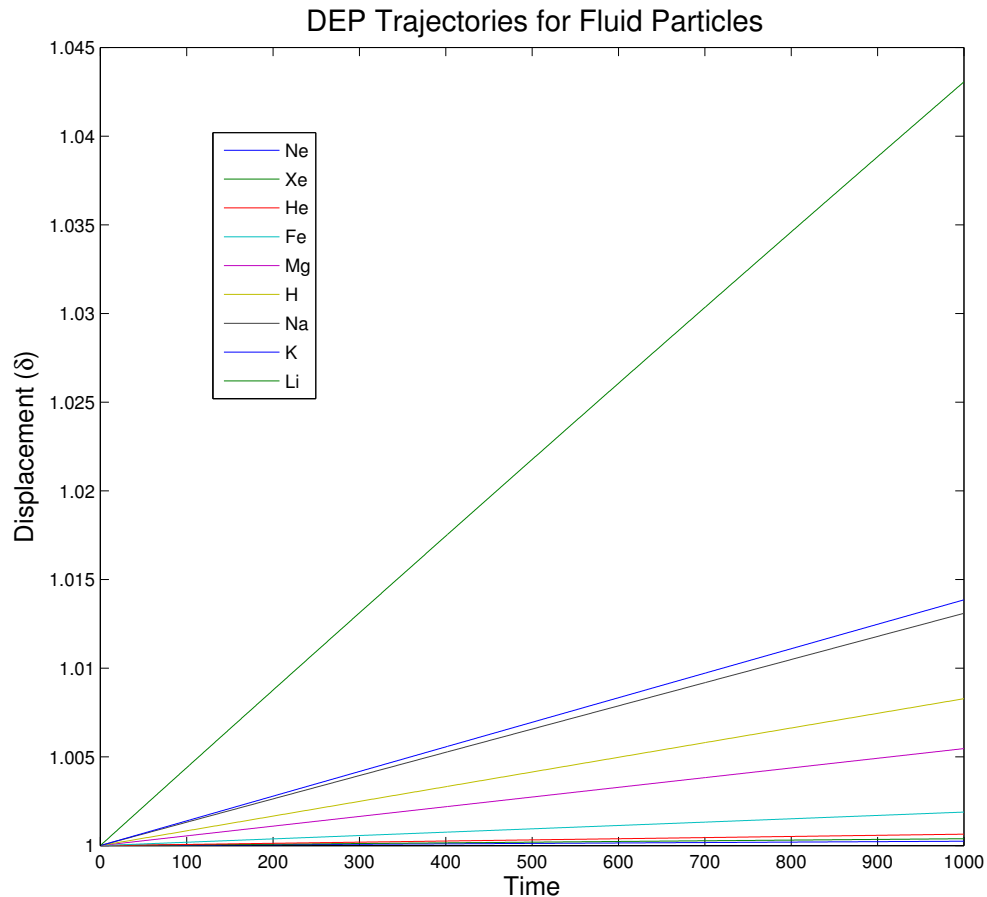


Figure 6.5: The trajectories of fluid elements for select atomic species under a DEP force. The magnitude of the force and thus the particle's displacement depends on the polarizability to mass ratio of each species.

Even when there is clearly a noticeable difference in trajectory between gas species of different p/m or α/m ratios we can not conclude that a gas flow would at all stratify out into bands of each element. To do so requires the DEP effect to overcome any a turbulent or convective mixing motion such as those present in a hot atmosphere like the solar photosphere. The effect would need to be large in order to persist through this mixing.

Having seen how different polarizability to mass ratios affect the particle trajectories, we also wish to see how a single element is influenced by the presence of a magnetic

feature. If we have a flow of a polarized gas species with an initially homogeneous density then we would expect the path that the fluid elements of this flow takes to be important. Parts of the gas that encounter significant magnetic field will experience significant deflection and parts that experience no magnetic field will experience no deflection.

This means that if the flow enters and exits a magnetic feature then the final density will contain some memory of the field structure through which the flow passes.

To examine the details of this we take a 2-dimensional magnetic feature where the magnetic field is Gaussian in both x and y and is pointing entirely in the z direction, out of the plane of the figure. A flow with an initially homogeneous density and a velocity $v = v_x$ enters the magnetic feature. The DEP force is in the $v \times B$ or y -direction. A colour-map of the gas density of this situation is plotted in figure 6.6.

As the fluid moves along the x -direction then it tends to concentrate in central area. To better understand the origin of this behaviour we split the fluid into 3 regions.

The first is the fluid that does not see much magnetic field, this corresponds to areas near $y = 0$ and $y = 200$. In these areas the magnetic field remains low throughout the path taken by the fluid in this portion of the flow. There is never a strong electric field and thus never a strong polarization or a strong DEP force. Any fluid that flows along this path is largely unaffected.

The second region is middle group, corresponding to approximately to $y = 40 - 80$ and $y = 160 - 120$ on figure 6.6. This is the area where the magnetic field gradient is highest, the part where the magnetic field is in the steep slopes on the sides of the Gaussian. In this area, the DEP force is both strongest and is most strongly varying. Due to the symmetries of the problem this force will always directed towards the peak magnetic field whether the fluid is moving above or below the peak and whether the magnetic feature is a north or south pole. In this region the DEP force results in a net motion of gas towards the third region.

The third region is our central region. This area corresponds to approximately $y = 80 - 120$ on figure 6.6. In this region the magnetic field is strongest but the gradient is not only approximately 0 but it is also only slowly varying meaning very

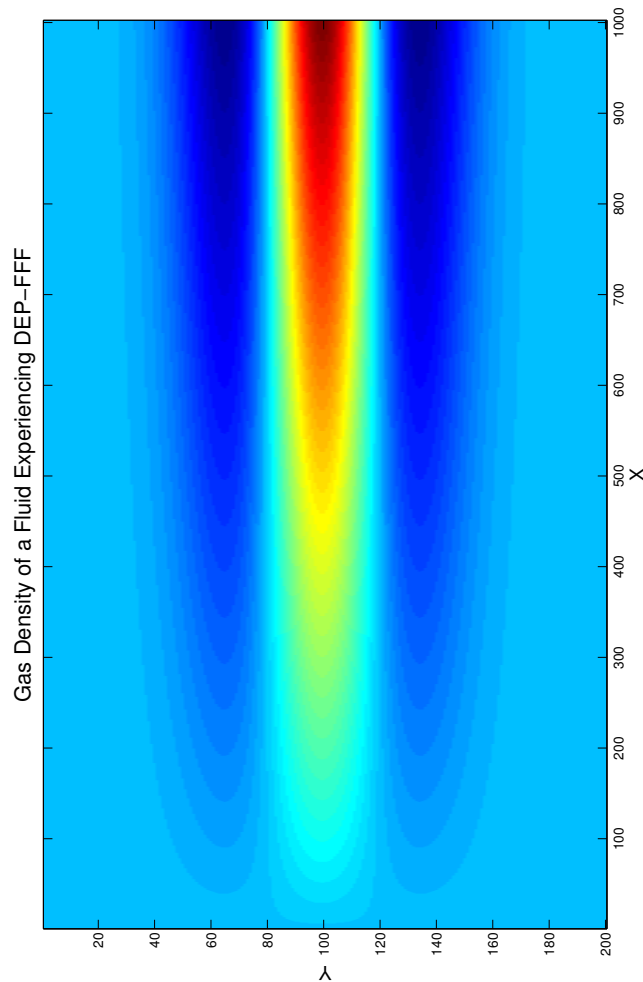


Figure 6.6: The evolving gas density of a flow consisting of a polarized particle moving through a magnetic feature. As the fluid moves along the x-axis, density becomes concentrated in the central region where the magnetic field is strongest. Z-axis is in non-dimensional units. Note that this figure is rotated by 90-degrees.

low divergences and thus almost no net change in density due to DEP.

The combination of the dynamics of these 3 regions results in the pattern of fluid concentrating in our central region seen in this figure.

6.4 Conclusions

We have shown that a dielectrophoretic force exists in a partially ionized plasma, even though that plasma can not sustain electric fields. A moving gas in a magnetic field experiences an electric field and that electric field can provide a polarization to any element or molecule with a non-zero dipole moment or a non-zero polarizability.

By examining the trajectories of free particles under a DEP-like force (figure 6.4) or fluid motion of polarized species in a magnetic feature (6.5) we can see the potential for a DEP force to separate different degrees of polarization. This behaviour inherent to any polarized neutral particles is exploited in many experimental studies. We can also see the potential of a DEP-force to cause density stratification in a spatially varying magnetic structure that is in 6.6. All polarized species end up concentrated in peaks and troughs of the magnetic field but the most polarized species will experience the highest degree of concentration.

However, an examination of the average displacement that a polarized particle would experience after travelling through a typical solar magnetic feature is shown to be very small. The large scale nature of astrophysical magnetic fields results in low electric field strengths and low field gradients and that makes the DEP-force ends up very small in nature.

Even though we should not underestimate the ability of a persistent force, even if small, to make long term changes to the atmospheric composition. The presence of small and large scale mixing in hot atmospheres means that the DEP-force remains insignificant and can not stratify elements based on their polarizability. It can not explain the FIP effect.

Chapter 7

Conclusions

In this thesis we have examined some of the physics of partially ionized plasmas. In particular we have developed a novel fully non-linear finite difference MHD and hydrodynamics code that includes limited interaction between the neutral and ionized species of a partially ionized plasma. These interactions are due to collisions between the charged and neutral species in the plasma.

We explore some of the basic properties of plasmas and some of the interactions that can occur in a partially ionized plasma in chapter 1. We look at the fluid approximation of a plasma with ideal-MHD and we introduce some additional terms which result from the fluid approximations of kinetic effects that are only present when there are both charged and neutral particles present.

The first interaction term in our models is a frictional drag term, resulting from ion-neutral collisions, which we model as a momentum coupling term in the momentum equation of the two fluids. This was previously done in a linear finite difference MHD-Gas code that we refer to as the gas-MHD momentum coupling code (GMMC). The model equations, including the momentum coupling term, and numerical methods for this code are described in chapter 2.

Also in chapter 2, we show that the dispersion relation of a momentum-coupled gas-plasma fluid lacks the presence of the standard MHD modes. We examine how the presence of the momentum coupling term effects the pattern generated by the

constructive and destructive interference pattern from a pair of in-phase sources driving acoustic waves in the gas-plasma fluid. We find that the strength of the momentum coupling effects the phase speed of the hybrid coupled-wave that travels through the gas-plasma mixture and how this different phase speed effects the interference pattern.

Chapter 3 describe the model equations and numerical methods that were used in developing the non linear gas-MHD interactions code (GMIC). Just like GMMC, this code solves the equations of MHD and hydrodynamics to simultaneously model the fluid dynamics of a co-existing neutral gas and ionized plasma and includes terms which are used as fluid approximations of gas-plasma interactions.

This code is used in chapter 4 to explore the dynamics of a momentum coupled, partially ionized, magnetized plasma. First we look at the expansion of a non-equilibrium Gaussian density perturbation which we refer to as *spherical bombs*. These perturbations result in a reaction from the surrounding fluid where either an over-density in the centre results in a rapid expansion forcing surrounding material away, or an initial negative perturbation results in a rapid inflow to 'fill in' the hole in density.

We see how the frictional coupling effects the plasma like non-zero resistivity would. Instead of current (velocity) in the plasma being dissipated into heat it is dissipated into motions in the gas. It is a more complex damping term as if the two fluids have closely matched (in phase) waves then the damping is small; if there is a large mismatch then the damping is also large. This means it has a different effect on waves in the plasma than just a resistive term.

The explosion or implosion of these bombs is modified by the presence of momentum coupling. The presence of momentum coupling allows the magnetic field to influence the dynamics of both fluids instead of just the plasma while the gas allows some measure of cross-field diffusion previously not available to the plasma alone.

We also look at the interaction between a set of perpendicularly travelling waves in the mixed fluid. The phase speed is once again modified by the presence of the coupling with the gas, blurring the lines between the MHD modes and removing much of the directional dependence in speed of MHD waves. We also see the formation of blobs of over-dense plasma which we call 'plasmoids' and loops of magnetic field which

are not formed by the magnet-acoustic waves on their own.

The second interaction term that we add to ideal-MHD in both codes is a novel Alfvén ionization (AI) term. The theory of AI is described in chapter 1 and we derive criteria that have to be met for a partially ionized plasma to support AI in section 1.5.2.2. Laboratory experiments have shown the experimental confirmation of AI and we expect (in section 5.3) that there exist several astrophysical contexts where AI could be important, in particular, brown dwarf and the Solar atmosphere. The incorporation of a fluid approximation of this term into both codes is described in their respective chapters. The AI term captures the kinetic process of ion-neutral collisions, charge-separation, electron acceleration and electron-impact ionization into a single term that depends only on the fluid variables, the critical velocity and the a scalar ionization efficiency term, f .

By calculating the relative velocity between the plasma and neutral fluids this AI term calculates a rate of change of the two species. Effectively turning gas into plasma by ionization at the cost of the kinetic energy of the fluids.

This ionization mechanism significantly effects the plasma dynamics. In chapter 5 we see that AI is a directional, frequency and amplitude dependent damping term. This is once again a more complex damping term than the momentum coupling or a resistivity term causes. The damping only comes into play when the relative velocities exceed a threshold and instead of reducing the kinetic energy of the plasma to move the gas (or heat the plasma as resistive MHD does) the kinetic energy is exchanged for internal energy as plasma has a higher internal energy than the gas.

This damping term effects the waves that pass through a partially ionized plasmas as long as the criteria for AI are met and the relative velocity threshold is exceeded, this results in a replication of a limit, at the critical velocity, where a partially ionized plasma will resist any increase in relative velocity which is behaviour seen in experiment. The anisotropy of the effect only being in operation for motion perpendicular to the B-field results in an anisotropic influence on plasma dynamics.

New plasma created by AI is also seen to have an effect on the fluid. The new plasma creates regions of over-densities which naturally drive motion in the plasma;

these regions are the sources for new wave motion in the partially ionized plasma. The same is found in the gas where a reduction in density effects its dynamics.

We found a dependence on the plasma β for AI. High β plasmas are more susceptible to Alfvén ionization as the motion across the field is less effected by the magnetic field and as such relative velocities in the perpendicular direction can be higher. The plasma β can not be pushed to an arbitrary limit though because AI required the electrons to be magnetised which needs a magnetic field of sufficient strength.

We also see that the momentum coupling scenarios in chapter 4 where Gaussian shaped over and under densities are allowed to explode/implode can be exploited for AI. The double bomb scenario designed to simulate the AI at a pocket of partially ionized plasma that has undergone recent recombination. We show this scenario to be particularly effective at ionization but emphasise that it is not able to completely undo the recombination event.

This chapter also shows that momentum coupling effects the amount of AI that can take place. Higher momentum coupling terms reduce the total AI and the AI rates. This is expected since relative velocities are reduced by a momentum coupling term.

Importantly, have shown that the non-linear finite code GMIC is able to not only model both momentum coupling and AI from the novel fluid AI term but it also models knock-on effects of these mechanisms on both the gas and plasma. This results in a numerical code that simulates both an MHD-plasma and a neutral gas simultaneously, models the strength of the momentum coupling and AI that occurs from their interactions and models the effects of these mechanisms on both fluids. The motion of the fluids effects the neutral-plasma interactions and the neutral-plasma interactions effect the fluids.

Chapter 6 takes an aside from the finite difference gas-MHD simulations to explore the idea of a dielectrophoretic force stratifying the mixed species atmosphere of the Sun's photosphere. We show that there is a significant variation in the magnitude of this force on different elements due to the different polarizability to mass ratios of these elements and that the DEP-force can result in concentrations of polar molecules in regions of high magnetic field. However, we also calculate that the magnitude of the

displacement of these polar particles is incredibly small for both the E-field from the magnetic field and the ambi-polar field caused by the different diffusion rates of the electrons and ions.

7.1 Further Work

We shall now briefly describe possible extensions to this work.

GMIC is shown to be able to model partially ionized plasmas, where a lot of numerical approaches treat the neutrals as additional terms in the MHD model equations GMIC includes them as a separate fluid. This approach allows certain interactions to be modelled that wouldn't otherwise be possible. This could be extended to include more possible effects.

Radiative transfer through a gas is different than a plasma, it is therefore also different through a partially ionized plasma than a fully ionized plasma. This could also be extended to photoionization where the gas interacting with a radiation field can be ionized into plasma. GMIC would be able to model the effects of this on the dynamics of both fluids.

GMIC, without the AI subroutine, could be an effective tool for understanding plasmas where there is a source term of gas, even if that plasma is otherwise completely ionized. Imagine a fully ionized plasma into which is inserted a surface which is a source of neutrals, these neutrals diffuse into the plasma as a whole. There will exist a transition region surrounding this source where the plasma can be treated as a partially ionized plasma which will likely have different plasma and gas temperatures. This could be relevant in many contexts such as a comet interacting with the upper atmosphere of the Sun or a cryogenic fuel pellet injected into a tokamak plasma (Sagdeev et al. 1986)(Garzotti et al. 2010). This region may define the physics of the entire plasma and our gas-MHD interactions code could be used to understand this region.

The Alfvén ionization simulations can be put to use in directly simulating some of the astrophysical contexts described in 5.3. In particular, it could be that AI is very important in determining the ionization fraction of brown dwarf atmospheres.

GMIC itself (or the AI fluid approximation used for GMIC) could be used as part of a campaign to model atmospheres. A look at the ionization rates that would be expected in a plasma with the plasma parameters that a brown dwarf has (densities, pressures, magnetic fields etc.) could provide great insight.

The AI fluid approximation has great scope for improvement. We use a scalar term, that we call the AI efficiency term f . We also choose f based in a desire to capture both the dynamics of the fluids and the AI mechanism not from any physical insight. It is entirely possible that f is not a scalar, that it has some temperature or fluid velocity dependence. The limitations of our choice of f is discussed in section 5.4, where we conclude that f is likely much larger than the values we use for our simulations.

A closer look at the physical mechanism for AI would improve this term. We just approximate the microscopic physics that produces AI but a model that incorporates both the microscopic and macroscopic physics would be more accurate. Exactly what happens when a neutral gas impinges on an ionized, magnetized seed plasma is not known. If a kinetic or PIC model that can take the two, interpenetrating fluids and can simulate the displacement of neutrals, the formation of electrons, the acceleration of these electrons to ionization energies and then the ionizing collisions that these electrons undergo would allow us to have a direct link between fluid velocities and the ionization rate.

Even if a hybrid code, which simultaneously captures the kinetics and fluid dynamics, is not the end result the results from such a computational project could improve the AI term in the fluid code GMIC by taking f into a physically sound definition.

Bibliography

Alfvén, H. 1942, *Stockholms Observatoriums Annaler*, 14, 2

Alfvén, H. 1950, *Cosmical electrodynamics* (Clarendon Press)

Alfvén, H. 1960, *Rev. Mod. Phys*, 32

Allard, F., Hauschildt, P. H., Alexander, D. R., Tamanai, A., & Schweitzer, A. 2001, *ApJ*, 556, 357

Angerth, B., Block, L., Fahleson, U., & Soop, K. 1962, *Experiments with partly ionized rotating plasmas*, Tech. rep., Royal Inst. of Tech., Stockholm

Annaloro, J., Morel, V., Bultel, A., & Omaly, P. 2012, *Phys. Plasmas*, 19, 073515

Arber, T., Haynes, M., & Leake, J. E. 2007, *ApJ*, 666, 541

Arber, T. D., Longbottom, A. W., Gerrard, C. L., & Milne, A. M. 2001, *J. Comput. Phys.*, 171, 151

Aschwanden, M. J. 2002, *Space Science Reviews*, 101, 1

Asplund, M., Grevesse, N., & Sauval, A. J. 2005, in *Cosmic abundances as records of stellar evolution and nucleosynthesis*, Vol. 336, 25

Asplund, M., Grevesse, N., Sauval, A. J., & Scott, P. 2009, arXiv preprint arXiv:0909.0948

Bayliss, A., Gunzburger, M., & Turkel, E. 1982, *SIAM Journal on Applied Mathematics*, 42, 430

- Beckers, J. 1968, *Sol. Phys.*, 3, 258
- Bellot Rubio, L. R. 2009, *Astrophysical Journal*, 700, 284
- Berger, E., Basri, G., Fleming, T., et al. 2010, *ApJ*, 709, 332
- Boas, M. L. 2006, *Mathematical Methods in the Physical Sciences* (John Wiley & Sons, Inc)
- Bote, D. & Salvat, F. 2008, *Phys. Rev. A*, 77, 042701
- Boyd, T. J. M. & Sanderson, J. J. 2003, *The physics of plasmas* (Cambridge University Press)
- Brenning, N. 1981, *Plasma Physics*, 23, 967
- Brenning, N. 1992, *Space Science Reviews*, 59, 209
- Brenning, N. & Lundin, D. 2012, *Phys. Plasmas*, 19, 093505
- Brown, J. C. 1973, *Sol. Phys.*, 31, 143
- Brown, S. C. 1966, *Introduction to electrical discharges in gases* (John Wiley and Sons)
- Carroll, B. W. & Ostlie, D. A. 2007, *An Introduction to Modern Astrophysics*, 2nd edn., ed. S. F. P. Addison-Wesley
- Chen, F. F. 1984, *Plasma Physics and Controlled Fusion Volume 1: Plasma Physics* (Springer)
- Chitta, L., Van Ballegooijen, A., van der Voort, L. R., DeLuca, E., & Kariyappa, R. 2012, *ApJ*, 752, 48
- Cloutier, P., Daniell Jr, R., Dessler, A., & Hill, T. 1978, *Astrophys. Space Sci.*, 55, 93
- Colonus, T. 2004, *Annu. Rev. Fluid Mech.*, 36, 315
- Costall, A. W., McDavid, R. M., Martinez-Botas, R. F., & Baines, N. C. 2011, *Journal of turbomachinery*, 133, 021005

- Cowling, T. G. 1976, Bristol, Adam Hilger, Ltd., 1976. 145 p., 1
- Crockett, P. J., Mathioudakis, M., Jess, D. B., et al. 2010, *Astrophys. J. L.*, 722
- da Costa, A., Diver, D., & Stewart, G. 2001, *A&A*, 366, 129
- Danielsson, L. 1973, *Astrophys. Space Sci.*, 24, 459
- Danielsson, L. & Brenning, N. 1975, *Physics of Fluids*, 18, 661
- Delobbeau, F. 1971, *The Environment of the Earth* (D. Reidel Publishing Company), 13
- Dere, K., Landi, E., Mason, H., Fossi, B. M., & Young, P. 1997, *Astronomy and Astrophysics Supplement Series*, 125, 149
- DeVore, C. R. 1991, *J. Comput. Phys.*, 92, 142
- Diver, D. A., Fletcher, L., & Potts, H. E. 2005, *Solar Physics*, 227
- Diver, L., Potts, H. E., & Teodora, L. F. A. 2006, *N. J. Phys.*, 265
- Drawin, H. 1969, *Zeitschrift für Physik*, 225, 483
- Dudson, B., Umansky, M., Xu, X., Snyder, P., & Wilson, H. 2009, *Comput. Phys. Commun.*, 180, 1467
- Elmore, D. F., Rimmele, T., Casini, R., et al. 2014, in *SPIE Astronomical Telescopes+ Instrumentation*, International Society for Optics and Photonics, 914707–914707
- Fahleson, U. V. 1961, *Phys. Fluids*, 4, 123
- Falle, S. 2002, *ApJ*, 577, L123
- Feldman, U. & Laming, J. M. 2000, *Physica Scripta*, 61, 222
- Feldman, U. & Widing, K. G. 2002, *Phys. Plasmas*, 9, 629
- Feldman, U. & Widing, K. G. 2007, *Space Science Reviews*, 130, 115
- Formisano, V., Galeev, A., & Sagdeev, R. 1982, *Planetary and Space Science*, 30, 491

- Fridman, A., Chirokov, A., & Gutsol, A. 2005, *J. Phys. D: Appl. Phys.*, 38, R1
- Froula, D. H., Luhmann Jr, N. C., Sheffield, J., & Glenzer, S. H. 2011, *Plasma scattering of electromagnetic radiation* (Elsevier)
- Garzotti, L., Baylor, L., Köchl, F., et al. 2010, *Nucl. Fusion*, 50, 105002
- Gascoyne, P. R. & Vykoukal, J. 2002, *Electrophoresis*, 23, 1973
- Geiss, J. & Bochsler, P. 1985, *Isotopic ratios in the solar system*, 1, 213
- Givoli, D. 1991, *J. Comput. Phys.*, 94, 1
- Goedbloed, J. P., Keppens, R., & Poedts, S. 2010, *Advanced magnetohydrodynamics: with applications to laboratory and astrophysical plasmas* (Cambridge University Press)
- Goedbloed, J. P. & Poedts, S. 2004, *Principles of magnetohydrodynamics: with applications to laboratory and astrophysical plasmas* (Cambridge university press)
- Golden, D. & Bandel, H. 1966, *Physical Review*, 149, 58
- Golub, L., Krieger, A., Harvey, J., & Vaiana, G. 1977, *Sol. Phys.*, 53, 111
- Griffiths, D. J. & College, R. 1999, *Introduction to electrodynamics*, Vol. 3 (Prentice Hall Upper Saddle River, NJ)
- Guerra, M., Parente, F., Indelicato, P., & Santos, J. 2012, *Int. J. Mass Spectrom.*, 313, 1
- Gurnett, D. A. & Bhattacharjee, A. 2005, *Introduction to Plasma Physics: With Space and Laboratory Applications* (Cambridge University Press)
- Haerendel, G. 1986, *Geophys. Res. Lett.*, 13, 255
- Hagstrom, T. 1999, *Acta numerica*, 8, 47
- Helling, C., Jardine, M., & Mokler, F. 2011a, *ApJ*, 737, 38

- Helling, C., Jardine, M., Stark, C., & Diver, D. 2013, *ApJ*, 767, 136
- Helling, C., Jardine, M., Witte, S., & Diver, D. 2011b, *ApJ*, 727, 4
- Heyvaerts, J., Priest, E., & Rust, D. 1977, *ApJ*, 216, 123
- Hou, T. Y. & LeFloch, P. G. 1994, *Mathematics of computation*, 62, 497
- Huba, J. D. 2011, NRL: Plasma formulary, Tech. rep., DTIC Document
- Huo, W. M. & Kim, Y.-K. 1999, *Plasma Science, IEEE Transactions on*, 27, 1225
- Inokuti, M. 1971, *Rev. Mod. Phys.*, 43, 297
- Israeli, M. & Orszag, S. A. 1981, *J. Comput. Phys.*, 41, 115
- Jancel, R. & Kahan, T. 1966
- Kaganovich, I. D., Startsev, E., & Davidson, R. C. 2006, *N. J. Phys.* , 8, 278
- Keys, P. H., Mathioudakis, M., Jess, D. B., et al. 2011, *ApJ*, 740, L40
- Khodachenko, M., Arber, T., Rucker, H. O., & Hanslmeier, A. 2004, *A&A*, 422, 1073
- Kieffer, L. J. & Dunn, G. H. 1966, *Reviews of Modern Physics*, 38, 1
- Kim, Y.-K. & Rudd, M. E. 1994, *Phys. Rev. A*, 50, 3954
- Kneer, F. et al. 2006, *ApJ*, 636, 496
- Laidler, K. J. 1977, in *Chemical kinetics* (McGraw-Hill)
- Laming, J. M. 2012, *Astrophysical Journal*, 744, 115
- Landi, E., Del Zanna, G., Young, P., Dere, K., & Mason, H. 2012, *ApJ*, 744, 99
- Lax, P. & Wendroff, B. 1960, *Commun. Pure Appl. Math.*, 13, 217
- Leake, J. E., Lukin, V. S., Linton, M. G., & Meier, E. T. 2012, *ApJ*, 760, 109
- Lehnert, B. 1967, *Phys. Fluids*, 10, 2216

- Lehnert, B., Bergström, J., & Holmberg, S. 1966, *Nucl. Fusion*, 6, 231
- Lide, D. R. 2008, *The CRC Handbook of Chemistry and Physics (CRC)*
- Lites, B. & Skumanich, A. 1990, *ApJ*, 348, 747
- Lotz, W. 1967, *Zeitschrift für Physik*, 206, 205
- MacCormack, R. 2003, *Journal of spacecraft and rockets*, 40, 757
- MacLachlan, C. S., Diver, D. A., & Potts, H. E. 2009, *N. J. Phys.* , 11, 063001
- Marsch, E. 1991, *MHD Turbulence in the Solar Wind*, ed. R. Schwenn & E. Marsch, 159–241
- McBride, J. B., Ott, E., Boris, J. P., & Orens, J. H. 1972, *Phys. Fluids*, 15, 2367
- Mitchell, A. R. & Griffiths, D. F. 1980, *The finite difference method in partial differential equations (John Wiley)*
- Moestl, C., Hanslmeier, A., Sobotka, M., Puschmann, K., & Muthsam, H. J. 2006, *Sol. Phys.*, 237
- Newell, P. T. 1985, *Rev. Geophys.*, 23, 93
- Ofman, L. & Davila, J. 1995, *Journal of Geophysical Research: Space Physics (1978–2012)*, 100, 23427
- Overton, M. L. 2001, *Numerical computing with IEEE floating point arithmetic (Siam)*
- Pande, M., Gaur, V., & Tripathi, B. 1969, *Sol. Phys.*, 7, 17
- Pandey, B. & Wardle, M. 2008, *MNRAS*, 385, 2269
- Peng, H., Alvarez, N. T., Kittrell, C., Hauge, R. H., & Schmidt, H. K. 2006, *J. Am. Chem. Soc.*, 128, 8396
- Petelski, E., Fahr, H., Ripken, H., Brenning, N., & Axnas, I. 1980, *A&A*, 87, 20

- Pethig, R. 2010, *Biomechanics*, 4, 022811
- Pradhan, A. K. & Nahar, S. N. 2011, *Atomic astrophysics and spectroscopy* (Cambridge University Press)
- Press, W. H., Vetterling, W. T., Teukolsky, S. A., Flannery, B. P., & Greenwell Yanik, E. 1994, *SIAM Review*, 36, 149
- Reese, D. R. 2013, *A&A*, 555, A148
- Revercomb, H. & Mason, E. A. 1975, *Anal. Chem.*, 47, 970
- Richtmyer, R. D. 1963, *A survey of difference methods for non-steady fluid dynamics* No. 63 (National Center for Atmospheric Research)
- Riley, K. F., Hobson, M. P., & Bence, S. J. 2006, *Mathematical methods for physics and engineering: a comprehensive guide* (Cambridge University Press)
- Rimmer, P. & Helling, C. 2013, *ApJ*, 774, 108
- Rubio, L. B. 2009, *ApJ*, 700, 284
- Ruffini, R., Vereshchagin, G., & Xue, S.-S. 2010, *Physics Reports*, 487, 1
- Russell, A. J. & Fletcher, L. 2013, *ApJ*, 765, 81
- Rutherford, E. 1911, *The London, Edinburgh, and Dublin Philosophical Magazine and Journal of Science*, 21, 669
- Sagdeev, R., Shapiro, V., Shevchenko, V., & Szego, K. 1986, *Geophys. Res. Lett.*, 13, 85
- Saha, M. 1920, *Nature*, 105, 232
- Saha, M. N. 1921, *Proceedings of the Royal Society of London. Series A*, 99, 135
- Sandars, P. 1965, *Physics Letters*, 14, 194

- Scherrer, P., Schou, J., Bush, R., et al. 2012, in *The Solar Dynamics Observatory* (Springer), 207–227
- Schmelz, J. T., Reames, D. V., von Steiger, R., & Basu, S. 2012, *Astrophysical Journal*, 755, 33
- Sherman, J. 1973, *Astrophys. Space Sci.*, 24, 487
- Stark, C. R., Helling, C., Diver, D. A., & Rimmer, P. B. 2013, *ApJ*, 776, 11
- Stein, R. F. & Nordlund, A. 1998, *Astrophysical Journal*, 499, 914
- Steiner, O., Hauschildt, P., & Bruls, J. 2001, *A&A*, 372, L13
- Steiner, O., Knölker, M., & Schüssler, M. 1994, in *Solar surface magnetism* (Springer), 441–470
- Stephens, D., Leggett, S., Cushing, M. C., et al. 2009, *ApJ*, 702, 154
- Tonks, L. & Langmuir, I. 1929, *Phys. Rev.*, 33, 195
- Torbert, R. 1990, *Advances in space research*, 10, 47
- Tsynkov, S. V. 1999, *SIAM Journal on Scientific Computing*, 21, 166
- Utz, D., Hanslmeier, A., Müller, R., et al. 2010, *Astronomy and Astrophysics*, 511
- Vitas, N., Fischer, C., Vögler, A., & Keller, C. 2011, *A&A*, 532, A110
- Wallis, M. K. 1972, in *Cosmic Plasma Physics* (Springer), 137–140
- Wang, X.-B., Vykoukal, J., Becker, F. F., & Gascoyne, P. R. 1998, *Biophys. J.*, 74, 2689
- Wang, X.-B., Yang, J., Huang, Y., et al. 2000, *Anal. Chem.*, 72, 832
- Wilson, A. & Diver, D. A. 2013, *European Planetary Science Congress 2013*, held 8–13 September in London, UK. Online at: <http://meetings.copernicus.org/epsc2013>, id.EPSC2013-1030, 8, 1030

Zweibel, E. G., Lawrence, E., Yoo, J., et al. 2011, *Phys. Plasmas*, 18, 111211